A Hybrid Microfluidic Chip with Multielectrode Geometry for Cell Concentration using AC pDEP and Multiwave ACEOF

Thesis Submitted in accordance with the requirement of the University of Liverpool for the degree of Doctor in Philosophy in the Faculty of Science and Engineering by

Muhammad Wajih Ud Din Chughtai

August 2021

Department of Electrical Engineering and Electronics

Abstract

A Hybrid Microfluidic Chip using Multielectrode Geometry for Cell Concentration using AC pDEP and Multiwave ACEOF.

Muhammad W. Chughtai

Microfluidic systems for cell concentration are becoming increasingly important tools in life science research and diagnostics. The ability to handle life cells in a highly controlled environment offers opportunities to automate complex procedure such as IVF, liquid biopsy, and single-cell isolation. Despite promising applications, present-day cell isolation techniques, either lag efficiency or deal with specific cells only. On the other hand, AC Electroosmotic flow (ACEOF) apply force on fluid medium only and therefore does not rely on cell properties. From this point of view, AC EOF is an exciting alternative for current cell concentration techniques. This research combines two AC Electrokinetic phenomena, namely AC positive dielectrophoresis (AC pDEP) and AC Electroosmotic flow (ACEOF), to build a microfluidic device that is capable of providing a cell concentration factor of 100000/mL at the flow rate of $45\mu L/min$. To achieve this goal, firstly, AC pDEP and ACEOF response are thoroughly examined against the parameters such as electrode geometry, interelectrode gap, fluid conductivity, chamber height, AC signal strength and frequency, and it is established that $75\mu m$ interelectrode gap provide an ACEOF vortex size of $430\mu m$ at $10V_{PP}, 1kHz$ for the fluid conductivity of $10mS/m$ while $100\mu m$ interelectrode gap provides a vortex size of $290\mu m$ for the same parameters. On the other hand, $20V_{PP}, 1MHz$ provides AC pDEP efficiency of $\sim 50\%$ at $300\mu m$ chamber height for a pair of electrodes. Based on these results, a microfluidic device is built with ten individually addressable electrodes, which offers an AC pDEP efficiency of $> 95\%$ at $45\mu l/min$ flow rate, with overall ACEOF yield of $> 90\%$ and an concentration factor

of 100000 using 2000s AC pDEP and five waves of ACEOF. In the end, results of both AC pDEP and ACEOF are validated using finite element modelling that also provides a model for multi-vortex ACEOF.

Acknowledgement

I want to express my utmost gratitude and thanks to my primary supervisor, Dr Kai Hoettges, for giving me the golden opportunity to work as a full-time PhD student under his kind supervision. Without his guidance, persistent help, constant encouragement, and patience, this PhD work would not have been possible.

I am also deeply indebted to my secondary supervisor, Dr Harm V. Zalinge, for all his guidance and advice throughout my PhD research. My special thanks to my respected PhD assessors, Professor Steve Hall and Dr Ian Sandall, for the good assessment and constructive feedback of my research work. My gratitude extends to all technical team and supporting staff, especially Ms Alison Goodyear and Dr David Donaghy.

I want to specifically acknowledge the University of Liverpool for a full-time studentship award without which this PhD would be a dream.

Finally, and most importantly, I would like to thank my family, especially my parents Waheed and Saira, for their support and love and my siblings, Fasiha, Muneeza, Dr Salaha, Rabiya and especially Faiqa. I would love to mention my son Arslan whose smiles give me the courage to keep working hard and of course my wife Sameen.

Indeed, this work would never be possible without the hands of so many amazing people and friends, especially Ali and Dr Chitradeep, who have been encouraging my PhD journey.

Many thanks.

Contents

List of Tables

List of Figures

List of Abbreviation

AC	Alternating current
ACEK	AC Electrokinetic phenomenon
ACEOF	AC electroosmotic Flow
AMT	Active Mechanism Techniques
ACT	Advanced Cell Therapy
CRC	Capacitor – Resistor – Capacitor
CM	Clausius Mossotti
CTCs	Circulating Tumour Cells
DC	Direct Current
DCEK	DC Electrokinetic phenomenon
DEP	Dielectrophoresis
DEP FFF	DEP Field-Flow Fractionation
F_{DEP}	Dielectrophoretic Force
EDL	Electric double-layer
EHD	Electrohydrodynamic
EKP	Electrokinetic Phenomenon
EMI	Electromagnetic Isolation
EOF	Electroosmotic Flow
EP	Electrophoresis
EOT	Electrorotation
ETF	Electrothermal flow
FMC	Filtration Microwell Chip

FEM	Finite Element Modelling
FACS	Fluorescence-Activated Cell Sorting
HMW	Hydrodynamic Microwell
PAN	Immunopanning
PBS	Phosphate-Buffered Saline
IVF	In Vitro Fertilisation
IHP	Inner Helmholtz plane
iDEP	Insulated Dielectrophoresis
Int.DEP	Integrated Dielectrophoresis
iDMACS	Integrated Dielectrophoretic Magnetic-Activated Cell Sorter
ITO	Interdigitated Electrode Arrays
MACS	Magnetic Activated Cell Sorting
MM	Manual Micromanipulation
MFBS	Membrane Filtration-Based cell Sorting
MBPE	Modified Boltzmann-Poisson's Equation
MWACEOF	Multi wave ACEOF
MTB	Mycobacterium Tuberculosis
nDEP	Negative Dielectrophoresis
OTCS	Optical Tweezers
OHP	Outer Helmholtz plane
PO	Particle orientation
PMT	Passive Mechanism Techniques
PBE	Poisson Boltzmann Equation

PS	Polystyrene
AC pDEP	Positive DEP
REOF	Reverse Electroosmotic Flow
RM	Robotic Micromanipulation
SAM	Shoot Apical Meristem
SCA	Single or Isolated Cell Analysis
TWDEP	Travelling Wave Dielectrophoresis
TWEOF	Travelling Wave Electroosmotic Flow
YPD	Yeast extract Peptone Dextrose

List of symbols

Chapter 2

P_e	Peclet number
α	Particle radius
u	Fluid velocity
D_C	Diffusion constant for low Reynolds number
K_b	Boltzmann's constant
T	Temperature
η	fluid viscosity
$U_{settling}$	Stokes' settling velocity
P_ρ	Particles Density
ρ	Fluid density
g	Acceleration due to gravity

S	Spherical area of the solid surface
F_{drag}	Viscous drag coefficient
v_t	Relative velocity of the fluid to the boundary
F_q	Coulomb force
Q	Electric Charge
r	distance between the charges
K	Coulombs constant
E	Electric field
Z_{DL}	Reactance
C_{DL}	Series sum of Stern layer capacitance and diffusion layer capacitance
$\emptyset_E$	Electric potential
P_c	Volume charge density
N_i	Ion type
W_i	Magnitude of work done by the ions
Z_i	Number of valence electrons of each type
e	Elementary charge constant
κ	Debye's parameter
ω_r	Charge relaxation frequency
σ	Conductivity
E_t	Tangential component of Electric field
E_n	Normal component of Electric field
f_c	Characteristic Frequency
C_d	double-layer capacitance

R_m	fluid resistance.
g_d	Interelectrode gap
F_{DEP}	Electrophoretic force
σ_q	Surface charge density
l	Length of a dipole in metres
P_D	Dipole moment
E_{DIP}	Dipole field
$\propto$	Polarisability of material
P_{AVG}	Average dipole moment
$\varepsilon p'$	Complex permittivity of cells
$\varepsilon m'$	complex Permittivity of fluid medium
σ_P	Particle's conductivity
σ_M	Medium's conductivity
ω_{co}	Cross over frequency
ω_r	Maxwell-Wagner relaxation frequency
τ_r	Relaxation time
v_{DEP}	DEP velocity
v_{EOF}	Electroosmotic velocity
v_{REOF}	Reverse electroosmotic velocity
u_o	Initial particle velocity
r	Distance to the centre of the gap
Y_{DEP}	DEP Yield
K_n	Knudsen number

λ	Intermolecular distance of the fluid
l	Characteristic length scale of the system
ρ_m	fluid density
u	Fluid Velocity
P	Fluid Pressure
f_t	Total applied body force
ρ_m (u.∇)	Inertial term
$-\nabla P$	Pressure gradient
$\eta\nabla^2.u$	Viscous term
R_e	Reynold's number
S_n	Stoke's number
D_P	Particle diameter
u_{EOF}	DC Electroosmotic velocity
ζ	Zeta potential
E_t	Tangential electric field
ΔC	Distributed capacitor of constant value
d	Electrode length
V_d	Potential drop across the EDL
V_o	AC potential applied to the electrodes
Σ_q	Surface charge density in diffuse layer
K	Reciprocal of Debye length
ω	Angular frequency
x	Centre of the interelectrode gap

Ω	Dimensionless frequency
Φ	Potential at a given point in the bulk electrolyte
Z_{DL}	Impedance of double layer
Λ	Ratio of the potential drop across the diffuse layer to the potential drop across the EDL

Chapter 3

$V_D(x, y, z)$	Potential drop across the double layer
V	Applied potential
V_{eff}	Effective Voltage
V_{PP}	Peak to peak Voltage

Chapter 4

DIW	Deionised water
N_2	Nitrogen gas
Au	Gold
Cr	Chromium
I_c	Electrical current

Chapter 5

RPM	Revolutions per minute
I_{uv}	Incident energy
EUV	Incident light energy

T	Exposure time
I_{UV}	Incident energy
UV	Ultraviolet
H	Chamber height
W	Chamber width
L	Chamber length

Chapter 6

V	Electrical potential for the fluid flow
σ_q	Fluid conductivity
V_n	Potential applied to each Electrode
V_0	Applied potential
i	An imaginary number
θ	phasor angle
n	number of the electrode
Z_{DL}	Debye's length impedance
ω	AC signal frequency
λ_D	Debye's length
κ^{-1}	Huckle's parameter
Z	Electron assumed Shell
K_B	Boltzmann's constant
T	Temperature
ε	Absolute permittivity

ε_o	Vacuum permittivity
ε_r	Relative permittivity
n^o	Ionic concentration

List of Units

Pressure	$Pa - Pascals$
	$Bar - Bar$
Conductivity	$S/m - Siemens\ per\ meter$
	$mS/m - Mili\ siemens\ per\ meter$
	$\mu S/cm - Micro\ siemens\ per\ centimetre$
Geometry	$mm - Milimeter$
	$cm - Centimeter$
	$\mu m - Micrometer$
	$nm - Nicrometer$
Frequency	$Hz - Hertz$
	$kHz - Kilohertz$
	$MHz - Megahertz$
Voltage	$V_{PP} - Peak\ to\ Peak\ voltage$
	$V_{RMS} - Root\ mean\ squre\ Voltage$
Time	$s - Seconds$
	$\min - Minutes$
	$hrs - Hours$

1 Introduction

1.1 Chapter Overview

This chapter introduces the research area outlining the background and rationale that motivates this current research work. Next, it reviews the state-of-the-art cell concentration techniques highlighting their respective advantages and disadvantages. This chapter then outlines the importance of target cell concentration, which is the primary objective for this current project. Subsequently, this chapter describes the aims and objectives of the proposed research. Furthermore, in this chapter, we presented a holistic overview of the novelty and significant contribution of the proposed work over the existing domain-specific state-of-the-art. Finally, a chapter-by-chapter outline of the thesis is explained.

1.2 Research Motivation

1.2.1 Cell Concentration

Cell concentration is a process that allows the separation of specific types of cells from the heterogeneous mixture of billions of diverse cells and collects the target cells' in the desired zone, therefore increasing cells' concentration [1]. This project aims to provide $\sim 100000\ cells/mL$ cell concentration using AC electrokinetic principles AC pDEP (positive dielectrophoresis) and AC EOF (electroosmotic flow).

The cell concentration has attracted significant attention in academia and clinics due to its applications in the life-science, pharmacy, and medical industries. This new-age technique enables the collection of the rare cell for further analysis. Therefore, it can lead to discovering highly effective drugs and micromachines that could significantly

improve the quality of life [2, 3]. Furthermore, cell concentration helps to examine and investigate a large population of specific types of cells for more comprehensive analysis. Cell concentration technology can study the pathology of specific life-threatening diseases such as cancer, produce more effective vaccinations, and enhance drugs delivery [4,5].

1.2.2 Applications of Cell Isolation and Concentration

This section describes some of the most significant cell isolation and concentration applications:

i. In Vitro Fertilisation

In vitro fertilisation (IVF) is a technique that helps women with fertility issues to have children. IVF requires an egg to be removed from the ovaries and fertilised with motile sperm cells to form an embryo. It is then inserted in the womb to grow and develop [5]. IVF is an expensive process with a success rate between 2% to 29% and often requires two or more attempts. The success rate of IVF depends on women's age, quality of female eggs (oocytes), and most importantly, motility and concentration of sperm cells [5,6].

At least 1 million sperms/ml, of which a minimum of 30% motile and 15% having progressive motility, are required for successful IVF procedures even though pregnancies can be achieved with a 10% population of motile sperm cells, i.e., 100 000 cells [6]. Currently, no device can remove and concentrate motile sperm cells. Therefore, one of the device's applications is to help improve IVF efficiency by providing 100 000 concentrations of pure motile sperm cells only.

ii. Circulating Tumour Cells

Circulating tumour cells (CTCs) are the cancerous cells that break off from the tumour and mix with billions of blood cells. They start circulating in the blood vessels afterwards, most of them do not harm the body, but if any of them get stuck with the vessels, it causes cancer to spread across the body [1, 7-9]. CTCs are responsible for 90% of cancer deaths and therefore are considered an important biomarker for the metastatic progression in cancer [10-12]. Hence, isolating CTCs from the blood samples and performing a liquid biopsy can help early cancer detection. Conventional EpCAM-based concentration method helps isolate CTC from blood but provides a concentration factor of only one after 5Litres of blood throughput [13, 14]. Therefore, there is a need for a device that can provide a greater concentration of CTCs.

iii. Advanced Cell Therapy

Advance cell therapy (ACT) is a technique in which cells are more than minimally manipulated [15]. It involves regenerative medicines surrounded by specific cells [16]. ACT offers a wide range of benefits in the medical landscape, particularly in oncology, cellular immunology, and functional modification of T and natural killer cells [2, 7, 16]. ACT is set to replace traditional medicines in 20 years [16]. Current concentration techniques in the ACT are achieved by using molecules at a specific time during culture; however, it provides limited to moderate cell concentration and limits the use of ACT. Therefore, an improved cell concentration method is vital for the bright future of ACT [17].

iv. Importance of single-cell analysis

Single or isolated Cell analysis (SCA) offers researchers to study cell physiology, biochemistry, and cell to cell variation within a cell population [8]. Single-cell omics allows uncovering the insights of functional diversity of cells genomes and epigenomes that help develop new techniques and medicines to help cure diseases and produce vaccinations [18]. Single-cell analysis and cell Concentration have a significant role in immunology, medicine, life science, and botany [19, 20]. In complex fields such as oncology, neurology, and pharmacy, SCA provides an ideal tool for understanding biological heterogeneity and contributing to its cure [1]. For instance, SCA has played a vital part in developing a solid knowledge of breast cancer, brain cancer, blood cancer, Leukaemia, and melanoma [21-23]. Therefore, a device capable of capturing target cells only and enriching them at a designated area for further studies can help improve life-sciences and medicine.

In summary, cell concentration offers a wide range of applications in specialised fields. For example, as discussed, circulating tumour cells (CTCs), which cause the metastatic spread of cancer, break off from the primary tumour and mixed with blood cells, can be isolated from the bloodstream using cell concentration techniques to be analysed as 'liquid biopsies' [7, 8]. In Vitro Fertilisation (IVF) is a ray of hope for many infertile couples [5]. Cell concentration techniques can isolate motile sperm cells from deformed cells and enrich them to improve IVF process efficiency. Capturing the shoot apical meristem (SAM) cells are also essential for the epigenetic analysis of plants which can also be an application of cell concentration techniques [19]. Advanced cell therapy (ACT) has revolutionised the pharmaceutical and medicine industries' effectiveness, especially in the complex fields of oncology and

regenerative medicines [2, 16, 24]. However, its limitations lie in the impurity of the collected cell samples [25], which can be addressed by utilising cell concentration that provides targeted, pure, and healthy cells. Early cancer detection and CTCs isolation from blood [7, 26], drug discovery and diagnosing [2], food safety [27], precision medicines [15], tissue and organ regeneration [28], targeted gene therapy [29], single-cell analysis [30], and regeneration medicines [31] are some of the applications of cell concentration that can completely transform the way we look at life-science, food safety, and medicine fields.

1.2.3 Present Cell Concentration Techniques

Several techniques have been deployed for single-cell isolation and cell concentration based on the target cell's properties, surface antigen, and labelling tag [29, 32-35]. These techniques are divided into two main categories based on their methodology, applications, and efficiency. The following parameters measure the **efficiency** of these techniques:

i. **Throughput yield** is determined by the total number of cells isolated and collected at the end of the process, divided by the total number of cells before the process [36]. In this project, this is described as the device's overall efficiency.

ii. **Efficacy** is the ability of the process to produce the desired results [37]

iii. **Post-process cell viability** deals with the measure of live and healthy cells within the sample[38].

iv. **The accuracy and purity of the collected sample** is the percentage of target cells in the collected sample. If the sample contains cells apart from the desired cells, it is impure, and the process lags accuracy [39].

v. **Processing speed** takes time to produce the desired throughput [40].

vi. **The cell concentration factor** is the ratio of the number of cells present in the Concentration area divided by the number of cells expected in the concentration area after the process is completed.

vii. **Cell losses** are the number of cells missing from the concentration area after the process is completed. Higher cell loss leads to lower cell efficiency.

The following section summarises the most popular cell concentration techniques, highlighting their merits and demerits.

1.2.3.1 Non - Microfluidic Techniques

Non – microfluidic cell sorting technique is a widespread field ranging from simple membrane filter-based cell Concentration to complex immune magnetic-based Activated Cell Sorting. Following are a few non – microfluidic techniques and their principles.

i. **Fluorescence-Activated Cell Sorting (FACS)** uses principles of flow cytometry (FC) technique. First, the cells are tagged with fluorescent markers and fluorophore-conjugated monoclonal antibodies, as seen in figure 1.1a. The mixed cell suspension is then allowed to run through cytometry. Next, a laser-based fluorescent detector detects the cells based on fluorescent markers. Then, an electrical charge is spread over

the target cells. Finally, cells are sorted with the help of an electrostatic deflection from where particles are added into collection tubes, as shown in figure 1a. FACS is an efficient system with high throughput and a processing speed of 20000 cells/s. However, the process is expensive, with low post-process cell motility, high cell loss of approximately 70%, and requires at least 10,000 cells in each suspension to start the procedure, making FACS not applicable to low cell samples [32, 41-44].

ii. **Magnetic Activated Cell Sorting (MACS)** perform the task by firstly marking the cells with streptavidin-coated magnetic beads and then placing the cell suspension in the magnetic field as seen in the schematic fig 1.1b. The process starts by first magnetising cells. These cells are then attracted towards the field and finally separated from the matrix, as shown in fig 1.1b. The process offers higher throughput than FACS, but the collection contains low purity and impaired cells due to cell labelling. Nevertheless, it is reported in [45] that MACS has $\sim 50\%$ less cell loss.

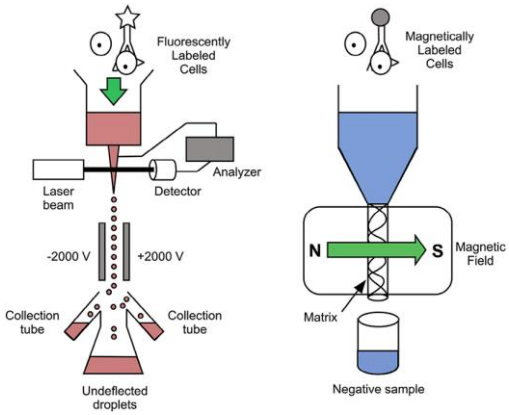

Figure 1.1: Schematic of FACS (left) and MACS (right)[45].

iii. **Density Gradient Centrifugation (DGC)** separates particles based on their size and density, using a medium of graded densities [46], as

illustrated in figure 1.2. Firstly, the mixture of cells is pushed down the medium under a centrifugal force. Then cells float down the medium and are separated based on cell reaction to the density [47]. The technique is label-free and simple to follow. However, the process takes more than 60 minutes to complete [46, 48, 49]. Moreover, cells experience a high level of stress, damaging cell viability. Despite its drawbacks, it offers a separation efficiency of $> 90\%$ and high cell concentration. [45, 47, 49].

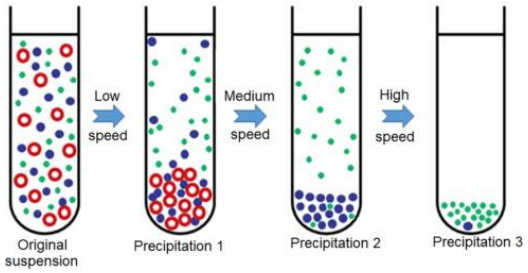

Figure 1.2: Schematic of Density Gradient Centrifugation [46].

iv. **Membrane Filtration-based cell sorting (MFBS)** is a simple pressure-driven separation technique that separates cells based on their size. It offers a low-cost working platform with high throughput. However, the formation of air bubbles and cell clogging affects its efficiency [50].

v. **Manual Micromanipulation (MM)** uses ultrathin glass micropipettes to pick cells manually with an inverted microscope. Figure 1.3a explains the MM principle, where it can be seen that cells are sucked up through pressurised micropipettes and are transferred to the collection vessel via a dispensation unit. This technique isolates embryo cells and has played a role in Dolly sheep cloning by capturing the donated cells. However, despite its simplicity, the technique has low throughput, low yield and high probability of impaired cells [19, 39].

vi. **Robotic Micromanipulation (RM)** is the artificial intelligence (AI) version of MM. Cell isolation is a highly delicate task and requires a skilful expert to perform it. Therefore, a computer vision-based robotic system was introduced for target cells concentration. The robot uses the fluorescent intensities of the marked cells, as seen in figure 1.3b. It removes them from the mixed cell suspension by a slight vacuum connected to the glass micropipettes. The process keeps repeating until target saturation is reached. RM improves cell purity and motility of target cells. The process promises high throughput and a higher motility rate. However, the process is slow and can take more than 24hours to achieve the target concentration [51, 52].

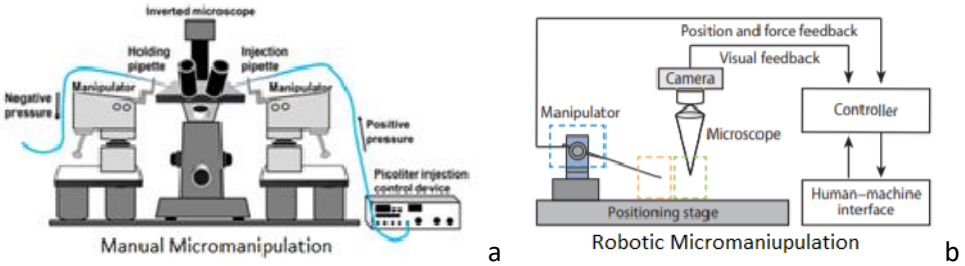

Figure 1.3: Schematic of Manual (a) and Robotic Micromanipulation (b) [52].

vii. **Immunopanning (PAN)** cell suspension is incubated with the antibodies coated plate. Target cells bind with antibodies while remaining cells are washed away. Figure 1.4 illustrates the separation of Papain (Rat retina cells) from a mixture of mixed retina cells wherein 3 step process cells are separated. PAN's efficiency lies in the specificity of antibodies used, making it a costly process with limited applications. Moreover, antibodies produce tension on the cell surface which produces impaired cells [53, 54].

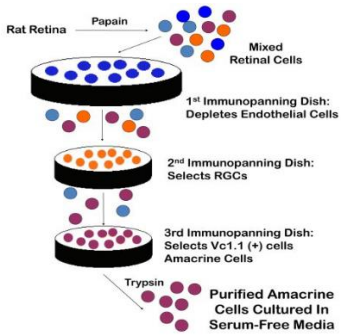

Figure 1.4: Schematic of Immunopanning [54].

viii. **The optical tweezers (OT)** technique uses optical properties of cells, such as a refractive index to sort cells. Then, cells are fluorescence tagged and removed using an optical tweezer, as seen in figure 1.5. However, this technique reduces cells' effectiveness due to contaminations. In addition, it offers low throughput and low efficiency [11, 55, 56].

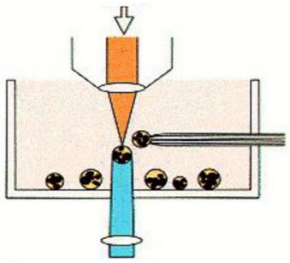

Figure 1.5:Schematic of optical tweezers [55].

ix. **Acoustic technology (AT)** enriches cells using acoustic waves with a wavelength comparable to specific cells dimensions. This creates pressure on the cell and separates them, as shown in figure 1.6. However, despite its low cost and high controllability, the technique has limitations in cell size selectivity, which significantly compromises its efficiency [22, 40].

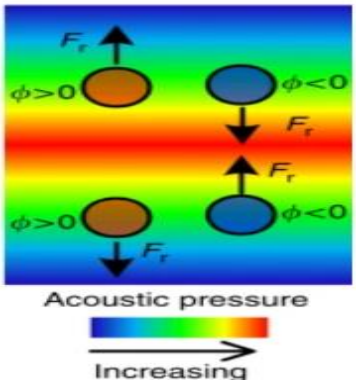

Figure 1.6: Schematic of Acoustic Technology where F_T is terminal force, F_r is reaction force and Ø is acoustic force[40].

Non – microfluidic cell concentration techniques offer a wide range of benefits in medical science. It allows for high volume samples, mainly used for industrial applications; for example, membrane filtration covers 60% of the water treatment industry [57]. In addition, FACS, MACS, OTCS, and AWCS have widespread applications in medicine, pharmacy, research and other biomedical applications [22, 43, 57-60], especially when integrated with microfluidic processes such as dielectrophoresis [26, 27, 61-63].

However, avoiding cell contamination remains a challenge due to cell labelling and tagging [33]. Cell viability is also compromised due to strong magnetic field interactions in MACS [43]. In addition, the probability of cell mixing remains high in the optical tweezers technique, limiting its use in having pure cell concentration [55]. Also, limitations exist in-vivo applications due to non-microfluidic platform size, restricting cell analysis applications [59]. Due to high volume sampling, processing speed is compromised, limiting its use in isolating CTCs from the bloodstream, which requires a high-speed process [10, 12]. Therefore, despite having its advantages, non – microfluidic cell concentration techniques offer low efficiency, limited cell purity, slow speed, and limited applications.

Moreover, non-microfluidic approaches like FACS, MACS, and PAN require cellular tagging, which physically manipulates the cell, thus reducing the cell's motility. Furthermore, MACS and FACS require 3 – 4 hours of processing time to provide the desired efficacy, while DGC can take up to an hour to process the sample. Therefore, such approaches are not ideal for academic research and clinical purpose [36, 59, 64, 65]. For clinical diagnosis, simple, reliable, label-free, cost-effective methods are required that provide a high concentration of motile cells for research, analysis, and applications [45, 47, 49].

1.2.3.2 Microfluidic Techniques

Microfluidic devices mainly focus on intrinsic cell properties such as cell size, shape, electric polarisability, and hydrodynamic properties for cell concentration [30, 35, 62, 66]. Microfluidic devices have many advantages, including low cost, high throughput, easy manufacturing, integration, non-toxicity, and good stability [35, 36, 67]. Because of these characteristics, microfluidic devices are increasingly becoming an essential tool in cell studies. The advantages of microfluidic devices include a high surface to volume ratio, which allows requirements for the starting samples [62, 66, 70], high controllability, speed, cell motility, cell purity, and label-free cell sorting [26, 30, 59, 67]. Microfluidic based cell concentration techniques are further divided into two sub-categories as seen in figure 1.7 (a – h), where figure 1.7 (a – d) are passive microfluidic techniques, and 1.7 (e – f) are active microfluidic techniques.

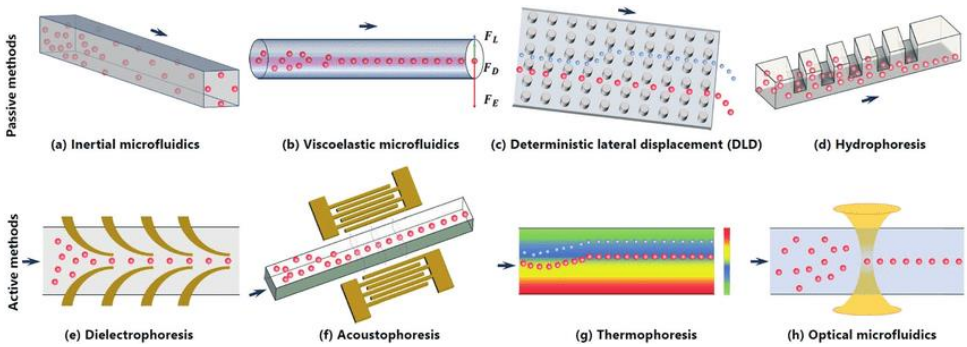

Figure 1.7: Schematic passive and active microfluidic techniques [17].

i. Passive Mechanism Techniques (PMT)

PMT (figure 1.7 a - d) sort cells by deploying cell-intrinsic properties such as density, size, and deformability. These mainly include hydrodynamic microwell (HMW) [65, 80] and filtration microwell chip (FMC) [39].

a. **Hydrodynamic microwell (HMW) concentration technology** relies on its device structure to capture cells with a particular size and shape. However, due to only relying on the cells' size, the probability of anomalies remains high. In some cases, cells tagging/staining is required reducing cells analysis feasibility after capture. Also, the probability of cluster formation remains high [65, 80].

b. **Filtration microwell (FMW) concentration technology** separates the target cell by obstructing cells other than target cells. It is a fast process; however, isolated cells have extremely low purity. Moreover, microporous membranes are functional until clogged [79, 81].

ii. Active Mechanism Techniques (AMT)

AMT (figure 1.7 e - h) is based on the use of specialised integrated features such as electrodes or magnetic geometry [71]. These techniques mainly include dielectrophoresis (DEP) [70, 72, 73], electromagnetic isolation of cells (EMI) [10], and integrated dielectrophoresis iDEP [26, 27, 62, 74] .

a) **Dielectrophoresis**' principle is to separate and capture cells based on the difference in their dielectric properties. This DEP feature allows exceptionally high cell specificity and label-free throughput yield offering pure cell analysis after capture. However, highly optimised electrode geometry is required for maximum efficiency. Moreover, the cell capture rate is slower than MACS. Sometimes, slower speed can cause the Joule heating effect, affecting cells' viability [64, 72]. DEP advantages include biological cell sorting, purification of cell cultures, removing toxic substances from water and food, cell isolation, and concentration of stem cells in bone marrow or peripheral blood. Moreover, DEP has a 'Lab – On – A – Chip' prospect.

b) **Electromagnetic isolation (EMI)** is a microfluidic device with a mid-section of the device installed with a magnet. The technique offers fast separation with low efficiency, and in some cases, cell labelling is required [12].

c) **Integrated Dielectrophoretic (intDEP)** principle integrates non-microfluidic and other microfluidic methods with DEP to generate a combined effect for an improved cell concentration [26]. For instance, DEP is integrated with MACS [76, 77], AW [27, 40, 71], FACS [33, 78]. The technique greatly improves concentration factor with an efficiency of $\sim 75\%$ [38]. However, a combined effect increases the overall cost and processing speed and low cell motility [38, 79].

Despite complex manufacturing and cell clusters formation [24, 72, 82], microfluidic-based concentration technologies offer several advantages over non-microfluidic technologies. For instance, microfluidic devices allow lower volume sample use, enhanced spatial resolution, higher specificity, and increased accessibility [62, 63, 83,

84]. Table 1.1 summarises principles of cell concentration techniques discussed above alongside their efficiency parameters listed as advantaged and disadvantages.

Table 1.1: List of cell isolation and concentration techniques highlighting processing speed, efficiency, efficacy, and cell viability as advantages and disadvantages.

Techniques	Principles	Advantages	Disadvantages
Membrane Filtration-based cell sorting (MFBS)	Size variations of cells	Cost-Effective	Air Bubbles formation Low Efficiency due to Cell Clogging
Manual Isolation	A micropipette is used to pick up the cell manually.	High motility rate Medium paced process	Low throughput Cell Impairing Need a high skill level
Robotic Micromanipulation (RM)	AI-based isolation	High Motility High Throughput	Cell Labelling Slow process
Optical Tweezers	Optical Properties of cell and cell tagging Microfluidic	Work well with cells of similar optical properties.	Very Low Throughput Cell tagging
Immunopanning (PAN)	Immunoprecipitation	High Specificity Fast Speed	Expensive Less Throughput Impaired cells
Acoustic Sorting	Applying acoustic radiations Microfluidic	No labels/tagging required	Very Low Efficiency
Fluorescence-Activated Cell Sorting (FACS)	Fluorescence-based auto cell isolation	Low efficiency High Purity levels	Low Cell Motility Expensive Cell impairing
Magnetic Activated Cell Sorting (MACS)	Cells Tagging with magnetic beads Non-Microfluidic	High efficiency Can operate with parallel samples	Difficult to control Contaminations due to cell tagging Slow processing speed
Density Gradient Centrifugation (DGC)	Cell and medium-density matching Non-microfluidic	High efficiency Cost-effective	Slow processing speed Cell damage due to stresses
Hydrodynamic Microwells (HMW)	Size variation of cells Microfluidic	High Throughput	Specific design for each type of cell
Dielectrophoresis (DEP)	Electrical Properties of cells	High efficiency Efficient Label-free Cost-Effective	Slow process Joule heating effects at high
Int.DEP	Electrical properties of cells and integrator properties	High efficiency	Cell non-viability, Expensive and at times slow

1.3 Research Proposal

It is already established in section 1.2.2 that single-cell sorting and cell concentration have gained attention to analyse specific cells to make clinical decisions and improve procedure efficiency. Therefore, advances in cell concentration techniques have become more critical than ever to meet higher accuracy, efficiency, and process speed. As a result, considerable gains have been made in technological developments for cell sorting. However, as seen in Table 1.1, despite obvious advantages, all the current techniques have their limitations in either low efficiency or low processing speed, decreasing their overall effectiveness.

Moreover, as seen in figure 1.8, while MACS provides low cell losses, the processing speed is slow. On the other hand, robotic manipulation is faster but have higher cell losses than MACS. Also, techniques like acoustic cell sorting and optical tweezers are slow and contribute to high cell losses. Hence, there is still vast room for improvement, especially in decreasing cell loss and improving processing speed. The green spot on figure 1.8 shows the project's target, i.e., the fast device and low cell losses.

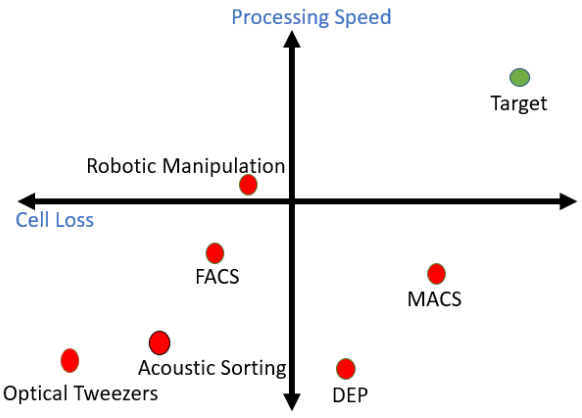

Figure 1.8: Efficiency of state-of-the-art cell concentration techniques illustrated by red spots and green as project targets.

Therefore, the research presents an innovative and highly efficient novel microfluidic device that presents a label-free high collection of target cells by utilising two AC-Electrokinetic phenomena, namely ACDEP and ACEOF. The designed microfluidic device aims to capture target cells from the pressure-driven flow created by a syringe pump and then push the target cell to one specific area on the device, providing a label-free, motile, and highly efficient cell concentration ratio of 100000 at a rapid pace.

1.4 Overview of Project Approach

Now that it is established that the project's objective is to develop a device that provides the cell concentration $> 100\ 000$. This goal is achieved by designing an array of parallel individually addressable coplanar electrodes on a microfluidic device that uses AC pDEP and ACEOF to produce a cell enrichment factor of $> 100\ 000$ in less than $45min$ with an overall efficiency of $> 95\%$. AC pDEP is measured for cell trapping, while ACEOF is used to sweep cells to one end of the device and increase cell concentration. The formula measures cell concentration factor (CF):

$$CF = \frac{Total\ cells\ in\ the\ concentration\ area}{Expected\ cells\ in\ the\ concentration\ area} \quad 1.1$$

AC pDEP and ACEOF are AC Electrokinetic phenomena explained in chapters 2 and 3. In a nutshell, AC pDEP traps cells on the electrode's edges while ACEOF applies force on the fluid and pushes the trapped cells to the 'concentration area'. In this project, a concentration area is defined as the place on the device where all cells are collected. The device is invented in two main sections.

1.4.1 Design and methodology of the proposed cell concentration and trapping device

The primary objective is to model and design a robust and efficient cell concentration and trapping device that could perform hybrid functionality of cell trapping and cell concentration. Figure 1.9 illustrates the device consisting of ten parallel individually addressable electrodes in yellow colour while the concentration area is green. The device has an inlet from which fluid containing cells enter and leave via outlet.

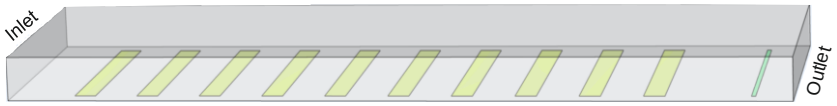

Figure 1.9: The proposed device's schematic, yellow rectangles illustrate electrodes, and green rectangle shows concentration area.

1.4.1.1 Cell Trapping Stage – Cell trapping using AC pDEP

In the project's first stage, fluid containing cells are allowed to flow in the microfluidic chamber on top of electrodes using pressure-driven flow. When these cells pass over the electrodes in a microfluidic chamber, AC pDEP is deployed, capturing the target cells from at the electrodes' edges, as shown in figure 1.10.

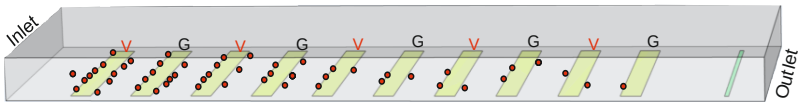

Figure 1.10: Cell trapping at electrode edges under the influence of AC pDEP, red circles illustrate cells.

Cells are captured at the electrode's edges because AC pDEP attracts the cells towards the region that has a maximum electric field gradient. It is achieved by selecting the most appropriate frequency that allows selective capture of cells from the flow. The process can continue for an optimum time to capture rare cells as a part of the first concentration stage. AC DEP is thoroughly discussed in chapter 2.

It can be observed from figure 1.10 that after AC pDEP process, most of the cells are trapped on the initial electrodes while very few on the later ones. It is because few cells enter the chamber at a height outside the range of its electric field gradient and do not get trapped by electrodes. However, as they move along the chamber, their linear velocity decreases and they are pushed down by the last few electrodes and get trapped.

1.4.1.2 Cell Concentration Stage – Sweeping Cells using ACEOF

Once the target cells are captured, the device's mode is switched, and the project's second stage starts. In this stage, ACEOF is applied to the fluid in the chamber, forming vortices that apply force on the fluid, causing the fluid to flow towards the concentration area. This fluid motion will cause the particles trapped at the electrode edges to move with it and collect at the end of the vortices, as shown in figure 1.11. It can be observed from the figure that two vortices are not equal in size. It is because the first vortex is formed only due to one electrode, while the second larger vortex is formed due to the last nine electrodes connected to the ground.

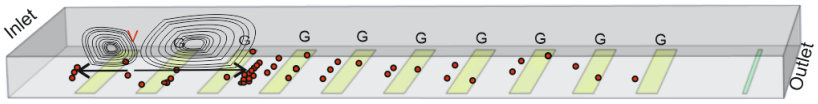

Figure 1.11: Cell forming wavefront after 3rd electrode due to ACEOF.

Once the particles are collected and forms a wavefront, the next set of electrodes are switched again, forming new vortices, as shown in figure 1.12. It can be observed from figure 1.12 that cells collected initially after the 3rd electrode also moved after the end of the second vortex, i.e., the 4th electrode forming a wavefront.

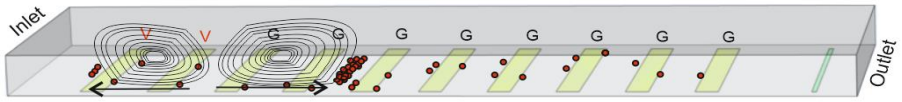

Figure 1.12: Cell forming wavefront after 4th electrode due to ACEOF.

This electrode switching process continues until cells have reached the concentration area, as shown in figure 1.13.

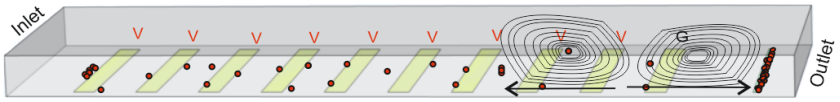

Figure 1.13: Cell forming wavefront at concentration area after one complete wave of ACEOF.

1.4.1.3 Multiwave ACEOF (MWACEOF):

It can be observed from figure 1.13 that after the first wave of ACEOF is completed, some cells are dispersed back or attached with the electrode edge. Therefore, once the wavefront is formed at the concentration area, another wave of ACEOF is switched on. The process repeats to increase the cell concentration ratio by moving the remaining cells to the concentration area. This is the second wave of ACEOF. The number of ACEOF waves continues until the maximum possible cells have reached the concentration area. This process is called multi-wave ACEOF (MWACEOF). Many factors can influence MWACEOF and cell switching patterns. For example:

i. Fluid moves in the opposite direction (often known as reverse electroosmosis flow).
ii. The fluid does not move at all, or weak movement is observed.
iii. Bi-directional flow takes place.
iv. Multiple ACEOF vortices are generated, cancelling the effect of each other.

Therefore, it is essential to optimise pDEP and ACEOF variables and carefully find the optimised electrodes switching pattern for the hybrid functionality of the device.

Using MWACEOF for this stage is advantageous because:

a- It applies force only on the fluid and hence does not rely on the cell properties. Therefore, eliminating the risk of cell contamination due to labelling is the problem in the most efficient cell concentration technologies such as MACS, FACS, Optical tweezers. Moreover, as it does not rely on the cell type, it does not limit its use to any specific cell type, which is a problem with most current-day cell isolating and concentration technologies.

b- It offers a much faster processing speed than technologies such as DEP, integrated dielectrophoresis, MACS, FACS, DGC. For instance, AC pDEP has a lower velocity than ACEOF. Hence deploying ACEOF will provide faster cell collection. It is because velocity (v_{EOF}) is much higher than DEP velocity (v_{DEP}). Moreover, due to the higher processing speed, the probability of experiencing a Joule heating effect becomes zero.

1.4.2 Methodology Overview

As discussed earlier, the same device performs both AC pDEP and MWACEOF hence offering the hybrid functionality, making it critical to optimise parameters that influence both AC pDEP and ACEOF response to achieve the desired cell concentration. The concentration factor is divided into two main stages.

The first stage is the optimisation stage, in which a device with a pair of electrodes is designed. It is essential to optimise maximum particle displacement and the time required for maximum particle displacement in this stage. These parameters are not found in current literature and research. These parameters are optimised as a

function of applied AC signal, AC signal frequency, electrodes geometry, chamber height, electrode width, and fluid conductivity.

In contrast, for AC pDEP, AC signals, frequency of the signal, cell suspension point and chamber height are optimised for AC pDEP efficiency. Moreover, both AC pDEP and ACEOF parameters must be examined and optimised against each other to gauge the best response of the device without compromising AC pDEP efficiency, ACEOF efficiency, and overall efficiency of the device.

The second stage of the project is called the concentration stage. A device with ten individually addressable symmetric electrodes is prepared in this stage. This device helps to quantify AC pDEP response for cell's linear speed, chamber height, inter-electrode gap, time to reach maximum cell trapping and throughput that can be achieved with maximum pDEP yield. On the other hand, the MWACEOF response is optimised for the interelectrode gap, electrodes switching pattern, maximum electrode switching time, maximum collection distance reaching time, and maximum ACEOF waves. Finally, combinational AC pDEP – MWACEOF is used to achieve 100000 concentration factor at the concentration area within $45 minutes$.

In the end, the FEM model for ACEOF and AC pDEP is produced to match experimental results with numerical studies. Numerical analysis is repeated for all parameters studied during experiments for a pair of electrodes and ten individual electrodes geometry. Moreover, the numerical model is also presented for multi-vortices ACEOF to establish a number of control switches for an 'n' number of electrodes.

1.5 Project Novelty

The project offers various additions to the emerging field of ACEOF while offering novelty in terms of device design, its functionality, and capability.

i. Electrodes parameters and chamber height in specific are designed such as the device performs both AC pDEP and ACEOF. These are two different phenomena, thus requiring different scaling. This information is essential to build a hybrid device.

ii. It is the first device that utilises AC pDEP and ACEOF for cell concentration. Also, the device can work and function with all types of cells.

iii. In previous research, ACEOF parameters were only optimised for ACEOF velocity. However, in this study, all parameters are optimised for how far the particles can be pushed. This information is essential to scale the cell concentrator.

iv. The device offers label-free, rapid and pure cell concentration $> 100\ 000$ within the period of $45min$ with an overall efficiency of $> 95\%$. The concentration increases to $>\ 400000$ in $75min$ with an overall efficiency of $>\ 98\%$. Moreover, with AC pDEP, it is not possible to concentrate these number of cells in area $<\ 10\mu m^2$.

v. The device uses multi-wave ACEOF for its concentration.

vi. A new type of fluid flow, named anomalous flow, was successfully encountered during experiments.

vii. Based on the experimental results first ACEOF numerical model is built for multi-electrode geometry. Moreover, simultaneous wave ACEOF (SWACEOF) is also provided.

1.6 Chapters Outline

Chapter 2 - Physics and Mathematical Theory: This chapter discusses in-depth physical principles and mathematical equations governing ACDEP and ACEOF. The chapter also explores the physics of fluid dynamics in microchannels and provides the basis for numerical modelling performed in chapter 6.

Chapter 3 - Literature Review: This chapter provides an extensive literature review of the design, principles, and results of the devices constructed using ACDEP and ACEOF. The chapter focuses on the research gaps and open-ended challenges in ACDEP and ACEOF. This section also emphasizes on the efficacy of these techniques based on the recent results.

Chapter 4 Optimisation Stage: This chapter discusses the methodology and results of optimising ACEOF response as a function of the AC signal, AC frequency, fluid conductivity, chamber height, and interelectrode gap for maximum particle displacement. In contrast, AC pDEP response is quantified for AC signal, AC frequency, and chamber height for maximum cell capture. This chapter also discusses the compromise made in the parameters of two phenomena for maximum AC pDEP and ACEOF response. The results of this chapter then serve as the template for the device designed in chapter 5.

Chapter 5 Concentration Stage: This chapter builds on chapter 4 results and presents the methodology and results for AC pDEP and MWACEOF to achieve desired

cell collection. AC pDEP in this chapter is studied as a function of the cell's linear speed in the chamber, the time required to achieve the desired yield, the percentage of cell capture by each electrode, and the chamber height. MWACEOF response is quantified for; the number of ACEOF waves, electrode switching pattern, and electrode switching time required to produce 100000 cell concentration.

Chapter 6 Finite Element Modelling: This chapter provides FEM for ACDEP and ACEOF. Results are simulated for the parameters studied in chapters 4 and 5. In this chapter, simulation results are matched with the results achieved in chapters 4 and 5. This chapter presents the numerical model for a pair of electrodes and ten electrodes geometry. The simultaneous wave ACEOF (SWACEOF) model is presented to predict device behaviour for the 'n' number of electrodes.

Chapter 7 Conclusion: This chapter summarises the goals achieved during the research, set during chapter 1. The chapter focuses on cell concentration outcomes to discuss its advantages over the technologies discussed in chapter 1. Finally, the chapter presents future suggestions and the questions that arose during the progression of the research.

2 Physical and Mathematical Theory

2.1 Chapter Overviews

This chapter presents the principles and mathematical equations that govern ACEOF and ACDEP. First, the chapter discusses forces impacting particle and fluid motion in microfluidics before explaining the physics of ACDEP and ACEOF and the parameters affecting their cell concentration-response. The last section explains the mathematical equations governing ACDEP and ACEOF finite element modelling.

2.2 Forces in microfluidics

Microfluidics is the science that studies the behaviour and interaction of fluids in the microchannels. It helps to develop microminiaturized devices (Fig 2.1). Microminiaturised devices contain chambers and tunnels which navigates fluid on the device [18].

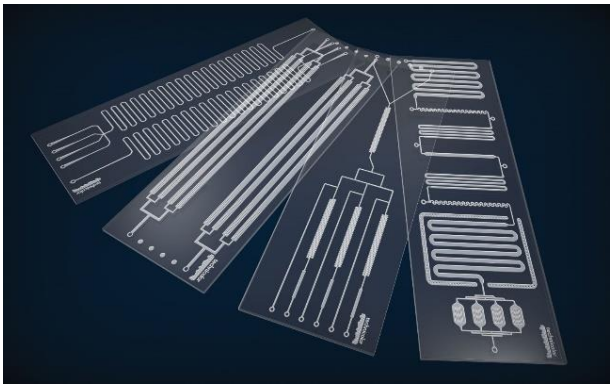

Figure 2.1: Microfluid devices.

In microfluidics channels, forces that cause particles motion and fluid flow are classified into two main categories, stochastic forces and deterministic forces [85].

2.2.1 Stochastic Forces

Stochastic forces make particles move in random directions in the microfluidic channel causing the Brownian motion effect. Brownian motion occurs due to

particles' jittering and collisions, increasing thermal and internal energy in the system [86]. Overcoming Brownian motion is cumbersome; however, a good microfluidic system is designed to have a negligible Brownian motion effect [87]. Peclet number (P_e) plays vital role to determine Brownian motion effect in the microfluidic chamber because if Peclet number $>>$ 1 then the Brownian motion has little or no effect on the particles [90]. P_e is the ratio between diffusion time and conventional time [88] and is calculated by the equation 2.1.

$$P_e = \frac{au}{D_c} \tag{2.1}$$

Where a is particle radius, u is the fluid velocity, D_c is the diffusion constant determined by Einstein – Stokes equation 2.2 [85, 89]:

$$D_c = \frac{K_b T}{6\pi\eta a} \tag{2.2}$$

Where K_b is Boltzmann's constant, T is Temperature, and η is fluid's dynamic viscosity.

In microfluidics and for particles in the size range of microns, the Peclet number is in the range of 15000 to 25000, which means stochastic forces have negligible effect in this project.

2.2.2 Deterministic Forces

Deterministic forces generate unidirectional flow in microfluidic channels [92]. These forces include magnetic forces, electrical forces, forces due to gravity, and viscous forces [93]. The force due to gravity can be ignored because the colloidal particle has negligible mass (20 billion yeast cells = 1g) [92, 93]. However, viscous force plays a

vital role because it causes friction between the cell's surface and fluid which causes drag force (F_{drag}) 2.3 [95]:

$$F_{drag} = S \text{ x } f_{drag} \quad 2.3$$

Where S is a spherical area of the solid surface, and f_{drag} is the viscous drag coefficient.

AC- Electrokinetic forces are chosen to make particles and fluid move in defined directions while overcoming Brownian, gravitational and viscous forces. It is the branch of surface and colloid science that deals with the tangential movement of particles or fluid suspension under the influence of the AC electrical field [96]. Electrophoresis, dielectrophoresis, electroosmotic flow, electrothermal flow, and electrorotation [97, 98] are some electrokinetic forces. These forces use the AC electric field to flow particles in the conductive media in a defined direction as desired and act both on particles and the suspended media [73, 96].

2.3 AC Dielectrophoresis

The translational motion of a polarisable particle generated by a dipole movement; caused by interaction with an inhomogeneous field is called AC Dielectrophoresis (ACDEP) [99-101]. When the particle suspended in electrolyte experiences a uniform field, it has zero net movements because the force applied on the particle is equal in magnitude and opposite in direction. However, in an AC field, the non-uniform field is applied, and the magnitude of two forces are not equal, which causes a unidirectional flow of particles, as shown in figure 2.2 [99, 100, 102]. AC DEP is necessary for this project because it helps trap cells on the electrode edge, creating a cell trap.

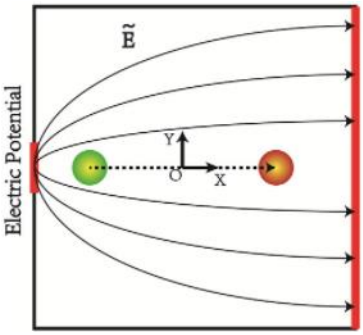

Figure 2.2: Displacement of particle from green spot to orange spot under the influence of non-uniform electric field [99].

2.4 Types of Dielectrophoresis

AC DEP is mainly divided into two main types depending on particle direction.

2.4.1 Positive Dielectrophoresis (AC pDEP)

In AC pDEP, particles move towards the highest field region at the electrodes' edges. It is because the particle is more polarised than the fluid suspension. Therefore, during AC pDEP, the dipole's direction is with the electric field's direction, making the particle move towards the highest field region (Figure 2.3a) [99, 100, 103].

2.4.2 Negative Dielectrophoresis (nDEP)

When the particle is less polarised than the fluid suspension, particles move in the region of lowest field areas, usually in the middle of the inter-electrode gap or elevated away from the electrode edges to a levitation point where the electric field is minimum. It is called nDEP. In nDEP, the dipole's direction is opposite to the direction of the applied electric field, which makes the particle moves away from the highest field region (Figure 2.3b) [99, 100, 103].

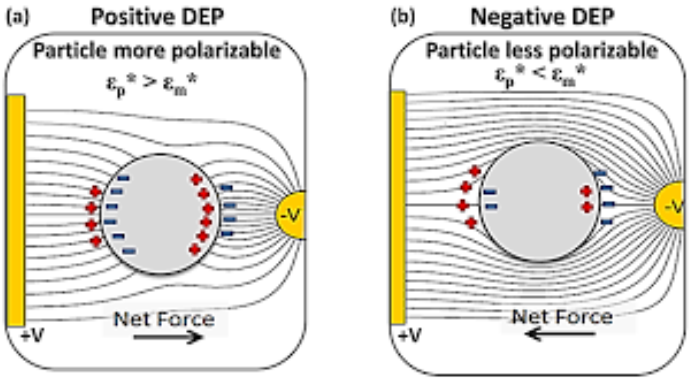

Figure 2.3: (a) Positive DEP (b) Negative DEP, where ε_p^* is polarizability of particle and ε_m^* is polarizability of material [101].

2.5 AC Dielectrophoresis Physics

2.5.1 Dipole

At the heart of DEP exists dipole as it provides polarizability to particles suspending in the fluid medium. A dipole is formed due to the formation of charges on the particles. It causes dipole moment (equation 2.4) due to interaction between the inhomogeneous electric field and dipole, which causes translation motion of particles [99, 100].

$$P = Ql \tag{2.4}$$

Where Q is charge in Coulombs (C), l is the length of a dipole in metres (m), and P is dipole moment measured in Coulomb – metre (Cm) or Debye ($1\ Debye\ =\ 3.33$ x $10^{-30}\ Cm$).

In spherical polar coordinates dipole field, the dipole force experienced by the cells is F_{DIP} is given by Equation 2.5 [99].

$$F_{DIP} = (P.\nabla)E_{DIP} \tag{2.5}$$

Where E_{DIP} is dipole electric field. Equation 2.5 explains that in a uniform electric field gradient $(\nabla) \rightarrow 0$, consequently F_{DIP} only exist in a non-uniform electric field.

2.5.2 Dielectric

The material is said to be dielectric if it contains charges that polarise under an electric field [104]. In dielectric materials, opposite charges move in opposing directions to form an induced dipole. Therefore, the dipole moment of dielectric material is given by Equation 2.6 [99, 100]:

$$P_{AVG} = \propto E_{DIP} \tag{2.6}$$

Where $\propto$ is polarizability of material, and P_{AVG} is average dipole moment measured in Fm^2.

Dielectrics can be both polar and non-polar [100]. Polar dielectric shows a permanent dipole moment independent of the applied electrical field. While in non-polar dielectrics, a dipole is only induced due to an applied electrical field and disappears when the electric field is removed [100].

Life cells mainly consist of water, and hence they are polar. Therefore, it is easy to manipulate them with the help of AC DEP. However, care should be spent to avoid permanent polarizing of the cells, which may damage them [78, 90]. For a spherical particle (yeast cell, for example), equation 2.6 changes to Equation 2.7 [100]:

$$P_{EFF} = v \propto' E_{DIP} \tag{2.7}$$

Where $\propto'$ is given by Equation 2.8 [100]:

$$\propto' = 3\varepsilon_m \left(\frac{\varepsilon_p' - \varepsilon_m'}{\varepsilon_p' + \varepsilon_m'}\right) \quad 2.8$$

$\left(\frac{\varepsilon_p' - \varepsilon_m'}{\varepsilon_p' + \varepsilon_m'}\right)$ is referred to as Clausius – Mossotti factor, CM. It is an essential parameter to determine dielectrophoresis' direction, i.e., nDEP or pDEP [73, 96, 99, 100].

2.5.3 Clausius – Mossotti factor

Biological cells have the following characteristics:

i. The cell contains the homogenous core [73, 96, 100].

ii. The cell membrane is not a perfect insulator [73, 96, 100].

iii. The cell is lossy and not a perfect dielectric [73, 96, 100].

CM factor for biological cells is modified to Equation 2.9 [100]:

$$CM(\omega) = \left(\frac{\varepsilon_p' - \varepsilon_m'}{\varepsilon_p' + 2\varepsilon_m'}\right) \quad 2.9$$

Where $\varepsilon_p' \; and \; \varepsilon_m'$ are complex permittivity of cells and fluid medium respectively and are given by Equation 2.10 and 2.11, respectively [100]:

$$\varepsilon_p' = \varepsilon_p - \frac{j\sigma_p}{\omega} \quad 2.10$$

$$\varepsilon_m' = \varepsilon_m - \frac{j\sigma_m}{\omega} \quad 2.11$$

Where σ_p and σ_m are the conductivities of particle and medium, respectively.

Separating real and imaginary components of CM factor is given by Equation 2.12 [105, 106] and Equation 2.13 [106, 107] respectively:

$$\Re[(CM(\omega)] = \frac{\omega^2(\varepsilon_p - \varepsilon_m)(\varepsilon_p + 2\varepsilon_m) + (\sigma_p - \sigma_m)(\sigma_p + 2\sigma_m)}{\omega^2(\varepsilon_p + 2\varepsilon_m)^2 + (\sigma_p + 2\sigma_m)^2} \quad 2.12$$

$$\Im[(CM(\omega)] = \frac{\omega(\sigma_m - \sigma_p)(\varepsilon_p + 2\varepsilon_m) - (\varepsilon_p - \varepsilon_m)(\sigma_p + 2\sigma_m)}{\omega^2(\varepsilon_p + 2\varepsilon_m)^2 + (\sigma_p + 2\sigma_m)^2} \quad 2.13$$

Figure 2.4 illustrate the real and imaginary components of CM factor for the frequency for E.Coli 5K and E.Coli K38 cells for the same fluid conductivity of $5mS/m$. Maximum F_{DEP} occurs for E.Coli K38 at $1MHz$ while for E.Coli 5K, it occurs at $4MHz$.

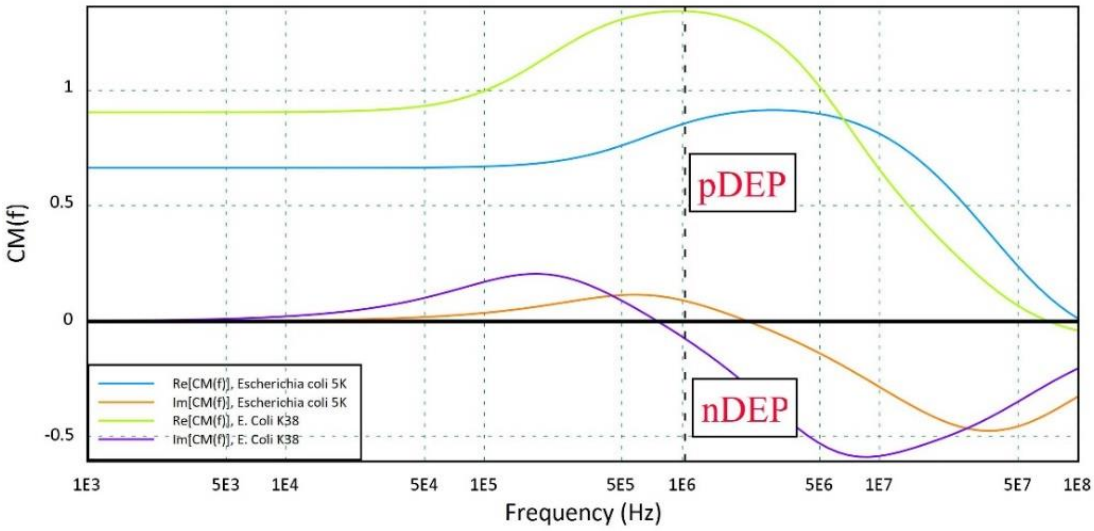

Figure 2.4: Real and Imaginary Clausius Mossotti factors E. Coli 5K and E. Coli K38 for the fluid conductivity of $5mS/m$ [108].

The magnitude of polarizability and direction of DEP depends on CM factor, as shown in figure 2.4 [99, 106].

At low frequencies, Equation 2.12 becomes [105, 106]:

$$\Re[(CM(\omega \to 0)] = \frac{(\sigma_p - \sigma_m)}{(\sigma_p + 2\sigma_m)} \quad 2.14$$

At high frequencies, Equation 2.13 becomes [105, 106]:

$$\Re[(CM(\omega \to \infty)] = \frac{(\varepsilon_p - \varepsilon_m)}{(\varepsilon_p + 2\varepsilon_m)} \quad 2.15$$

Equation 2.14 and 2.15 summarises that:

i. If the particle polarizability is equal to conductive media's polarizability, electric field lines are continuous and parallel everywhere. In this case

$\sigma_p = \sigma_m$ and $\varepsilon_p = \varepsilon_m$ and therefore, $\varepsilon'_p = \varepsilon'_m$ and therefore, CM factor = 0 and hence no DEP occurs [98, 100].

ii. If the particle is more polarised than conductive media, the electric field lines bend towards the particle, meeting it at a right angle. In this case $\sigma_p > \sigma_m$ and $\varepsilon_p > \varepsilon_m$ and therefore, $\varepsilon'_p > \varepsilon'_m$ and therefore, CM factor > 0, resulting in AC pDEP [98, 100] as shown in figure 2.5.

iii. If the particle is less polarised than conductive media, then electric field lines bend around the particle. In this case $\sigma_p < \sigma_m$ and $\varepsilon_p < \varepsilon_m$ and therefore, $\varepsilon'_p < \varepsilon'_m$ and therefore, CM factor < 0, resulting in nDEP [98, 100] as shown in figure 2.5.

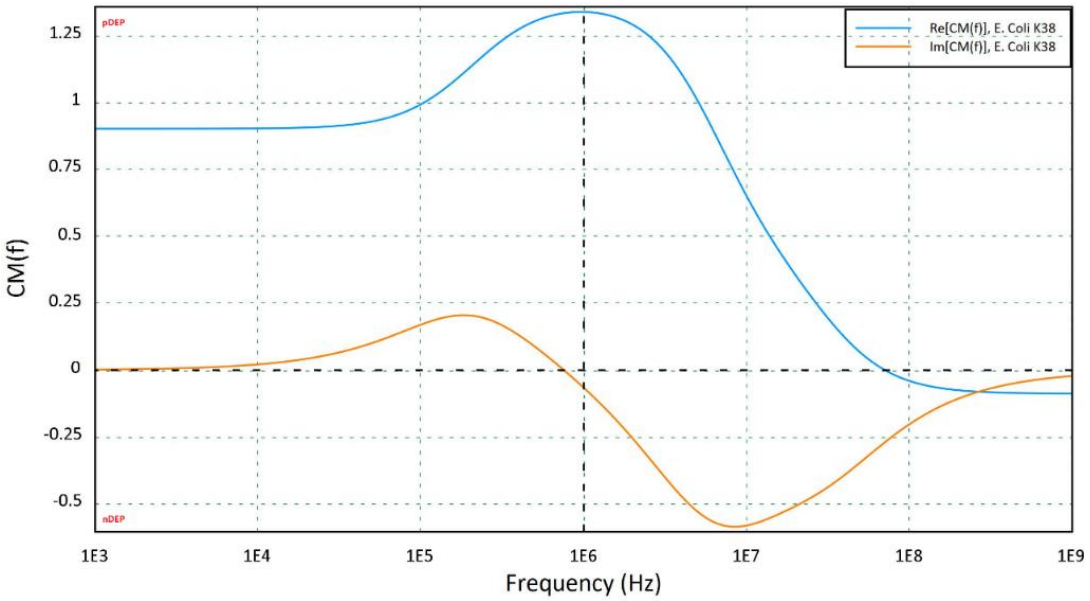

Figure 2.5: Clausius Mossotti effect on the direction of dielectrophoresis [108].

2.5.4 Cross over Frequency

Cross over frequency (ω_{c_o}) is defined as the frequency at which DEP's strength vanishes from the system of AC pDEP into AC nDEP and vice versa, therefore reversing the direction of DEP [109]. Cross over point occurs when the real component of CM factor becomes 0. Cross over frequency (ω_{c_o}) is given by the equation 2.16 [109].

$$\omega_{c_o} = \sqrt{\frac{(\sigma_m - \sigma_p)(\sigma_p + 2\sigma_m)}{(\varepsilon_p - \varepsilon_m)(\varepsilon_p + 2\varepsilon_m)}} \quad 2.16$$

Figure 2.6 demonstrate the ω_{c_o} for rhoplema nomdaica nematocyst untreated capsule. It can be seen from the figure that two crossover frequencies took place at 403.42kHz and 27.71MHz.

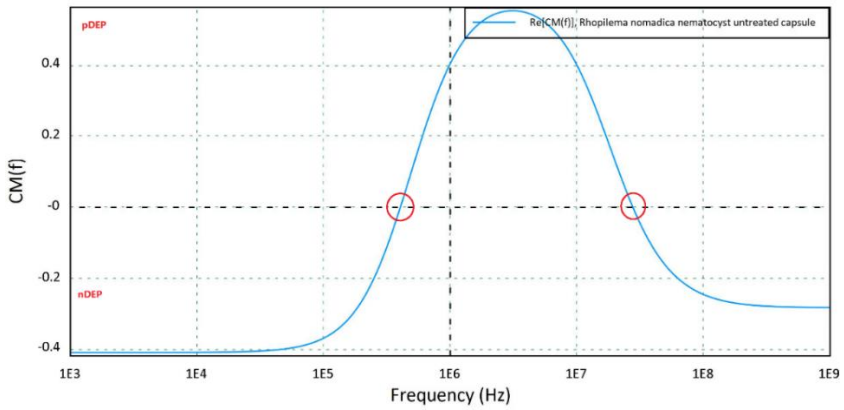

Figure 2.6: Cross over frequency for Rhoplema Nomdaica Nematocyst Untreated Capsule using Clausius Mossoti factor [108].

Cross over frequency for live yeast cells is 9362kHz and 66.34MHz figure 2.7 [110, 111]. It is essential to determine the cross over points for yeast cells as experiments will be conducted with yeast cells being test particles.

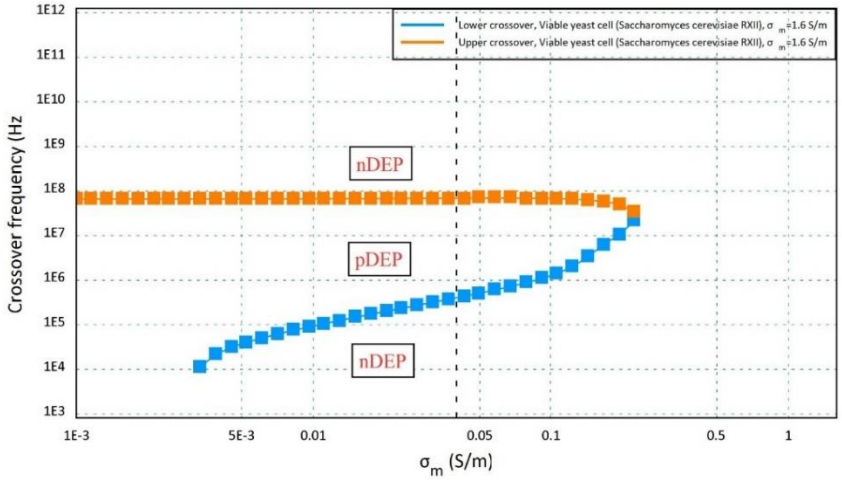

Figure 2.7: Crossover frequency (Hz) for viable yeast cells for conductivity sweep from $10mS/m$ to $1.6S/m$.

2.5.5 Dielectrophoretic Force

The force experienced by particles suspended in electrolytic media in a non – homogenous electric field experience a force causing translation motion. This force is called Dielectrophoretic force, F_{DEP} [101, 103]. For spherical particles, F_{DEP} is given by Equation 2.17 [101, 103]:

$$F_{DEP} = 2\pi\varepsilon_o\varepsilon_m a^3 \Re[CM(\omega)]\nabla E_{rms}^2 \quad 2.17$$

Where a^3 is cell volume, ∇E_{rms}^2 *the* gradient of the root – mean – square of the applied electric field squared. From Equation 2.17, it is concluded that:

1 – F_{DEP} is proportional to the cell volume and medium permittivity.

2 – F_{DEP} direction is towards the electric field gradient and depends on the Clausius Mossotti (CM) factor sign. The negative sign CM factor corresponds to AC nDEP, while the positive CM factor causes AC pDEP.

2.5.6 Dielectrophoresis Velocity

Dielectrophoresis velocity is the speed with which particles get trapped by the DEP trap. DEP velocity (v_{DEP}) of a spherical particle is given by Equation 2.18 [101, 103].

$$v_{DEP} = \frac{1}{3\eta}\varepsilon_m a^2 \Re[CM(\omega)]\nabla E_{RMS}^2 \quad 2.18$$

Where η is the dynamic viscosity of fluid measured in $Pa.s$ (Pascals x Seconds).

A simplified electric field model can be considered semi-circular lines between the electrodes [100, 101]. Hence electric field is given by Equation 2.19.

$$E_{rms} = \frac{V_{RMS}}{\pi r u_o} \quad 2.19$$

Where u_o is initial particle velocity, and r is the distance to the centre of the gap. For $CM = 1\ and\ u_o = 1um.s^{-1}$. v_{DEP} is given by Equation 2.20 [101, 103, 112]

$$v_{DEP} \sim \frac{0.03a^2\varepsilon_m V_{RMS}^2}{\eta r^3} \quad 2.20$$

Equation 2.20 is used both in numerical studies and to evaluate experimental results.

2.6 Quantifying Dielectrophoresis Response

It is difficult to measure F_{DEP} directly. Therefore, various techniques have been deployed to assess DEP response. For instance, measuring particle levitation helps calculate nDEP, while impedance sensing technique help calculates AC pDEP response. However, the scope of this section precludes this, and the following techniques are utilised to measure DEP response:

2.6.1 Collection Rate

The collection of particles is usually termed as DEP Yield (Y) [101]. This technique involves directly calculating the yield for the factors affecting DEP response, such as frequency, fluid conductivity, chamber height, electrode geometry, and AC field [113]. This method is adapted because it helps measure the efficiency of the AC pDEP trap during the cell capturing stage of the project.

2.6.2 Particle Velocity Measurement

Particle velocity is measured as a function of distance by the particle in the calculated time [112]. Various electric fields and parameters affecting DEP response can be examined to quantify optimum values for best results. The effect of both nDEP and AC pDEP can be studied using this process. Measuring particle velocity is important because it helps analyse the time required to capture particles and can be adjusted by quantifying electrical field strength or frequency.

2.7 Factors affecting DEP Yield

Factors affecting DEP yield are categorised into two categories:

2.7.1 Physical Parameters

2.7.1.1 Electrodes Geometry

Electrode geometry plays a vital role in all Electrokinetic phenomena because it can directly affect the efficacy and yield variables. It involves an interelectrode gap, as a smaller gap corresponds to the larger electric field and hence greater F_{DEP} [114]. An interelectrode gap of 30 times cell size provides excellent DEP yield [115]. Moreover, different electrode designs correspond to a distinct type of DEP, applications, and yield [115]. For example, interdigitated parallel electrodes give rise to AC pDEP to capture cells, while interdigitated castellated electrodes help generate nDEP [103, 113, 115].

2.7.1.2 Voltage

DEP yield is directly proportional to the applied voltage as it generates the electric field gradient required to trap the cells [101, 103]. However, at significant magnitudes and higher frequencies, the liquid's stirring becomes prominent due to the Joule heating effect diminishing ACDEP and giving way to ACETF [116]. Joule heating is the physical effect by which the pass of current through the fluid medium, thus causing a rise in the fluid temperature [117]. In the project, care is taken to limit the joule heating effect by carefully switching the electrodes.

2.7.1.3 Cell concentration

Sample size impacts both nDEP and AC pDEP yield. For any cell type, samples containing higher cell concentrations provide a higher DEP yield [101]. However, this

trend increases as more cells are trapped on the electrodes' edges due to AC pDEP or levitated above electrodes due to nDEP [101, 118].

2.7.1.4 Time

According to Wheeler relation, DEP yield varies directly with the square root of time t, Equation 2.21 [101]:

$$Y = \sqrt{t} \qquad 2.21$$

t is measured in minutes. However, as the collection increases, the relationship becomes more complicated. It is because as more sample passes from the device, more cells get captured to the electrode edges decreasing the electric field effect on the non-captured cells.

2.7.1.5 Chamber Height

Chamber height is inversely proportional to DEP [101, 103], and hence it has a significant impact on DEP. A larger suspension point minimises the electric field effect on the particle, which results in zero or exceedingly low DEP yield [73, 103, 113].

2.7.1.6 Linear speed

Linear speed is inversely proportional to the DEP yield [115]. It relates to yield since particles need time to move towards the electrode. If the particle moves too fast, it moves out of the field before being captured at the electrode. Hence slower the infusion pump greater is the yield. However, slowing linear speed can increase the processing time and joule heating effect in the system.

2.7.1.7 Frequency

ACDEP is a frequency-dependent phenomenon. Depending on the particle type and conductivity of the medium, at low and very high frequencies, nDEP or AC pDEP takes place. [101, 103, 113]. For example, at $10mS/m$ DIW medium yeast cells experience nDEP while at a higher frequency, AC pDEP takes place [103].

2.7.1.8 Fluid Conductivity

For DEP experiments, particles are suspended in the medium. The direction of DEP, F_{DEP}, v_{DEP} and yield is influenced by medium conductivity [101, 103]. Although higher AC pDEP yield can be achieved at lower fluid conductivities for life cells such as yeast cells. However, at conductivities $< 3mS/m$ is not a practical idea because fluid absorbs CO_2 overtime [73] which changes conductivity during the experimental procedure making findings ambiguous.

2.7.2 Biological Parameters

2.7.2.1 Cell Type

Cell type is a substantial factor in determining DEP type (direction), strength, and yield as cells polarizability plays a vital role in DEP. Biological cells are highly polarised because:

a) – Biological cells are mostly made up of water and remain highly polar [73, 113].

b) – Polar compounds such as DNA, RNA, proteins, lipids and sugars are intracellular organelles that contribute to an overall increase in cell polarization [101, 113].

c) – Lipid layers induce capacitive regions inside the cell. These capacitive regions cause charge distribution acting as an ionic double layer producing intense polarization [101, 113].

As different cell types polarise differently; therefore, each cell has a specific response to the electric field at a particular frequency band. Figure 2.8 shows the maximum AC pDEP frequency of viable yeast cells (1MHz), nonviable yeast cells (500kHz), E.Coli (4MHz) and highly toxigenic clostridium (HTCD) cells (900kHz). This property of cells responding to DEP helps to perform successful cell sorting.

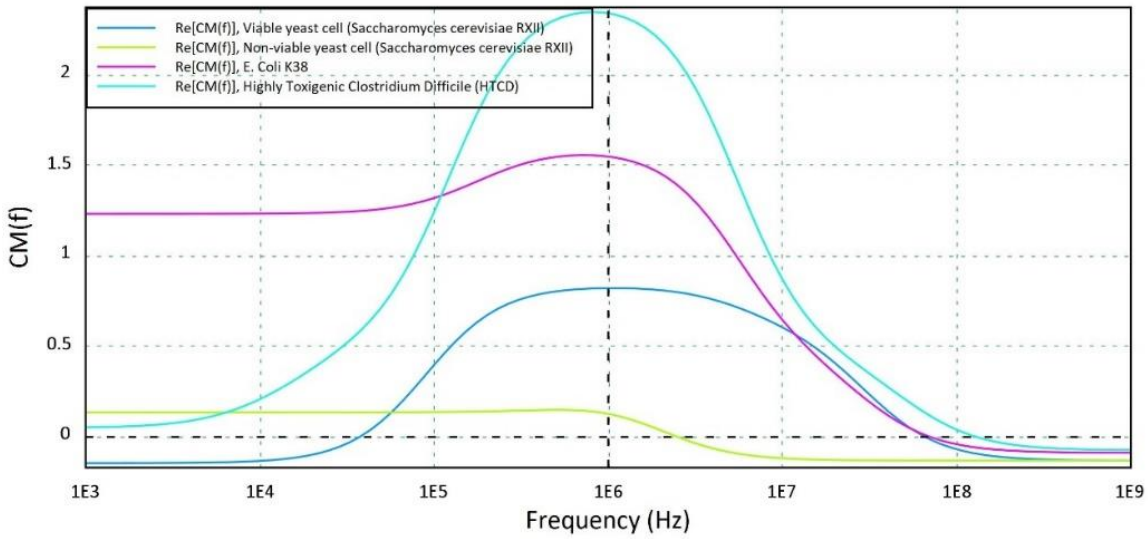

Figure 2.8: Real component of the CM factor depicting DEP frequency band of different cell types.

2.7.2.2 Cell Colony Age

Life cell colony age plays a vital role in DEP yield. For instance, one-day-old yeast cells produce twice as much DEP yield as three-day-old cells. It is because as cells colony age, polarising factors such as RNA, DNA, and water levels in the cell reduces [101]. This property of the cells helps to sort different types and ages of cells [115]. In addition, this property helps to remove dead or old cells from motile or young cells.

2.8 AC Electroosmotic flow

When an electric field is applied to the fluid, it induces the movement of net charges in the electric double layer (EDL) due to the Coulomb's force dragging the bulk fluid due to viscous drag force [100, 120, 121]. This flow is termed AC electroosmotic flow (ACEOF) when a non–uniform electric field causes this motion [120-122]. The main advantage of ACEOF is that it is a rapid process for cell concentration, and it eliminates the necessity of mechanical pumping and mixing in microscale devices [124]. Furthermore, as ACEOF applies force on a fluid only, it fits well with any cell, and therefore cells remain unaffected after the process.

2.8.1 Electric Double Layer (EDL)

EDL is the core of ACEOF as it determines the magnitude of v_{EOF} and the vortex height co-relates to the distance particles move from the electrode edge. When a charged solid surface comes in contact with an electrolytic surface, electrical layers are formed. It is because the electrolyte gets oppositely charged while preserving global electroneutrality [99, 120]. To maintain electroneutrality solid surface has a net charge that attracts oppositely charged ions in the electrolytes towards itself while repelling the like charges, as shown in figure 2.9, where a positively charged electrode attracts negative charge ions. These fluid ions, which are collected near the wall, form a layer called an electric double layer. EDL is usually a few nm to $100nm$ in-depth [95, 99, 120, 126].

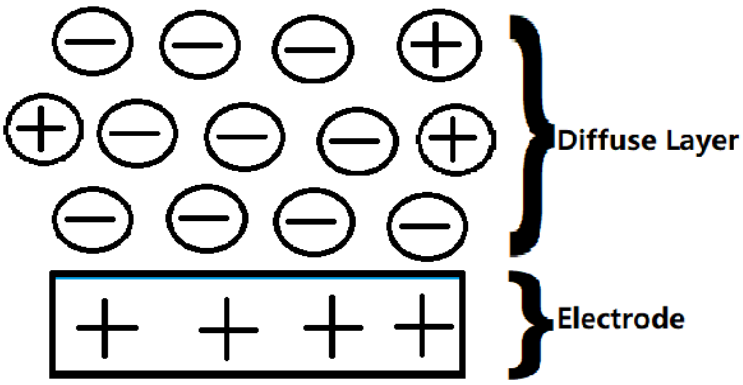

Figure 2.9: Electrode attracting oppositely charged ions to form a diffuse layer.

As the name depicts, EDL consists of two-component layers, shown in figure 2.10. The layer closest to the wall surface is the Stern layer, typically less than one nanometre thick [99, 126, 127]. A Stern layer is an immobile layer of ions bound to the surface of an oppositely charged stable interface. Hence also called a bound layer or thick layer [99, 126].

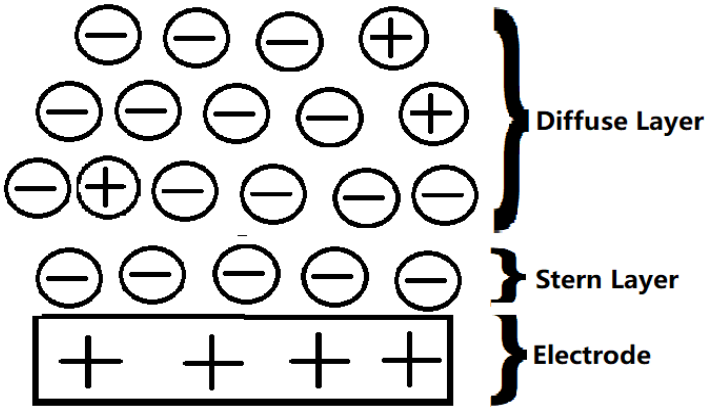

Figure 2.10 Components of the electric double layer. The Stern layer consists of counter ions only, and the diffuse layer consists of counterions majority.

The Stern layer consists of two sub-regions, as shown in figure 2.11. The inner layer consists of non–hydrated ions and therefore absorbed to the electrode surface; this is known as the inner Helmholtz plane (IHP), sometimes referred to as a non-slip plane. This region consists of both counter and co–ions. The outer layer consists of a layer of bound hydrated ions and contains counter ions only [99, 100, 127]. The

interface between this layer's outer edge and the diffuse layer is the outer Helmholtz plane (OHP) or slip plane, which is the point at which the fluid moves relative to the plane [99, 100, 127]. The potential drop across the slip plane is known as zeta potential, which is directly proportional to the diffuse layer potential [99, 126]. In the Stern layer, potential drops linearly from surface value (electrode potential) to the value at the outer Helmholtz plane [99].

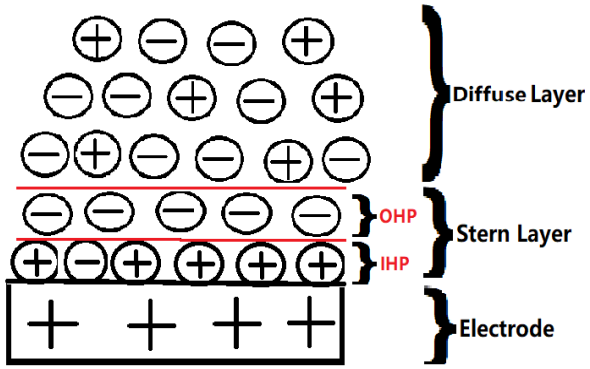

Figure 2.11: Electric double-layer illustrating the Stern layer's inner and outer Helmholtz plane.

The second layer is the diffuse layer, and it is the mobile layer of ions mainly composed of counter ions to that of the tangible interface and contains some coions [99, 104]. Potential drops exponentially in the diffuse layer with a characteristic distance of Debye's length [127]. The diffuse layer's mobile charges are responsible for electroosmotic flow in the form of micro vortices, producing a fluid motion along with the electric field [104]. The fluid moves with a velocity that reaches its maximum value near the surface and minimum value as it moves away from the surface [100]. When an electric field is applied to a pair of electrodes, EDL is formed. The formation of EDL co-occurs as the AC field is applied. This AC field is composed of tangential (E_t) and normal (E_n) components.

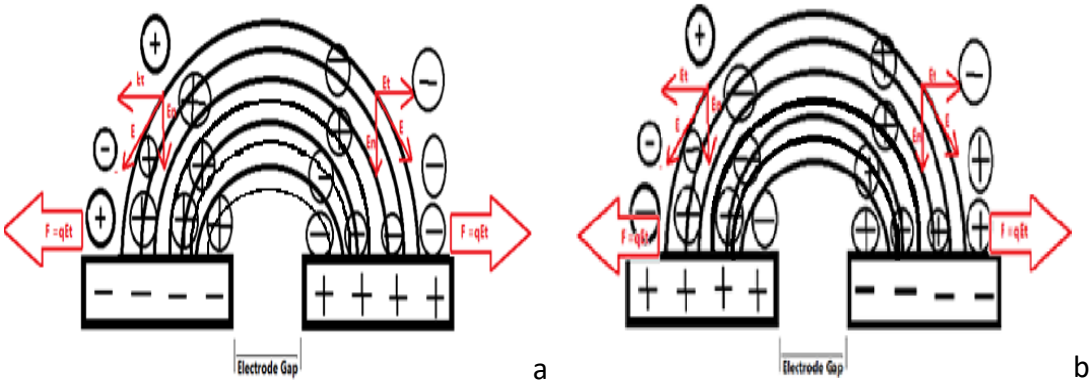

a b

Figure 2.12: Motion of fluid depicted by red arrows in (a) first half of the AC signal (b) second half of the AC signal.

However, when the AC signal varies with time, the electric field continuously changes, causing EDL to reverse its charge constantly.

The tangential component of an electric field induces Coulomb's force on the charges of EDL [121], causing particles to move away from the edges of electrodes onto the electrodes where the electric field becomes negligible [136]. When the polarity of microelectrode is reversed, a new EDL is formed. However, the electric field's polarity also reverses; therefore, the direction of the Coulomb's force remains the same, and therefore there is no imbalance between viscous force and drag force [136, 137]. Hence fluid flow remains unidirectional [136-138], as shown in figure 2.12a and 2.12b.

EDL shows double layer capacitance C_{DL} with reactance Z_{DL}, Equation 2.22 [99].

$$Z_{DL} = \frac{1}{i\omega C_{DL}} \qquad 2.22$$

C_{DL} is a series sum of Stern layer capacitance and diffusion layer capacitance, Equation 2.23 [99, 100].

$$\frac{1}{C_{DL}} = \frac{1}{C_s} + \frac{1}{C_D} \qquad 2.23$$

As discussed already, the Stern layer consists of two sublayers; hence, the Stern layer capacitance is further given by Equation 2.24 [99].

$$\frac{1}{C_S} = \frac{1}{C_{s_1}} + \frac{1}{C_{s_2}} \quad 2.24$$

Potential drops linearly through the Stern layer; hence, Stern layer capacitance is a good capacitor model and only depends on the Stern layer's thickness, Equation 2.25[102, 122].

$$C_S = \frac{\varepsilon_S}{d_S} \quad 2.25$$

On the other hand, the Diffuse layer capacitance depends upon Debye's length κ^{-1} in which charges are distributed over a volume of layers. Hence, C_d is given by Equation 2.26[99]:

$$C_d = \frac{\varepsilon}{\kappa^{-1}} \quad 2.26$$

Therefore, the electrode-electrolyte model can be modelled as an RC series circuit discussed later by Ramos, Equation 2.27 [122].

$$Z_{DL} = R_{DL} + \frac{1}{i\omega C_{DL}} \quad 2.27$$

Using ohm's law, Potential across the double layer V_{DL} is given by Equation 2.28:

$$V_{DL} = I.Z_{DL} \quad 2.28$$

Equation 2.28, therefore, explains when $\omega \to \infty$, Z_{DL} is pure resistive while as $\omega \to 0, Z_{DL}$ is purely resistive. Therefore, an optimum ω is required for comprehensive ACEOF functionality. Helmholtz's EDL model ignored electrolysis at the electrode surface [128].

2.9 Variables affecting ACEOF

Understanding variables affecting ACEOF is vital because of ACEOF velocity (v_{EOF}) and hence vortex size depends on these factors. A larger vortex size means larger particle displacement from the electrode's edges. Variables affecting ACEOF are listed below:

2.9.1 Frequency v ACEOF

The frequency of the applied signal plays a vital role in determining the magnitude of v_{EOF} [139]. Maximum v_{EOF} occurs at optimum frequency f_c, while above and low this frequency it reaches zero [122, 139-142]. It is because at frequencies > f_c, there is insufficient time for EDL to form and therefore, the potential across the fluid medium is the same as electrode potential. In contrast, at frequency < f_c, complete EDL forms in each half-cycle, causing total potential drop across EDL causing little or no ACEOF [122, 139, 141, 143, 144]. Optimum frequency is measured in Hertz (Hz), usually in kHz and is given by Equation 2.29 [145]:

$$f_c = \frac{1}{2\pi C_d . R_m} \tag{2.29}$$

Where f_c is optimum frequency, C_d is double-layer capacitance, and R_m is the fluid resistance.

2.9.2 Conductivity v ACEOF

From equation 2.30, recall that EDL is the measure of Debye's length (κ^{-1}). κ^{-1} is inversely proportional to the fluid conductivity (σ) [122, 139, 141, 146].

$$\kappa^{-1} \propto \frac{1}{\sigma} \tag{2.30}$$

Therefore, at higher fluid conductivities, the diffuse layer of EDL is depleted as a result large percentage of electrode potential is dropped across the Stern layer resulting in v_{EOF} to decrease to 0 [122, 139, 141, 143, 146]. Decreasing v_{EOF} causes micro – vortex to diminish as well [141, 143, 147]. Conductivity is measured in S/m.

2.9.3 Electric Field v ACEOF

v_{EOF} depends on applied AC voltage and the AC electric field [122, 146], as seen from equations 2.31 and 2.32.

$$V_{EOF} \propto V_{APP}^2 \quad 2.31$$

$$V_{APP} = \int E.dz \quad 2.32$$

An electric field is measured in V/m.

2.9.4 Inter – Electrode Gap v ACEOF

The Interelectrode gap (g_d) is critical in determining v_{EOF} as it controls the strength of the electric field, Equation 2.33 [139, 145].

$$E = \frac{dV_{APP}}{dg_d} \quad 2.33$$

Therefore, the smaller the interelectrode gap, the greater the electric field, resulting in greater v_{EOF}. The interelectrode gap is measured in meters (m), but for microfluidic devices, it is usually in micrometres (μm).

2.9.5 Chamber Height v ACEOF

The size of the vortex formed also determines the ACEOF response. Chamber height does not influence v_{EOF}. However, it does determine the vortex's height, and in some cases, the structure of the vortex formed [148]. Greater chamber height corresponds to greater vortex size [148]. Chamber height is measured in micrometres (μm).

2.9.6 Discussion of ACEOF variables

It is essential to optimise the variables discussed above for optimum particle collection. These factors affect v_{EOF}. However, as discussed later, compromise is made to maximise particle collection on the microdevice. For instance, a more considerable chamber height does correspond to a larger vortex size, but it reduces DEP's effect on the particles. Moreover, all these variables are strongly interlinked with each other and hence influence the outcome of each other. Hence, all these factors are investigated in collaboration during the optimising stage to maximise the collection efficiency. Finally, this section has provided considerable insight into the equations that shall be used in the numerical analysis of ACEOF modelling.

2.10 Reversible Electroosmotic flow (REOF)

Reverse electroosmotic flow is a nonlinear electrokinetic phenomenon that occurs when ACEOF starts moving backwards [149, 150]. Reverse electroosmotic flow is first observed by Bazant and Squires [151]. The phenomenon is used since fluid mixing with $> 90\%$ efficiency [124, 136, 152-154]. This flow increases efficiency compare to ACEOF because REOF velocity is higher than electroosmotic flow velocity [149, 154-158]. Studies reported that $v_{REOF} > 10v_{EOF}$ [156, 159-162]. REOF has been utilised in ACEOF based micromixers. These studies have either used asymmetric electrodes or phase-shifting AC signals, also known as travelling wave electroosmotic flow (TWEOF) [137, 163-185]. Though a complete theory of REOF is still lacking. However, several attempts were made to explain the phenomena.

Ellerington [159] argued that the reverse flow occurs due to the principle of mass conservation at high voltages ($> 20V_{PP}$). Mass conservation law states that, the mass

of a closed system always remains constant during its motion over time [186, 187]. Bazant [166] rejected this idea and instead argued that reversal flow occurs at high voltage because at such voltage EDL becomes thinner, causing faradaic reactions, which causes flow reversal due to nonlinear effects. However, Gregersen et al. [188] observed reversal flow due even at low voltage ($\sim 1.5V_{RMS}$).

Many theories have been put forward to explain physics causing REOF however, none of these have provided a solid foundation to build on. For example, Huang et al. [172] suggested that the cause of reverse flow is an imbalance between viscous and drag force, while Kim et al. [173] claimed that reversal flow occurs due to specific electrode geometries. On the other hand, Vazquez – Pinon et al. [184] suggested that in the normal ACEOF, the dominating vortex establishes the flow direction forward. However, when the size of the dominant vortex increases due to factors such as AC Signal. It touches chamber height, and fluid flow is stopped. Further increase in the height of the dominant vortex causes flow reversal because it obeys the principle of mass conservation.

2.11 AC Electroosmosis Modelling

This section explains the physics and numerical equations required during the numerical model in Chapter 6.

2.11.1 Gouy – Chapman Model of EDL

Gouy – Chapman model helps to calculate Debye's thickness [129] which is an important parameter when calculating ACEO velocity v_{EOF}. Debye's length is calculated using the Poisson Boltzmann Equation (PBE). For electrostatic theory, Poisson's equation is given by Equation 2.34 [131].

$$\frac{\partial^2 \emptyset_E}{\partial x^2} = -\frac{\rho_c}{\varepsilon} \quad 2.34$$

Where $\emptyset_E$ is electric potential, ρ_c is volume charge density.

Thermal energy also influences the charge in the fluid. The Boltzmann equation helps to calculate the number of ions by equation 2.35 [131].

$$n_i = n_i^o . e^{-\frac{W_i}{K_B T}} \quad 2.35$$

Where n_i is ion type, W_i is the magnitude of work done by the ions. W_i is given by Equation 2.36 [131]

$$W_i = Z_i . \mathrm{e} . \emptyset_E \quad 2.36$$

Z_i is the number of valence electrons of each type, e is elementary charge constant.

Combining equations 2.35 and 2.36:

$$n_i = n_i^o . e^{-\frac{Z_i . \mathrm{e} . \emptyset_E}{K_B T}} \quad 2.37$$

$$\rho_c = \sum_i n_i^o . Z_i . \mathrm{e} . e^{-\frac{Z_i . \mathrm{e} . \emptyset_E}{K_B T}} \quad 2.38$$

From Equations 2.37 and Equation 2.38:

$$\frac{\partial^2 \emptyset_E}{\partial x^2} = -\frac{\sum_i n_i^o . Z_i . \mathrm{e} . e^{-\frac{Z_i . \mathrm{e} . \emptyset_E}{K_B T}}}{\varepsilon} \quad 2.39$$

Equation 2.39 provides the potential of EDL [129, 131]. The model assumes that the surface charge is the force that generates a distribution of ions in the electrolyte [129, 130].

2.11.2 Debye – Huckel Theory

For colloidal particles, there is no analytical solution to equation 2.53. However, if the electrical energy of the particles is less than its thermal energy, such that $|Z_i * \mathrm{e}| < K_B . T$, Debye – Huckel approximation theory can be used, which limits Equation 2.53

to the first two terms of Taylor's expansion only, therefore, providing with an Equation 2.40 [132, 133].

$$\frac{\partial^2 \emptyset_E}{\partial x^2} = -\frac{1}{\varepsilon}\left(\sum_i n_i^o . Z_i . e - \sum_i Z_i^2 . e^2 . n_i^o . \frac{\emptyset_E}{K_B . T}\right) \quad 2.40$$

The first term of equation 2.54 is ignored to maintain electroneutrality in the bulk solution, which generates Debye's parameter (κ), as shown by equation 2.41[129, 133].

$$\frac{\partial^2 \emptyset_E}{\partial x^2} = \kappa^2 . \emptyset_E \quad 2.41$$

Where κ is the debye's parameter and given as:

$$\kappa = \sqrt{\frac{\sum_i Z_i^2 e^2 n_i^o}{\varepsilon K_B T}} \quad 2.42$$

Reciprocal of Debye's parameter gives us Debye's length Equation 2.43, [129], which is the length of EDL [102].

$$\kappa^{-1} = \sqrt{\frac{\varepsilon K_B T}{\sum_i Z_i^2 e^2 n_i^o}} \quad 2.43$$

For symmetric electrodes: $Z^+ = Z^- = Z$,

Hence Equation 2.43 becomes [129],

$$\kappa^{-1} = \sqrt{\frac{\varepsilon K_B T}{2Z^2 e n_o}} \quad 2.44$$

For asymmetric electrodes geometry, the ratio of $Z^+$to the Z^- is used depending on the length of electrodes [129]. Equation 2.44 is a vital parameter in calculating v_{EOF} as discussed in chapter 6.

2.11.3 AC – EOF Models

Ramos Model for symmetric geometry in 1999 [195] and Adjari Model for asymmetric geometry in 2000 [196] laid the foundation for ACEOF models and remained an integral part of many research studies for two decades. The current study is based on symmetric geometry, and therefore, the Ramos Model presented below laid the foundation of numerical analysis in the current studies.

2.11.3.1 Ramos slip velocity model

Ramos [195] presented ACEOF slip velocity model by representing EDL as Capacitor – Resistor – Capacitor (CRC) series circuit. CRC represents electrolytes as discrete current flux tubes in parallel in which the electric field passes. EDL is assumed as a distributed capacitor of constant value $\Delta C = \varepsilon\kappa d\Delta x$, where d is electrode length. Because all flux tubes have different capacitance, hence they charge differently. At low frequencies, the impedance of the electrolyte is purely resistive, for which resistance is given by Equation 2.45:

$$R(x) = \frac{\pi x}{\sigma_q d\Delta x} \qquad 2.45$$

The model presented voltage drop across double layer as, Equation 2.46:

$$V_d(x) = \frac{V_o}{2+\frac{j\omega\pi x\varepsilon\kappa}{\sigma_q}} \qquad 2.46$$

V_d is the potential drop across the EDL, V_o is AC potential applied to the electrodes, σ_q is the surface charge density in diffuse layer, κ is reciprocal of Debye length, η is the fluid's viscosity, and ω is the angular frequency. The model provides time-averaged electroosmotic velocity v_{EOF}:

$$v_{EOF} = \frac{1}{2}\,\Re\left(\frac{\Delta\sigma_q E_t^*}{\eta\kappa}\right) \quad 2.47$$

$$v_{EOF} = \frac{\varepsilon V_o^2 \Omega^2}{8\eta x(1+\Omega^2)^2} \quad 2.48$$

Where E_t is the tangential electric field, x is the centre of the interelectrode gap, and Ω is dimensionless frequency:

$$\Omega = \frac{\omega \varepsilon x \pi \kappa}{2\sigma_q} \quad 2.49$$

Maximum v_{EOF} occurs when $\Omega = 1$ and as seen from equation 2.48 above and below this frequency $v_{EOF} \to 0$. It can also be concluded that v_{EOF} is inversely proportional to both the interelectrode gap and fluid conductivity.

2.11.3.2 Green slip velocity model

Ramos Model was able to follow the prediction of fluid flow; however, it could not match with experimental data. Green [197] further built on the Ramos model to improve the mismatch between experimental and numerical work. Green model [197] used coupled ACEO approach in which potential drop across EDL was investigated first by using Equation 2.50:

$$(n.\nabla\varphi) = \frac{1}{\sigma_q}\left(\frac{\varphi - V_o}{Z_{DL}}\right) \quad 2.50$$

Where φ is potential at a given point in the bulk electrolyte. Z_{DL} is the impedance of the double layer and is given by Equation 2.51:

$$Z_{DL} = \frac{1}{i\omega C_{DL}} \quad 2.51$$

C_{DL} is the capacitance of EDL, Equation 2.52:

$$C_{DL} = \frac{\varepsilon}{\kappa} \quad 2.52$$

Green's model assumed EDL as an ideal capacitor. v_{EOF} is then given by Equation 2.53:

$$v_{EOF} = -\frac{\varepsilon}{4\eta}\Lambda\frac{\partial}{\partial x}|\varphi - V_o|^2 \qquad 2.53$$

Where Λ is the ratio of the potential drop across the diffuse layer to the potential drop across the EDL. [197] further discussed that maximum v_{EOF} occurs for $\Lambda = 1$. However for $\Lambda \sim 0.25$ numerical results match with experimental results.

With the introduction of Λ, Green's model significantly improves Ramos' model. This project combines both Ramos and Green models alongside Modified Boltzmann-Poisson's Equation (MBPE) for mathematical modelling.

2.12 Fluid dynamics Modelling

This section discusses principles and equations governing fluid dynamics in microfluidics.

2.12.1 Navier – Stokes Equation

The equations of motion for viscous fluids having constant density and viscosity are known as Navier – Stokes (NS) equations. For an incompressible, Newtonian fluid NS equation is given by Equation 2.54 [189]

$$\rho_m.\frac{du}{dt} + \rho_m(u.\nabla)u = -\nabla P + \eta\nabla^2 u + f_t \qquad 2.54$$

Where ρ_m is the fluid density, u the fluid Velocity, P is the fluid Pressure, η is Dynamic velocity of the fluid, f_t is the total applied body force, $\rho_m(u.\nabla)u$ is Inertial term, $-\nabla P$ is pressure gradient, $\eta\nabla^2 u$ is the viscous term, and f_t is body force term and corresponds to electrothermal flow. NS – Equations can be simplified based on

Reynold's number, which is the ratio of the inertial term to viscous forces. Reynold's number is a dimensionless quantity and is given as, Equation 2.55 [189]:

$$R_e = \frac{\rho_m u l}{\eta} \tag{2.55}$$

Where l is the characteristic length of the microfluidic device.

For a typical microfluidic system $R_e < 1$. Therefore, inertial terms of NS – Equations are ignored [189]. Moreover, at low conductivity and frequencies $ETF = 0$ [73] hence body force f_t is neglected. Equation 2.56, therefore becomes:

$$\rho_m . \frac{du}{dt} = -\nabla P + \eta \nabla^2 u \tag{2.56}$$

The above equation is termed Stokes' equation. Whilst equation 2.67 represents laminar flow, creeping flow is represented by equation 2.69. Furthermore, the Knudsen number and stokes number are < 1, making flow laminar and particles move with the fluid without any damage.

2.12.2 Derivation of Navier Stokes Equation for 2D and 3D Model Analysis

Equation 2.56 expands to Equation 2.57 – 2.60 for 3D model [190, 191]:

$$\frac{\partial \rho_m}{\partial t} + \frac{\partial \rho_m u}{\partial x} + \frac{\partial \rho_m v}{\partial y} + \frac{\partial \rho_m w}{\partial z} = 0 \tag{2.57}$$

$$\frac{\rho_m \partial u}{\partial t} + \rho_m \left(u\frac{\partial u}{\partial x} + v\frac{\partial u}{\partial y} + w\frac{\partial u}{\partial z}\right) = -\frac{\partial P}{\partial x} + \eta \left(\frac{\partial^2 u}{\partial x^2} + \frac{\partial^2 u}{\partial y^2} + \frac{\partial^2 u}{\partial z^2}\right) + \rho_m g x \tag{2.58}$$

$$\frac{\rho_m \partial v}{\partial t} + \rho_m \left(u\frac{\partial v}{\partial x} + v\frac{\partial v}{\partial y} + w\frac{\partial v}{\partial z}\right) = -\frac{\partial P}{\partial y} + \eta \left(\frac{\partial^2 v}{\partial x^2} + \frac{\partial^2 v}{\partial y^2} + \frac{\partial^2 v}{\partial z^2}\right) + \rho_m g y \tag{2.59}$$

$$\frac{\rho_m \partial w}{\partial t} + \rho_m \left(u\frac{\partial w}{\partial x} + v\frac{\partial w}{\partial y} + w\frac{\partial w}{\partial z}\right) = -\frac{\partial P}{\partial z} + \eta \left(\frac{\partial^2 w}{\partial x^2} + \frac{\partial^2 w}{\partial y^2} + \frac{\partial^2 w}{\partial z^2}\right) + \rho_m g z \tag{2.60}$$

Where g is the acceleration due to gravity, $u, v, and\ w$ are fluid velocities in $x, y, and\ z$ direction.

For Finite element model (FEM) analysis g is assumed to be 0. For the 2D model, z axis is ignored. Therefore, the above equations are reduced as follow:

$$\frac{\rho_m \partial u}{\partial t} + \rho_m \left(u\frac{\partial u}{\partial x} + v\frac{\partial u}{\partial y}\right) = -\frac{\partial P}{\partial x} + \eta \left(\frac{\partial^2 u}{\partial x^2} + \frac{\partial^2 u}{\partial y^2}\right) \quad 2.61$$

$$\frac{\rho_m \partial v}{\partial t} + \rho_m \left(u\frac{\partial v}{\partial x} + v\frac{\partial v}{\partial y}\right) = -\frac{\partial P}{\partial y} + \eta \left(\frac{\partial^2 v}{\partial x^2} + \frac{\partial^2 v}{\partial y^2}\right) \quad 2.62$$

$$\frac{\partial u}{\partial x} + \frac{\partial v}{\partial y} = 0 \quad 2.63$$

As already established $R_e << 1$. Therefore, the right-hand side (RHS) of Equation 2.61 and Equation 2.62 is limited to:

$$-\frac{\partial P}{\partial x} + \eta \left(\frac{\partial^2 u}{\partial x^2} + \frac{\partial^2 u}{\partial y^2}\right) = 0 \quad 2.64$$

$$-\frac{\partial P}{\partial y} + \eta \left(\frac{\partial^2 v}{\partial x^2} + \frac{\partial^2 v}{\partial y^2}\right) = 0 \quad 2.65$$

$$\frac{\partial u}{\partial x} + \frac{\partial v}{\partial y} = 0 \quad 2.66$$

Equations 2.64 – 2.66 are used for FEM model fluid flow in chapter 6.Finite Element Models

2.12.3 Dielectrophoresis Modelling

2.12.3.1 Governing Equations

As discussed earlier, both fluidic medium and suspending cells get polarised due to an external electric field. It induces a net F_{DEP} as already shown by equation 2.67:

$$F_{DEP} = 2\pi\varepsilon_o\varepsilon_m a^3 \Re[CM(\omega)]\nabla E_{rms}^2 \quad 2.67$$

which is unique for different cells by exploiting the differences in their dielectric properties. Equation 2.15 – Equation 2.30 are the governing equations for DEP modelling in the time-varying electric field [192-194].

2.12.3.2 Cells Two Shell Model

Two shell model for yeast cells is shown in figure 2.13 [108, 189].

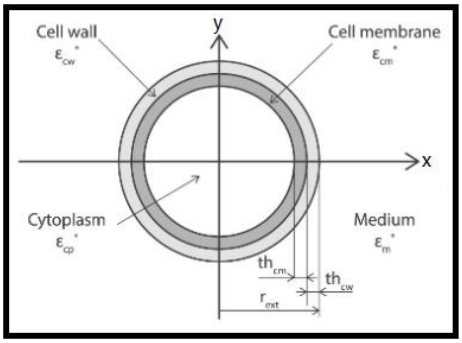

Figure 2.13: Two shell model for yeast cell [108].

In this model, cells are assumed to possess two concentric layers, namely cell wall and cell membrane. These layers consist of electric and dielectric properties [101, 189]. These parameters are summarised in Table 2.1 for both live and dead yeast cells. [79, 98]. These parameters tend to change for different fluid conductivities, but for modelling, these are kept consistent for all conductivities.

Table 2.1: Yeast cells Properties for double layer DEP Numerical Modelling.

Yeast Cell Layers	Layer Properties	Live Yeast Cells	Dead Yeast Cells
ta ***Permittivity***	*Cytoplasm*	50	50
	Cell Membrane	6	6
	Cell Wall	60	60
Conductivity (S/m)	*Cytoplasm*	0.3	7×10^{-3}
	Cell Membrane	2.5×10^{-7}	$1.6 \times \times 10^{-3}$
	Cell Wall	2.4×10^{-2}	1.5×10^{-3}
Thickness (nm)	*Cell Membrane*	8	5
	Cell Wall	220	170

It can be observed in table 2.1 that the thickness of the dead cell is less than live cells. It is because when yeast cells die, the intercellular water retained in the cytoplasm is reduced; therefore, yeast cells experience water stress, which results in wrinkling the cell membrane, which reduces the cell diameter. Furthermore, as cell size reduces, conductive properties of cells are also reduced because cytoplasm loose ions due to osmosis until equilibrium is reached [108, 189], as shown in table 2.7.

Figure 2.11 shows that the viable and nonviable yeast cells have different behaviour for the same conductivity of $10mS/m$. As $F_{DEP} \propto \Re\,|CM(\omega)|$ therefore, for viable yeast cells F_{DEP} is always greater than in nonviable yeast cells. As seen in figure 2.14, the frequency domain of viable and nonviable yeast cells is different; hence, cell separation occurs.

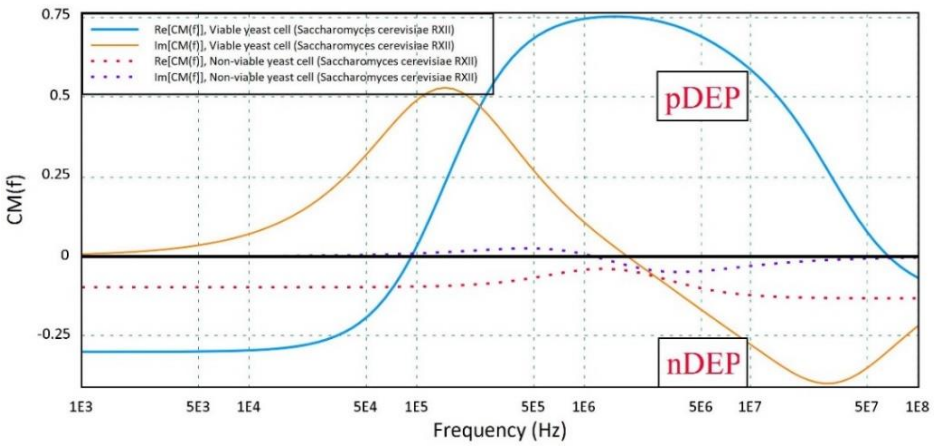

Figure 2.14: Real and imaginary components of viable and nonviable yeast cells suspended in $10mS/m$ solution.

2.12.4 Modelling Assumptions

AC Electroosmosis and dielectrophoretic models are based on several assumptions, which are listed below:

i. Microelectrodes are sufficiently broad in the zone; hence the model can be reduced to 2D [195, 197].

ii. The Debye-Huckle approximation model only accounts for low voltages [195, 197].

iii. The upper layer of electrodes is treated as the outer edge or Helmholtz slip wall [143].

iv. Electrodes are perfectly polarisable, while all other surfaces are insulators [143, 195-197].

v. A convection current is neglected because the ratio of convection to conduction current is negligible. This assumption allows for solving the electrostatic part of FEM separately from fluid flow velocity [143, 197].

vi. The fluid medium is symmetrical, along with electrolyte [197].

vii. The fluid is Newtonian and incompressible [189].

viii. Fluid viscosity is independent of the electric field strength [144, 189].

ix. There are no external body forces on the fluid [189].

x. Gravitational forces acting on the particle is zero [95].

xi. There is no Brownian motion [89].

xii. The bulk charge density is zero [123].

xiii. The electrode's effective voltage is uniform and not a function of position on the electrode surface [195, 197].

xiv. The electrodes are inert, and there are no electrochemical reactions [129, 195, 197].

xv. Electrodes are a perfect conductor and have slip velocity, while the glass is a perfect insulator; therefore, obtain a no-slip condition [195, 197].

3 Literature Review

3.1 Chapter Overview

This chapter reviews the literature for ACDEP and ACEOF phenomena and the factors that affect cell manipulation, cell concentration, and cell collection. Next, the chapter critically analyses the principles and key findings of microfluidic devices established over the years to perform cell manipulation using ACDEP and ACEOF. Afterwards, an overview of ACEOF and DEP applications developed over the years is discussed. The final section presents the chapter synopsis highlighting study gaps in the literature.

3.2 Literature Analysis

3.2.1 AC Dielectrophoresis

Muth studied the interaction between electric fields and biological materials for the first time in 1927 and found that fat emulsion particles form pearl chains (figure 3.1) when subjected to high frequencies [101]. The same pear chains formation was later observed in Liebesny erythrocyte cell in 1939 [101, 200] and Heller, variable cell size experiments in 1960. Despite the same results, the critical difference was that all these particles formed chains at different frequencies. It shows that the electric field gradient is crucial for particle manipulation. Schwar further explored this idea in 1960, where he explained that in the suspension of the same conductivity, cell behaviour is subjected to cells' and suspension's dielectric constants [201].

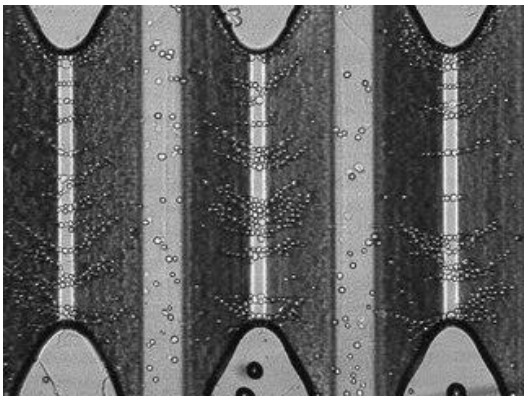

Figure 3.1: Pearl Chain formation of yeast cells under AC pDEP [201].

Pohl built on Schwar's dielectric concept and presented the separation of dead and living yeast cells using high frequencies AC field and pin–plate platinum electrode geometry [200]. Because dead and yeast particles have different dielectric constants, therefore, the separation among them took place. Pohl called this phenomenon AC DEP. However, the experiment showed $< 10\%$ efficiency because of the 'Wien effect' [200] – which is an experimentally observed increase in the conductivity of electrolytes at a high field gradient [105]. Wien effect reduces the polarizability of cells affects DEP, as seen in chapter 2.

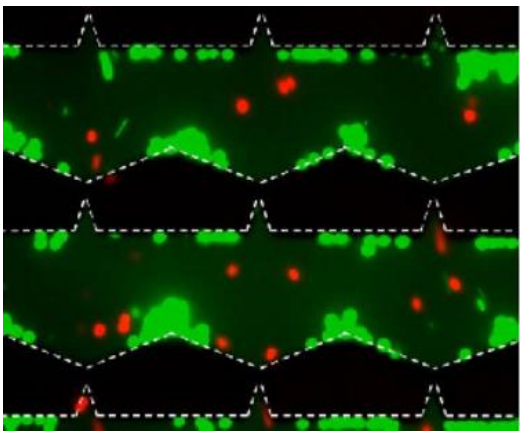

Figure 3.2: Live yeast cells (green) separation from dead yeast cells (red) due to DEP [105].

To improve efficiency, Pohl changed the electrode geometry from pin – plate to pin–pin electrode and repeated the experiment and reported 45% efficiency, which at

$10V_{RMS}, 100kHz$ [202]. The efficiency was further increased by 10% by using $12V_{RMS}$ [118]. Pohl [202] also observed that live yeast cells move away from the electrode at 10kHz and towards the electrodes at 1MHz. Pohl's series of experiments helped to understand that not only frequency but electrode geometry and electric field strength also play a vital role in DEP. Electrode geometry effect on cell collection with DEP was studied by Hughes [214, 215]. He used an array of interdigitated parallel electrodes and interdigitated castellated electrodes for cell trapping. He found that higher cell trapping took place using interdigitated castellated electrodes. Furthermore, it was added that higher cell separation occurs using asymmetric electrode geometry than symmetric ones.

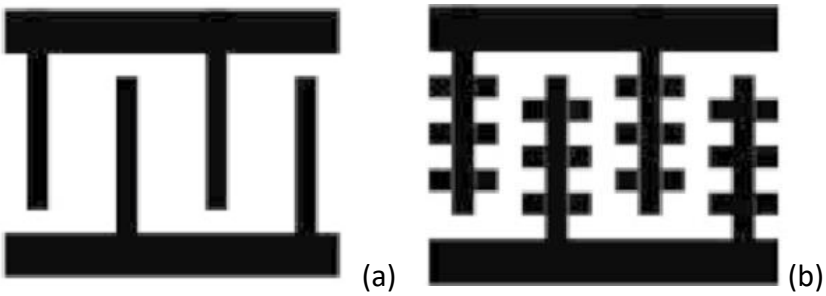

Figure 3.3: (a) Interdigitated Parallel Electrodes (b) Interdigitated castellated Electrodes.

Green's [206,207] experiments helped understand that the same particle can experience nDEP or pDEP based on frequency. It is because, at different frequencies, particles get polarised differently. Green [206, 207] castellated electrodes array experiments showed a mixture of $92nm$ and $216nm$ particles were separated at $500kHz$ due to nDEP and pDEP respectively proving that different particles experience different F_{DEP} under exact same conditions and geometry. Green [141] then demonstrated in the same study that HSV – 1 cells were collected using polynomial geometry for 5Vpp at 6MHz with nDEP.

Huang [203] expanded on factors affecting DEP by using interdigitated electrodes and yeast cells. He concluded that in addition to AC signal, geometry, and frequency, conductivity medium is also critical for particle trapping. It is due to cell polarizability will always remain lower than medium at higher conductivity, resulting in a negative CM factor.

Markx [110] separated live yeast cells from dead yeast cells [110] using 2.5mS/m suspension and $5V_{PP}$,1MHz signal. However, Markx [110] found that the final motile cells sample contained 22% dead cells. It occurred because particles were subjected to the electric field for long enough to be destroyed and permanently polarised. Similar results were also found in Huang's [205] study where MDA – MB – 231, 435, and 468 cells from human breast cancer were removed and polarised after exposure to the electric field. Therefore, electrode geometry, AC signal, frequency, and fluid conductivity are essential in this project alongside electric field exposure to the cells to avoid cell damage or permanent polarization.

Arai [211] performed high-speed random separation of biological cells by deploying DEP. Results conclude that at $45V_{RMS}, 1MHz$ a F_{DEP} of 1.2pN was applied on the yeast cells, which causes the separation of yeast cells from $216nm$ PS at $19\mu m/s$. Moreover, it was also studied that higher F_{DEP} is generated for lower chamber heights and higher AC signal amplitudes.

In chapter 2, it was discussed that it is critical overcoming Brownian motion to ensure particles move in the required direction only. Hughes [208] performed a DEP analysis of HSV – 1 (Herpes simplex virus type 1) over the range of $10kHz - 20MHz$ using polynomial electrode array. The study not only showed DEP cross over frequency of

$4.5MHz$ but also discussed that despite Brownian motion was observed throughout the experiment, but it has minimal effect on the final cell collection. Brown [209] also confirmed that Brownian motion does not affect the overall yield of micron size cells. Cross over frequency of $56kHz$ was also observed by Schnelle [210] using hyperbolic quadrupole electrodes spaced. However, the study also observed an interesting DEP trend different from conventional DEP at frequencies $\sim 1kHz$. The trend was named 'anomalous AC pDEP' then which is now known as ACEOF. The same trend was also observed by Gascoyne [216] when he introduced differential DEP affinity method - in which particles are separated using nDEP at slow frequency modulation fields. This method is used for non-living cells with same dielectric properties.

Arai [211] and Ogata [212] studied the DEP cell capture time. Studying this is important for the project to optimise cell's linear speed and throughput measurement. Arai concluded that $45V_{RMS}, 1MHz$ yeast cells are captured at the speed of $19\mu m/s$ while Ogata reported the speed of only $3\mu m/s$ at $2V_{RMS}, 1MHz$. This shows that V_{DEP} is directly related to the applied signal. Furthermore, in the Arai experiment, chamber height was at $100\mu m$ heigh while Ogata experimental setup had chamber height at $200\mu m$. Borgatti [218] also showed improvement in DEP yield by dropping chamber height from $200\mu m$ to $100\mu m$. This shows that lower chamber height correspond to better DEP yield and it is a factor to be addressed while performing experimental studies.

Several studies were then conducted that worked on optimising frequency [219, 223], AC Signal strength [219,220], chamber height [219, 222], or geometry [221] to obtain maximum cell collection. Studies were also conducted to build concentrators

using DEP alone. However, their critical problem was slow processing speed and low throughput [217 - 223]. Wiklund [219] addressed the low throughput issue by combining DEP and ultrasonic standing waves (USW). However, DEP yield was dropped down by 27%. Yan [220] also observed that higher flow rates ($0.6\ \mu l/\min$), yields only 65% yield which can be improved to 90% by slowing the flow rate to $0.2\ \mu l/min$ but then through put is compromised. Tai [221], Yuan [222], and Kusigbor [223] also observed same issue to lower yield in an attempt o increase processing time and throughput. However, the desired results were not achieved mainly because of the electrode geometry. Figure 3.4 provides cell capture comparison of studies [217 – 223]. The figure shows an increment of cells capture via DEP as flow rate decreases.

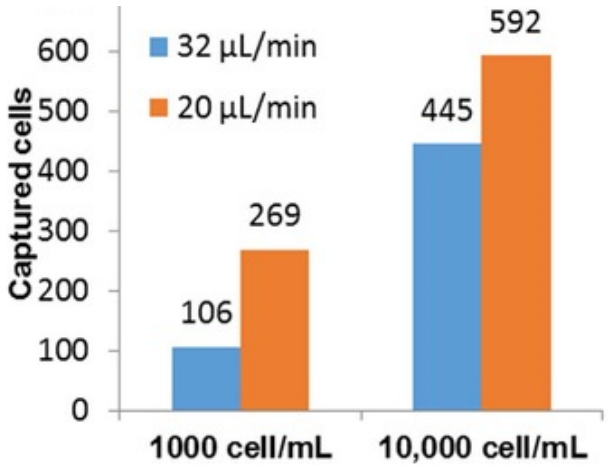

Figure 3.4: Effect of flow rate on cell capture in previous studies.

In 2021 Han [224] and Bacheva [225] reported cell concentrators using DEP and ACEOF. The key difference is DEP direction, where Han used nDEP and Bacheva used pDEP. In both studies, ACEOF pumps fluid towards the DEP trap. However, efficiency as low as 45% with a maximum 50 cell concentration is achieved in both studies. The main reason for their low efficiency is that factors affecting DEP and ACEOF were not

optimised. In addition, particles travelled in the chamber at particle velocity $>$ $80\ \mu m/s$ providing no time for DEP to trap particles.

3.2.2 AC Electroosmosis

ACEOF was initially confused with the low-frequency nDEP or anomalous dielectrophoresis [203, 204, 208, 226]. Ramos [120] was the first who reviewed forces influencing particles in microfluidics and observed that the new motion of particles is not due to nDEP. He concluded that particles move due to the fluid motion in this new particle movement. This new fluid flow was named AC electroosmotic flow (ACEOF). The conclusion was made using a parallel pair of electrode geometry with $25\mu m$ interelectrode gap; it is fluid flow rather than F_{DEP}, which is responsible for collecting yeast cells at low frequency ($1kHz$). Ramos [122] concluded that fluid velocity is both frequency and conductivity dependent in further investigation. However, the maximum fluid velocity is observed when both frequency and conductivity are optimised. Carefully analysing the data from Ramos [120,121], it can be observed that changing one variable effect all other variables as well. Furthermore, it can be seen that ACEOF occurs at a low frequency $\sim 1kHz$ which makes it different from Electro thermal flow (ETF) which occurs at a higher frequency $\sim 500kHz$ [190]. Maximum velocity of $240\mu m/s$ was observed $10\mu m$ away from the electrode edge. Figure 3.5. illustrated that velocity is maximum at optimum frequency and drops before and after that. This is because lower and higher frequencies affect EDL directly hence affecting v_{EOF}.

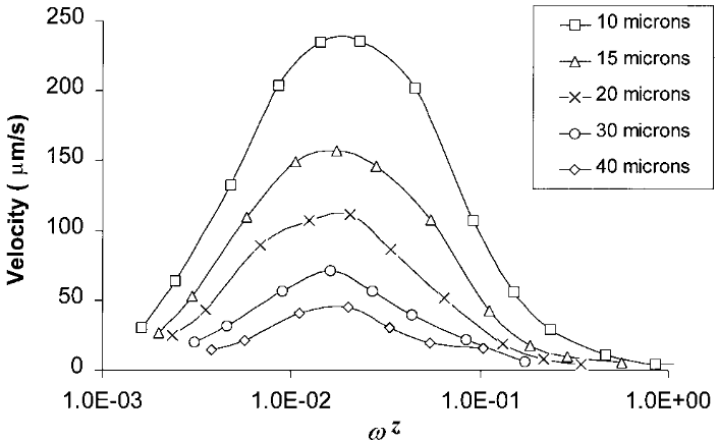

Figure 3.5: ACEOF velocity trend as measured at different distances from the electrode edge at different frequencies [122].

Whilst Ramos [122] calculated ACEOF response as a function of frequency, Green [141], using the same experimental setup as Ramos [122], quantified ACEOF response as a function of AC signal ($1V_{PP}, 2V_{PP}$, and $5V_{PP}$), frequency ($1.1kHz, 8.3kHz, and\ 100kHz$), and fluid conduction ($2.1mS/m, 8.6mS/m$, and $86mS/m$). Experimental observations showed an improved v_{EOF} of $550\mu m/s$ occurring at $5V_{PP}, 1.1kHz$ by dropping conductivity to $2.1mS/m$. The phenomenon was also observed by Hyeng [164], where he found a decrease in velocity by increasing conductivity. The study was an improvement over Ramos's [122] experimental study as a significant increase in velocity was measured by changing signal from $1V_{PP}$ to $5V_{PP}$. This sharp rise in fluid velocity is also observed by Brown [231] using asymmetric electrodes. However, the optimum frequency is shifted to $1.3kHz$ which also shows that geometry also plays its role in ACEOF.

Ramos [122] ACEOF model is discussed in chapter 2; Gonzalez [143] modified it for the linear double layer to investigate the behaviour of ACEOF by assuming that electrodes are perfectly polarisable and used Poisson's Boltzmann's equation to solve for electrode potential. This was an attempt to improve numerical and experimental

similarity; however, results are 70% off mark between numerical and experimental results. Due to this mismatch, Scott [227] criticised Ramos [122] and Gonzalez [143] models by arguing that these models depict EDL as a lumped capacitor array for a double-layer model, which makes these models oversimplified and hence numerical values are way off than experimental results. Scott [227, 228] provided a model with a potential drop across the bulk solution just outside the double layer, which improved the match by 10%. Scott [227, 228] termed this potential as V_{eff}, and proposed a new boundary condition, Equation 3.3:

$$V_D\,(x,y,z) = V - V_{eff}\,.\,g(x,y,z) \qquad 3.3$$

$V_D(x,y,z) =$ Potential drop across the double layer, $V =$ Applied potential, $V_{eff}.\,g(x,y,z) =$ Effective potential voltage drop on entire electrode geometry.

However, Ramos [229] strongly rejected Scott's [228] electrode polarization model by asserting that even though Scott [228] provided better qualitative results as compared to Ramos [122] and Gonzalez [143] However, the model not only underestimates the maximum v_{EOF} by the significant magnitude, but also provides incorrect optimum frequency values. Moreover, V_{eff} polarization model contradicts fluid movement in an open capillary's slip walls hence ignoring the basics of Electrokinetics which make Scott [228] model irrelevant. Ramos [229] further added that despite there is room for improvement in Ramos and Gonzalez models. However, Scott's [228] argument about the linear double layer model is not valid because both models ignore Stern layer effects, causing EDL to behave non–linearly. Green [197] improved on the numerical work of Ramos [122] and [143] to provide an accurate agreement between the theoretical and practical findings in Green [141].

The experimental setup was adapted from Ramos [122] while an AC signal of $2V_{PP}$ energised electrodes at three different frequencies $100Hz, 300Hz$ and $1kHz$. Results validate Ramos [122] analysis that maximum v_{EOF} occurs at a optimised frequency, $1kHz$ in this case, and nearest to the electrode, and tends to zero when calculated away from the electrode. Green [197] improved the agreement of the numerical and experimental results by introducing a double layer impedance which is the impedance of the bulk layer that tends to zero at very low or high frequencies. Therefore, at low frequencies, the system becomes quasi-equilibrium allowing Laplace equation instead of the Poisson-Boltzmann to solve for the electric potential, as depicted in equation 3.4:

$$\sigma \frac{\Delta\phi}{\Delta y} = \Delta q_{DL}/\Delta t \qquad 3.4$$

However, the measured impedance of the double-layer correlates with the electrode potential, which modifies the Laplace equation to a new set of boundary conditions, as shown in equation 3.5.

$$\sigma \frac{\Delta\phi}{\Delta y} = (\phi - V_j)/Z_{DL} \qquad 3.5$$

Green [197] solved the fluid problem in the diffuse layer by Helmholtz – Smoluchowski formula while the solution in bulk is solved with the help of Navier – Stokes equation which gives fluid velocity by equation 3.6.

$$v_{EOF} = -\frac{\varepsilon}{4\eta} \Lambda \, \Delta|\phi - V_j|/\Delta \mathrm{x} \qquad 3.6$$

The symbol Λ is called a 'correction factor'. It is the ratio of the capacitance across the double layer to the capacitance across the diffuse layer, Equation 3.7.

$$\Lambda = \frac{C_{DL}}{C_d} \quad 3.7$$

For maximum velocity $\Lambda = 1$, while at $\Lambda \sim 0.25$, experimental and numerical velocity magnitude match. Loucaides [232, 233] utilised $\Lambda \sim 0.25$ in the numerical model. However, the numerical results do not match experimental results, which shows that Λ is different for different experiments. However, no value for Λ is provided to match the results. Adjari [196] and Cahil [234] used the Green model with no evident match between results. Carefully study of these models, and these papers revealed that the mode is based on PB equations which are required to be modified for ACEOF to find fluid velocity. This approach was adopted by Zhang [239], Adamiak [240], Urbanski [165], Pham [241], Huang [164], Yang [242], Macros [249, 250] ,Moghadam [247], Mpholo [243-245], Liao [246], Debesset [248]. The device is used as a micro-pumping device because it provides unidirectional flow in a closed-loop channel.

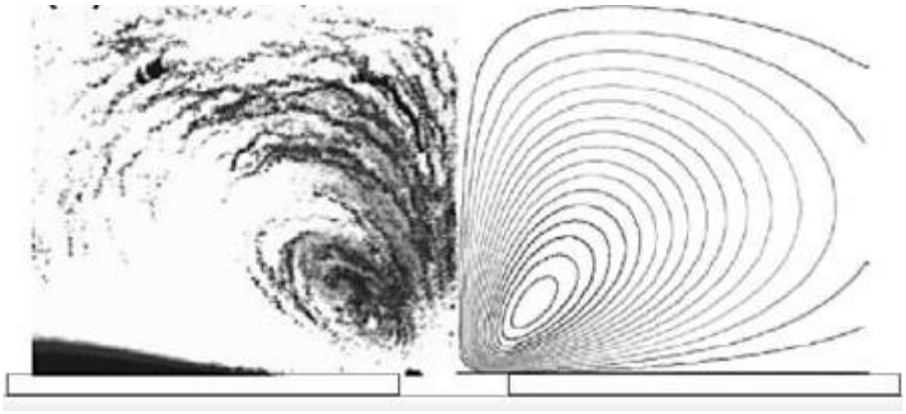

Figure 3.6: Green's experimental (left) and numerical (right) vortex results comparison [196,197].

Wong [235] used an asymmetric ring electrode geometry to demonstrate a concentrator using ACDEP-ACEOF. He concluded that bioparticles could flow with the bulk fluid to the edges of the electrodes using ACEOF. They can then be trapped with the help of other electrokinetic forces such as AC pDEP. Tanguy [237] applied this

technique and found a low concentration; however, the processing speed is 200 times faster than classical diffusion concentrators. Cummings [238] attempted to improve concentration by generating flow governed by electroosmosis and electrophoresis. This flow took the cells to the electrodes, where DEP trapped them. However, analysis of the study suggested that when cell flow is higher than DEP force, particles were not trapped.

Hoettges [247] improved cell concentration by introducing interdigitated interlocking teardrop shape – zipper electrodes geometry having opposite electric potentials to demonstrate particle collection by combining DEP and EOF. Different size electrodes were built from ITO on glass with a chamber height of $100\mu m$. $800nm$ BG (Bacillus subtilis var niger) spores, $110nm$ latex beads and yeast cells were suspended as tracers in KCl solution with conductivity between $1mS/m\ to\ 1S/m$. The distance of particles collection from the electrode edge (bus) towards the inner electrode (pad) gap depends on the vortex size, a function of frequency, fluid conductivity, and electrode size. Results show that the most extensive collection of particles occurs when the vortex radius equals the zipper pads radius. 250 spores were collected in $400sec$ at $10V_{PP}$, $1kHz$ and $575\mu m$ pad size. Vortex size of $200\mu m$ is produced at $250Hz$ while $100\mu m$ at $500Hz$. Collection of particle diminishes after $9mS/m$ fluid conductivity and $300\mu m$ interelectrode gap. Mohtar [276] built on Hoettges [247] electrodes geometry to investigate factors limiting particle collection by ACEOF. The results reported that using $500\mu m$ wide ITO zipper electrodes; ideal chamber heights are $390\mu m$ and $650\mu m$ for the electrode gap of $100\mu m$ and $150\mu m$, respectively. Moreover, it was also found that at smaller electrode gaps particles concentration decreases due to higher fluid velocity giving less chance for particles to come at rest,

indicating larger gaps are better for particle collection. However, EOF becomes negligible at $300\mu m$ interelectrode gap. The same results were found again in Mohtar [277] Hoettges [278] found $100\mu m$ interelectrode gap ideal for highest concentration factor. $10V_{PP}, 1kHz$ signal was used in all these research studies.

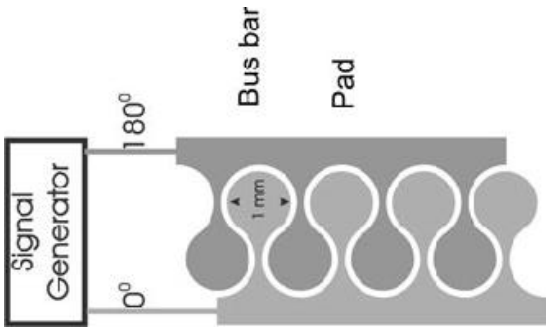

Figure 3.7: Zipper Electrodes used in Hoettges [247] and Mohtar [276].

Wu [251] concentrator used a pair of $2mm$ long, $80\mu m$ wide, and $10nm/90nm$ thick Ti/Au parallel electrodes separated by $40\mu m$ and $20\mu m$ interelectrode gaps to concentrate bioparticles as a function of frequency, applied AC signal, and fluid conductivity. Chamber height was set at $500\mu m$ while $5\mu m$ PS were used as test particles suspended in $50\mu S/m$. The experiments were conducted at $1V_{RMS}$ and $2.2V_{RMS}$ for the frequency range of $200Hz\ to\ 1kHz$. The results illustrated that the particles moved due to EOF and assembled between the two electrodes at $2.2V_{RMS}, 100kHz$. Above and below this frequency or at higher conductivity, ACEOF is weak, and therefore no particle collection occurred. On the other hand, the cell impedance measurement technique detects particles collection. The study shows a rapid concentration of particles; however, only 38% concentration is reported. Wu [252] further added that particle collection could improve by tuning ACEOF parameters. However, the study does not provide ACEOF parametric analysis. Furthermore, no study has provided any data towards particle displacement, that is, how far particles can be pushed if parameters are tuned against each other. It makes

this project of fundamental importance, and therefore, before jumping to cell concentration, it is critical to optimise the factors affecting ACEOF.

Hoettges [278] described the use of ACEOF in a continuous flow system to concentrate nanoparticles by pushing them at one end of the flow cell. The electrodes were constructed using different electrode widths at $10°, 15°$ and $20°$ with flow cell depth of $75\mu m, 120\mu m, 175\mu m$, and $300\mu m$. $100nm$ diameter green fluorescent latex beads were conducted in $3mS/m$ DIW. Flow rates were evaluated between $200\mu L/hr$ to $1.5mL/hr$. $20V_{PP}, 1kHz$ AC signal was applied to electrodes. Results demonstrate that $100\mu m$ interelectrode gap, with $200\mu m$ wide electrode angled at $15°$ against the flow with optimum flow cell depth $200\mu m$ the best concentration is achieved with the flow rate of $4.1\mu L/min$ and $6.2\mu L/min$. The model was developed with MATLAB and showed a good agreement with the experimental results. The device offered higher collection potential than cascading devices.

Wong [253] built on the work from Wong [235] to produce a bio-concentrator by combining ACEOF, EP (Electrophoresis), and DEP. The flow was generated with ACEO and when cells were captured using DEP and EP. Results show that by combining ACEOF, EP and DEP cells are concentrated in the region of $100\mu m$ at $14V_{PP}$. However, 56% efficiency is reported at slow speed because DEP and EP are slow processes. An improved efficiency of 62% was achieved by increasing signal strength by $2V_{PP}$ while Bown [147] expanded on Wong [235, 253] to provide only 2% increase in efficiency by decreasing chamber height.

Garcia – Sanchez [255] used travelling wave electroosmosis flow (TWACEOF) using asymmetric and symmetric coplanar interdigitated electrodes. $100nm$ thick gold electrodes consist of an array of five pairs with $100\mu m$ and $10\mu m$ wide electrodes with an interelectrode gap of $10\mu m$ and $200\mu m$ chamber height. In contrast, symmetric electrodes were $20\mu m$ wide and $20\mu m$ interelectrode gap with $260\mu m$ chamber height. $500nm$ latex particles were suspended in $1.3mS/m\ KCl$ solution as tracer particles. Phase-shifting AC potential was applied on symmetric electrodes that give rise to TWEOF, while the AC signal without phase shifting is applied to asymmetric electrodes. Results show that $8V_{PP}, 1kHz$ generates maximum v_{EOF} of $200\mu m/s$ in asymmetric electrodes array, while TWEOF generates $80\mu m/s$ v_{EOF} at $5.1V_{PP}, 500Hz$. During experiments, unexplainable flow reversal was observed. The same flow reversal was also observed by [256] using a pair of asymmetric electrode geometry. Garcia – Sanchez [160] later utilised this reverse electroosmotic flow to perform highly efficient micro-mixing of fluids.

Wong [235] demonstrated contact-free trapping of biological cells by utilising ACEOF as a pump and ACDEP as a cell trap; however, the low yield was reported. Hoettges [247] reported 200 spores collection using ACEOF. Wu [251] depicted 48% particle concentration deploying ACEOF, while with asymmetric electrodes, Wong [253] reported 56% particle collection at slower speed occurred when DEP and EP are added with ACEOF. Cell separation using DEP is performed by Zhou [217]. Gagnon [254] reported rapid cell collection with a low reported yield. Wei [258] reported that using ACEOF to flow cells in the chamber rather than pressure-driven flow provides 30% better results when DEP is applied. Loucaides [232] pumped fluid using ACEOF and captured 46% pure cell sample with AC pDEP; better yield is reported when

ACEOF is replaced with REOF. [237] argued that ACEO based concentrator has 200times faster and 40times better concentration than traditional diffusion concentrators. ACEO provides faster concentration than traditional ones as velocity up to $500\mu m/s$ is reported.

Loire [261] showed a combined 40% Concentration at two different sites on the device. Yeo [269] discussed the cell concentration of 50% at $260\mu m/s$. Ishida [275] used symmetric electrodes to improve 20% concentration compared to Melvin's [148] results. Motosuke [174] provided with 700x concentration factor. Chen [296] achieved a concentration factor of 3.1. Yuan [286] reported efficiency of 56.8%. Das [280] provided an efficiency of 60% for biosensors which was later improved by [283] to 65%. Zhao [287] presented with a concentration factor of 1200. [290]) only provided with a low concentration factor of 3, while [224]) reported a concentration factor of 50.

Furthermore, researchers have also found that ACEOF based micro-pumping offers simplicity, stability, rapid speed, low cost, and up to 90% efficiency over other techniques such as passive micro-pumping, mechanical micro-pumping, and magnetic micro-pumping [258, 297, 298]. ACEOF micropumps have been developed by [252], [299], [297] with the pumping speed of $1mm/s$, $1.3mm/s$, and $1.8mm/s$ respectively. [300], [301], [302],. [303], [304]. [273], [184, 305] offered REOF based micro-pumping which not only improves the speed and efficiency of fluid pumping but also make the process rapid by a factor of ~ 11. Over the years, ACEOF based micropumps have seen advancement with the reported efficiency of more than 95% by [274], [306], [307], [308], and [295]. On the other hand, ACEOF micromixers are

low cost, rapid, and provide an improved mixing efficiency compared to conventional passive and active micromixers [309] and [310]. ACEOF improves the speed of micro-mixing with the flow velocity up to $12mm/s$ in $0.18s$ [311]. Micro-mixing has been successfully deployed with an efficiency of 78% [265], 83% [307], 90% [312], 80% [296], 82% [283] while recently [161] offered an ACEOF micromixer with the efficiency of up to 92%.

3.3 Open Questions

The following open questions are found from the study, which must be answered to achieve the project targets.

i. The correction factor must be calculated, which provides information between numerical and experimental velocities and vortex size.
ii. The velocity profile is not examined thoroughly for ACDEP and ACEOF parameters.
iii. Vortex size is briefly described, but no information on how far particles can be pushed with different variables of ACEOF are discussed, which is an essential part of this research.
iv. Chamber height that suits both AC pDEP and ACEOF is not mentioned and need optimisation.
i. Velocity and vortex size relation is not discussed
ii. A numerical model for multiple electrode geometry is not described
iii. The vortex correction factor is not discussed
iv. Electrode width in terms of ACEOF particle displacement is not found yet.

v. Electrode switching pattern for maximum cell concentration is not discussed

vi. Cell concentration factor and efficiency of yield are not discussed together.

vii. There is no hybrid device that can utilise AC pDEP and ACEOF with the same electrode geometry. This requires a lot of optimisation of variables for both AC pDEP and ACEOF against each other.

3.4 Synopsis

The following points have been established from the literature review:

i. It is essential to optimise ACEOF response as a function of electrode geometry, AC signal [236, 313], AC frequency [122, 229, 236, 278, 313-315], fluid conductivity [142, 313, 314], interelectrode gap [142, 313, 314], and chamber height [148, 236, 273, 316]. All these parameters are interrelated and influence each other [148, 220, 242, 270]. These parameters are not optimised for ACEOF particle displacement or in the scenario of DEP, whereas to make a hybrid device, these parameters must be optimised against each other.

ii. Maintaining electrode symmetry is crucial to avoid biased flow as fluid flows towards the larger electrode [147, 196, 220, 242, 270, 280, 295].

iii. ACEOF does not depend on cell type [142].

iv. Maximum v_{EOF} occurs at a f_c above and below it, v_{EOF} tends to 0. Hence a bell shape graph is observed [147, 197, 236, 278, 313].

v. Higher v_{EOF} occurs at lower interelectrode gaps and low conductivities [256, 275].

vi. Maximum v_{EOF} is at the electrode edge, and velocity between the centre of the electrodes become zero. Velocity decreases when calculated away from the electrode [122, 197, 236, 249]

vii. EOF occurs at low voltages and frequency – with a maximum reported $v_{EOF} \sim 550\mu m/s$ as at $1.1kHz - 5Vpp$ [197].

viii. Higher conductivities and frequencies correspond to ACETF rather than ACEOF [236, 316].

ix. EDL parameters, zeta potential and ionic concentration control v_{EOF} and maximum velocity occurs at the EDL region in the numerical model [250].

x. Faster velocities correspond to larger vortex size [197, 274, 278].

xi. Slower linear speeds provide higher yields for DEP [147, 267].

xii. A point where velocity becomes zero in numerical simulations is termed a collection point [262].

xiii. REOF arises due to an imbalance between viscous and drag forces [317].

xiv. Chamber height does not affect fluid velocity; however, vortex size is directly proportional to the chamber height [148].

xv. Ten electrodes geometry as a hybrid device is never used in any study before, plus MWACEOF is never reported. Moreover, cell collection has never been reported using AC pDEP first and then washing away cells with the help of ACEOF.

xvi. There is no numerical model for AC pDEP and ACEOF for multielectrode.

xvii. The maximum concentration factor reported in the literature review is 1200, and the maximum efficiency given in the literature review is 65%. However, these two factors are not discussed together and are found in different studies.

4 Optimising AC pDEP and ACEOF

4.1 Chapter Overview

The chapter discusses the results for ACpDEP and ACEOF parameters that influence particle collection and, therefore, cell concentration. In chapter 2, it has been established that both AC pDEP and ACEOF depends on AC signal strength, AC signal frequency, electrode geometry, fluid conductivity, and chamber height for their optimum response. However, a thorough literature analysis in chapter 3 has found the range of parameters that require optimisation to complete this project successfully. These parameters are mainly involved in optimising AC pDEP and ACEOF that affect particle collection and the concentration factor. Therefore, this chapter aims to explore these parameters and provide a complete template for the microfluidic device geometry and parameters required to produce the concentration factor of 100000 cells/mL.

The chapter first discusses the experimental approach for the optimisation stage, while the second section covers the methodology to achieve these target goals. The following section provides the results and a detailed discussion and analysis of the results. In the final part, a synopsis of the chapter is provided.

4.2 Approach

From chapter 2, it has already been established that ACEOF response depends on various factors such as AC signal, AC frequency, fluid conductivity, fluid viscosity, fluid density, electrode geometry, interelectrode gap, chamber height and cell population [197, 236, 293, 313, 315, 317].

A buffered solution of deionised water (DIW) in the range of $3mS/m$ to $20mS/m$ remained the preferred choice during all experimental procedures and numerical analysis. Therefore, the viscosity and density of the fluid remain constant during experiments. Dynamic viscosity and density of DIW is $8.90 \text{ x } 10^{-4}\ Pa.s$ and $1g/mL$, respectively, at $20°C$ [318].

Moreover, symmetric parallel coplanar electrode geometry is adapted in the experiments. It is because asymmetric electrodes initiate fluid reversal [256], which influence the fluid to move backwards. Hence fluid mixing rather than particle collection occurs [274, 275]. Also, ACEOF applies force only fluid [122, 243] and does not depend on the type of suspended cells. Therefore, live yeast cells (1 day old) were used to quantify the response of ACEOF.

ACEOF response is gauged by the maximum particle displacement from the electrode edge and v_{EOF} [276, 290, 319]. In the experiments, maximum particle displacement response is measured by the maximum distance yeast cells moved from the electrode edge and formed a wavefront in the given time. In the study, yeast cells are used because they are live, tough, and can sustain extreme temperature and pressure conditions [99,121]. Latex beads were ignored in the study because these are not live cells, and the study also aimed to see if cells motility remains intact at the end of the experiment. Measuring maximum particle displacement is important because it provides information on how far cells can be pushed to form a wavefront, which is missing in current research, as seen in chapter 3.

Moreover, this also explains the size of the cell concentration area, which is the project's core discussion point. Providing a detailed analysis of particle displacement

as a function of ACEOF parameters fills the open research questions and provides a template for the multielectrode geometry of the device. Vortex size was measured continually monitored for $3mins$.

On the other hand, v_{EOF} is measured by the distance moved by the particle from the electrode edge per second (14 frames). Measuring v_{EOF} from the electrode, the edge is critical because it provides evidence on how fast particle forms wavefront. Moreover, finite element modelling packages provide v_{EOF} analysis only, and no information about how far cells are moved can be simulated. Therefore, to match experimental results with numerical analysis v_{EOF} is important. Also, there is no experimental data in the literature review on v_{EOF} as a function of the combinational effect of different ACEOF parameters such as ACEOF signal strength, frequency, interelectrode gap, fluid conductivity, and chamber height on v_{EOF}. Velocity is also measured at different points between $5\mu m$ to $40\mu m$ from the electrode edge to investigate v_{EOF} trends as fluid moves away from the electrode edge. This trend helps to understand vortex behaviour at different ACEOF parameters, which is not discussed in the previous literature. Therefore, the goal is to quantify ACEOF response for the following parameters:

i. AC signal
ii. AC frequency
iii. The conductivity of the fluid
iv. Interelectrode gap
v. Chamber Height

Mohtar [276,278] established that fluid viscosity and density influence ACEOF response. However, because only DIW is used for this experiment, these two parameters are considered constant throughout the experimental work and will not be explored.

On the other hand, AC pDEP response is measured by v_{DEP} and particle collection. v_{DEP} is measured by the time taken by the cell suspended in the fluid medium to reach the electrode edge [267, 320]. Cell speed is measured from the cell suspension point, 10μm, and 5μm from the electrode edge. In this stage two coplanar parallel gold electrodes will be used. Based on the result of the optimisation stage, ten parallel individually addressable electrodes will be constructed.

Particle collection is measured by calculating cells using a haemocytometer before the experiment and visually counting cells per μm^2 after the experiment, as shown in figure 4.1a shows $5000\ cells/mL$, while figure 4.1b shows $10000\ cells/mL$.

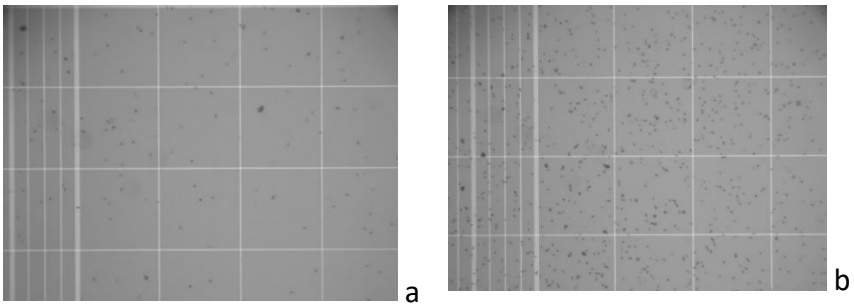

a b

Figure 4.1: The microscopic view of haemocytometer for cell concentration of (a) $5000\ cells/mL$ and (b) $10000\ cells/mL$.

Cells were counted every 30seconds for 20minutes. From equation 2.5, it has been established that AC pDEP strongly depends on the fluid conductivity. To add with, equation 2.7 shows that v_{DEP} and hence AC pDEP response depends on the interelectrode gap as it generates an electric field. However, as the project is ACEOF

based; therefore, AC pDEP response is not measured on these two parameters. Moreover, contrary to ACEOF, AC pDEP depends on cell type. Therefore, live yeast cells (1 day old) were used as test particles during the AC pDEP stage and to demonstrate cell separation, dead yeast cells (5 days old and heat-shocked) mixed with live cells were also used as test particles. AC pDEP is therefore quantified for the following parameters:

i. AC signal

ii. AC frequency

iii. Chamber Height

4.3 Methodology

4.3.1 Electrodes Fabrication/Patterning

4.3.1.1 Material

The first step in electrode fabrication is the choice of material. For this purpose, 1000μm thick, 2500μm wide and 7500μm long transparent LaboQuip microscope glass slide was cut in half and used as an electrode substrate. Glass is used as the substrate because it is an insulator with the sheet resistance in the range of $M\Omega$. Moreover, glass is inert, transparent to microscopic light, and mechanically tough [321, 322]. Electrodes were fabricated using $100nm$ gold (Au) layer on top of $5nm$ Chromium (Cr) seed layer. Kurt J. Lesker 99.9% pure chrome plated tungsten 4-inch-long rod is used for Cr deposition, while Kurt J. Lesker 99.9% Gold $1mm$ diameter wire is used for Au deposition. Cr is used because it increases adhesion between the substrate and Au. Au is used because it provides high conductivity while offering low oxidation behaviour [267]. $5mm$ wide and $20mm$ long stainless-steel

shadow mask is used (Photo figure) to fabricate 8 parallel 2000μm long and 500μm wide Cr/Au recesses with $1mm$ inter – recess gaps on the glass substrate.

4.3.1.2 Cleaning Process

Shadow mask, glass slides, Au wire, Au evaporation basket, and Cr rods were cleaned in the cleanroom facility located in the Electrical Engineering and Electronics department of the University of Liverpool before deposition. Samples were dipped in separate precleaned glass beakers containing 5% Decon-90 and 95% DIW and left for 4 hours before placing in the RS PRO Ultrasonic Cleaner bath for 15 minutes (Appendix C1). It removes all inorganic impurity from the material [323]. Ultrasonic cleaners generate cavitation bubbles induced by ultrasonic sound waves, which agitate the liquid in the beakers. This agitation produces enough energy to destroy and strip the attached impurities on the samples [324]. Samples were taken out of beakers with precleaned tweezers and were flushed thoroughly using DIW before placing them in beakers containing 100% DIW and placed again in an ultrasonic bath for 15minutes to remove any decon-90 left on samples. Samples were washed with DIW and dried up completely using 99.999% pure Nitrogen (N_2) gas using a nitrogen gun. Due to the inert nature of N_2 gas, it is cleaner and and drier than air, therefore, completely dries and removes debris from the samples [324]. Samples were then placed in glass beakers containing 100% acetone and left in the ultrasonic bath for 15minutes. Acetone completely dissolves all organic impurities on the samples [324]. Samples were then placed immediately in glass beakers containing 100% isopropyl alcohol (IPA) and left in the ultrasonic bath for 15minutes. It ensures no acetone masks are left on samples [324]. Samples were dried thoroughly using N_2 gas. Glass slides were then placed in UV sanitiser for 15minutes to clean any organics left and

process the glass surface. Samples were then packed in precleaned boxes and sealed using parafilm, and covered with aluminium foil. Beakers and tweezers were cleaned using the above method and placed in the cleanroom boxes for subsequent use.

4.3.1.3 Thermal evaporation for thin-film metal deposition

Thermal evaporation is a process in which a metal placed in a filament or basket is heated to the temperature where it starts to evaporate and deposit a thin film on the substrate. The process requires an ultra-high vacuum-tight deposition chamber to ensure that vapour molecules move freely without reacting with other atoms inside the chamber. The process was preferred over sputtering due to its low cost, simplicity, and efficiency [325]. Figure 4.2 shows the schematic illustration of a thermal evaporation system.

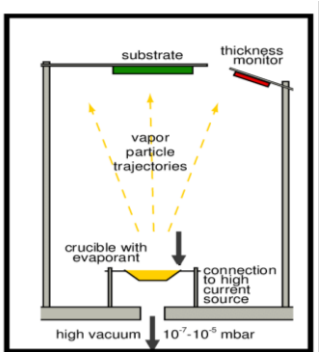

Figure 4.2: The schematic illustration of a thermal evaporation system [325].

Moorfield minilab 060 thermal evaporator, available at Laboratory Number G06, EEE Department, University of Liverpool, is used to perform thermal deposition of Cr/Au onto the glass substrate. Figure 4.3 demonstrates the thermal evaporation process used during this experimental stage.

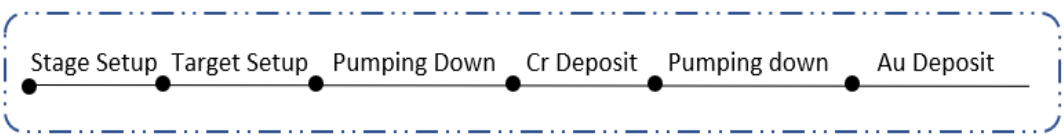

Figure 4.3: Thermal evaporation Working flow.

Firstly, the evaporator stage was cleaned with acetone and IPA. The pre-cleaned glass substrate was placed on the stage. The Shadow mask is then tightly screwed on the glass slide to remove any spacing between the glass substrate and shadow mask. It avoids producing rough edges. Cr rods were placed in the 2nd Target (TE2) while Au wire was placed in the 4th target (TE4) of the evaporator using Au basket. Quartz-crystal provides the sheet thickness of the deposited layer. Therefore, the life of quartz-crystal is checked before the evaporator is allowed to pump down to 5 x $10^{-7} bar$. If quartz-crystal life is $< 50\%$, it is changed as it does not provide the correct thickness (Appendix C2). Evaporator was controlled using the Q – POD programming tool available with the Moorefield evaporator. Z ratio of Cr and Au was set at 0.305 and 7.200, respectively [325]. The Z ratio is a parameter that corrects the frequency-change-to-thickness transfer function for the effects of acoustic-impedance mismatch between the crystal and the deposited material [325]. While the density of Cr and Au was set at 7.2 and 19.3. Once the process begins, Cr deposition starts at 45Amp, 2.5 x $10^{-6} mbar$. $2nm - 5nm$ Cr layer was deposited on the glass substrate as a seed layer which is essential because this allows Au to stick on the glass substrate. Once Cr seed layer is deposited evaporator is allowed to pump down again to 5 x $10^{-7} mbar$ before $75nm$ – $100nm$ Au is deposited at 70Amp, 0.8 x $10^{-6} mbar$ on top of Cr seed layer. Evaporator was allowed to vent to $1000 mbar$ before samples were taken out and sealed in boxes as discussed before.

4.3.1.4 Sheet Resistance (R_s) Measurement

Two methods measured sheet resistance.

i. Ohmmeter Technique

In this method, ohmic meter probes were placed on two different ends of the same electrodes.

ii. Kelvin Technique:

Kelvin technique is also known as the four-probe method. It consists of four electrical probes in line with equal spacing between them. Electrical current (I_c) was supplied on the outer two electrodes, and resultant voltage (ΔV) is measured from between the inner two electrodes. Sheet resistance is measured using the following formula:

$$R_s = \frac{\pi \Delta V}{\ln(2) I_c} \quad 4.1$$

Cr electrodes provide the sheet resistance in the range of a few hundred ohms ($> 350\Omega$) while Au electrodes give a sheet resistance in the order of a few Ohms ($< \sim 5\Omega$) were recorded.

4.3.1.5 Laser Milling

After Cr/Au the pattern is ready and tested for low sheet resistance. The electrode pattern with multiple interelectrode gaps is created using a laser mill. The device was placed on the stage of laser mil, and the shutter was shut completely. If the shutter remains open laser does not start. After several attempts, it was established that a green laser with 30% intensity is an optimum laser beam to cut the metallic electrode with sharp edges without destroying the electrodes. Above this intensity, electrodes get destroyed, while the laser produces rough electrode edges below this intensity. The laser gun was set at the height of $5.618mm$ (z-axis), while the box size of 8 x 10 is achieved by using $59.658mm$ (x-axis) x $64.821mm$ (y-axis). Box size of 8 x 10 achieves a size of the interelectrode gap of $100\mu m$. The frequency was set at

20Hz, and the process was repeated twice to confirm there was no metal left in the gate width area. Figure 4.4 provides the schematic diagram of the laser machine system.

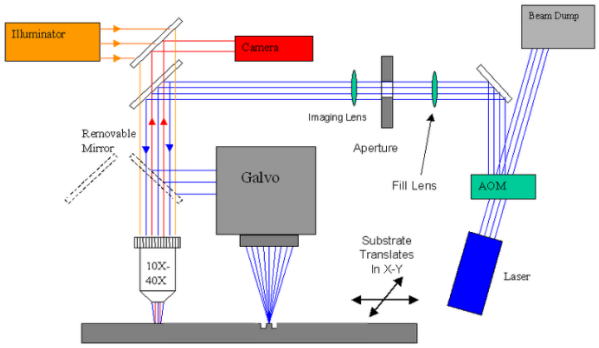

Figure 4.4: The schematic illustration of the laser machine system.

$500\mu m$ wide and $800\mu m$ long coplanar electrodes were produced with an interelectrode gap of $20\mu m$, $50\mu m$, $75\mu m$, $100\mu m$, and $150\mu m$ (Appendix 4a). The symmetry between electrodes geometry was ensured, as discussed above. Electrode cutting was monitored using a computer attached to the laser mill machine, while electrode gaps were confirmed using ImageJ software. The device was given a quick wash using DIW to remove electrode residue and dried up using N_2 gas.

4.3.2 Device preparations

4.3.2.1 Silver paint or Conductive epoxy

Silver wires were connected with electrode pads using RS PRO silver conductive paint or MG chemicals silver conductive adhesive epoxy. The device was left for one day to produce strong contacts and was heated on the hotplate at $200°C$ for 10minutes. An ohmmeter was utilised to ensure no short circuits or open circuits between the electrodes. Several other attempts were made to connect electrodes with wires. These include the use of copper tape and direct solder. However, extremely weak or no connections were produced.

4.3.2.2 Microfluidic Chamber

Chamber Height was made using a pre-clean microscope glass slide. Glass slide was cut into small sections to cover electrodes. Then, chamber height was made using parafilm (single layer thickness = 130μm). Parafilm was selected because it is cheap, extremely waterproof, flexible, highly thermoplastic, and has excellent adhesion [99].

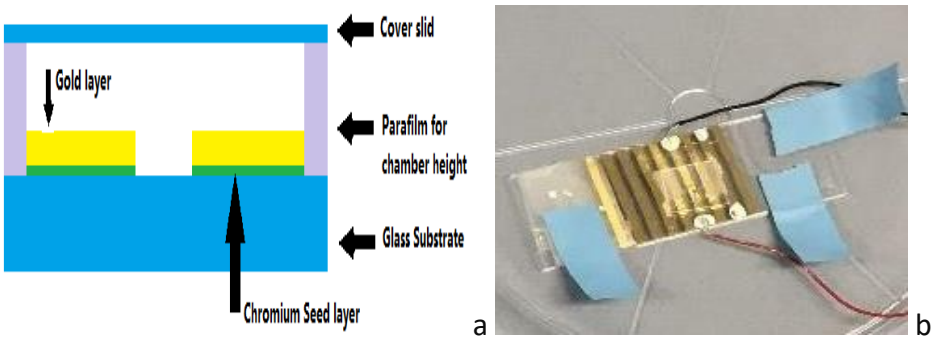

Figure 4.5: Microfluidic device used in optimising stage (a) Schematic illustration of the device. (b) An example of the final device used in the optimisation stage.

Several chamber heights built by stacking parafilm layers onto each other and tested to yield maximum vortex size as chamber height influences vortices formed but do not influence v_{EOF} [148, 184, 244]. Chamber height was measured at 100μm, 200μm, 300μm, 400μm, 600μm and 700μm. Desired thickness was achieved by folding and pressing parafilm and confirmed using a digital calliper. Figure 4.5a illustrates a schematic of the final device used in this chapter, while figure 4.5b presents an example of the final device used.

4.3.3 Conductive Media

The cell suspension is made using DIW while its conductivity was controlled by mixing Thermo fisher phosphate-buffered saline (PBS) buffer solution. The buffer solution was made by dissolving one PBS capsule $(5g)$ in 200ml DIW (Appendix 8.4). DIW has conductivity in the range of $3mS/m$ to $20mS/m$; hence it was

adjusted by adding PBS solution in DIW. Fluid conductivities were adjusted at $3mS\ /m$, $7mS\ /m$, $10mS\ /m$, $14mS\ /m$, and $20mS\ /m$. It is observed that $1ml$ of the PBS solution changes the conductivity of $50ml$ DIW by $1m\ S/m$ –$1.2mS/m$. Some experiments were also performed at $1mS/m$ and $1S/m$.

4.3.4 Cells preparation

4.3.4.1 Broth preparation

Yeast cells are used as test particles in experiments. First, yeast cells were grown in culture media, made with 5g of yeast extract peptone dextrose (YPD) in 100ml DIW. Baker's yeast was put in Cole – Parmer tubes containing $100ml$ culture media. Tubes were left overnight in an incubator at the temperature of 35°C to grow yeast. The tube's lid is kept slightly open to allow yeast cells to perform anaerobic respiration. DIW, glass bottles, and tubes were sterilised in an autoclave before use. It kills any bacterial growth and allows a healthy yeast cells population.

4.3.4.2 Cell's cleaning/wash

$1mL$ of cell suspension is placed in sigma centrifuge vials. Yeast cells were washed three times in the electrolytic media made earlier using a Millipore centrifuge. Each wash was given the rotation of 20000 rpm for 10minutes. After each wash, the fluid was replaced with a new medium. The reason to wash cells is to ensure the complete removal of culture media from the cells. Otherwise, it creates osmotic pressure during the experiments causing ambiguity in results [326].

4.3.4.3 Cell Counting

Hawksley BS748 haemocytometer is cleaned with IPA before use. A coverslip is moistened with DIW and affixed on a haemocytometer until newton's refraction rings

under the coverslip appear, indicating proper adhesion. The cell suspension was pipetted on the haemocytometer chambers, which reached the counting chamber using capillary action. Cells were counted in 4 large squares as well as a middle square. Any cells touching the outer boundary was neglected in counting, while clumps were counted as two cells. Counted cells are multiplied by 10^4 to achieve a final count per mL. Hemocytometer is cleaned, and the process is repeated three times from the same pellet. The desired cell population is achieved by diluting cells with suspension.

4.3.5 Experimental setup

The microfluidic chip was set on the microscope stage, and the electrodes were connected with the Digimess FG100 functional generator and Tektronix two-channel digital oscilloscope (Appendix B). Fluid containing yeast cells was pipetted on the device and allowed to settle down. ACEOF response is measured for an AC signal of $5V_{PP}$, AC frequency range of $0.256kHz - 2.8kHz$ $(0.256, 0.384, 0.5, 0.65, 0.8, 1, 1.25, 1.5, 1.8, 2.2, 2.5, 2.8\ kHz)$, for the fluid conductivity, interelectrode gaps and chamber heigths discussed above. Experiments were repeated for $10V_{PP}$ for the AC frequency between $0.5kHz - 1.5kHz$. Experiments were repeated 12 times for AC signal, AC frequency, chamber Height, interelectrode gap, and fluid conductivity.

AC pDEP is measured at $10V_{PP}$, and $20V_{PP}$ for the AC frequency range of $1MHz$, which is determined from the literature review. Moreover, to find cross over frequency between AC n- DEP and AC p – DEP, the frequency was swiped from $0.1MHz$ to $10MHz$. Experiments were repeated three times for each AC signal, inter-

electrode gap and chamber height. The cell population is kept constant in all experiments and is measured using a haemocytometer.

The experimental observations are recorded using the FlyCapture SDK software system attached with a 3 MegaPixel microscope c-mount video camera. ACEOF experiments are recorded for 4 minutes, while AC pDEP experiments are recorded for 3min videos. For ACEOF results, videos were analysed at 30 seconds to observe the maximum distance moved by cells for 4 minutes. It provides the maximum vortex size and the maximum time required to achieve it. v_{EOF} was observed by the distance moved by the yeast cells from the electrode edge in 1s. v_{EOF} is also observed at cell movement from $5\mu m$ to $40\mu m$ in one second to predict v_{EOF} trends at a distance from the electrode. In contrast, results for AC pDEP were analysed by cell capture each minute, and v_{DEP} was observed from the levitation point of cells, $10\mu m$, and $5\mu m$. In both cases, cell movement was observed visually and using cell tracking in MATLAB. Results for each experiment were plotted in MATLAB.

4.4 Results and Discussion

4.4.1 Optimising ACEOF Response

4.4.1.1 ACEOF Velocity

4.4.1.1.1 *Fluid conductivity, Interelectrode gap and AC Frequency*

Fluid velocity is measured as a function of the AC signal, AC frequency, fluid conductivity, interelectrode gap, and chamber height. The videos are analysed from the experimental videos recorded, with a self-programmed particle tracing technique in MATLAB. In this technique, the video is allowed to run using MATLAB. Required frames to be analysed are extracted and zoomed in. A specific particle is selected from the cursor, and the remaining background is deleted. Therefore, particle

presence was traced by keeping particle position bright and particle absence dark. Distance particle moved in one frame provides instantaneous velocity from the electrode edge; an example is shown in figure 4.6. The program draws a redline in the photograph as a particle is moved from the electrode edge.

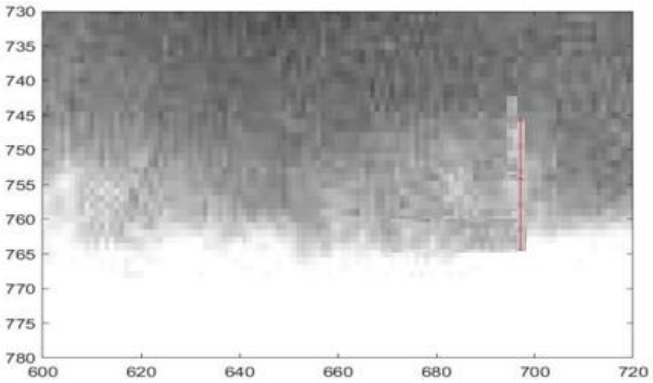

Figure 4.6: An example of cell movement under the influence of ACEOF measured by a self-programmed particle tracing technique in MATLAB.

Velocity is calculated from the electrode edge and at the different points between $5\mu m - 40um$ vertical distance away from the electrode edge. It provides the pattern of fluid velocity as the particle moves away from the electrode edge. Chamber height is kept constant for initial experimental observation at $700\mu m$.

4.4.1.1.1.1 $\boldsymbol{ACEOF\ Velocity\ at\ V_{PP} = 5V}$

It is observed from figures 4.7(a - f) that maximum v_{EOF} of $555\mu m/s$ is recorded at $75\mu m$ interelectrode gap, for the fluid conductivity of $10mS/m$ at $1kHz$ while $22\mu m/s$ is the lowest v_{EOF} reported for $150\mu m$ interelectrode gap for the same fluid conductivity at $525Hz$. These results correspond with the results obtained in [148, 236, 276] in terms of velocity trends. However, the maximum reported velocity at $5V_{PP}$ is $< 100\mu m/s$ in all previous studies [122, 164, 229]. One possible reason for this could be because all these studies focused on either one or two variables at one time. For example, while [148 236, 276] relied on chamber height only, [142 313 314] focused on the interelectrode gap. Furthermore, AC frequency and fluid conductivity

are considered in [122, 123, 236, 278]. This shows that if all variables are examined against each other, there is a definite velocity increase.

Moreover, it is seen that the optimum frequency is shifting as the interelectrode gap reaches $75\mu m$ while in the previous studies, maximum velocity occurred at $25\mu m$ interelectrode gap [212]. On the other hand, for $100\mu m$, optimised frequency shifted from $780Hz$ to $1kHz$ when the fluid conductivity increased from $3mS/m$ to $20mS/m$. The results show that maximum velocity occurs at the optimised frequency and reaches zero above and below this frequency. This trend follows the results discussed by Ramos and Green [101-102]. However, the optimised frequency of $1kHz$ is only reported in another study by Hoettges [276].

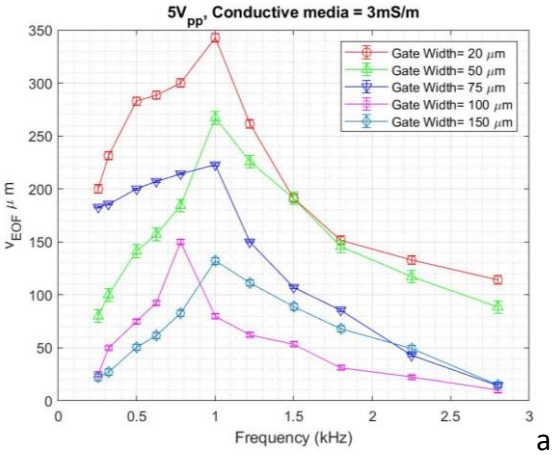

a

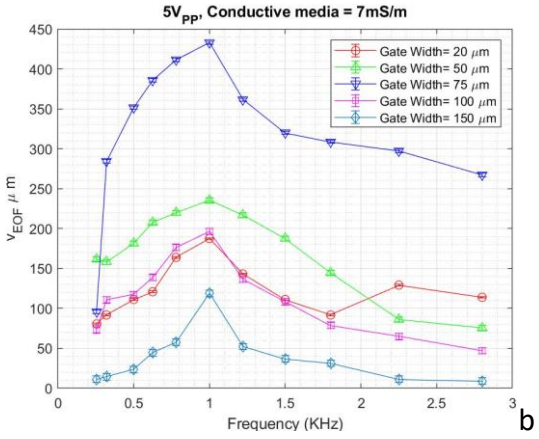

b

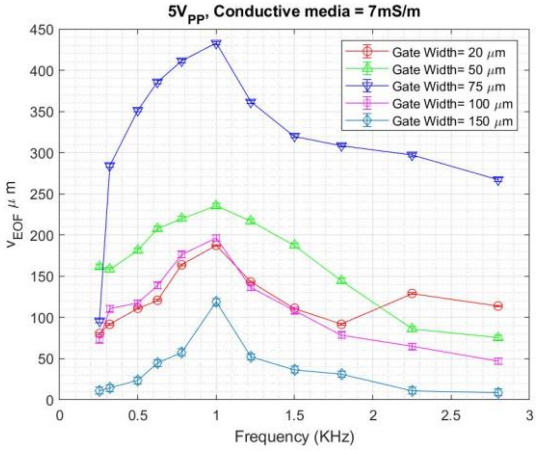

c

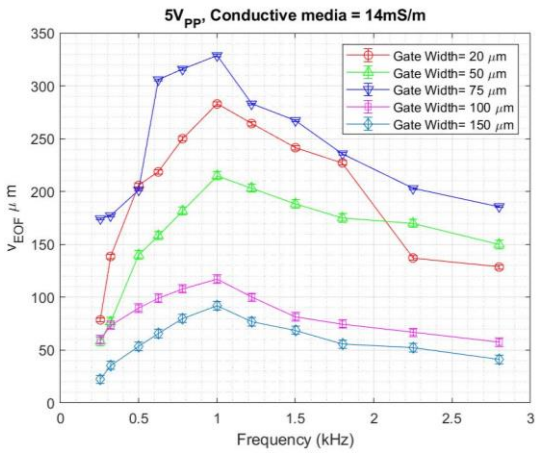

d

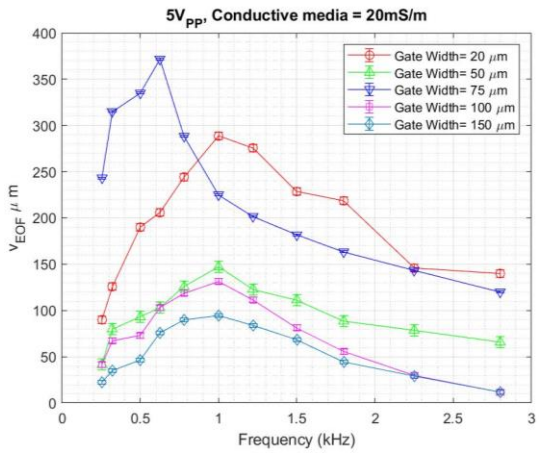

e

Figure 4.7: v_{EOF} $(\mu m/s)$ measured as a function of frequency and interelectrode gap, at $5V_{PP}$ and fluid conductivity of (a) 3mS/m, (b) $7mS/m$, (c) $10mS/m$, (d) $14mS/m$, and (e) $20mS/m$.

Moreover, figure 4.8 explains v_{EOF} versus fluid conductivity trend at different interelectrode gaps. It is observed from figure 4.8 that for $50\mu m$, $75\mu m$, and $100\mu m$ v_{EOF} reaches its maximum point at $10mS/m$ and decreases to 0 before and after this. However, $20\mu m$ and $150\mu m$ v_{EOF} decreases as fluid conductivity increase with an anomaly of $20\mu m$ at $0.02S/m$. Maximum v_{EOF} of $340\mu m/s, 260\mu m, 310\mu m/s, 130\mu m/s$ is calculated for $20\mu m, 50\mu m, 100\mu m, 150\mu m$ interelectrode gap respectively. Comparing figure 4.8 - 4.12 with figure 4.17 (a-e) gives us a clear picture that v_{EOF} directly corresponds to maximum particle displacement.

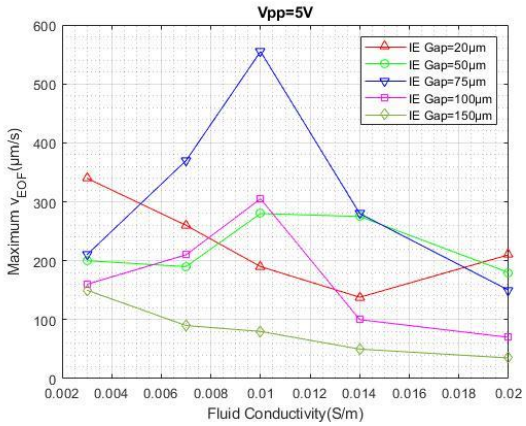

Figure 4.8: Maximum v_{EOF} $(\mu m/s)$ measured as a function of fluid conductivity (S/m), at $5V_{PP}$ for interelectrode gap $20\mu m$ – $150\mu m$.

4.4.1.1.1.2 *ACEOF Velocity at* $V_{PP} = 10V$

Figure 4.9 (a - e) shows the line plots of v_{EOF} when V_{PP} changes from $5V$ to $10V$. A significant difference is observed with v_{EOF} increases to almost double in some cases. For example, maximum v_{EOF} becomes $800\mu m/s$ as compared to $555\mu m/s$ while minimum velocity becomes $45\mu m/s$ compared to $22\mu m/s$. These results show that by changing AC Signal strength and if all other parameters are kept the same, then v_{EOF} increase as seen in [148, 236, 276] where increasing AC signal from 1V to 5V increases the v_{EOF} by 30%.

Moreover, the optimised frequency remains the same for $5V_{PP}$ and $10V_{PP}$ except for the interelectrode gaps of $50\mu m$ and $150\mu m$ in $20mS/m$ and $14mS/m$, respectively, where frequency has shifted from $780Hz$ to $1kHz$. This trend also matches Figure 4.9(a-e), where the maximum vortex for $50\mu m$ occurs at $1kHz$. For interelectrode gaps of $20\mu m, 50\mu m, 100\mu m,$ and $150\mu m$ maximum v_{EOF} is calculated as $480\mu m, 340\mu m, 440\mu m, and\ 160\mu m$ respectively which is an apparent increase as compared from $5V_{PP}$. The reason for larger v_{EOF} taking place at higher AC signal strength is because higher voltage increases the zeta potential occurring at the outer layer of the Helmholtz surface, also known as the slip plane of EDL, as discussed in chapter 2. Higher zeta potential, therefore, corresponds to higher v_{EOF}.

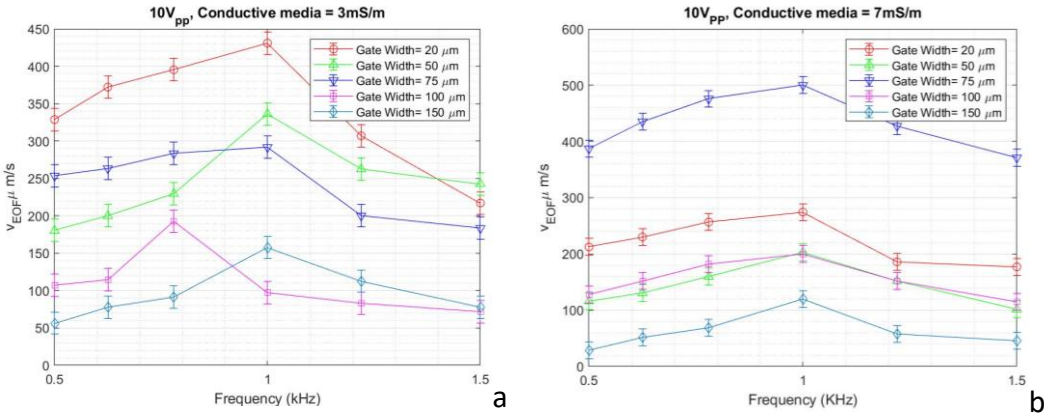

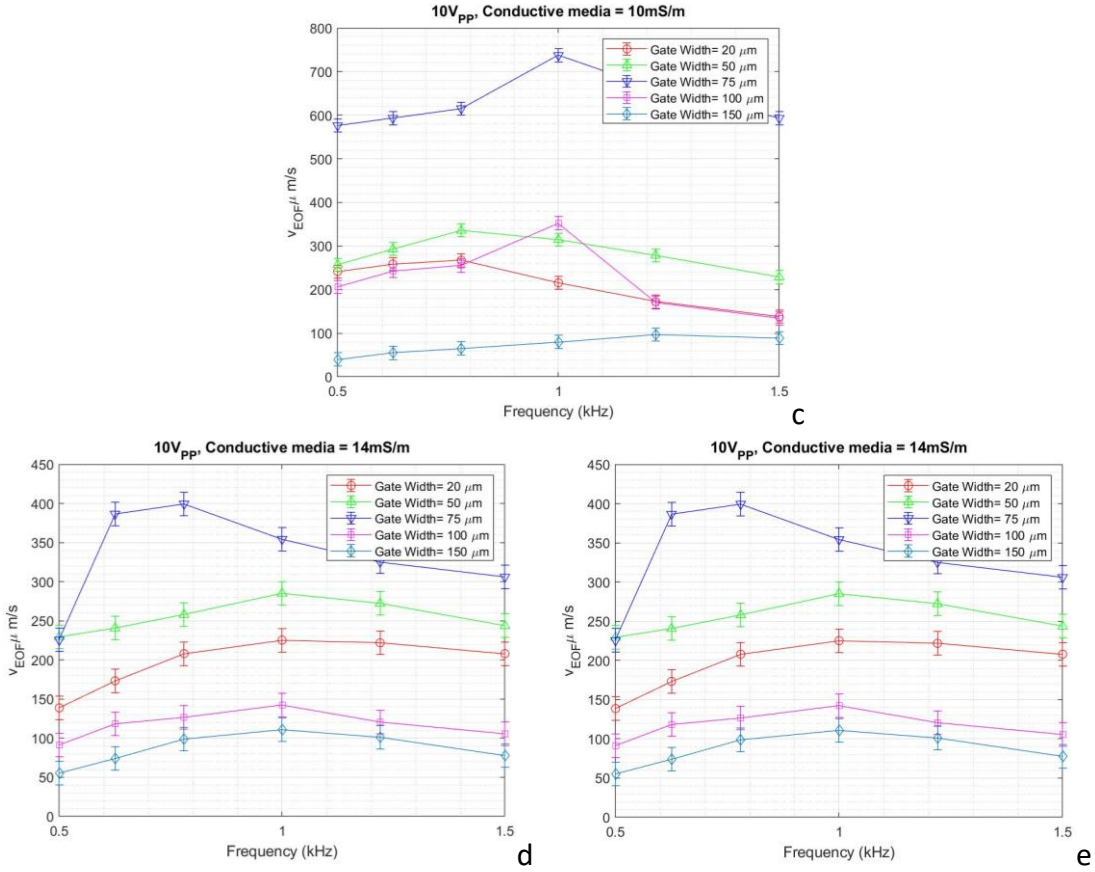

Figure 4.9: v_{EOF} $(\mu m/s)$ measured as a function of frequency and interelectrode gap, at $10V_{PP}$ and fluid conductivity of fluid conductivity of (a) 3mS/m, (b) $7mS/m$, (c) $10mS/m$, (d) $14mS/m$, and (e) $20mS/m$.

Figure 4.10 summaries the effect of AC signal on the v_{EOF} as a function of fluid conductivity for the interelectrode gap of $75\mu m$. This interelectrode gap is chosen because maximum velocity occurred at this electrode gap, and it is easy to understand the v_{EOF} difference.

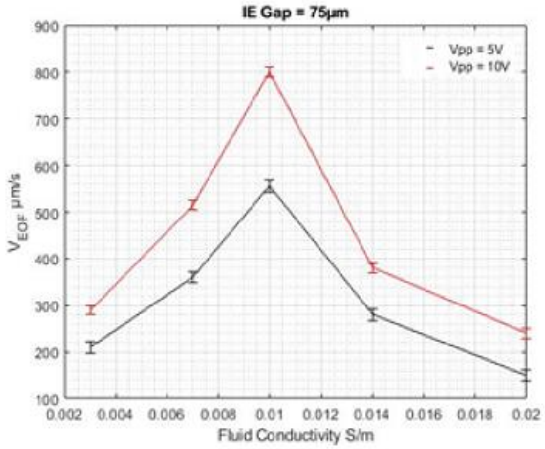

Figure 4.10: Maximum v_{EOF} $(\mu m/s)$ comparison between $5V_{PP}$ and $10V_{PP}$, for $75\mu m$ interelectrode gap and fluid conductivities between $3mS/m$ – $20mS/m$.

It is observed that maximum velocity occurred at $10mS/m$ for both voltages. Moreover, line plots show that the maximum difference of $245\mu m/s$ exists between two velocities at $10mS/m$. For all other conductivities, the velocity difference remains within $< 150\mu m$.

In theory, a smaller interelectrode gap should provide with higher v_{EOF} because a smaller interelectrode gap generates a higher electric field, and it is observed in [231]. But it is seen in results that the highest velocity is generated at $75\mu m$ interelectrode gap. It is because smaller for $20\mu m$ interelectrode gap, vortices formed are close to each other and hence cancel each other effects.

4.4.1.1.2 *Velocity as a function of distance from the Electrode Edge*

This section discusses results when v_{EOF} is measured as a function of distance from the electrode edge. Figure 4.11a and 4.11b are comparisons of velocities measured at different positions, i.e., $10\mu m, 20\mu m, 30\mu m$, and $40\mu m$ from the electrode edge as a function of interelectrode gaps for $5V_{PP}$ and $10V_{PP}$. It provides insight into how velocity behaves throughout the vortex and is helpful to compare results in chapter 6.

Figure 4.11a and 4.11b depict that velocity decreases as the cell moves away from the electrode edge both at $5V_{PP}$ and $10V_{PP}$ respectively. Calculations show a drop of 67%, 71%, 32%, 54%, and 80% in the fluid velocity for the interelectrode gaps of $20\mu m, 50\mu m, 75\mu m, 100\mu m$, and $150\mu m$ respectively, by the time particle has moved $40\mu m$ distance from the edge of the electrode. This trend is previously observed by Ramos [123]. However, the percentage decrease was not discussed in [123], which is an important finding, especially when comparing results in chapter 6.

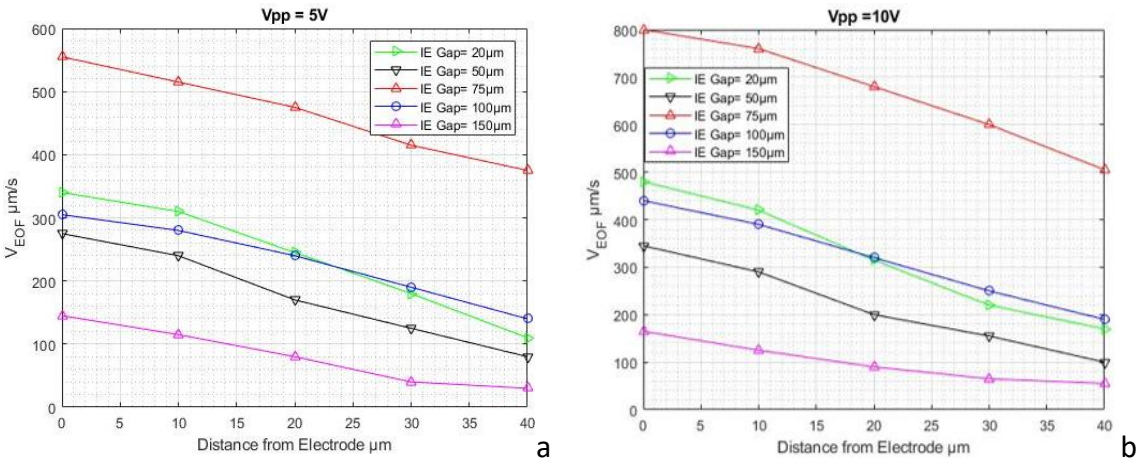

Figure 4.11:Maximum v_{EOF} $(\mu m/s)$ measured as a function of distance from the electrode at (a) $5V_{PP}$ and (b) $10V_{PP}$ for interelectrode gap $20\mu m$ – $150\mu m$.

4.4.1.1.3 ***Fluid conductivity, Interelectrode gap and AC Frequency***

The particle displacement was measured as a function of fluid conductivity interelectrode gap and AC frequency. Results are quantified for the AC signal of $V_{PP} = 5V\ and\ 10V$. During these initial investigations, chamber height is kept constant at $700\mu m$. This ensures that particle displacement reaches its maximum potential and is not limited by the chamber height, as seen in previous studies [255, 276, 278], where chamber height was a limiting factor to achieve maximum particle displacement. It is because smaller chamber heights limit the fluid vortex size, and therefore it can influence the particle displacement.

4.4.1.1.3.1 $V_{PP} = 5V$

Figure 4.12 illustrates the results of the particle displacement vs AC frequency at different interelectrode gaps for the fluid conductivity of $3mS/m$. The plot shows that $1kHz$ is the optimised frequency for all interelectrode gaps, except $100\mu m$, which has an optimised frequency of $780Hz$. It is also observed that the particle displacement decreases as the interelectrode gap increases. The line plots also depict

that a maximum vortex size of 248μm is achieved at $1kHz$ for the interelectrode gap of 20μm. At the same time, the minimum particle movement of 18μm is recorded for the interelectrode gap of 100μm at $2.8kHz$.

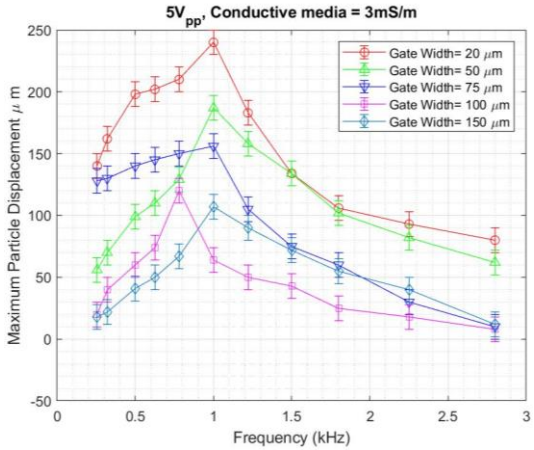

Figure 4.12: Maximum particle displacement (μm) measured as a function of frequency and interelectrode gap, at $5V_{PP}$ and fluid conductivity of $3mS/m$.

However, as fluid conductivity increases, optimum frequency shifts towards wider electrode gaps, as observed in figures 4.13 – 4.16. For $7mS/m$ (figure 4.13), 305μm is the maximum particle displacement achieved at $75\mu m$ while for $20\mu m$ it is dropped down to $150\mu m$, $4\mu m$ below from $100\mu m$ interelectrode gap. A maximum particle displacement of $11\mu m$ is observed for $150\mu m$ interelectrode gap. For all interelectrode gaps, $1kHz$ is observed as optimised frequency.

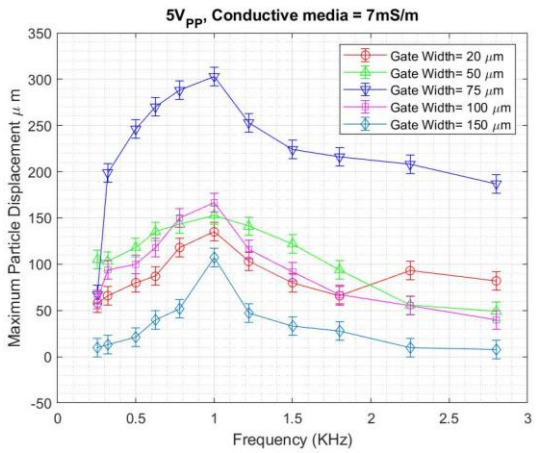

Figure 4.13: Maximum particle displacement (μm) measured as a function of frequency and interelectrode gap, at $5V_{PP}$ and fluid conductivity of $7mS/m$.

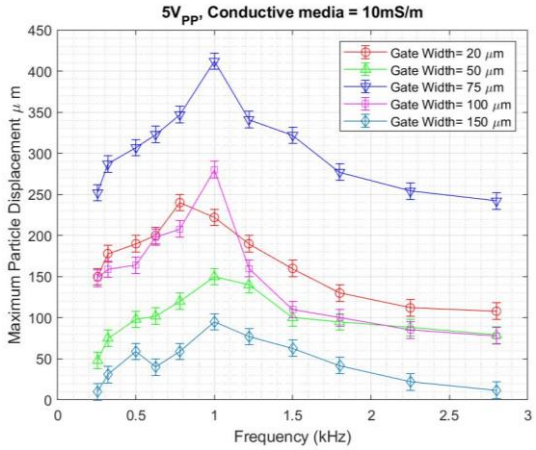

Figure 4.14: Maximum particle displacement (μm) measured as a function of frequency and interelectrode gap, at $5V_{PP}$ and fluid conductivity of $10mS/m$.

For $10mS/m$ fluid conductivity (figure 4.14), a maximum vortex size of 412μm is achieved for 75μm at $1kHz$. In all cases, maximum particle displacement occurs at the optimised frequency of $1kHz$ except for 150μm where a maximum particle displacement of 98μm is achieved at $1.25kHz$. A minimum vortex size of 12μm occurs for 150μm.

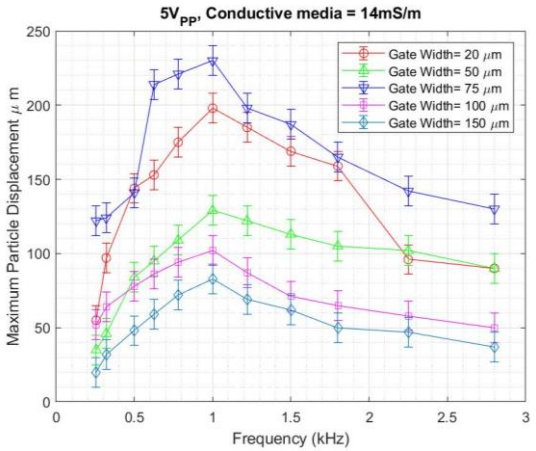

Figure 4.15: Maximum particle displacement (μm) measured as a function of frequency and interelectrode gap, at $5V_{PP}$ and fluid conductivity of $14mS/m$.

As fluid conductivity increases to $14mS/m$ (figure 4.15) drop in the vortex size for all interelectrode gaps is observed. However, a maximum vortex size of $225\mu m$ still occurs at $75\mu m$ gate width. The optimised frequency for each electrode gap is $1kHz$.

The smallest vortex size is reported at 30μm for 150μm at 2.8kHz. It is an increase from 11μm to 30μm.

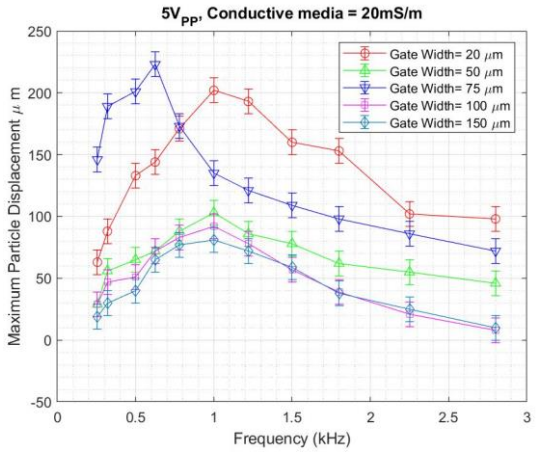

Figure 4.16: Maximum particle displacement (μm) measured as a function of frequency and interelectrode gap, at 5V_{PP} and fluid conductivity of 20mS/m.

For 20mS/m (figure 4.16), it shows the mix trends for interelectrode gaps and frequency. 212μm is the heights vortex size achieved at 20μm at 780Hz, while the frequency for 75μm is reported at 625Hz. 11μm, the minimum vortex size is also shifted to 0.26kHz from 2.8kHz for the interelectrode gap of 100μm.

4.4.1.1.3.2 $V_{PP} = 10V$

Experiments were repeated for 10V_{PP} for the range of 628Hz to 1.8kHz, as established from the previous section results that optimised frequency for all given interelectrode gaps (gate widths) and fluid conductivities remain within this range. Results are discussed below with the help of MATLAB plots. Figure 4.17 (a-e) illustrates that there is a very slight difference in the maximum vortex size obtained when V_{PP} is switched from 5V to 10V. For instance, a maximum particle displacement of 430μm is obtained for the interelectrode gap of 75μm, at 10mS/m, and optimised frequency of 1kHz. It is the minimal increase in the vortex size from 412μm to 430μm.

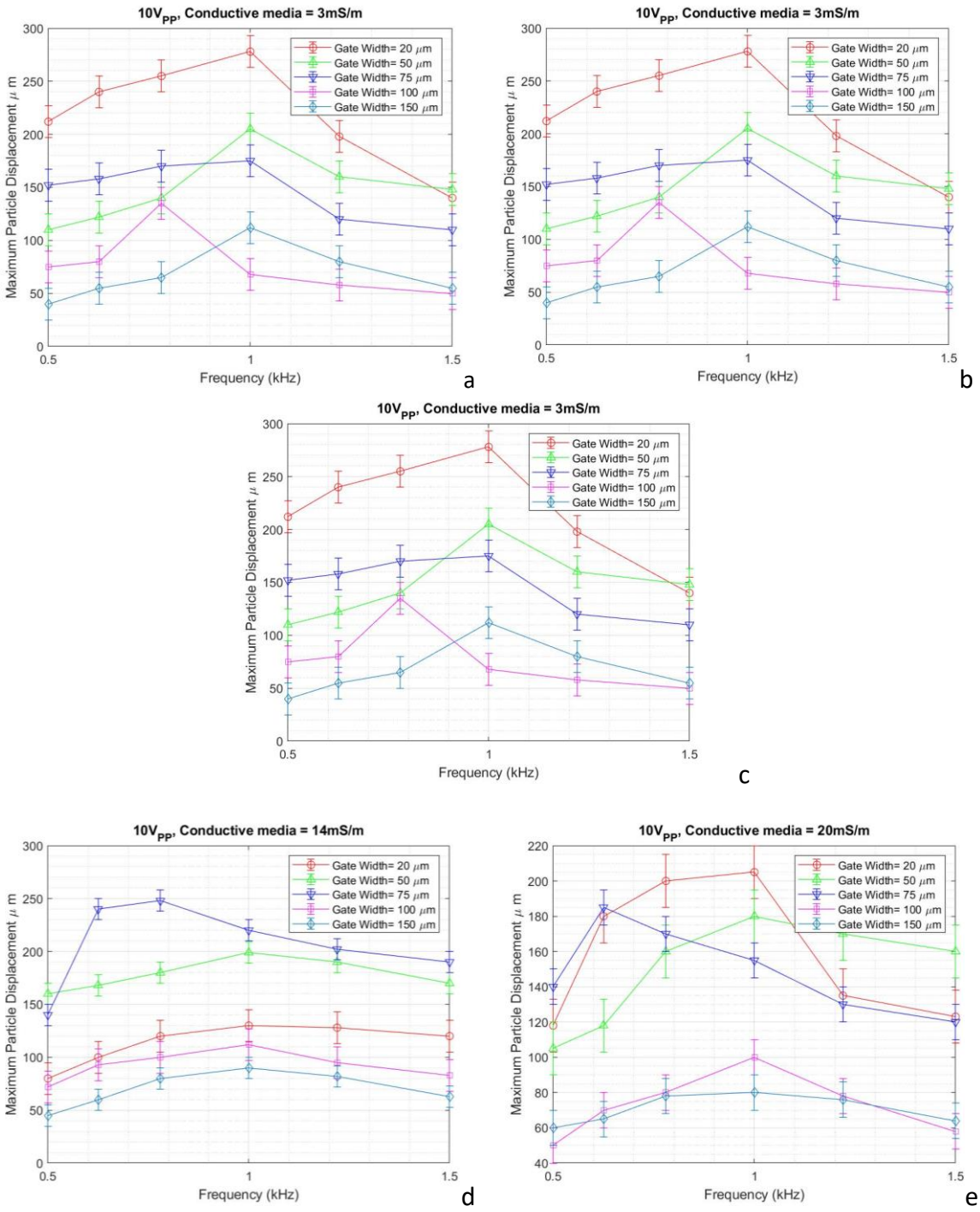

Figure 4.17: Maximum particle displacement (μm) measured as a function of frequency and interelectrode gap, at $10V_{PP}$ and fluid conductivity of (a) $3mS/m$, (b) $7mS/m$, (c) $10mS/m$, (d) $14mS/m$, and (e) $20mS/m$.

Figure 4.17 (a-e) illustrates that there is a very slight difference in the maximum particle displacement obtained when V_{PP} is switched from $5V$ to $10V$. For instance, a maximum particle displacement of 430μm is obtained for the interelectrode gap of

$75\mu m$, at $10mS/m$, and optimised frequency of $1kHz$. It is the minimal increase in the particle displacement from $412\mu m$ to $430\mu m$. Also, in all cases, the optimised frequency is the same as $5V_{PP}$ except $20\mu m$, at $20mS/m$ where the frequency is swept from $750Hz$ to $1kHz$. However, particle displacement is decreased from $212\mu m$ to $205\mu m$.

This shows that despite velocity being influenced by AC signal, as seen in [236, 313], particle displacement is not affected by a great division. These results are of fundamental importance because, in previous studies, particle displacement was not discussed except in Mohtar [277] and Hoettges [278]. In these studies, particle collection was limited to 200 pores only, and due to zipper electrode, geometry particles were concentrated inwards towards the centre of the electrode gap. Also, it has been observed that maximum particle displacement occurred with the lowest fluid conductivity and narrowest electrode width. However, this is not the case, as seen in the experimental work where $75\mu m$ electrode gap provided with both highest velocity and particle displacement. It shows that particle displacement is a velocity-dependent phenomenon. There is not much literature available to counter-argue this trend. However, Hoettges [278] found maximum particle displacement at $100\mu m$ with zipper electrodes.

Furthermore, while $75\mu m$ produced the largest particle displacement while $150\mu m$ produced the smallest particle displacement, this employs that smaller percentage drop produces bigger particle displacement and vice versa. It is also concluded that the fluid velocity drops by 64%, 67%, 36%, 56%, and 75% for the interelectrode gap of $20\mu m, 50\mu m, 75\mu m, 100\mu m,$ and $150\mu m$ respectively by the time particle move to the $40\mu m$. It means that voltage increase has little on particle displacement. That

is why voltage change has little effect on overall particle displacement. It is evident from the results that changing the AC signal does not change particle displacement as expected from the literature [275, 244, 288]. Despite there being a slight increase in the particle displacement but maximum change reported is only $18\mu m$, which is negligible if compared with velocity profiles studied in [198, 277].

4.4.1.1.4 ***Particle displacement v chamber height***

Section 4.4.1.1 determines that for all given AC signals, AC frequencies, fluid conductivities, and interelectrode gaps, maximum particle displacement achieved is $412\mu m$ for $5V_{PP}$ and $430\mu m$ for $10V_{PP}$. However, these results were quantified for the chamber height of $700\mu m$. Hence, in this section, results are presented for the experiments performed at different chamber heights to achieve optimal chamber height for the desired results. Experiments were repeated three times and averaged for each interelectrode gap at its optimised frequency and conductivity at $10V_{PP}$ as it provides a slightly larger particle displacement as compared to $5V_{PP}$. As the maximum particle displacement achieved for any experiments is 430µm, seven chamber heights were used from 100µm - 700µm. Each experiment was recorded for 2min, and results were analysed every 15s. Figure 4.15 shows the results obtained during the experiments.

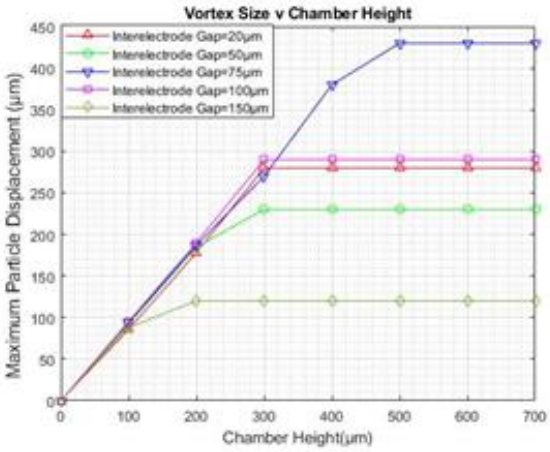

Figure 4.18: Maximum particle displacement (μm) relation as a function of chamber height (μm).

Figure 4.18 shows that in all cases except $75\mu m$ particle displacement gets plateau at chamber height of $300\mu m$ while for $75\mu m$ a chamber height of $500\mu m$ is the optimum chamber height as it allows to reach particle displacement of $430\mu m$. Result analysis shows that for the chamber height of $300\mu m$, the largest particle displacement of $290\mu m$ occurs at $100\mu m$ interelectrode gap, which is only slightly higher than $20\mu m$ and $75\mu m$ gate widths. This is because maximum particle displacement $20\mu m$ can reach. At the same time, for $75\mu m$, higher velocity occurs, allowing fluid and particle to reach chamber height at a higher velocity and then reflects from them until particle are settled at around $270\mu m$ distance from the electrode edge. Therefore, it is determined that if smaller chamber heights are required, then the interelectrode gap of $100\mu m$ is an optimum value. The study improves Mohtar's [278] chamber height effect on particle collection because Mohtar [278] compared the particle collection with respect to chamber height and showed that fewer particles are collected at lower chamber height. Therefore, increasing chamber height increases the particle collection. However, in this study, it can be seen that by increasing chamber height, particle displacement increases but

gets plateaus after around $300\mu m$ displacement. In Mohtar [278] case, the particle displacement chamber height up to $1300\mu m$ was studied because, in this study, DEP is also required, so a chamber height of $250\mu m$ is selected. Furthermore, in Mohtar [278], particle displacement was not plateau even at $1300\mu m$, which was because of the zipper electrode geometry.

4.4.1.1.5 ***Maximum particle displacement v Time***

Experimental videos are analysed to measure the time to reach maximum particle displacement. Results are analysed for each AC signal, AC frequency, interelectrode gaps and fluid conductivity for the chamber height of $700\mu m$. Each video was measured for 4 minutes. However, results are plotted for 60 seconds as maximum particle displacement is achieved well within this time frame. Results are plotted for characteristic frequencies and fluid conductivities where the maximum particle displacement is achieved at $5V_{PP}$ (figure 4.14a) and $10V_{PP}$ (figure 4.14b). Observations are made at five-second intervals.

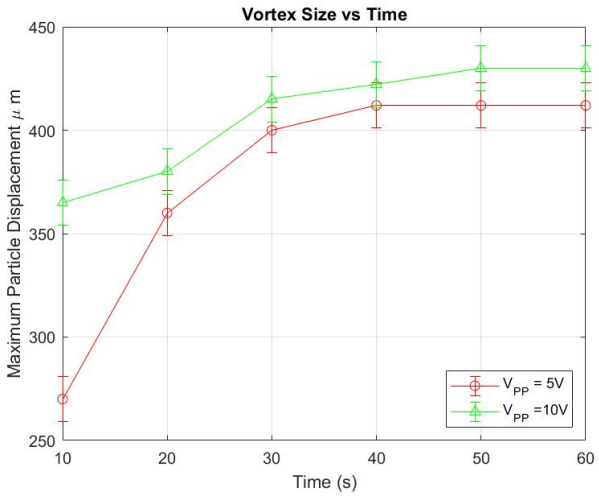

Figure 4.19: Maximum particle displacement (μm) measured at $5V_{PP}$ and $10V_{PP}$ in one minutes.

4.19Figure 4.19 show that the maximum particle displacement is recorded for the first 20 seconds, after which the particle displacement begins to decay. It is because

v_{EOF} is highest near the electrode edge and decreases as the particle moves away from the particle. Also, it is noted that higher displacement in the first 20 seconds occurred for $10V_{PP}$ as compared to $5V_{PP}$. This shows that velocity is higher at the electrode edge and decays as the particle moves further away from the electrode edge. The decay of particle displacement and velocity is because the particle experience shear forces that tend to stall its motion.

4.4.1.2 Electrode width effect on v_{EOF} and Particle displacement

As discussed earlier, all experiments are performed using $500\mu m$ wide coplanar gold electrodes. However, using $500\mu m$ width for a multi-electrode geometry is not a practical choice as it not only increases the characteristic length of the device but also in the final device-width must be small enough that particles can pass away from it and makes the wavefront after the electrode. Therefore, experiments are repeated with narrower electrode widths to quantify particle displacement and velocity response. Electrodes with $300\mu m$ and $400\mu m$ electrode widths were tested as it provides with a good idea of how electrodes' width affect velocity and particle displacement. Experiments are performed for $100\mu m$, and $75\mu m$ interelectrode gap only as the maximum particle displacement occurred for these interelectrode gaps. Moreover, the fluid medium used for this section is $10mS/m$ and electrodes are energised with $10V_{PP}$, 1kHz signal.

Results are shown in figure 4.20a for particle displacement and 4.20b for v_{EOF}. Results confirm that decreasing electrode width decreases particle displacement and fluid flow velocity. It is because narrower electrodes affect the distribution of field lines and the angle they intersect EDL. It implies that a weaker ACEOF response takes place due to which slower v_{EOF} is produced [327-329]. Fluid velocity is dropped from

$800\mu m/s$ to $580\mu m/s$ for $75\mu m$ electrode interelectrode gap while $100\mu m$ interelectrode gap decreases velocity from $440\mu m/s$ to $290\mu m/s$. Furthermore, maximum particle displacements decrease from $440\mu m$to $390\mu m$ for $75\mu m$ interelectrod gap which is $\sim 36\%$ drop in particle displacement and $290\mu m$ to $210\mu m$ for $100\mu m$ interelectrode gap corresponding to $\sim 27\%$ drop.

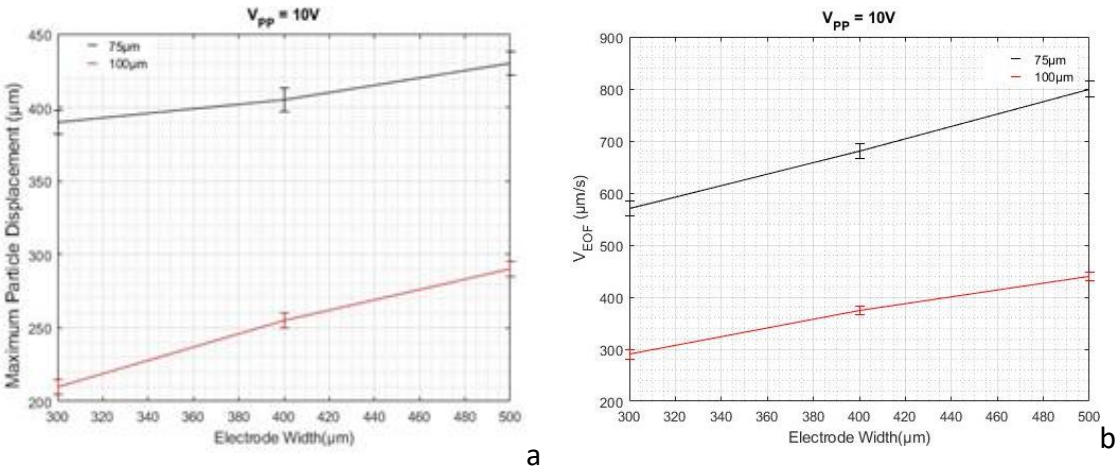

Figure 4.20: Effect of changing electrode width on (a) maximum particle displacement (μm) (b) v_{EOF} $(\mu m/s)$.

4.4.2 ACEOF Analysis

In this section, ACEOF parameters, namely; AC signal strength ($5V_{PP}$ and $10V_{PP}$), AC signal frequency ($260Hz$ – $2.8kHz$), fluid conductivity ($3mS/m$ – $20mS/m$), interelectrode gap ($20\mu m$ – $150\mu m$), Chamber height ($100\mu m$ – $700\mu m$), the velocity at a distance from the electrode ($5\mu m$ – $40\mu m$), and electrode width ($300\mu m$ – $500\mu m$) are comprehensively analysed for each other to quantify ACEOF velocity and most importantly maximum particle displacement.

The significance of ACEOF velocity and particle displacement for the project is explained earlier. In a nutshell, quantifying ACEOF velocity and maximum particle displacement is essential as it provides the best parametric for maximum particle displacement. These results are not only in agreement with the ACEOF principles

discussed in chapter 2 but has quantified information about particle displacement that was so far not covered in the scientific literature, as seen in chapter 3.

Detailed examination of the results in this section summarises that:

1- Maximum particle displacement of $412\mu m$ for $5V_{PP}$ and $440\mu m$ for $10V_{PP}$ occurred at the optimised frequency of $1kHz$ for the fluid conductivity of $10mS/m$ and the interelectrode gap of $75\mu m$. Second highest particle displacement of $280\mu m$ for $5V_{PP}$ and $290\mu m$ for $10V_{PP}$ is observed at $100\mu m$ interelectrode gap, which occurred at the same frequency and fluid conductivity. Comparing previous studies, it is found that optimum frequency is in the range of 1.1 – 1.6kHz [122, 229, 236] while [278] has optimum frequency of 1kHz.

2- Maximum particle displacement is slightly affected by the change in an AC signal because velocity drops significantly as the particle moves away from the electrode edge. However, shifting from an AC signal of $5V_{PP}$ to $10V_{PP}$ helps to reach maximum particle displacement 10seconds faster. It is because v_{EOF} is directly proportional to the AC signal with a maximum velocity of $555\mu m/s$ at $5V_{PP}$ and $800\mu m/s$ at $10V_{PP}$ is calculated for $75\mu m$ interelectrode gap and $305\mu m/s$ at $5V_{PP}$ and $430\mu m/s$ at $10V_{PP}$ for $100\mu m$ interelectrode gap. Moreover, maximum velocities occur at $1kHz$ and $10mS/m$ as well. Furthermore, the study shows a clear improvement of v_{EOF} of $800\mu m/s$ compared to $<100\mu m/s$ from previous studies [142,313].

3- Particle displacement has an inverse relation to the chamber height. Maximum particle displacement achieved is $290\mu m$, and $440\mu m$ for

$100\mu m$ and $75\mu m$ interelectrode gaps. Therefore, $300\mu m$ and $500\mu m$ chamber heights are optimum values for these interelectrode gaps. On the other hand, velocity is not affected by chamber height because it initiates from the electrode edge and tends to zero as it moves away from the electrode edge.

4- Narrower electrode widths decrease particle displacement, and fluid velocity with $\sim 9\%$ less particle displacement drop is calculated with $100\mu m$ interelectrode gap compared to $75\mu m$.

5- Higher fluid conductivities correspond to lower values of ACEOF. Therefore, the smallest particle displacement and velocities take place at higher conductivities. Moreover, at frequencies lower than $260Hz$, bubbles formation occurs due to electrolysis.

6- Maximum fluid flow occurs at the optimised frequency for all interelectrode gaps, tending to zero before and after this frequency. Moreover, change in the interelectrode gap, and fluid conductivity shifts the optimised frequency.

Based on the results summarised above, it is concluded that:

i. A combination of $75\mu m$ interelectrode gap, at AC signal of $10V_{PP}$, $1kHz$ for $10mS/m$ fluid conductivity and chamber height of $500\mu m$ collects yeast cells at a distance of $430\mu m$.

ii. On the other hand, using the same parametric combination chamber height of $300\mu m$, $100\mu m$ interelectrode gap collects particles $290\mu m$ from the electrode edge. Therefore, henceforth these parameters are used in the project.

iii. $10V_{PP}$ does not has a significant effect on the particle displacement but helps to form particle wavefront 10sec faster than $5V_{PP}$. Hence AC voltage of $10V_{PP}$ is going to be utilised in the multielectrode stage.

4.5 Optimising AC pDEP Response

AC pDEP strongly depends on other factors such as electrode geometry, interelectrode gap, and fluid conductivity. It is already established that coplanar electrode with $75\mu m$ or $100\mu m$ interelectrode gaps is used in the experiments for $100mS/m$ fluid conductivity. From DEP models and literature review [118,202], it has been established that 1MHz provide the strongest AC pDEP for yeast cells. Therefore in this section, the main parameter to be examined is chamber height as it is observed that lower chamber heights provide higher yield DEP [214, 215] while higher chamber height provides higher ACEOF yield [277, 278]. Therefore, a compromise is required for the chamber height for which quantifying AC signal strength and AC frequency is crucial. Moreover, the AC signal and AC frequency response are also discussed to help match results with the finite element model developed for DEP in chapter 6. AC pDEP response is measured for the AC signal $10V_{PP}$ and $20V_{PP}$ and swiped between $100kHz\ to\ 10MHz$. Chamber heights from $100\mu m - 500\mu m$ are investigated to achieve maximum trapping efficiency. One day old yeast cells are grown and used as test particles because yeast cells are tough easy to use, and literature is available on yeast cells to relate results. Cell's flow rate is $0\mu l/min.$ $4\ \text{x}10^4$ cells per ml are counted and used during the experiments. Fluid medium conductivity throughout these experiments is kept at $10mS/m$.

4.5.1 AC pDEP vs AC frequency, AC Signal, and Interelectrode Gap

The DEP yield corresponding to $300\mu m$ chamber height is measured as a function of the AC signal ($10V_{PP}, 20V_{PP}$) and measured for frequency (10kHz, 100kHz, 1MHz,10MHz) as shown in figures 4.21a and 4.21b for the interelectrode gap of $75\mu m$ and $100\mu m$, respectively. The reason for only four frequency points is that it has already been established that the strongest AC pDEP occurs at 1MHz.

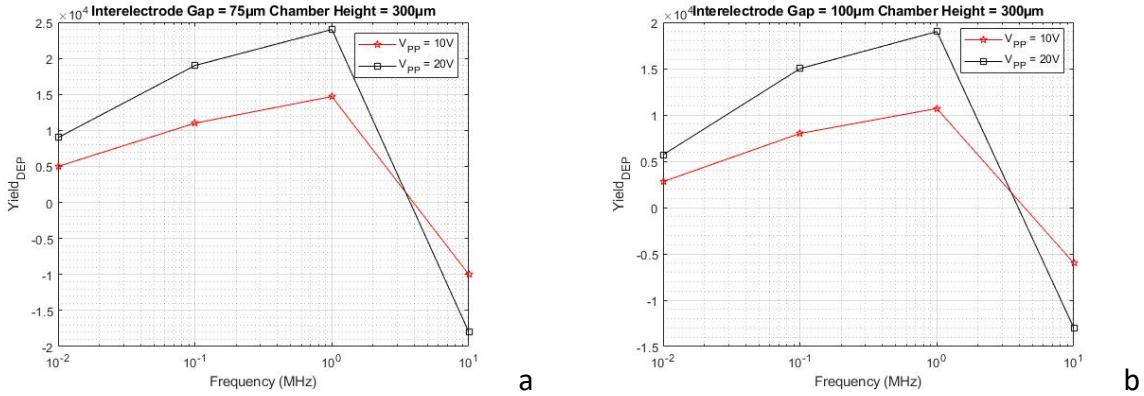

Figure 4.21: AC pDEP yield as a function of frequency at $300\mu m$ for the interelectrode gap of (a) $75\mu m$ and (b) $100\mu m$.

Results show that AC pDEP yield increases with an increase in the AC signal. A higher AC signal generates a higher electric field. Moreover, a narrower interelectrode gap provides a higher electric field, meaning AC pDEP has an inverse relation with the interelectrode gap. Therefore, $75\mu m$ interelectrode gap provides a higher yield compared to $100\mu m$. Moreover, $20V_{PP}$ also has higher cell trapping compared to $10V_{PP}$. Maximum yield is reported at ~ 2.3 x 10^4 at $75\mu m$ at $20V_{PP}, 1MHz$, compared to ~ 1.9 x 10^4 cells at $100\mu m$ at $20V_{PP}, 1MHz$. Moreover, weak AC pDEP occurs at $0.01MHz$, which gets stronger as frequency increases. Maximum AC pDEP yield occurs at $1MHz$ after which yield starts to drop. At around $6MHz$, DEP changes direction from AC pDEP, and AC nDEP starts to occur for $75\mu m$ interelectrode gap

while crossover took place at $6.3MHz$ for $100\mu m$ interelectrode gap, which gets stronger nDEP took place at $10MHz$.

Maximum AC pDEP yield efficiency of $\sim 57.5\%$ is achieved for $75\mu m$ interelectrode gap, while $100\mu m$ interelectrode gap provides $\sim 49.3\%$ efficiency. The reason for low cell efficiency is that the experiment was only allowed to run for 10 minutes. Moreover, cell trapping is performed using only one pair of electrodes. Therefore, cell trapping can be increased by applying AC pDEP for a longer time and using more electrodes, as discussed by Hughes [214,215]. These results are per [208, 209] for $1MHz$ frequency to provide the strongest AC pDEP where the strongest AC pDEP yield occurred at $1MHz$.

4.5.2 AC pDEP vs Chamber Height

After quantifying AC pDEP response for AC Signal and frequency, as a next step, AC pDEP is quantified as a function of chamber height from $100\mu m - 500\mu m$, chamber height beyond $500\mu m$ is irrelevant as maximum particle displacement achieved during ACEOF is $430\mu m$. Experiments are performed for $10V_{PP}$, and $20V_{PP}$ at $1MHz$ for $75\mu m$ and $100\mu m$ interelectrode gaps. Experiments were repeated three times. The results are averaged and summarised in figures 4.22a and 4.22b.

Results indicate that chamber height is inversely proportional to the yield as expected from [211, 215]. Results show that $75\mu m$ interelectrode gap provides $\sim 92\%$ trapping efficiency at $20V_{PP}$ compared to $\sim 65\%$ at $10V_{PP}$ for the chamber height of $100\mu m$. In both cases, net yield drops to less than $\sim 28\%$ as chamber height approaches $500\mu m$ mark. Also, $100\mu m$ interelectrode gap at $100\mu m$ chamber height gives

$\sim 88\%$ efficiency for $20V_{PP}$ in contrast to $\sim 50\%$ for $10V_{PP}$. Both interelectrode gaps efficiency drops down to less than 11% for both AC signals at $500\mu m$ chamber height.

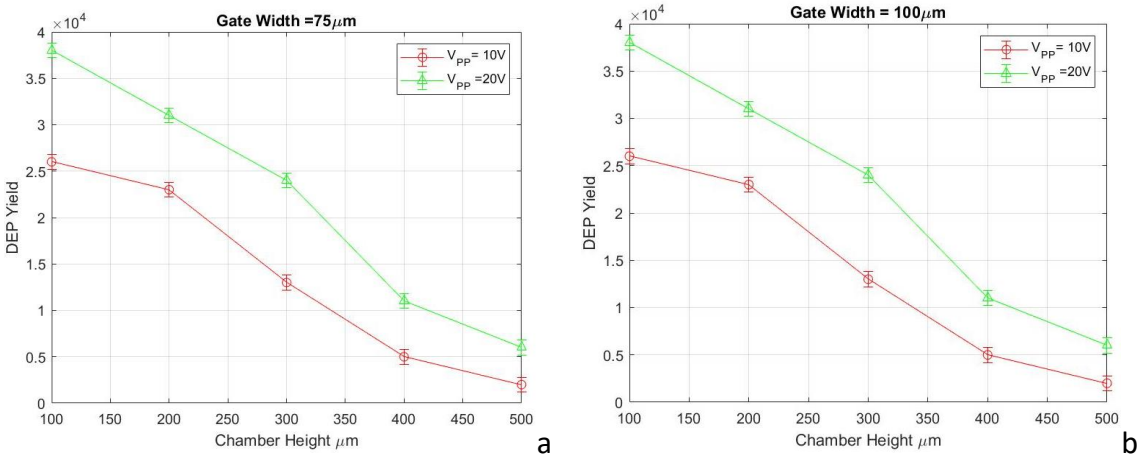

Figure 4.22: AC pDEP yield as a function of Chamber height (μm) at $10V_{PP}$, and $20V_{PP}$ for the interelectrode gap of (a) $75\mu m$ and (b) $100\mu m$.

Higher trapping efficiency with smaller chamber heights is because of the cell suspension point, which is the vertical distance of the cell from the electrode. Smaller chamber heights mean that most cells are closer to the electrode edge. Therefore, these cells experience a stronger electric fields gradient and get trapped at electrode edges under the influence of AC pDEP.

As the suspension point increases in response to the higher chamber heights, cells get less affected by the electric field gradient resulting in low net yield. It can be visualised from figure 4.23a and 4.23b, which summarise the v_{DEP} response to the particle's suspension point. v_{DEP} is calculated when the cell is suspended at $50\mu m, 25\mu m \; and \; 5\mu m$ away from the electrode edge. Results are summarised for $75\mu m$ and $100\mu m$ interelectrode gaps at $10V_{PP}$ and $20V_{PP}$., $1MHz$.

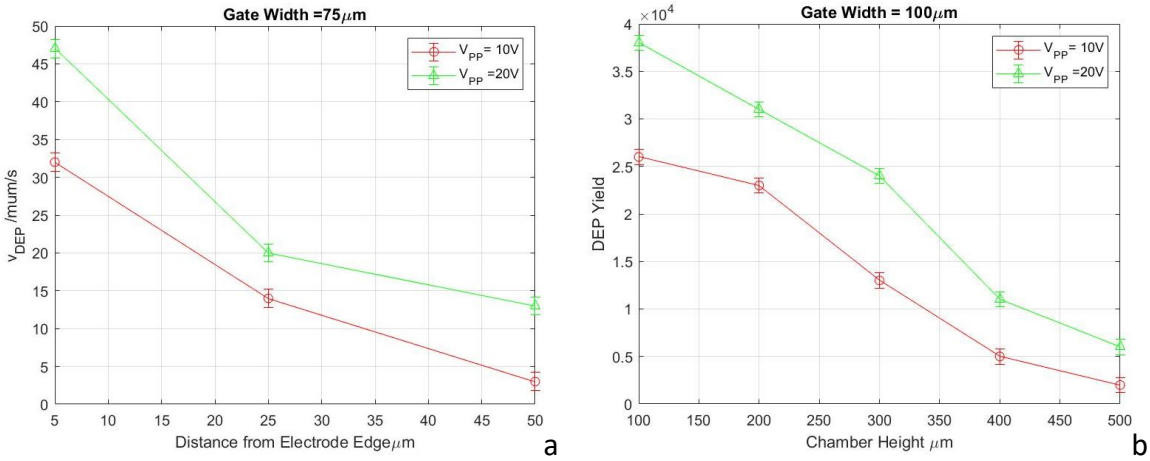

Figure 4.23: v_{DEP} $(\mu m/s)$ as a function of Chamber height (μm) at $10V_{PP}$, and $20V_{PP}$ for for the interelectrode gap of (a) $75\mu m$ and (b) $100\mu m$.

In summary, v_{DEP} increases as the cell move closer to the electrode edge. In all cases v_{DEP} is lowest at $50\mu m$ levitation point and increases significantly at $5\mu m$ from the electrode edge. For example, using $75\mu m$ interelectrode gap, v_{DEP} increases from $12.35\mu m/s$ to $47.2\mu m/s$ as the particle moves from $50\mu m$ to $5\mu m$ under the influence of $20V_{PP}$. On the other hand, comparing the highest velocity of $47.2\mu m/s$ at $75\mu m$ interelectrode gap with $39.20\mu m/s$ generated with $100\mu m$ interelectrode gap helps to conclude that smaller interelectrode gap generates higher electric field gradient and hence the highest v_{DEP} takes place as discussed in [220].

4.5.3 AC pDEP vs Time

Calculating AC pDEP response as a function of time is necessary as it provides insight into the behaviour of cell yield for the AC signal in the given time frame. Figure 4.24a and 4.24b summarises the results of DEP yield throughout 120s with 20s step size, for $10V_{PP}$ $1MHz$, and $20V_{PP}$, $1MHz$. Cells are counted visually at 20 seconds intervals. Results conclude that cell trapping starts as soon as electrodes are energised, with most cells trapped in the first 20 seconds. After 20 seconds, DEP yield starts to slow down. It is because cells suspended near the electrodes are trapped

quicker than those further away from the electrode edge. Moreover, yield at $10V_{PP}$ starts to plateau almost after 60 seconds while it continues to grow for $20V_{PP}$ even at 120 seconds. It shows that the electric field generated by $10V_{PP}$ is limited to cells suspended at a certain height only.

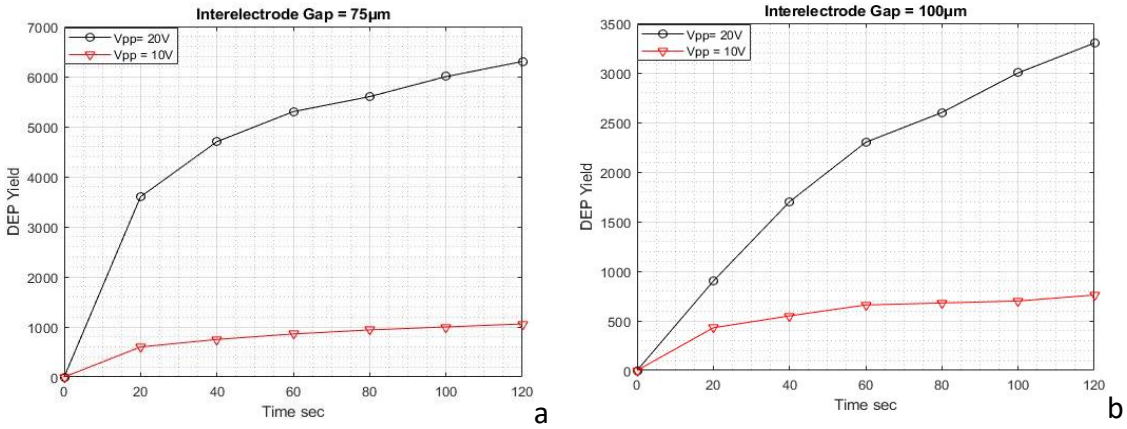

Figure 4.24: DEP yield as a function of time (s) at $10V_{PP}$, and $20V_{PP}$ for for the interelectrode gap of (a) $75\mu m$, and (b) $100\mu m$.

4.5.4 AC pDEP conclusion

In this section, AC pDEP parameters, namely; AC Signal strength ($10V_{PP}, 20V_{PP}$), AC signal frequency ($10kHz - 10MHz$), and chamber height ($100\mu m - 500\mu m$) are investigated in depth for the interelectrode gap of $75\mu m$ and $100\mu m$ at fluid conductivity of $10mS/m$ to quantify AC pDEP response for AC pDEP yield and time to the desired yield. Quantifying AC pDEP yield is crucial for the project because final cell concentration is directly proportional to the AC pDEP efficiency of the device, while time to the desired yield helps to measure the v_{DEP}.

Detailed examination of the results in this section summarises that:

1- The strongest AC pDEP for yeast in $10mS/m$ conductive medium takes place at $20V_{PP}$, $1MHz$ for both interelectrode gaps. It is the frequency that has been found in [202 – 211] for yeast cells' AC pDEP yield.

2- $75\mu m$ interelectrode gap and $100\mu m$ chamber height provide the highest and fastest DEP yield. DEP yield decreases as chamber height and interelectrode gap increase. Less than $\sim 11\%$ AC pDEP efficiency is achieved at $500\mu m$ chamber height which increases to $\sim 45\%$ at the chamber height of $300\mu m$. This is 15% higher efficiency at this chamber height than [210] but requires further improvement, especially when the flow rate is in use.

3- v_{DEP} increases as cells move closer to the electrode edge; it is because the greater of electric field gradient near the electrode edge and therefore F_{DEP} increases as cells move closer to the electrode edge.

4- It interprets that $20V_{PP,}1MHz$ and $10mS/m$ fluid conductivity are efficient electrical parameters for yeast cell trapping. These results are comparable to [202,203,208] regarding AC signal and frequency but are different to fluid conductivity [211,212].

Based on the results summarised above, it is concluded that:

i. Although higher yield occurs at $75\mu m$, however, both $75\mu m$ and $100\mu m$ interelectrode gaps are feasible for AC pDEP yeast cell trapping.

ii. $20V_{PP}, 1MHz$ provides with fastest and highest DEP yield for both interelectrode gaps. Henceforth, it is used in the AC pDEP experiments.

4.6 Chapter Synopsis

This chapter aims to optimise AC pDEP and ACEOF parameters. Through a detailed experimental analysis of each parameter, it is established that $75\mu m$ interelectrode gap, at the AC signal of $10V_{PP}$, $1kHz$ for $10mS/m$ fluid conductivity and chamber height of $500\mu m$ provides with maximum particle displacement and hence collects

yeast cells at the distance of $430\mu m$ which is only $18\mu m$ higher and 10 seconds faster collection than particle displacement achieved with $5V_{PP}$. However, less than 15% AC pDEP yield is achieved at chamber height of $500\mu m$ even with $20V_{PP}, 1MHz$ voltage. Decreasing chamber height and performing ACEOF at $75\mu m$, therefore, becomes irrelevant as it can induce flow reversal.

On the other hand, $100\mu m$ interelectrode gap produces a particle displacement of $290\mu m$ at $10V_{PP}$, $1kHz$ for $10mS/m$ with the chamber height of $300\mu m$. This chamber height corresponds to $\sim 49.3\%$ cell trapping at $20V_{PP}, 1MHz$. Using Chamber height less than $300\mu m$ provides higher AC pDEP but reduces ACEOF efficiency due to stunt particle displacement and possible flow reversal. Therefore, a compromise is made, and an AC signal of $20V_{PP}, 1MHz$ for AC pDEP and $10V_{PP}$,$1kHz$ for ACEOF at fluid conductivity of $10mS/m$ is chosen along with $100\mu m$ interelectrode gap and $300\mu m$ chamber height. The results of this chapter which are used as a template for building the hybrid device that can perform both AC pDEP and ACEOF efficiently during the cell Concentration in chapter 5, are summarised in table 4.1.

Table4.1: AC pDEP and ACEOF parameters optimised for cell Concentration stage.

Parameters	**AC pDEP**	**ACEOF**
AC signal	$20V_{PP}$	$10V_{PP}$
AC frequency	$1MHz$	$1kHz$
Fluid Conductivity	$10mS/m$	$10mS/m$
Interelectrode Gap	$100\mu m$	$100\mu m$
Chamber Height	$300\mu m$	$300\mu m$

The parameter combination in Table 4.1 provides an AC pDEP efficiency of $\sim 49.3\%$ and ACEOF particle displacement of $290\mu m$ with the velocity of $440\mu m/s$. To improve this efficiency, more electrodes are required. However, this results in a

device with an undesirable characteristic length. Therefore, the width of the electrode needs to narrow down. But it is seen in section 4.4.1.3 that decreasing electrode width by 40% decreases ACEOF particle displacement and fluid velocity by 27%. Therefore, it is essential to determine the number of electrodes and their widths to provide the desired cell concentration in the next chapter.

5 Cell Concentration Stage

5.1 Chapter Overview

This chapter presents the design of a hybrid microfluidic device and its cell concentration ability, which is the main objective of the research as described in chapter 1. In chapter 4, the parameters that were optimised for AC pDEP and ACEOF response are now used in this chapter to design a novel microfluidic device. In addition, this chapter explains further optimisation of the device to combine AC pDEP and ACEOF response that provides a desired cell concentration factor.

The chapter describes the approach adapted to achieve desired concentration goals and describes the methodology deployed to achieve target results. The following section presents and discusses the results illustrating a concentration factor of $100000/mL$ with an overall ACEOF yield of $> 90\%$ in less than $40minutes$ at $45\mu l/min$. Finally, in this chapter, results with a concentration factor of 400000/mL are also presented with an overall ACEOF yield of $> 90\%$ within $75minutes$ at $45\mu l/min$.

5.2 Approach

The primary approach to achieve the required cell concentration is:

i. Trap yeast cells from the fluid medium passing through the microfluidic chamber due to pressure-driven flow on the electrode edge using AC pDEP. Therefore, AC pDEP is run for a particular time to capture the required number of cells.

ii. The trapped cells are then washed away towards the concentration area using ACEOF. However, as some cells are dispersed in different device regions by the ACEOF vortex, not all cells are moved to the concentration area after the first ACEOF wave. Therefore, several ACEOF waves are required to push all the particles at the concentration area until the desired concentration factor is achieved.

Parameters for desired AC pDEP and ACEOF response are found in chapter 4, where it is established that a pair of coplanar gold electrodes with $100\mu m$ interelectrode gap, $10mS/m$ fluid conductivity, and $300\mu m$ chamber height generates a v_{EOF} of $430\mu m/s$ at $10V_{PP}, 1kHz$ that pushes yeast cells at a distance of $290\mu m$ from the electrode's edge. In contrast, $50\mu m$ interelectrode gap moves particles at a distance $212\mu m$ at the velocity of $345\mu m/s$ at $0.8kHz$. Therefore, $100\mu m$ gate width is chosen for the microfluidic device. Experiments are repeated with $50\mu m$ interelectrode gap to compare results with $100\mu m$ interelectrode gap and to provide the ability of the device and parameters optimised. Table 5.1 lists the AC pDEP and ACEOF parameters optimised in chapter 4 and are used for the cell concentration stage.

Table 5.1: AC pDEP and ACEOF parameters used for the cell concentration stage.

Parameters	**$50\mu m$**		**$100\mu m$**	
Phenomenon	ACAC pDEP	ACEOF	ACAC pDEP	ACEOF
AC Signal Strength	$20V_{PP}$	$10V_{PP}$	$20V_{PP}$	$10V_{PP}$
AC Signal Frequency	$1MHz$	$0.8kHz$	$1MHz$	$1kHz$
Fluid Conductivity	$10mS/m$		$10mS/m$	
Chamber Height	$200\mu m, 300\mu m$		$300\mu m$	

On the other hand, the same parametric combination produces $< 50\%$ pEP yield at $20V_{PP}, 1MHz$. This yield is less than the cell concentration techniques discussed in chapter 1 and requires improvement. Moreover, a $< 50\%$ yield is achieved at $\sim 0\mu m/s$ linear speed in chapter 4 as particles were pipetted on the device and allowed to settle before AC pDEP starts. Therefore, a much lower yield is expected when the cell moves in the chamber with a predetermined linear speed. Thus, $50\mu m$ wide ten parallel coplanar gold electrodes with $100\mu m$ interelectrode gap are constructed on the glass substrate. $50\mu m$ wide electrodes are chosen because:

i. It is observed in chapter 4 results analysis that the highest particle displacement observed is $430\mu m$. Moreover, using a $100\mu m$ interelectrode width highest particle displacement produced is $275\mu m$. Therefore, an electrode width smaller than $275\mu m$ is required to push particles over the next interelectrode gap. However, narrower electrode width generates weaker v_{EOF}, and therefore, smaller particle displacement is produced. Thus, a smaller electrode width is required to generate enough particle displacement to push particles over the next interelectrode gap.

ii. Secondly, $50\mu m$ electrode width also reduces the characteristic length of the device, especially for a more significant number of electrodes.

Moreover, ten individually addressable electrodes are used because:

This approach improves AC pDEP yield because there are more electrodes to trap particles. However, if the first few electrodes do not trap some cells, these

electrodes still pull the cells down from their suspension points and therefore, the following electrodes trap these particles.

Moreover, using ten electrodes also allows for faster cell linear speed, which increases the processing speed of the process. Therefore, six experiments are repeated for each experiment. In this stage, the main goal of AC pDEP is to improve the cell trapping efficiency, which requires the following parameters to be analysed:

i. Cell linear speed.

ii. Cell collection time.

iii. Chamber height for $50\mu m$.

The trapped cells are then moved with the fluid flow generated by ACEOF, ideally moving all the trapped cells in the concentration area. However, some cells are left behind due to cells dispersing or sticking to the electrodes. Therefore, the ACEOF process is repeated from the first to the tenth electrode to move the remaining cells forward. It is called multi-wave ACEOF (MWACEOF). Moreover, the electrodes switching pattern needs to be optimised to generate a perfect forward flow. Electrode switching pattern combines signal and ground connections to the electrodes required to move fluid due to ACEOF. If electrodes are not switched correctly, then the abnormal fluid flow is produced, which causes fluid to reverse its flow, or fluid flow velocity is compromised. Electrode switching time also determines the time required between electrode switching. Six experiments are repeated for each experiment. Therefore, ACEOF is quantified for the following parameters:

i. Electrodes Switching Pattern.

ii. The number of ACEOF waves.

iii. The time required per wave.

Once AC pDEP and ACEOF response for cell concentration is quantified, the AC pDEP-MWACEOF combination is applied on $100\mu m$ interelectrode gap for diverse cell populations to measure cell concentration ratio. Six experiments are repeated for each cell population. In addition, investigations are repeated for $50\mu m$ interelectrode gap to emphasise the device's ability to enrich cells at the concentration area and compare results with $100\mu m$ interelectrode gap. As defined in chapter 1, the concentration area is the target area where cells are accumulated. The cell concentration area is designed soon after the 10th electrode. It is because fluid moves under pressure-driven flow from the 1st electrode towards the 10th electrode, and hence most of the particles are trapped on the initial electrodes. Therefore, it is essential to push these particles first.

Cell concentration ratio (EF) is calculated by the ratio of the total number of cells in the concentration area (A_{cells}) to the number of cells expected in the concentration area (E_{cells}), as given by equation 5.1.

$$CF = \frac{A_{cells}}{E_{cells}} \quad 5.1$$

Depending on the cell properties once the cells are moved to the concentration area, they can offer several advantages, for example:

i. An Improved IVF success rate is achieved when healthy sperm cells are removed from the mixture of motile and deformed sperm cells using AC pDEP and then push sperm cells to the concentration area using ACEOF. These cells are then integrated with the oocytes, female reproduction

germ cells, present in the concentration area. It can assist the countries such as Taiwan that are keen to improve their reproduction rate of only 1.202 per woman reported in 2020 [18 -20].

ii. For further analysis, an improved understanding of specific cells such as CTCs or T- cells.

5.3 Methodology

5.3.1 Lithography

Ten $50\mu m$ wide, $1000\mu m$ long individually addressable coplanar Cr/Au electrodes with $100\mu m$ the interelectrode gap are patterned onto the glass substrate using a lithography technique. Lithography is used because it is a low cost, highly efficient, and convenient method for manufacturing micro-and nanostructures [330, 331]. Shipley MICROPOSIT Positive photoresist S1813 is used to produce a thin film on the glass substrate. S1813 is chosen because it provides detect-free and robust adhesion on a glass substrate with a wide range of film thicknesses [332]. MICROPOSIT gold developer and DIW is used to remove the photoresist and develop electrodes pattern after exposure. In the end, acetone is used to lift off the metals with S1813 beneath, forming the required pattern on the substrate.

5.3.2 Lift-off

In the lift-off process, firstly, metal is deposited on the existing photoresist structure, and then the device is developed to produce the desired pattern. The lift-off process is shown in figure 5.1. The first step in any microfabrication method is cleaning. Therefore, the substrate and material are cleaned using the approach discussed in Chapter 4.

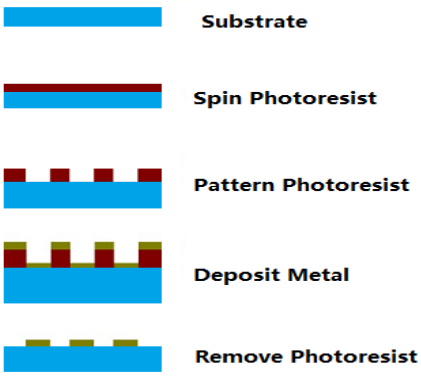

Figure 5.1: Lift-off process.

5.3.2.1 Spinning

Laurell spin coater is used to deposit photoresist film on the glass substrate. N_2 gas is attached to the spinner's vacuum chamber, which generates the required vacuum to hold substrate onto the spinner's chuck, thus preventing it from falling during spinning. Vacuum pressure is set at $4bar$. Spinning does not start if pressure is less than $4bar$. A clean substrate is placed on the spinner's vacuum chuck with sterile tweezers. The spinning program is solved using PLC attached with the spinner. S1813 is coated on the glass substrate in three steps:

i. In the first step, the substrate is spun at $4000\,rpm$ for $30\,seconds$ without S1813. This step is vital as it removes any particles left on the glass and provides a smooth coat.

ii. S1813 is poured onto the glass substrate with the help of a disposable plastic pipette. The substrate is spun at 500 rpm for 15 seconds. It allows the photoresist to dispense evenly on the substrate.

iii. The substrate is then spun at 4000 rpm for 45 seconds. The spinning speed is a factor that determines film thickness and, therefore, the success of lithography. If the photoresist coat is too thin or thick, the electrode pattern fails to form. Figure 5.2 provides the spin speeds to

gain desired results as provided in the datasheet. Spinning is performed at 3000 and 5000 rpm as well. However, it is observed that ideal effects occur at 4000 rpm.

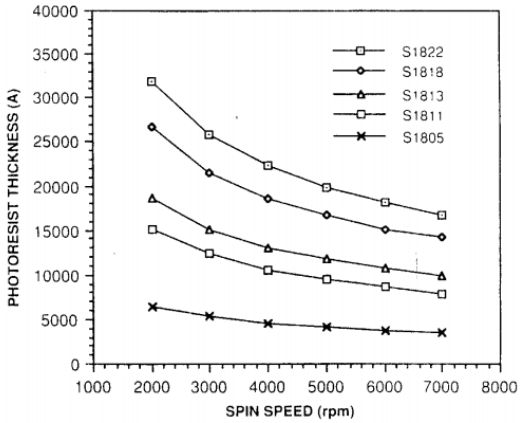

Figure 5.2: Photoresist thickness (A) as a function of spin speed (rpm) [45].

5.3.2.2 Soft Bake

S1813 contains about 15% solvent, generating stress in the coated film [75]. Therefore, the substrate is soft-baked after coating to avoid stress, remove the remaining solvent, and increase adhesion [75, 333]. Soft bake is performed on a hot plate $115°C$ for 60 $seconds$ as per data sheet (Appendix). Substrate is allowed to cool down for 10 $minutes$ at room temperature before exposure.

5.3.2.3 Ultraviolet Exposure

An aligner with $365nm$ UV source is used for light exposure on the photoresist. The photoresist is composed of polymer, sensitisers, and a casting solvent [75, 331]. The polymer changes its structure when exposed to intense radiation. It causes a photochemical reaction and weakens the bonding between photoresist and substrate [333]. Ultraviolet (UV) radiation is used to induce a chemical reaction in the exposed area of the S1813 leading to break and polymerase the resist. Incident energy, I_{UV} $(J.cm^{-2})$ of UV light is measured by Incident light energy:

$$\mathrm{I}_{UV} = E_{UV} \times T \qquad 5.2$$

Where E_{UV} (W/cm^2) is incident light energy, and T (seconds) is exposure time. As E_{UV} is fixed in the aligner hence I_{UV} is controlled by T only.

Chromium mask is designed using klayout software. It can be seen from figure 5.3a that the interelectrode gap is $100\mu m$ while electrode width is $50\mu m$. Two nitrogen cylinders are used. The first cylinder keeps the glass holder's mask at $4bar$, while the second cylinder controls aligner movement at $1.8bar$. For best results, the UV light source is switched on $30minutes$ before the exposure. Mask is placed in the glass holder with the mask's emulsion side facing downwards while the substrate is placed on the aligner's chuck. The aligner is adjusted, such as the substrate is positioned under the mask. Chuck lever is adjusted to place the substrate close to the mask without switching on the aligner's contact light.

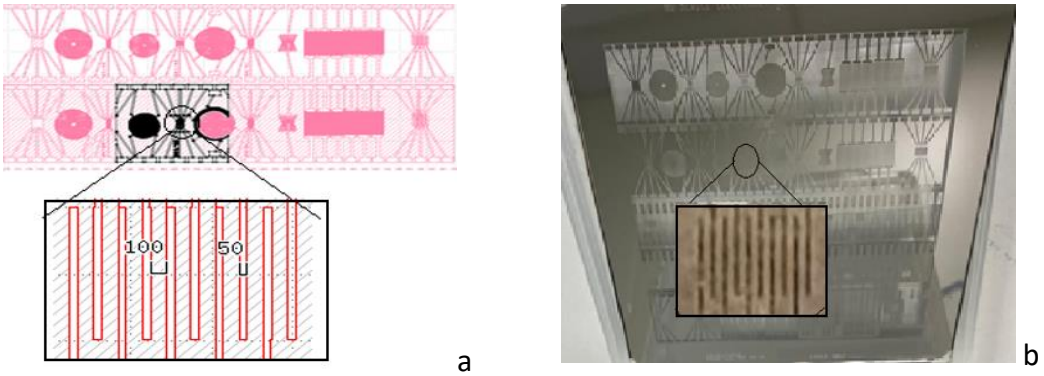

a b

Figure 5.3: An example of the mask used in lithography, electrode width is $50\mu m$ and interelectrode gap is $100\mu m$ (a) kLayout and (b) Chromimum Mask.

Once the substrate is set under the mask, it is exposed to UV light for $18\ seconds$. Exposing it for less or more than $18\ seconds$ does not produce desired results during lift-off.

5.3.2.4 Pattern Development

One pyrex beaker is filled with 25% Microposit developer and 75% DIW, while another beaker is filled with 100% DIW. The S1813 coated substrate is placed in the first beaker and agitated mildly for $30\ seconds$. The sample is immediately placed in DIW for $60\ seconds$ to stop the developing process. Using the DIW spigot sample is thoroughly rinsed for $30\ seconds$ before drying the sample using N_2 gun. The sample is observed under the microscope to check if the pattern is clear and well defined. Care should be taken that the S1813 coated sample should not get in contact with light before developing a pattern; otherwise, the photoresist gets destroyed.

5.3.2.5 Thermal Evaporation and Lift-off

Thermal evaporation is performed, as discussed in Chapter 4, in the absence of a shadow mask. It is because the pattern is already placed on the sample. After evaporation, the sample is placed in the pyrex beaker filled with acetone and left for $15min$. Acetone-filled beaker is then placed in an ultrasonic bath for $5min$ to completely lift-off gold and create electrodes. The sample is then placed under DIW spigot for $60\ seconds$ to remove any gold particles left on the device and dried using N_2 gun. The device is observed under the microscope for any short- or open circuits. Finally, the sheet resistance is measured using the methodology discussed in chapter 4.

5.3.3 Device Preparation

A 2mm wide and 3mm long rectangular gap is cut on a single-sided stripboard. The device is glued on the board such that the observing electrodes are placed on top of the gap. Pin headers soldered on the stripboard, connected to the electrodes

using wires. Electrodes are connected to the cables using silver paint, as discussed in Chapter 4. Connections are checked for short- and open circuits.

5.3.3.1 Chamber Lid

2mm thick acrylic plastic is used as a chamber lid. Acrylic is used because it provides excellent optical clarity and adhesion [330]. Three chamber lids are constructed, as shown in figure 5.5. Chamber lid 1 is 2.5mm wide and 6mm long with a 2mm gap between inlet and outlet, while chamber lid 2 is 3mm wide and 8mm long with a 4.5mm gap between inlet and outlet, while chamber lid 3 is 2.5mm wide 5mm long with 2mm gap between inlet and outlet. All lids have $0.23mm$ inlet and outlet holes diameter because it perfectly fits the injection needle which is 31 gauge.

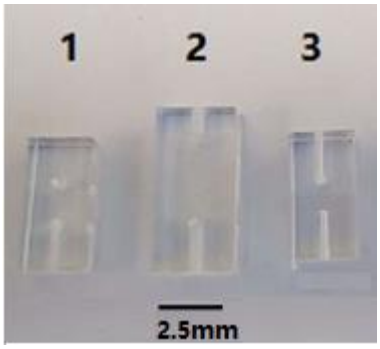

Figure 5.4: Chamber lids used during the experiments performed.

It can be seen from figure 5.4 that in lid 1, fluid enters from the side and flows out from the top of the lid after passing from the electrodes. While in lids 2 and 3, fluid moves in from the side and flows out from the other end. Lid 1 is rejected after several trials because it accumulates fluid on the chamber lid during experiments, making the microscopic image blur. Moreover, lid two is also excluded after experiments because fluid takes extra time to reach electrodes, reducing processing speed. Therefore, lid three is chosen, from which liquid flows in and out from the side. The chamber lid is attached to the device using $300\mu m$ thick parafilm. Non-

conductive epoxy gives a stronghold between the chamber lid and the device. The advantage of using epoxy is that there is no fluid leakage, while the disadvantage is that once the chamber lid is fixed, it becomes impossible to remove it. Therefore, a new device is required for new experiments after a few experiments. The designed device is shown in figure 5.5. The holes are blocked with toothpicks because epoxy can seep into the holes due to capillary effects. Before the experiments, toothpicks are removed, and holes are flushed with DIW to ensure no blockage.

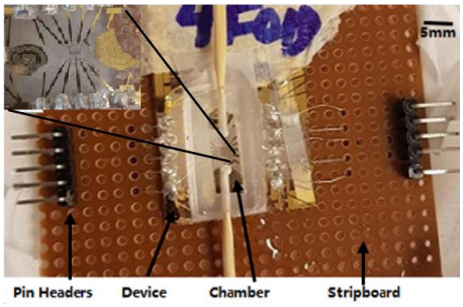

Figure 5.5: An example of the designed microfluidic device.

5.3.4 Chamber Volume Calculation

Chamber Volume, $Vol\ (\mu L)$ is measured by equation 5.3:

$$Vol = H \text{ x } W \text{ x } L \qquad 5.3$$

Where $H(mm)$, $W(mm)$, and $L(mm)$ are chamber height, width, and length, respectively. Characteristic length for $100\mu m$ interelectrode gap device is $1400\mu m$ compared to $950\mu m$ for $50\mu m$ interelectrode gap. $200\mu m$ length is left before the 1st electrode to develop a smooth creeping flow in the device, as shown in figure 5.6.

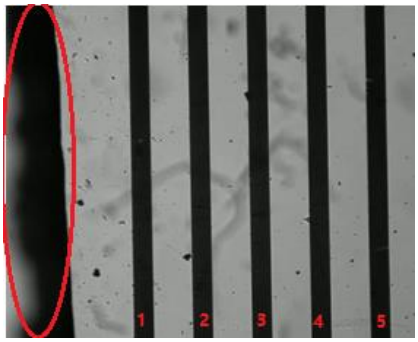

Figure 5.6: Smooth fluid flow reaching electrodes.

While $400\mu m$ and $250\mu m$ length is left for $100\mu m$ interelectrode gap is left after 10th electrode for $100\mu m$ and $50\mu m$ interelectrode gaps respectively. Therefore, the total length for $100\mu m$ interelectrode gap device is $2000\mu m$ $(2mm)$ while $50\mu m$ interelectrode gap is $1400\mu m$ $(1.4mm)$. For both interelectrode gaps, chamber width is $1000\mu m$ $(1mm)$, while chamber heigh of $300\mu m$ is used for both interelectrode gaps while further $200\mu m$ is used for $50\mu m$ interelectrode gap as well. Therefore, using equation 5.2, chamber volume for $100\mu m$ interelectrode gap is $0.6\mu L$ $(0.3mm$ x $2mm$ x $1mm)$. On the other hand, for $50\mu m$ interelectrode gap chamber volume are $0.28\mu L$ $(0.2mm$ x $1.4mm$ x $1mm)$ and $0.42\mu L$ $(0.3mm$ x $1.4mm$ x $1mm)$ for $200\mu m$ and $300\mu m$ chamber height, respectively.

The device is filled with $10mS/m$ DIW buffered solution before the experiments to ensure that the microscope focus is set before observations begin and do not need to change once the fluid is on the device as fluid acts as a lens. If the microscopic lens is adjusted during the experiment, it induces Brownian motion during experiments, impacting the results.

Table 5.2: Chamber volume calculation.

Interelectrode Gap $(\boldsymbol{\mu m})$	**Length** $(\boldsymbol{mm})$	$\boldsymbol{Width}$ $(\boldsymbol{mm})$	**Chamber Height** $(\boldsymbol{mm})$	**Chamber Volume** $(\boldsymbol{\mu L})$
50	1.4	1	0.2	0.28
	1.4	1	0.3	0.42
100	2	1	0.3	0.6

5.3.5 Relay Switching Board

A relay switchboard is required because it controls ten electrodes individually and automates the experimental process. If ten electrodes are switched manually, cells can disperse due to jittering. Also, automatic switching guarantees a precise switching time, making the process swift and reliable. Eight relay switches control the second to the ninth electrodes while the first and tenth electrodes are permanently attached with signal and ground supply. An alternative electrode potential pattern is used for AC pDEP, as shown in Table 5.3, which represents 'S' as signal and 'G'as ground.

Table 5.3: Multielectrode Switching Pattern for AC pDEP.

Electrode	1	2	3	4	5	6	7	8	9	10
Potential	S	G	S	G	S	G	S	G	S	G

5.3.6 Fluid dispensed setup

Fluid containing cells are dispensed on the device with the help of a syringe pump, a small infusion pump that gradually administers a small fluid volume on microfluidic devices. Details of syringe pump construction are given in Appendix 8.2.2. This project deals with a small fluid volume moving in the chamber at speed in the order of $\mu m/s$. Therefore, a syringe pump is built to supply fluid at a predetermined velocity into the chamber. It is essential to confirm the pump's smoothness as even a minor pulsing of the pump can cause turbulent flow in the microfluidic channel. For this purpose, a fluid-filled syringe is placed in the pump. Shaft movement is observed with a ruler after each $0.05ml$ liquid is dispensed $30\mu m/s$ linear speed. Figure 5.7 shows that for each $0.05ml$ fluid dispensed, the shaft moves for $0.3mm$ precisely. In $1000seconds$ syringe pump's shaft moves by $0.66mm$ at $30\mu m/s$.

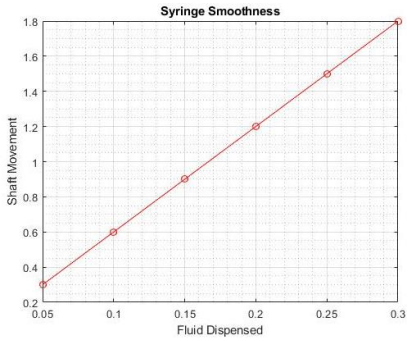

Figure 5.7:The syringe smoothness illustrated by shaft movement as a function of fluid dispensed.

5.3.7 Final Setup

The device is set on the microscope stage, and the Infusion pump is set at the height of 5cm higher than the microscope stage. The syringe pump is connected to the device's inlet via a tube. The outlet is connected with a pipe that drains in the beaker. Both inlet and outlet tubing connections are sealed to avoid leakage. Electrodes are connected to the relay switching board. The computer controls microcontrollers of the relay switching board and syringe pump, which monitors and records microscope video footage via microscope camera discussed in chapter 4. The relay switching board is attached to the function generator. The output of the function generator is continuously monitored using an oscilloscope. In this chapter, all photos are taken such that fluid moves from the left to the right side. Therefore, the first electrode is the one that is at the extreme left.

5.4 Results and Discussion

5.4.1 AC pDEP response for multielectrode geometry

This section presents the results of the AC pDEP response for multielectrode geometry. The parameters which are quantified for this section are:

i. **Cell linear speed** is the speed with which a cell passes through the chamber. It is essential to calculate optimum cell linear speed that

allows maximum trapping of cells without compromising the experiment processing time. Too fast cell linear speed will lower the cell capturing while too slow will increase experiment time. Cell linear speed is adjusted such that an overall AC pDEP efficiency of $> 95\%$ is achieved with most of the cells trapping on the initial electrodes. Cell speed is also measured in terms of **flow rate,** which is the process of measuring the speed with which fluid containing cells is dispensed through the chamber.

ii. **Processing time** is the total time the device is in DEP mode. Therefore, it is essential to optimise the minimum time for which the device remains in DEP mode to provide maximum concentration.

As shown in table 5.1, during the AC pDEP process, electrodes are energised using a $20V_{PP}, 1MHz$ AC signal. Yeast cells are used as test particles in $10mS/m$ fluid conductivity. Electrodes switching pattern for AC pDEP is already discussed in table 5.2. AC pDEP yield is measured for the cell linear speed. Cell linear speed is driven by the syringe pump and is calculated by the cell's movement between two electrodes divided by time. AC pDEP response is also measured by cell yield on each electrode.

5.4.1.1 AC pDEP vs Flow rate

AC pDEP efficiency is measured at several syringe pump speeds. Flow rate illustrates syringe pump speed and its relevant linear cell speed along with the x20 magnification lens microscopic images for AC pDEP yield at each speed.

Table 5.4: Cell Linear speed effect on AC pDEP yield.

Experiment No.	Cell Linear Speed $(\mu m/s)$	Flow rate $(\mu L/min)$	Figures
1	7	11	5.8 a
2	18	25	5.8 b
3	30	45	5.8 c
4	48	62	5.8 d
5	66	70	5.8 e
6	93	85	5.8 f

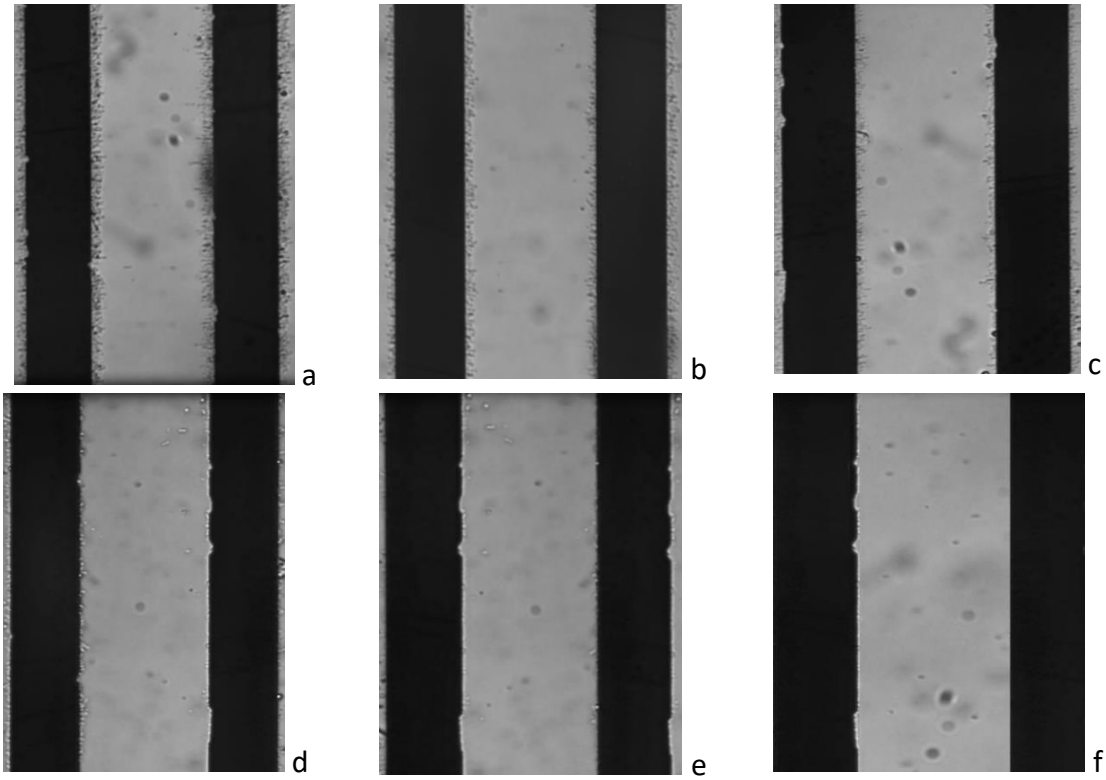

Figure 5.8: AC pDEP response measured as a function of flow rate (a) $11\mu l/min$, (b) $25\mu l/min$, (c) $45\mu l/min$, (d) $62\mu l/min$, (e) $70\mu l/min$, and (f) $85\mu l/min$.

It is observed from figure 5.8 (a – f) that as linear speed increases, AC pDEP yield decreases significantly. It is because, at lower linear speed, the electric field gradient has more time to trap the cells. If speed is too fast, the particle will be out

of the electric field range and will not get trapped. The AC pDEP yield as a function of linear speed is plotted in figure 5.9.

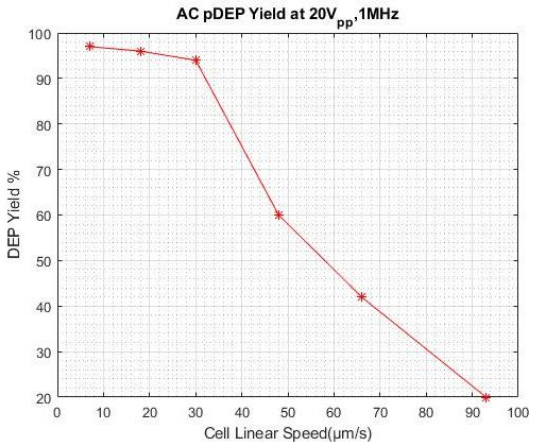

Figure 5.9: DEP yield percentage as a function of the cell's linear speed.

The graph shows that till $30\mu m/s$ linear speed, more than 94% of yield is obtained with ten electrodes. Furthermore, yield decreases rapidly to 60% as linear velocity increases to $48\mu m/s$. Finally, the yield percentage drops to 20% as linear speed increases to $93\mu m/s$. These results follow [203-214], where lower flow rates accommodate higher DEP yield. However, compared to the literature device offers $\sim 30\%$ higher DEP yield by utilising multiple electrodes.

The particle's speed through the chamber plays a vital role in AC pDEP yield as slower linear speed yields a much higher AC pDEP yield. Therefore, an optimum linear speed is required to produce optimum AC pDEP yield results. Therefore, a flow rate of $45\mu l/min$ is chosen, which provides not only an AC pDEP yield of 94% but also provides optimum processing speed. Figure 5.10a and figure 5.10b show AC pDEP yield at $45\mu l/min$ for the first five and last five electrodes, respectively.

It is observed from the results that more cells are trapped at the first five electrodes compared to the last five electrodes. It confirms that at $30\mu m/s$ linear speed, the device is working to the expectations that initially, more cells are

trapped, and electrodes also pull down and get trapped on the later electrodes. Moreover, figure 5.10 shows that cells in the interelectrode gap decrease with every passing electrode because cells are trapped. Hence, fewer cells are passed to the next electrode gap. Experiments are repeated with $50\mu m$ interelectrode gap at $30\mu m/s$ and $200\mu m$ chamber height. Figure 5.10 shows that most cells get trapped at initial electrodes compared to very few to none in the end.

Figure 5.10: Microscopic view of the device (with $50\mu m$ interelectrode gap) to show AC pDEP yield for each electrode at $45\mu l/min$.

5.4.1.2 Device Throughput

The device's throughput is measured by the quantity of liquid that can be dispensed from the device in a given time. Adjusting the device's throughput was crucial because if throughput is high, more sample can be processed, providing higher yield efficiency. Therefore, a compromise must be made to ensure that maximum throughput of the device was achieved without decreasing the DEP yield. Therefore, once the cell linear speed is optimised, device throughput is measured for $45\mu l/min$ cell linear speed, calculated to be $1.5mL$. It is still a significant increase compared to [272, 273, 277], where the highest flow rate reported was only $4\mu L/min$. This can be increased by increasing the speed of the process; however, DEP yield is compromised. Throughput can be further improved by increasing larger electrodes and increasing electrodes.

5.4.1.3 AC pDEP vs Time

AC pDEP ran for $60minutes$ with a large population of cells at $30\mu m/s$. Electrodes are monitored every $10minutes$ for $60\ minutes$ to record AC pDEP cell capture response. Figure 5.11 illustrates that cell capture increases with time almost linearly until $20\ minutes$ after which cell capture starts to decay and become almost plateau. This is because as more cells pass on top of electrodes, cells get trapped on the edges of the electrodes due to AC pDEP and electrodes getting saturated with cells, causing fewer cells to get trapped afterwards.

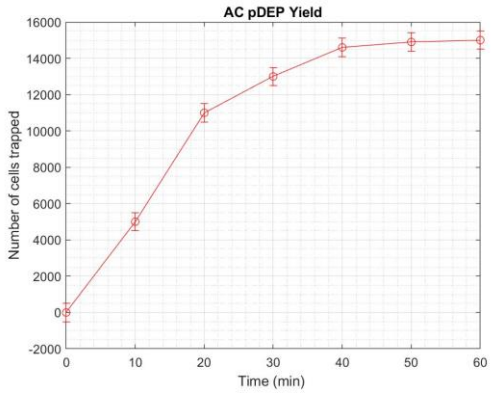

Figure 5.11: Number of cells as a function of time $(minutes)$.

Therefore, it can be concluded that AC pDEP yield increases with time while the cell population is the limiting factor. Unfortunately, the process is only tested for $60minutes$ because of overheating of the stepper motor.

5.4.2 Multiwave ACEOF

This section presents the results for optimising ACEOF response for the following parameters:

i. **Electrode Switching Pattern** helps generate the motion of cells in fluid in one direction towards the cell concentration area. Therefore, the correct electrode switching pattern is expected to produce two vortices, one for the electrodes connected to the signal and the second

for the electrodes attached to the ground, as discussed in chapter 1. Such vortices formation moves particles with the fluid towards the concentration area. However, suppose the electrode switching pattern is not arranged correctly. Then, it can cause more than two vortices to form or particles to move in the opposite direction from the concentration area. The phenomenon is described as reverse electroosmosis flow [128].

ii. **Electrode Switching Time** helps to quantify the timings between electrode switching. At the start of the experiment, only 1st electrode is connected to the signal while the rest of the electrodes are connected to the ground connection. However, once the wavefront has passed the next inter-electrode gap, the next electrode has switched the signal. This time between electrodes switching is called electrode switching time. If electrodes are switched before the wavefront has progressed sufficiently, cell loss is expected, causing a decrease in the device efficiency. On the other hand, if electrodes are switched after the particles have adequately moved, the overall processing time increases.

iii. **The number of ACEOF waves** requires to provide maximum cell concentration. It is necessary because not all cells are accumulated in the concentration area after one ACEOF wave. After all, the device does not move all cells in one ACEOF wave. Moreover, some cells are dispersed in the chamber and do not accumulate at the concentration area. Therefore, several ACEOF waves are required to move the remaining cells left in the chamber into the concentration area and

obtain maximum cell concentration. Consequently, it is essential to optimise the electrode switching pattern and switching time before the number of ACEOF waves required to gain optimum concentration is measured.

Experiments in this section are performed at $10V_{PP}$, $1kHz$ for fluid conductivity of $10mS/m$. Yeast cells are grown and counted, as discussed in chapter 4 and used as test particles. Particles are moved on the device containing $50\mu m$ wide ten individually addressable electrodes using the syringe pump with no AC pDEP condition. They are allowed to settle down, as shown in figure 5.12.

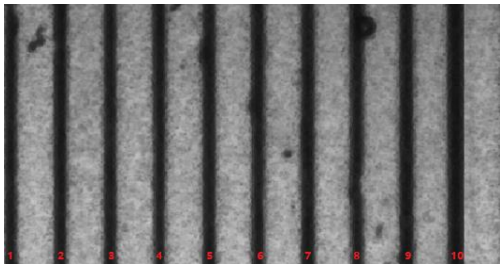

Figure 5.12: The microscopic view of the microfluidic device containing cells before experiments begin.

A $1000000/mL$ population of cells are used initially to ensure that process is observable with the x10 objective lens. The movement of cells is tracked visually using video recordings. This technique helped to quantify electrode switching time and electrode switching pattern. This section also discusses the methodology to overcome otherwise challenging flow reversal. Once the desired electrode combination is formed, experiments are repeated ten times to confirm replication.

5.4.2.1 Electrode Switching Pattern

Several electrode switching patterns were investigated to optimise ACEOF particle concentration. These mainly include a combination of electrodes changing

individually or in a group randomly. However, they do not generate the required fluid flow up to the expectation. Therefore, after several trials, two novel electrode switching patterns are established to concentrate particles in the concentration area using MWACEOF. These patterns are described below:

i. Full Switching Pattern

All electrodes are connected to either signal or ground to push particles towards the concentration area in a full switching electrode pattern. In this pattern, the 1st electrode is connected to the signal, while the 10th electrode is connected to the ground throughout the experiments. On the other hand, 2nd to 8th electrodes are controlled by relay switches which switch the connection between signals and ground as per experimental requirement. Table 5.5 shows the full electrode's switching pattern, which successfully moved particles towards the concentration area and figures 5.13 (a-i) correspond to the specific electrode pattern. In the table and figures, 'S' shows signal while 'G' stands for ground.

Table 5.5: Full Switching Pattern for MWACEOF.

Exp./Elec.	E1	E2	E3	E4	E5	E6	E7	E8	E9	E10	Observation	Figure
1	S	G	G	G	G	G	G	G	G	G	Forward Flow	5.13a
2	S	S	G	G	G	G	G	G	G	G	Forward Flow	5.13b
3	S	S	S	G	G	G	G	G	G	G	Forward Flow	5.13c
4	S	S	S	S	G	G	G	G	G	G	Forward Flow	5.13d
5	S	S	S	S	G	S	S	S	G	G	Forward Flow	5.13e
6	S	S	S	S	S	S	G	G	G	G	Forward Flow	5.13f
7	S	S	S	S	S	S	S	G	G	G	Forward Flow	5.13g
8	S	S	S	S	S	S	S	S	G	G	Forward Flow	5.13h
9	S	S	S	S	S	S	S	S	S	G	Forward Flow	5.13i
10	S	S	S	S	S	G	G	G	G	G	Flow reversal	

It can be observed from figure 5.13a that when only 1st electrode is attached to the signal and the rest are at ground connection; then cells create a wavefront after the 2nd electrode. Furthermore, it can be observed that the 1st interelectrode gap becomes brighter while the 2nd interelectrode gap becomes darker because cells from the 1st interelectrode gap are shifted to the 2nd interelectrode gap. Consequently, as the next electrode is switched to the signal, cells are pushed between the next electrode gap. The process continues until the first nine electrodes are switched to signal, and only the last one is grounded.

In this pattern, the electrode pushing cells forward is switched to signal and preceding electrodes during all experiments in full switching pattern except for the 5th experiment. It is because using the same pattern causes anomalous flow in which fluid starts to move backwards. Various combinations are tried to overcome this flow reversal, and after multiple attempts combination mentioned in experiment five is established.

It can be observed from figure 5.13(a-i) that strong particle wavefronts are forming after each electrode switching, however in figure 5.13h, the wavefront is weaker, it is because when the first eight electrodes are connected to signal and the last two to ground, most of the particles are already pushed towards the concentration area. Experiments are repeated for $50\mu m$ interelectrode gap, and particles form a wavefront $\sim 125um$ after the 10th electrode edge.

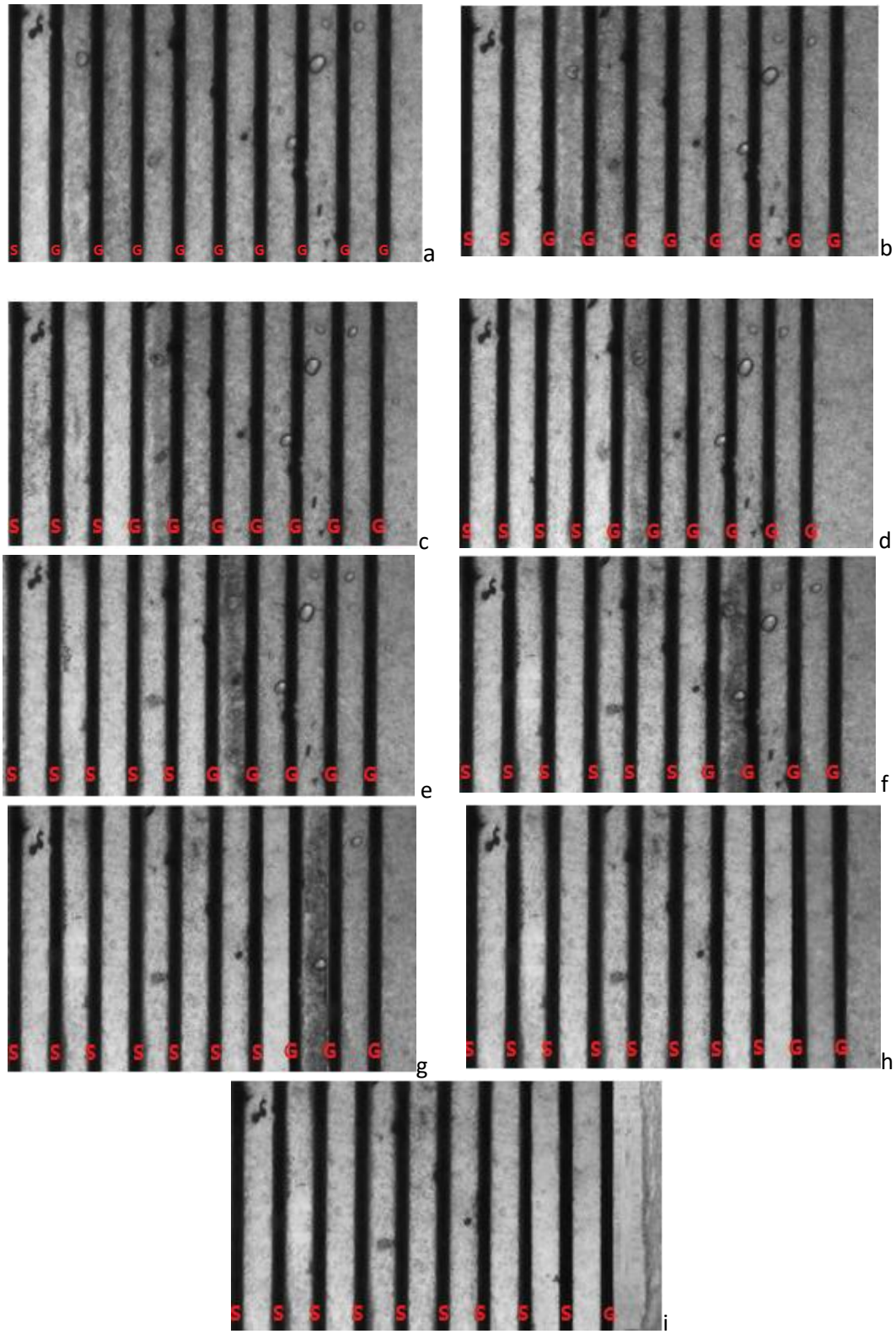

Figure 5.13: The particle motion observed under the influence of ACEOF after first ACEOF for the full switching of electrodes (with $100\mu m$ interelectrode gap), (a) first, (b) first 2, (c) first 3, (d) first 4, (e) first 5, (f) first 6, (g) first 7, (h) first 8, and (i) first 9, switches to signal.

ii. Partial Switching Pattern

Only the 1st electrode is permanently connected to the signal in this electrode pattern, while the rest are left unconnected (electrically floating). During the experiments, the specific electrode required to push cells forward is connected to the signal, and the preceding electrode is connected to the ground. The remaining electrodes are left unconnected, as shown in table 5.6. In table 5.6, 'X' stands for no connection, while 'S' and 'G' are signal and ground. This pattern is termed as partial switching pattern. The main advantage of using this pattern is that no anomalous flow is observed during this investigation. However, the main disadvantage is that electrodes are controlled manually, which can cause Brownian motion. It is avoided by using long wires and breadboard while switching timing is controlled by using a stopwatch. Results are shown in figure 5.14 (a-i).

Table 5.6: Partial Switching Pattern for MWACEOF.

Exp./Elec.	E1	E2	E3	E4	E5	E6	E7	E8	E9	E10	Observation	Figure
1	S	G	X	X	X	X	X	X	X	X	Forward Flow	5.14a
2	S	S	G	X	X	X	X	X	X	X	Forward Flow	5.14b
3	S	S	S	G	X	X	X	X	X	X	Forward Flow	5.14c
4	S	S	S	S	G	X	X	X	X	X	Forward Flow	5.14d
5	S	S	S	S	S	G	X	X	X	X	Forward Flow	5.14e
6	S	S	S	S	S	S	G	X	X	X	Forward Flow	5.14f
7	S	S	S	S	S	S	S	G	X	X	Forward Flow	5.14g
8	S	S	S	S	S	S	S	S	G	X	Forward Flow	5.14h
9	S	S	S	S	S	S	S	S	S	G	Forward Flow	5.14i

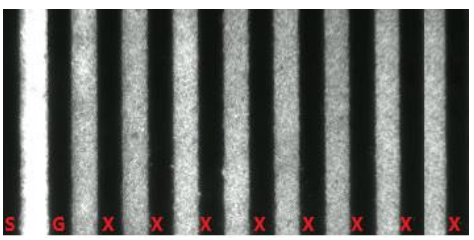

a

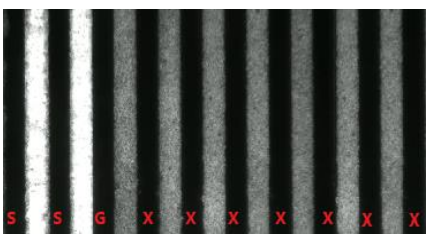

b

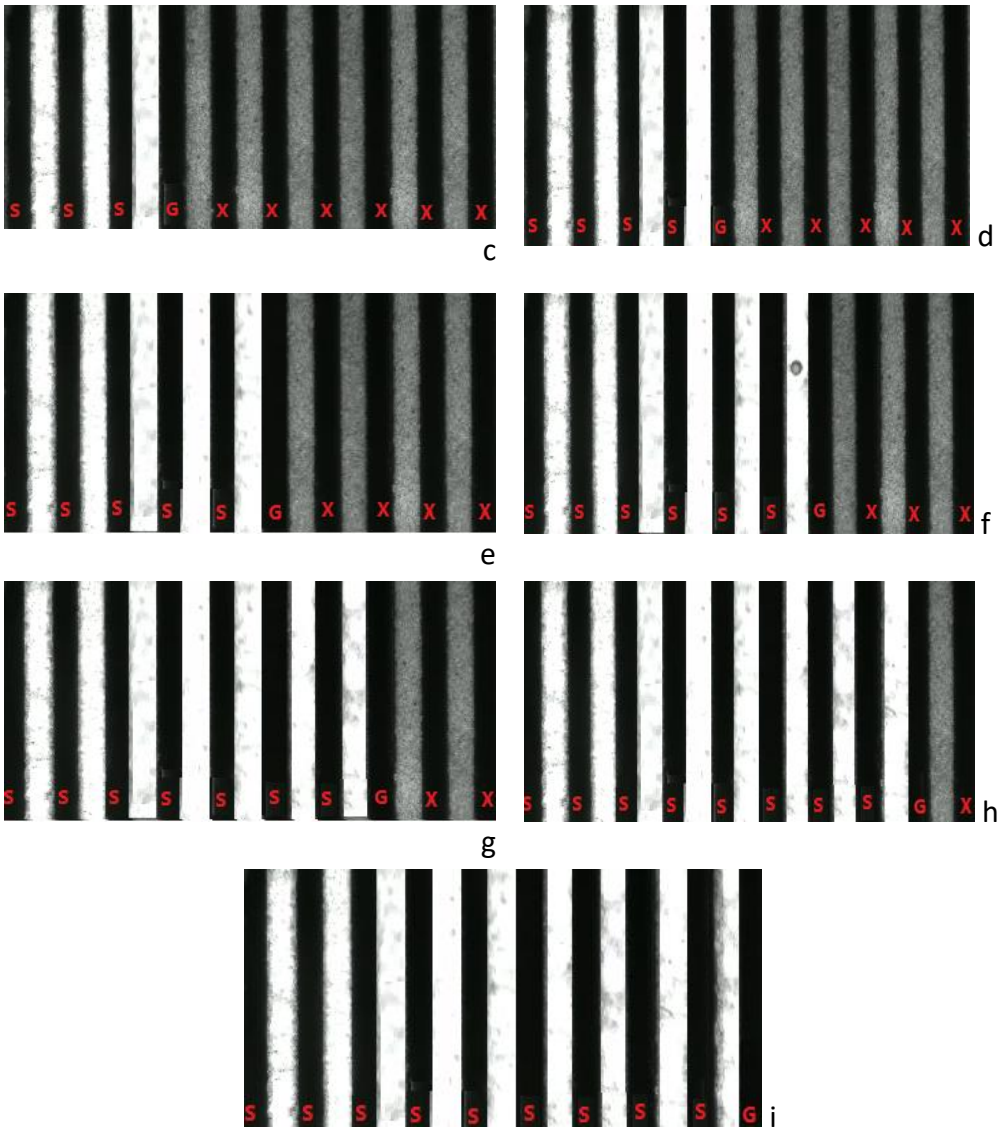

Figure 5.14: The particle motion observed under the influence of ACEOF after first ACEOF for partial switching of electrodes (with $50\mu m$ interelectrode gap), (a) first, (b) first 2, (c) first 3, (d) first 4, (e) first 5, (f) first 6, (g) first 7, (h) first 8, and (i) first 9, switches to signal.

5.4.2.1.1 ***Maximum Particle Displacement Comparison***

The full switching pattern generates a particle displacement of $\sim 175\mu m$ after each electrode from the electrode edge, forming a wavefront $\sim 175\mu m$ after the 10th electrode edge. It is also observed that using a partial switching pattern; a particle displacement is further reduced to $160\mu m$ and $110\mu m$ using $100\mu m$ and $50\mu m$ interelectrode gap, respectively. Figure 5.15 summarise the results of particle displacement formed using $50\mu m$ and $100\mu m$ interelectrode gap for the partial

and the full switching pattern. It can be observed from the figure that the particle displacement for the full switching pattern is less than the particle displacement formed for the partial switching pattern. In both cases, $50\mu m$ interelectrode gap produces a smaller particle displacement compared to $100\mu m$ interelectrode gap, which follows the results produced in chapter 4.

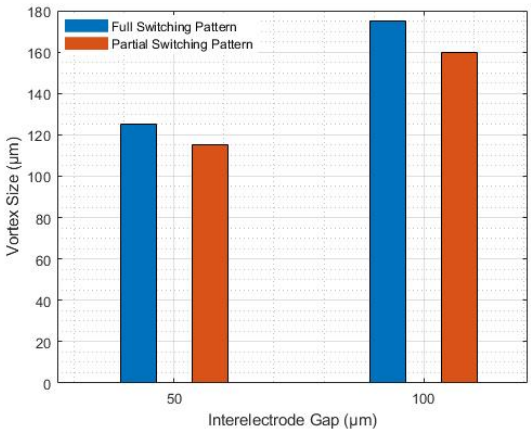

Figure 5.15: Bar graph illustrating the difference in particle displacement for $50\mu m$ and $100\mu m$ interelectrode gap during full switching pattern and partial switching pattern.

5.4.2.1.2 ***ACEOF Velocity***

It is observed that using the full switching pattern; for $100\mu m$ interelectrode gap fluid moves forward with the v_{EOF} of $250\mu m/s$ from the electrode edge. This velocity is $290\mu m/s$ less than velocity calculated at $10V_{PP}$, $1kHz$, in chapter 4 with $500\mu m$ wide electrodes. It is because in this chapter $50\mu m$ wide electrodes are used, and thinner electrodes offer smaller EDL to form, which implies a weaker ACEOF response takes place, therefore, slower v_{EOF} is produced [327-329]. Due to the same reason using $50\mu m$ interelectrode gap a v_{EOF} of $130\mu m/s$ is produced which is $150\mu m/s$ less than measured in chapter 4 but it is still higher than the maximum reported ACEOF of <30$\mu m/s$. On the other hand, using a partial switching pattern a v_{EOF} is further reduced by $40\mu m/s$ and $25\mu m/s$ for $100\mu m$

and $50\mu m$ interelectrode gap respectively compared to full switching pattern, as shown in figure 5.16. Comparing results with figure 5.16 shows that higher velocity corresponds to more significant particle displacement. Velocity is calculated from the electrode edge.

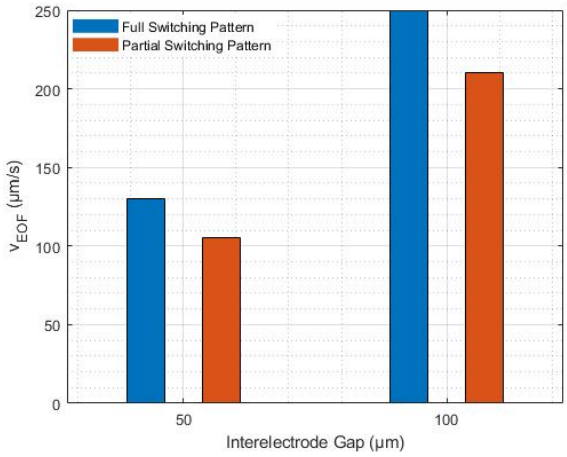

Figure 5.16: Bar graph illustrating the difference in v_{EOF} for $50\mu m$ and $100\mu m$ interelectrode gap during full switching pattern and partial switching pattern.

5.4.2.1.3 ***Anomalous flow***

An anomalous flow is generated during the experiments, which causes the fluid flow to reverse. This flow generated has a velocity of $\sim 1450\mu m/s$. It is observed that this flow is generated during all switching patterns except the pattern shown in table 5.5, row 11, where as soon as the 5th electrode is switched on, an abnormal flow occurs, which causes flow reversal. This flow reversal is overcome by changing the electrode pattern, as discussed in table 5.5, row 5. Although this anomalous flow is similar to reverse electroosmotic flow (REOF) because it has high velocity and reverses direction [160, 162, 184, 185, 334, 335]. However, it can be argued that REOF occurs with asymmetric electrode geometry or phase-shifting signal [160, 263, 307, 316, 335], whereas in the experiment, anomalous flow took place when the first five electrodes are switched to signal, and the last five electrodes are grounded which provides perfect symmetry of electrodes, moreover during all experiments signal

remained same at $10V_{PP}, 1kHz$. Therefore, flow reversal cannot be termed as REOF. In this case, flow reversal can be explained by the hypothesis that when the 5th electrode is switched on, the former vortex is already not settled down but dying, and the new vortex is formed, therefore, dominates, causing flow reversal. However, experiments are repeated by giving a 60seconds delay before switching on the 5th electrode, but flow reversal still exists. Moreover, this argument does not explain the reason for the increase in flow velocity. Another possibility can be that device built might have asymmetry in electrodes which is unnoticed. However, several experiments are performed during the cell concentration stage with $100\mu m$ interelectrode gap as well $50\mu m$ interelectrode gap and flow reversal took during each investigation if the first five electrodes are switched to signals while the last five are grounded in full switching pattern. The anomalous flow is overcome using the switching pattern shown in table 5.5 experiment row 5.

Although this anomalous flow has similarities with REOF, the origination of this flow reversal from the symmetric electrodes combination and velocity greater than reverse electroosmosis velocity dents the argument of this flow reversal being REOF. Therefore, this flow reversal in this project has been termed as 'anomalous flow.' The anomalous flow modelling is created and presented in chapter 6.

5.4.2.2 Why multi-wave ACEOF?

Chapter 1 discussed that several ACEOF passes are used during the experiments to achieve the desired concentration factor of 100000. It is termed as multi-wave ACEOF (MWACEOF) in this project. MWACEOF is required because during ACEOF, two vortices are formed, which majorly move particles forward and create a wavefront at

some distance from the electrode edge. However, some of these particles are either dispersed in different directions or left behind. It is illustrated with the help of figure 5.17. Figure 5.17a shows the first four electrodes before placing cells onto the device, while figure 5.17b shows the first four electrodes after particles are placed on it.

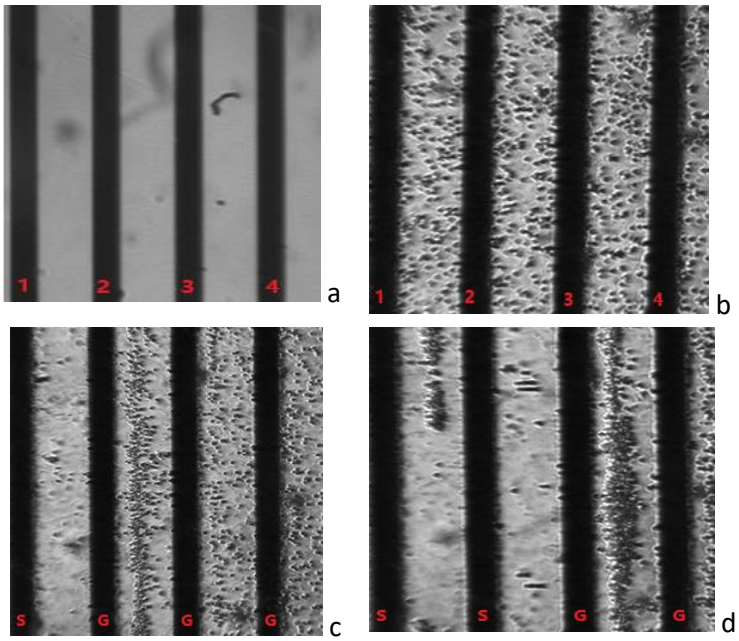

Figure 5.17: The microscopic view of the device with $100\mu m$ interelectrode gap, (a) first four before the sample is placed on the device, (b) first four after the sample is placed on the device, (c) wavefront forming after the second electrode as the first electrode is switched to signal, and (d) wavefront formed as first two electrodes are switched to signal, some particles are collected between the first two electrodes.

It is evident from figure 5.17c that when the first electrode is switched to the signal and the remaining are grounded, cells have moved forward and formed a wavefront after the second electrode leaving the first interelectrode gap empty. However, when the first two electrodes are switched to the signal and the remaining are grounded, a wavefront is formed after the third electrode; however, some particles have moved back in the first interelectrode gap shown in figure 5.17d. Therefore, decreasing the number of cells reaching the concentration area and thus limiting the concentration factor. Figure 5.18 illustrates the cell collection

after the 1st and 5th ACEOF pass. It is evident from figure 5.18 that cell concentration has increased from ~ 500 cells in the first wave to ~ 3000 cells in the fifth ACEOF wave. Therefore, several ACEOF passes are required to push particles left behind to the concentration area.

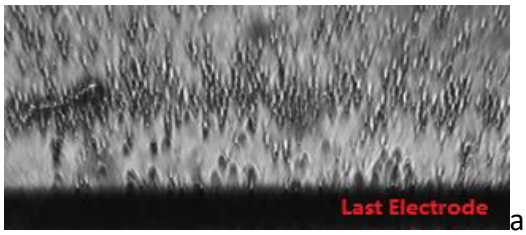

a

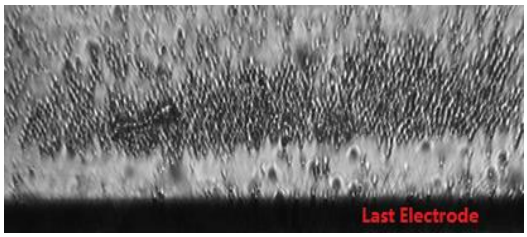

b

Figure 5.18: Cell concentration after (a) first ACEOF wave. (b) fifth ACEOF wave/.

It is important to note that particles do not move back under the influence of anomalous flow discussed earlier because neither an entire wavefront is formed in the first interelectrode gap nor the speed with which particles moved backwards is higher than the expected speed of $250 \mu m/s$.

While a greater number of waves increase the cell concentration ratio, however, after specific counts, equilibrium is reached, which means any more wave disperses the cells collected in the concentration area. This decreases the concentration factor and overall efficiency of the device. Therefore, an optimising number of waves is an integral part of the research.

5.4.2.3 Optimising the number of ACEOF waves

Eight ACEOF passes are used for $50 \mu m$ and $100 \mu m$ interelectrode gaps to quantify the optimise several ACEOF waves required to provide the concentration factor of 100000. Experiments are performed five times each for both full and partial switching patterns. By analysing videos observation of the device after each wave and counting cells left behind on the device and those that reached the concentration section, it is concluded that five ACEOF waves are sufficient to

achieve the desired cell concentration using $100\mu m$ interelectrode gap. However, after the 5th wave, some yeast cells start moving backwards as they get trapped in the vortex, or no new cell arrives at the concentration area. Figure 5.19 shows a microscopic view of the device with a $100\mu m$ interelectrode gap for the full switching pattern (figure 5.19a) and partial switching pattern (figure 5.19b) after five ACEOF waves. It is evident from figure 5.19 that after the 5th wave, cells have moved to the concentration section.

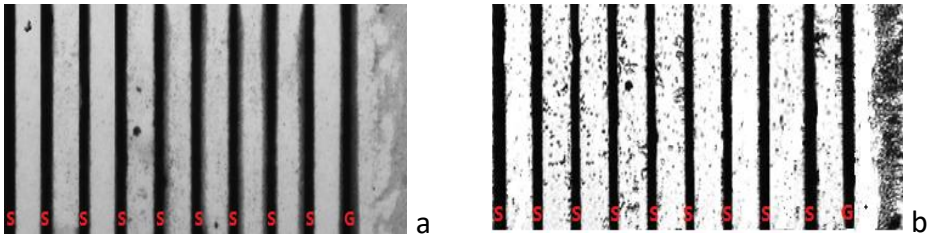

Figure 5.19: The microscopic view of the device (with $100\mu m$ interelectrode gap) after third ACEOF under the influence of (a) full switching pattern and (b) partial electrode switching.

Experiments are also performed for the device with $50\mu m$ interelectrode gap. The maximum particle displacement for $50\mu m$ is generated at $800Hz$ frequency for the fluid conductivity of $10mS/m$. Therefore, experiments are repeated at $10V_{PP}$, $800Hz$. $50\mu m$ is chosen because it allows smaller chamber height which increases device AC pDEP efficiency in the final section. Finally, $75\mu m$ interelectrode gap is ignored because it requires higher chamber height which decreases AC pDEP efficiency. Figure 5.21a shows a microscopic view of the device before ACEOF, while figure 5.20b clearly illustrates that all particles are pushed to the concentration area. Experiments are performed at the chamber height of $300\mu m$. The device is tested for both full and partial switching patterns.

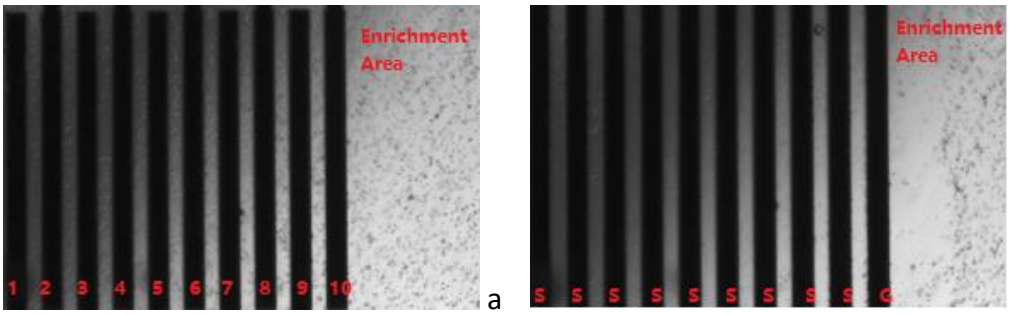

a b

Figure 5.20: Microscopic view of the device with $300\mu m$ chamber height (a) after the sample is settled on the device and (b) after seven ACEOF waves.

Experiments are then performed at the chamber height of $200\mu m$ chamber with an interelectrode gap of $50\mu m$. Smaller chamber height increases AC pDEP results and allows focusing electrode from much closer. Figure 5.21a and 5.21b show the results before ACEOF starts and after the 7th ACEOF wave.

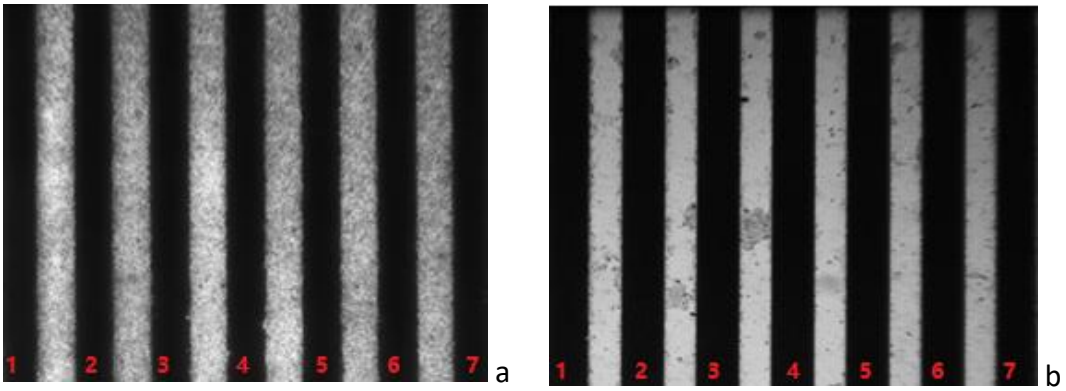

a b

Figure 5.21: Microscopic view of the device with $200\mu m$ chamber height (a) after the sample is settled on the device and (b) after seven ACEOF waves.

Therefore, by analysing videos and observing cells on the electrodes and in the concentration area, it is observed that it requires seven ACEOF waves to push all cells to the concentration area. Two extra waves are required because lower v_{EOF} and particle displacement is generated with $50\mu m$ interelectrode gap compared to $100\mu m$ interelectrode gap. Results confirm that the fluid velocity of $130\mu m/s$ is achieved from the electrode edge, which is $150\mu m/s$ less than observed earlier with $500\mu m$ wide electrodes. Therefore, taking seven waves to move cells onto the concentration area.

Figure 5.22 illustrates the maximum waves required to achieve the maximum cell concentration after five waves for the $100\mu m$ interelectrode gap and after seven waves after $50\mu m$ interelectrode gap. It is evident from figure 5.23 that it requires seven waves for $50\mu m$ interelectrode space while $100\mu m$ interelectrode gap produce slightly better results in five waves. Moreover, it can also be seen that in both cases, more than 50% of cells reach a concentration area in the first four waves. Cell collection grows almost linearly for the first five passes in the $100\mu m$ interelectrode gap while it continues to grow until the 7^{th} wave in $50\mu m$ interelectrode gap. The dip in the plot lines is because cells start to disperse from the concentration area.

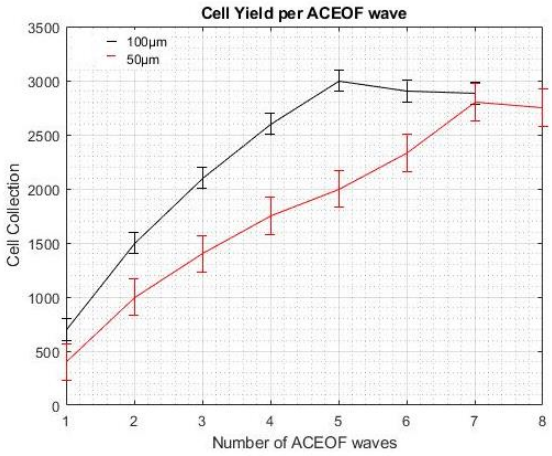

Figure 5.22: Cell Yield as a function of ACEOF waves for $50\mu m$ (red line plot) and $100\mu m$ (black line plot) interelectrode gaps.

Therefore, based on figure 5.22, it is concluded that the $100\mu m$ interelectrode gap provides cell collection in five waves compared to seven waves with a $50\mu m$ interelectrode gap.

5.4.2.4 Electrode Switching time

Two vortices are formed when the electrodes are switched to signal and ground, one for electrode connected to signals and the other for ground. These vortices then push cells away from the next electrode forming particles wavefront at a

certain distance past the inter-electrode gap. Once the wavefront has moved over the subsequent inter-electrode gap, the following electrode combination is applied to push particles further towards the concentration area. The time required to switch between electrodes is termed electrode switching time and is crucial in determining the device's overall processing speed. Table 5.7 summarises the switching time between electrodes for interelectrode gaps for the full and partial switching patterns.

Table 5.7: Effect of Switching Pattern on Process Timings.

Electrode Switching Pattern	Interelectrode Gap	1	2	3	4	5	6	7	8	9	Time per wave (s)
Full	$50\mu m$ Time (s)	19	27	27	27	27	27	27	27	27	235
	$100\mu m$ Time(s)	8	18	18	18	18	18	18	18	18	152
Partial	$50\mu m$ Time (s)	37	37	37	37	37	37	37	37	37	333
	$100\mu m$ Time(s)	30	30	30	30	30	30	30	30	30	270

It is evident from table 5.7 that for $100\mu m$ interelectrode gap, it takes 152 seconds for one ACEOF wave compared to 235 seconds for $50\mu m$ interelectrode gap, as shown in figure 5.23. Therefore, during the full switching pattern, $100\mu m$ interelectrode gap MWACEOF response requires 760 seconds compared to 1645 seconds for $50\mu m$ interelectrode gap in full switching pattern. On the other hand, during the partial switching pattern, $100\mu m$ electrode gap requires 1350 seconds compared to 2331 seconds for $50\mu m$ interelectrode gap.

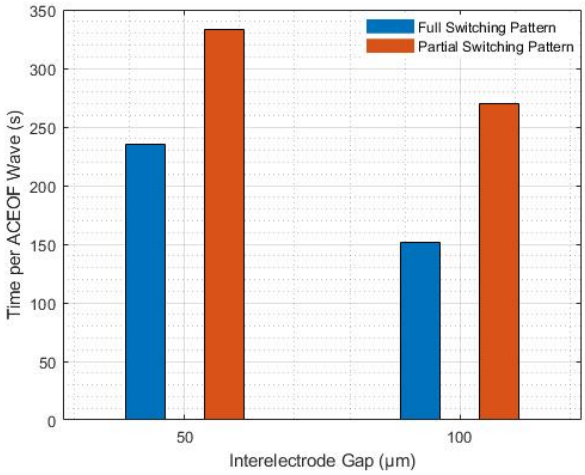

Figure 5.23: Bar graph illustrating the difference in the time taken per ACEOF wave for $50\mu m$ and $100\mu m$ interelectrode gap during full switching pattern, and partial switching pattern.

5.4.3 Synopsis

In this section, MWACEOF and AC pDEP responses are quantified separately using ten individually addressable parallel $50\mu m$ wide symmetric electrodes with $100\mu m$ and $50\mu m$ interelectrode gaps. It is concluded from the observation that:

1- With $100\mu m$ interelectrode gap device length is $1400\mu m$ and $950\mu m$ for $50um$ interelectrode gap. However, $100\mu m$ interelectrode gap pushes particles to $175\mu m$ into the concentration area while $50\mu m$ interelectrode gap pushes particles to a maximum of $125\mu m$.

2- v_{EOF} reported for $100\mu m$ interelectrode gap is $120\mu m/s$ higher than $50\mu m$ interelectrode gap. Also, $100\mu m$ interelectrode gap uses only 5 ACEOF waves than 7 ACEOF waves used during $50\mu m$ interelectrode gap. Also, $100\mu m$ interelectrode gap offers 83seconds advantage over $50\mu m$ electrode gap per wave. Hence using $50\mu m$ interelectrode gap requires 1645 seconds to move particles at the distance of 1055um from the first electrode at the speed of $130\mu m/s$. On the other hand, $100\mu m$ interelectrode provides particle

concentration at a distance of $1620\mu m$ from the first electrode in $760\ seconds$ at the rate of $250\mu m/s$.

3- As $100\mu m$ gate width forms a maximum particle displacement of $175\mu m$; therefore, a chamber height of $200\mu m$ is used for the device. Similarly, with $50\mu m$ interelectrode gap, a chamber height of $200\mu m$ is used because the maximum particle displacement is $125\mu m$. Lower chamber height increases AC pDEP response.

4- A partial switching pattern gives no anomalous flow during the experiment and is an excellent tool for working with fewer electrodes. However, it decreases processing time by almost 40% compared to the 'full switching pattern'.

5- For any AC pDEP process, most particles are trapped on initial electrodes compared to later ones. It is because cells near the electrodes get captured immediately, while cells moving into the chamber at higher suspension points are pushed down with each passing electrode until they get captured. $7\mu m/s$ linear speed provides near-complete cell capture; however, under no DEP condition, at this speed, the cell takes 207.14 seconds to travel from the first to the last electrode in $100\mu m$ interelectrode gap and 135.71 seconds in $50\mu m$ interelectrode gap. On the other hand, using $30\mu m/s$ linear speed, cell yield decreases to 94% but moves from first to the last electrode in 48.33 seconds and 31.67 seconds in $100\mu m$ and $50\mu m$ interelectrode gap, respectively. After $45\mu l/min$, cell yield decreases to less than 50%, reaching merely 20% at $93\mu m/s$.

Therefore, it is concluded that for the cell concentration stage using AC pDEP and MWACEOF following setup is adapted:

i. Yeast cells are suspended in $10mS/m$ conductive DIW solution.

ii. The chamber height of $200\mu m$ is used for both $500\mu m$ and $100\mu m$ interelectrode gaps.

iii. 1000 seconds AC pDEP is used at $30\mu m/s$ linear speed, providing an AC pDEP efficiency of $\sim 95\%$.

iv. The 'full switching pattern' is selected to switch electrodes in the experiments because it is faster than the 'partial switching pattern' and provide an autonomous response that reduces the Brownian motion effect.

v. Five ACEOF waves are utilised for cell concentration using $100\mu m$ interelectrode gap, while for $50\mu m$ interelectrode gap, seven ACEOF passes are used.

5.4.4 Cells concentration by combining AC pDEP and MWACEOF

This section discusses the cell concentration factor results and the device's efficiency by combing AC pDEP and MWACEOF for different cell concentrations. In this final section, first, AC pDEP is applied for 1000 seconds with $20V_{PP}, 1MHz$ signal. Once the AC pDEP process is completed then at 1000seconds, the syringe pump stops, and the device is allowed to capture the remaining cells for the next fifteen seconds, after which AC pDEP is completely eliminated. Five seconds later, ACEOF is switched on with a full switching pattern using an AC signal of $10V_{PP}, 1kHz$. Five ACEOF waves are applied to move cells to the concentration

area using $100\mu m$ interelectrode gap, while seven ACEOF waves are used for the device with $50\mu m$ interelectrode gap. The fluidic chamber is designed to leave $200\mu m$ space before the first electrode to allow fluid to develop a non-turbulent flow before reaching electrodes. In contrast, $400\mu m$ space is left after the tenth electrode for the cell concentration area. It provides a chamber volume of $0.60\mu L$ (from equation 5.2).

5.4.4.1 Concentration Area Calculation

Through detailed analysis of experimental videos and repetitive experiments, it is established that the 100um interelectrode gap gives a vortex height between the range of $160um$ to $175um$. On the other hand, $50um$ interelectrode pushes cells between the range of $115um$ to $125um$. Moreover, video analysis also showed that cells are collected in the form of a wavefront whose width is within the range of $50um$ as shown in figures 5.24a and 5.24b.

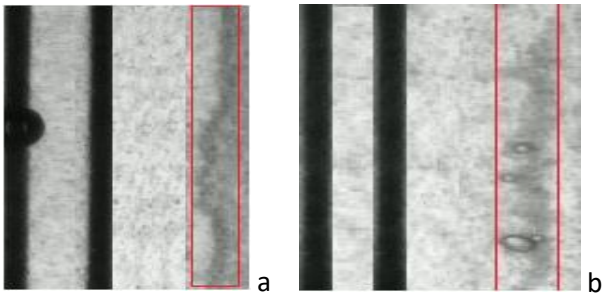

Figure 5.24: Cell forming wavefront for (a) $100\mu m$ interelectrode gap at $175\mu m$ (b) $50\mu m$ interelectrode gap at $125\mu m$.

Therefore, the concentration area is built $160\mu m$ and $115\mu m$ after the 10th electrode edge for $100\mu m$ and $50\mu m$ interelectrode gap. Moreover, this area's width is kept at $60\mu m$, as shown in figure 5.25, where the red box highlights the concentration area. It is chosen because this is the maximum width within which cell wavefront is compiled. Due to the microscope limitations length of the area is $700\mu m$ while the concentration area height is $200\mu m$. Therefore, the concentration area's

volume for both the $50\mu m$ and $100\mu m$ interelectrode gap devices is 8.4nL. Hence cells are allowed to settle down on the device in the collection area before analysis. Yeast cells have dimensions of a few micrometres. Therefore, cells should be collected within the height of 50um, making the concentration area's volume of 2.1nL.

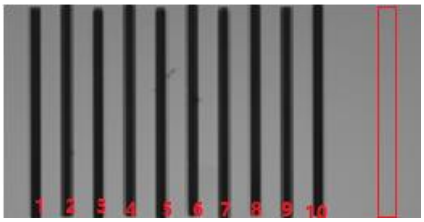

Figure 5.25: Microscopic view of the device with $100\mu m$ interelectrode gap and $60\mu m$ wide cell concentration area highlighted with a red box.

5.4.4.2 Processing Time

The processing time is defined as the time it takes to complete the total AC pDEP-MWACEOF process. The device first functions at $1000s$ for AC pDEP, after which it takes $760s$ with $100\mu m$ interelectrode gap for cell concentration using five waves of ACEOF. Therefore, in total, it takes $1760s$ to provide desired cell concentration. In contrast, with $50\mu m$ interelectrode gap, $1645s$ are required for seven ACEOF waves, making the processing speed $2645s$ in total. The processing speed comparison is shown in figure 5.26.

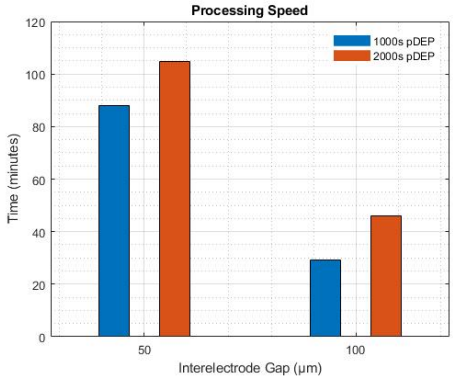

Figure 5.26: Processing time comparison between $50\mu m$ and $100\mu m$ interelectrode gap devices for 1000s and 2000s AC pDEP processing and multiwave ACEOF.

5.4.4.3 DEP and ACEOF Yield

Two device efficiencies are monitored during the project:

i. **AC pDEP yield** is defined as the number of cells captured during AC pDEP divided by the number of cells passed from the electrodes with the number of cells expected to pass in the chamber. The device can process $\sim 110\mu L$ solution in every $1000 seconds$ at the flow rate of $45\mu l/min$. The device efficiency is monitored for approximately $1500 cells/ml$, $5000 cells/ml$ and $10000\ cells/ml$; These cell populations provide around 165 cells, 550 cells and 1400 cells for $\sim 110\mu L$ solution. This efficiency is AC pDEP yield and is calculated as $> 95\%$. It is a significant increase from the current reported pDEP yields with microfluidic-based devices [101,108,112,120], where the maximum reported efficiency is $\sim 50\%$. Furthermore, this is a significant increase in the flow rate from current studies $6\mu l/min$ [146, 152]. This shows that by increasing more electrodes, both pDEP yield and flow rate can be further improved, increasing the device throughput.

ii. **ACEOF yield** is AC pDEP to ACEOF conversion efficiency. It counts how many trapped particles are washed away to the cell concentration (enrichment area). It is defined as the number of cells present in the concentration area after the ACEOF process divided by the number of cells captured during the AC pDEP process. This efficiency is termed conversion efficiency in this project and is calculated using the formula in equation 5.4:

$$ACEOF\ Yield = \frac{Cells\ in\ concentration\ area\ after\ MWACEOF}{Cells\ trapped\ during\ pDEP} \quad 5.4$$

Figure 5.26a shows the microscopic view of the device after $1000 seconds$ AC pDEP process for the cell concentration of $13000 cells/mL$. It can be seen in figure 5.26a that the device responded to the AC pDEP process as expected by capturing more than 80% of the cells with the first five electrodes and the remaining 20% with the last five. Moreover, after each electrode, cells concentration in the interelectrode gap decreases. Because cells are getting trapped by the electrodes by AC pDEP, they move along the chamber and get trapped.

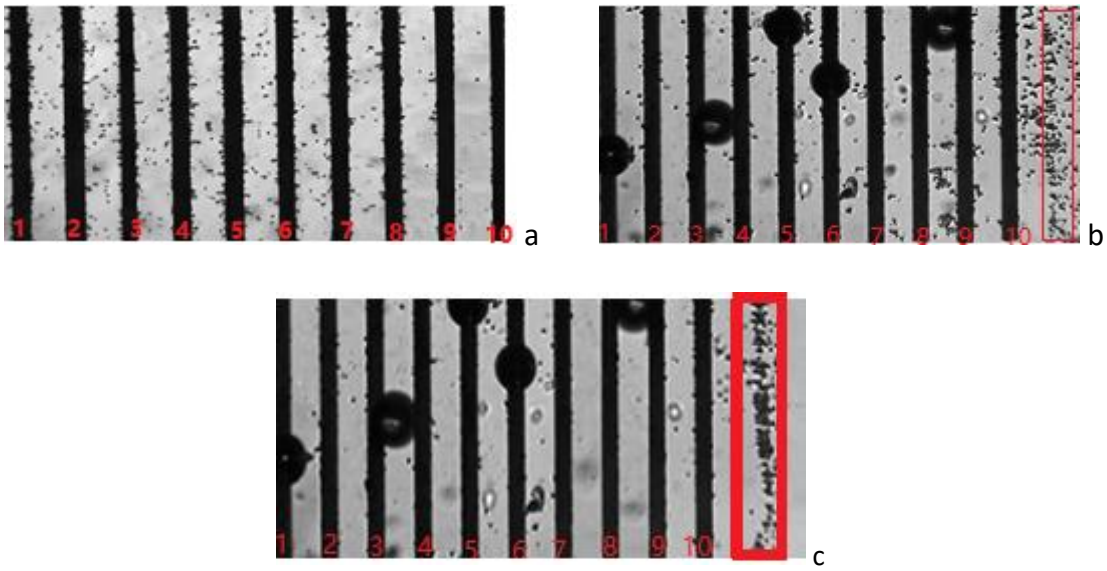

Figure 5.26: Microscopic view of the device (with $100\mu m$ interelectrode gap) to show (a) After 1000s AC pDEP (b) After 1st ACEOF waves, and (c) After 5th waves ACEOF wave.

Figure 5.26b and 5.26c show the cell accumulation after the 1st and 5th ACEOF wave, respectively. Results show that in the first ACEOF wave, 50% of cells are moved in the concentration area. However, with the 5th ACEOF remaining cells are also accumulated, a wavefront is formed at $\sim 170\mu m$ distance from the 10th electrode, therefore collecting cells within $60\mu m$ concentration area. However,

figure 5.29c shows that 40 cells are still left in the chamber after cell collection, including ten, after the 10th electrode. As discussed earlier, $110\mu L$ sample is processed from the chamber in 1000seconds, giving ~ 1400cells to travel from the chamber. It is established in section 5.4.1 that using ten electrodes provide a $>$ 95% AC pDEP yield. Therefore, providing ~ 1300 cells during the AC pDEP process. Analysis of the concentration area shows the collection of ~ 1250 cells which shows the conversion efficiency of $> 90\%$. Experiments are repeated with $1500\ cells/ml$, which estimates $\sim 175\ cells$. To calculate cells microscope is focused on the concentration area only. Results are shown in figure 5.27 after the 5th ACEOF, which offers a total count of $\sim 150\ cells$, providing an ACEOF yield of $> 92\%$.

a

Figure 5.27: Cell concentration after $1500\ cells/ml$.

Experiments are repeated with $50\mu m$ interelectrode gap to ensure the device can perform for different electrode geometry. $1500 cells/ml$ are prepared for the investigation. Results are shown for 1st ACEOF in figure 5.28a and 7th ACEOF in figure 5.28b. Results confirm that conversion efficiency of $> 92\%$ is achieved with the wavefront forming around $115\mu m$ from the last electrode edge. It can also be observed from figure 5.28a that after the 1st ACEOF wave, less than 20 cells have

reached the concentration area, while after the 7th ACEOF wave, 150 cells are collected in the concentration area, providing a conversion efficiency of $> 90\%$.

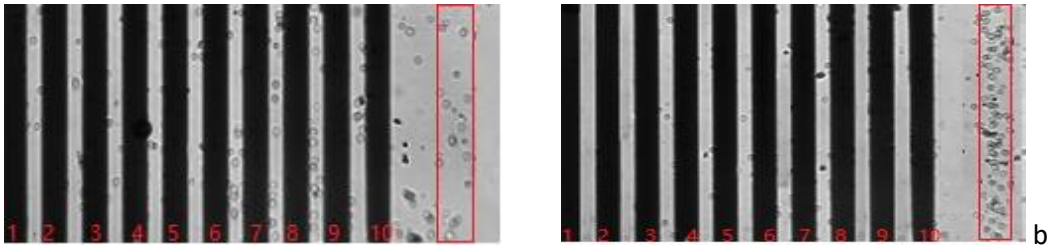

a b

Figure 5.28: Microscopic view of the device with $50\mu m$ interelectrode gap and $200\mu m$ chamber height after (a) first ACEOF wave and (b) seventh ACEOF wave.

Experiments are repeated for $1500 cells/ml$, $5000 cells/ml$, and $1000 cells/ml$ for $50um$ and $100um$ interelectrode gap devices. It can be observed from figure 5.29 that for all cell concentration, both sets of devices provides a conversion efficiency of $> 90\%$.

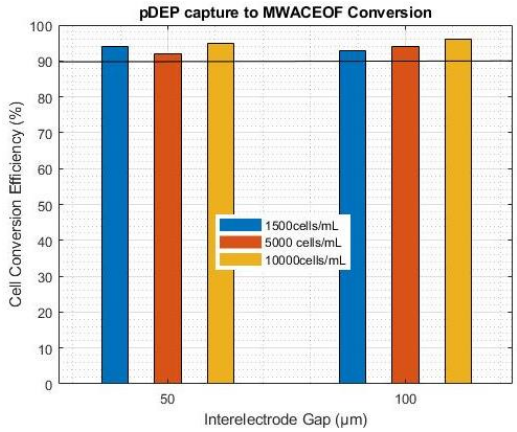

Figure 5.29: Cell conversion efficiency calculated for $50\mu m$ and $100\mu m$ for the cell count of $1500 cells/mL$, $5000 cells/mL$, and $10000 cells/mL$.

Moreover, experiments are repeated for 2000seconds AC pDEP (figure 5.30b) for $1500\ cells/mL$, which gives almost $310 cells$ compared to 150 cells in 1000seconds AC pDEP (figure 5.32a). The reason for the increased AC pDEP yield is that 1000s AC pDEP allows $110\mu L$ sample to process at $30\mu m/s$ while in $2000s$ AC pDEP, $220\mu L$ sample is processed.

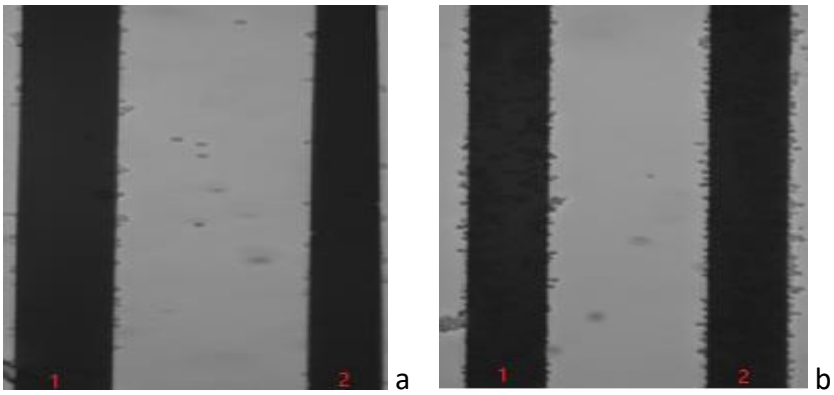

a b

Figure 5.10: Microscopic view of the device (with $100\mu m$ interelectrode gap) after (a) 1000s AC pDEP,(b) 2000s AC pDEP.

Figure 5.30 shows the number of cells trapped in $1500cells/mL, 5000cells/mL$, and $10000cells/mL$ in 1000s AC pDEP and 2000 AC pDEP. It can be observed from figure 5.31 that 2000s AC pDEP achieve approximately double cells as compared to 1000s AC pDEP.

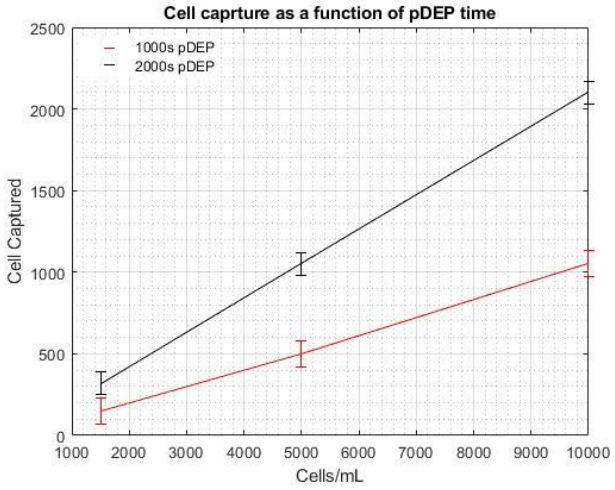

Figure 5.11: Cell capture as a function of AC pDEP processing time.

Therefore, it is concluded that an additional 1000s AC pDEP process will increase the concentration factor, as seen later in the chapter. It is because more cells captured during the AC pDEP process directly correspond to a higher concentration factor.

5.4.4.3.1 ***Reasons for cell loss***

The main reason for the loss of $< 10\%$ cells is because some cells are permanently stuck with the electrode, and they do not move with ACEOF because they are either

damaged or permanently polarised, as seen in [88,92]. Figure 5.32 shows the first two electrodes of the device. It can be seen in figures 5.32a (after AC pDEP) and figure 5.32b (after 5th ACEOF) that only 15 cells are left attached to the electrodes out of almost 400 cells which makes conversion efficiency of the device $> 96\%$.

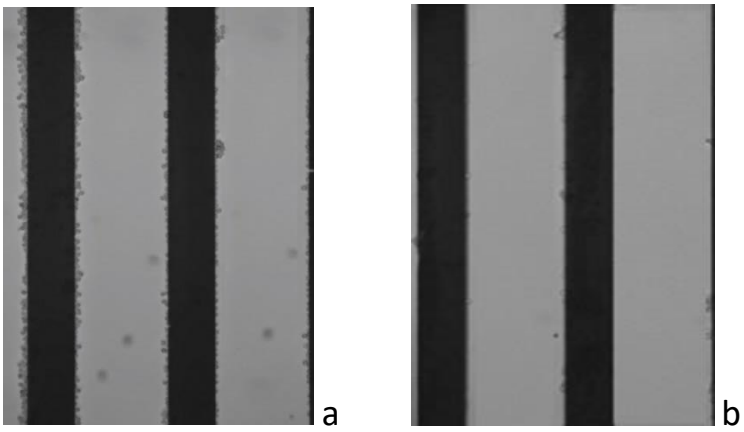

Figure 5.12: The microscopic view of the device with $100\mu m$ interelectrode gap with 400 cells (a) after AC pDEP and (b) after five ACEOF waves.

Figure 5.33 shows a microscopic view of the electrode edge as soon as ACEOF begins. It is observed from figure 5.33 that all cells move with ACEOF flow; however, one cell is still sticking at the electrode edge.

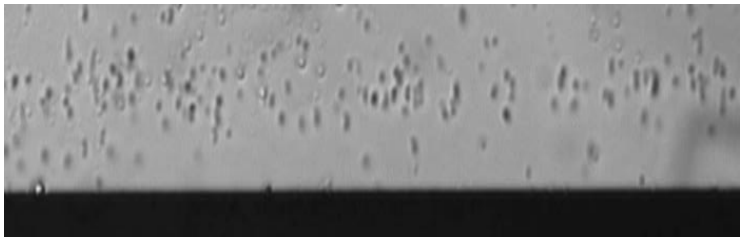

Figure 5.13: The microscopic view of the electrode edge, illustrating ACEOF while one cell is still sticking with the electrode.

This device's behaviour is further elaborated using figure 5.34a and figures 5.34b, which illustrate results after AC pDEP and 5th ACEOF wave focusing on the first two electrodes. When 200 cells are captured using the first two electrodes, only five cells are left after the 5th ACEOF, which provides a conversion efficiency of $> 97\%$. The current litterateur shows greater than 45% cell loss from ACEOF [120, 277].

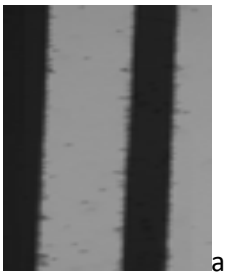

a b

Figure 5.14: The microscopic view of the device with $100\mu m$ interelectrode gap with 200 cells (a) after AC pDEP and (b) after five ACEOF waves.

5.4.4.4 Concentration factor

The cell concentration factor is achieved by dividing the cell collected in the concentration area by expected cell concentration. The concentration factor (CF) is calculated using equation 5.4.

$$CF = \frac{Total\ cells\ in\ the\ concentration\ area}{Expected\ cells\ in\ the\ concentration\ area} \quad 5.4$$

During the cell concentration stage, each experiment is repeated 20 times for both $50\mu m$ and $100\mu m$ interelectrode gap devices. In this stage, three cell samples of $1500\ cells/mL, 5000\ cells/mL$, and $10000\ cells/mL$ are used. The concentration factor is measured at the height of $50\mu m, 100\mu m$ and $200\mu m$ because vortices deposit all cells on the surface only.

Expected cells in the concentration area for different cell concentrations are given in table 5.9. Table 5.9 also shows the figures illustrating the number of cells present in the concentration area after the AC pDEP – MWACEOF process completion for 1000s AC pDEP, 2000s AC pDEP and 4000s AC pDEP. 4000s AC pDEP is only performed for $10000\ cells/mL$ because the DC motor heats up and limits its use.

Table 5.9: Cells expected in the chamber area.

$cells/mL$	Expected number of cells			AC pDEP - Time $(seconds)$		
	2.1nL	4.2nL	8.4nL	1000	2000	4000
1500	3.15×10^{-3}	6.3×10^{-3}	12.6×10^{-3}	5.35a	5.35d	
5000	10.5×10^{-3}	21×10^{-3}	42×10^{-3}	5.35b	5.35e	
10000	21×10^{-3}	42×10^{-3}	84×10^{-3}	5.35c	5.35f	5.37

Experiments are first performed for 1000s AC pDEP. Carefully counting cells, it can be seen that in the concentration area, 150cells (figure 5.35a), 500cells (figure 5.35b), and 1000 cells (figure 5.35c). Experiments are then performed for 2000s AC pDEP, which produces 310 cells (figure 5.35d), 1050 cells (figure 5.35e), and 2100 cells (figure 5.35f).

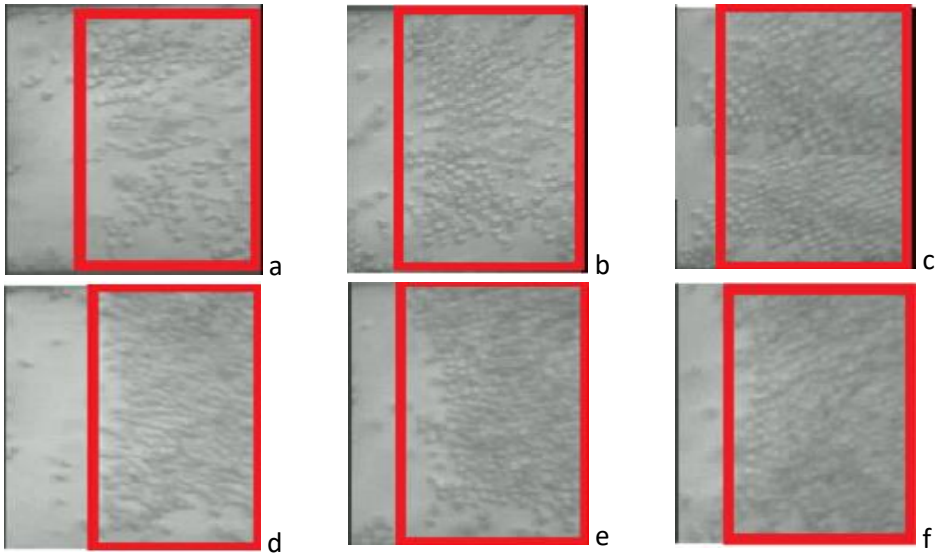

Figure 5.15: Cells present in the concentration area after AC pDEP-MWACEOF process completion for 1000s AC pDEP (a) $1500 cells/mL$, (b) $5000 cells/mL$, (c) $10000 cells/mL$ and for 2000s AC pDEP (d) $1500 cells/mL$, (e) $5000 cells/mL$, (f) $10000 cells/mL$.

Results are concluded in figure 5.36a for 1000s AC pDEP and figure 5.36b for 2000s AC pDEP. For 1000s AC pDEP, the maximum concentration factor of ~ 50000 is achieved with the chamber volume of $50 \mu m$ height, which decrease to ~ 25000 and ~ 12000 at $100 \mu m$ and $200 \mu m$ height, respectively. On the other hand, for the 2000s AC pDEP, the concentration factor of > 100000 is achieved at $50 \mu m$ chamber volume height, decreasing to ~ 50000 and ~ 25000 as chamber volume height increases to $100 \mu m$ and $200 \mu m$.

Figures 5.36a and 5.36b show that the cell concentration factor remains almost consistent for all samples.

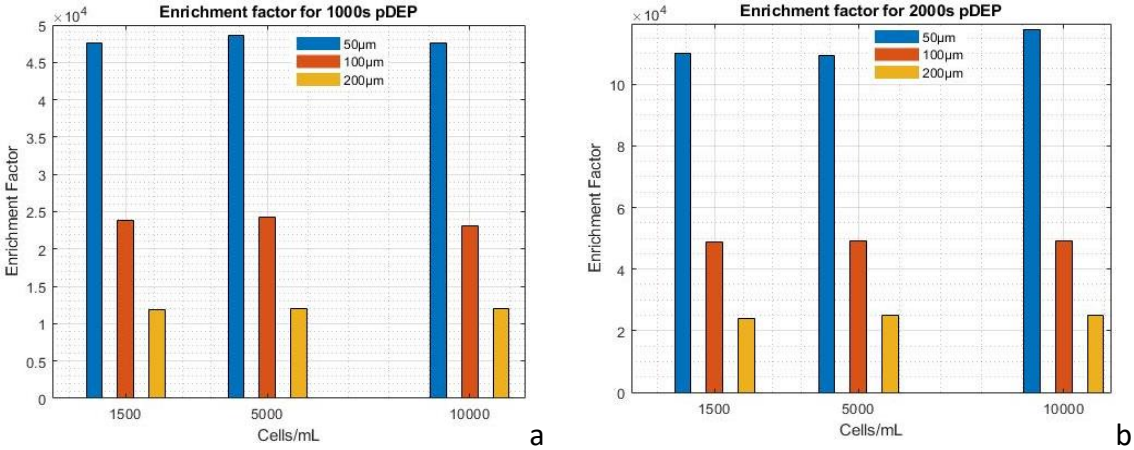

Figure 5.16: Concentration factor calculated at chamber volume with $50\mu m$, $100\mu m$, and $200\mu m$ height for the AC pDEP at (a) 1000s and (b) 2000s.

The experiment is performed with $10000 cells/mL$ for 4000s. Figure 5.37a shows the number of cells located in the concentration area, and figure 5.39b illustrates the concentration factor results after the 4000s AC pDEP process calculated at $50\mu m$, $100\mu m$, and $200\mu m$ chamber height volume.

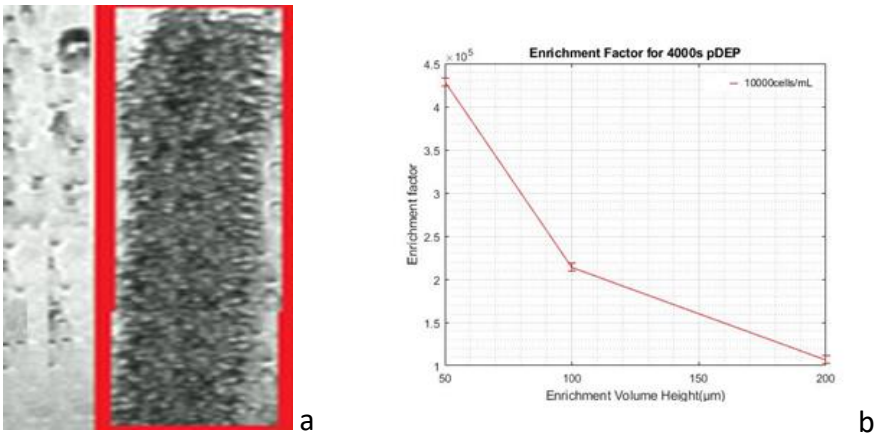

Figure 5.17: Cell concentration area after (a) 4000s AC pDEP for $10000 cells/ml$, and (b) Cell concentration factor at $50\mu m$, $100\mu m$, and $200\mu m$ chamber volume height.

It is evident from the results concluded in figure 5.37b that the maximum concentration factor has increased to > 430000 at $50\mu m$ height. The concentration factor decreases to 200000 at $100\mu m$ height and further decays to 100000 at

$200\mu m$ height. However, at AC pDEP has increased to 4000s concentration factor remained > 100000 for all heights. Therefore, the target concentration factor set during chapter 1 has been achieved with the 2000s and 4000s AC pDEP, while for 1000s ~ 50000 concentration factor is accomplished.

These results show significant improvement from the technology discussed in chapter 1, i.e., MACS, FACS, Manual or Robotic manipulation etc., in terms of cells viability and processing speed and cell concentration [6 – 29]. In addition, while [277,278] show cell concentration of a maximum of 200 pores, this device can perform the cell collection of up to 400 000 cells within 45min. Furthermore, the device has low cell loss <10%, which is significantly less than FACS, Manual or robotic manipulation, where more than 70% cell loss is reported [30, 32,33]. Also, the device does not require cell tagging, which means the captured cells can be used for analysis leading to valuable discoveries and procedural research such as IVF, etc. The maximum concentration factor reported in the literature review is 1200 [211], and the maximum efficiency given in the literature review is 65% [218]. Whilst the device is capable of >90% efficiency with approximately 400 000 cells/ml.

5.5 Chapter Synopsis

The chapter has presented cell concentration using ten individually addressable electrodes geometry by combining AC pDEP and MWACEOF phenomena. This chapter first presented the results for AC pDEP, where it was concluded that $30\mu m/s$ provides an AC pDEP yield of >95% using ten electrodes. It was found that $100\mu m$ interelectrode gap requires five ACEOF waves while $50\mu m$ interelectrode gap uses seven ACEOF waves for maximum cell concentration. The anomalous

flow produced during the experiments is overcome with a sophisticated and intelligent electrode switching pattern. Moreover, this flow has its properties matching with REOF. However, as the flow is generated from the perfect symmetry of electrodes, it is not REOF.

Five and seven ACEOF waves provide a conversion efficiency of $> 90\%$. After AC pDEP and ACEOF response are quantified, AC pDEP and ACEOF results are quantified for cell concentration. For 1000s, AC pDEP maximum concentration factor of 50000 is achieved, while in the 2000s, AC pDEP produced a concentration factor of 100000. The concentration factor increases to 430000 with 4000s AC pDEP. The device offers an AC pDEP efficiency of $> 95\%$, the conversion efficiency of $> 90\%$ with a concentration factor of > 48000 for 1000s AC pDEP, > 100000 for 2000s AC pDEP and > 430000 at 4000s AC pDEP.

6 Numerical Modelling

6.1 Aims and Objectives

This chapter's primary goal is to present the numerical model for ACEOF, MWACEOF and AC pDEP numerical model for cell trapping and separation. The numerical model is required to improve the theoretical and physical understanding of the fluid flow governed by ACEOF and cell sorting under AC pDEP principles. This chapter also targets to present corroboration between numerical and experimental results produced in chapters 4 and 5. Moreover, the chapter also provides a model for the device that can use an interdigitated electrodes group to provide a faster and more significant collection factor. Finally, this chapter aims to provide the methodology, mathematical equations, and boundary conditions for ACEOF and AC pDEP modelling. In the end, this chapter also provides a numerical model for anomalous flow and attempts to improve understanding of the phenomena.

6.2 Approach

The numerical modelling is performed using COMSOL Multiphysics 5.5. Ramos [122] and Green model [197] forms the bases of the numerical model used in this study for fluid flow. In contrast, Oh [192], Tang [193], and Yonghong [194] models laid the foundation for AC pDEP simulations with necessary modifications, as discussed in this chapter. The rationale behind using these models is that these models have been adapted in several previous studies with some modifications, which are thoroughly discussed in chapter 3, and proved to provide a good match between theoretical and experimental results. Furthermore, numerical modelling is a time-consuming

process, especially for fluid dynamic meshing nodes; therefore, analysis is made on 2D geometry to save the analysis's runtime.

Firstly, ACEOF and AC pDEP are studied for the same parameters as discussed in chapter 4 to compare numerical results with the experimental results produced in chapter 4, ACEOF. These include a pair of coplanar electrode geometry, AC signal strength and frequency, fluid conductivity, distance from the electrode, chamber height for both ACEOF and AC pDEP. These parameters are shown in table 6.1.

Table 6.1: ACEOF and AC pDEP parameters used for finite element modelling to compare results with chapter 4.

Parameter		**ACEOF**	**AC pDEP**
A pair of coplanar electrode Geometry (μm)	Interelectrode gap	$20, 50, 75, 100\ and\ 150$	
	Electrode Width	50, and 100 – 1100 with a step size of 100	
	Electrode Length	Assumed to be infinite in 2D Geometry	
Fluid Conductivity (mS/m)		$3, 5, 10, 14, and\ 20$	
AC Signal Strength (V_{PP})		5, 7.5, and 10	10, 15 and 20
AC Signal Frequency (Hz)		500, 1k, 1.5k,2k, 2.5k, and 3k	10k, 100k, 1M and 10M
Chamber Height (μm)		100- 1000 with a step size of 100	100- 600 with a step size of 100
Distance from the electrode (μm)		10, 25 and 40.	
Cell Linear Speed ($\mu m/s$)		Not applicable	10 – 40 with a step size of 5

There is no ACEOF model available for more than two symmetric electrodes; therefore, to compare numerical results in chapter 5, a numerical model for four individually addressable coplanar electrodes is built first. Afterwards, analysis is performed for ten electrodes for all the parameters discussed in chapter 5. Finally, the model is simulated for twelve individual electrode geometry and presented to

discuss flow reversal. Table 6.2 shows the parameters used for simulating results to compare with experimental results in chapter 5.

Table 6.2: Parameters used for simulating results to compare with experimental results in chapter 5.

Parameter		ACEOF	AC pDEP
Ten coplanar Individually addressable electrode Geometry (μm)	Interelectrode gap	100	
	Electrode Width	50	
	Electrode Length	Assumed to be infinite in 2D Geometry	
Fluid Conductivity (mS/m)		10	
AC Signal Strength (V_{PP})		10	20
AC Signal Frequency (Hz)		$1k$	$1M$
Chamber Height (μm)		300	300
Switching pattern		Full and Partial	Not applicable
Cell Linear Speed ($\mu m/s$)		Not applicable	35, 39, and 40

For ACEOF simulations, plots consist of three features.

Velocity Surface provides the velocity magnitude. It is measured in $\mu m/s$ and contains a colourmap to show velocity magnitude.

Surface Arrow describes the direction of fluid flow**.** Moreover, it also provides information about the velocity strength. More arrows depict higher velocity.

Streamline Plots describes the information about vortex height during chamber height analysis and velocity profile as streamline width become narrower at fast speed and expands at slower speeds.

Surface velocity, surface arrow, and streamline plots and shown in Figure 6.1a ($0.5kHz$), 6.1b ($1kHz$), 6.1c ($1.5kHz$). It can be observed from the figure that at 1KHz (6.1b), velocity is reaching $900\mu m/s$, and therefore narrower streamlines and denser surface arrows are produced. On the other hand, for 0.5kHz (6.1a) and 1.5kHz

(6.1c), velocities have dropped to $300\mu m/s$ and $600\mu m/s$, therefore, streamlines widths are expanded, and surface arrows have become lighter. It can also be noticed that the height of the streamlines remains the same in all cases. Fig 6.1d attempts to compare vortex with 6.1a,b,c showing that vortexes are formed on both sides of the electrodes both experimentally and numerically.

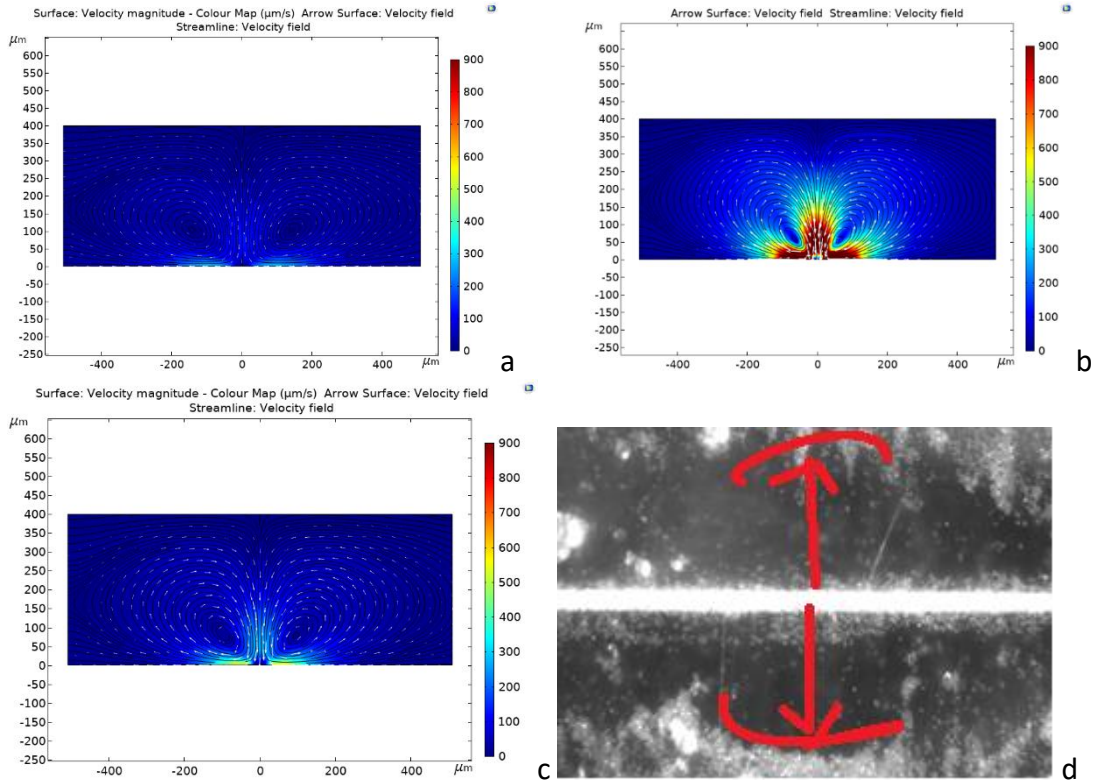

Figure 6.1: Streamline plots illustrating v_{EOF} velocity as a function of frequency (a) $0.5kHz$, (b) $1kHz$, and (c) $1.5kHz$ for $100\mu m$ interelectrode gap. (d) Experimental results forming two vortexes on either side of the electrode.

On the other hand, AC pDEP analysis is studied for AC signal, frequency, and chamber height for two electrodes to match experimental results in chapter 4. In contrast, analysis is repeated for AC signal, chamber height, and infusion pump speed for ten electrodes to match results in Chapter 5. Particle separation using AC pDEP is performed for live and dead yeast cells. Cells modelling is performed based on Wason [189] and Pohl [118] cell modelling techniques. Variables required to perform AC

pDEP is shown in table 6.1 and 6.2. For ACEOF and AC pDEP models, mainly the AC/DC module, microfluidics and particle tracing modules are used.

6.3 Methodology

6.3.1 ACEOF Modelling

COMSOL Multiphysics 5.5 is used for finite element modelling. 2D space dimension was chosen from the model wizard. Electric current and Creeping flow were selected for the physics interface. Electric current is preferred over electrostatics physics because it solves current conservation based on Ohm's and Gauss' law and computes for electric field and potential distribution in conductive media for variable frequency [336]. On the other hand, the electrostatics interface uses Gauss' law only and limits computation for static studies [336]. For fluid flow slip velocity conditions Creeping flow is preferred over laminar flow because it ignores Navier Stokes' equations at low Reynold number [337]. Ignoring inertial terms is already discussed in chapter 2, where Stokes' equation is derived for the 3D and 2D model from Navier – Stokes' equation. The time-dependent study is selected because field variables are changing over time.

6.3.2 Geometry

A perfect comparison between numerical and experimental results begins with an electrode geometry model comparable to the experimental geometry. As experimental geometry consists of parallel coplanar electrodes, therefore for the 2D model, two $500\mu m$ wide electrodes are made side by side to each other. The same technique has been deployed by [141, 143, 195, 197] for modelling coplanar electrodes geometry. The 2D model is shown in figure 6.2a (domains) and 6.2b (transparent) while figure 6.2c (transparent) depicts a 3D model for $500\mu m$ wide,

$1000\mu m$ long Au coplanar parallel electrodes with $20\mu m$ interelectrode gap and the of the initial investigation is solution space is $400\mu m$. Geometric unions are made to ensure all domains are placed together and the device function as one.

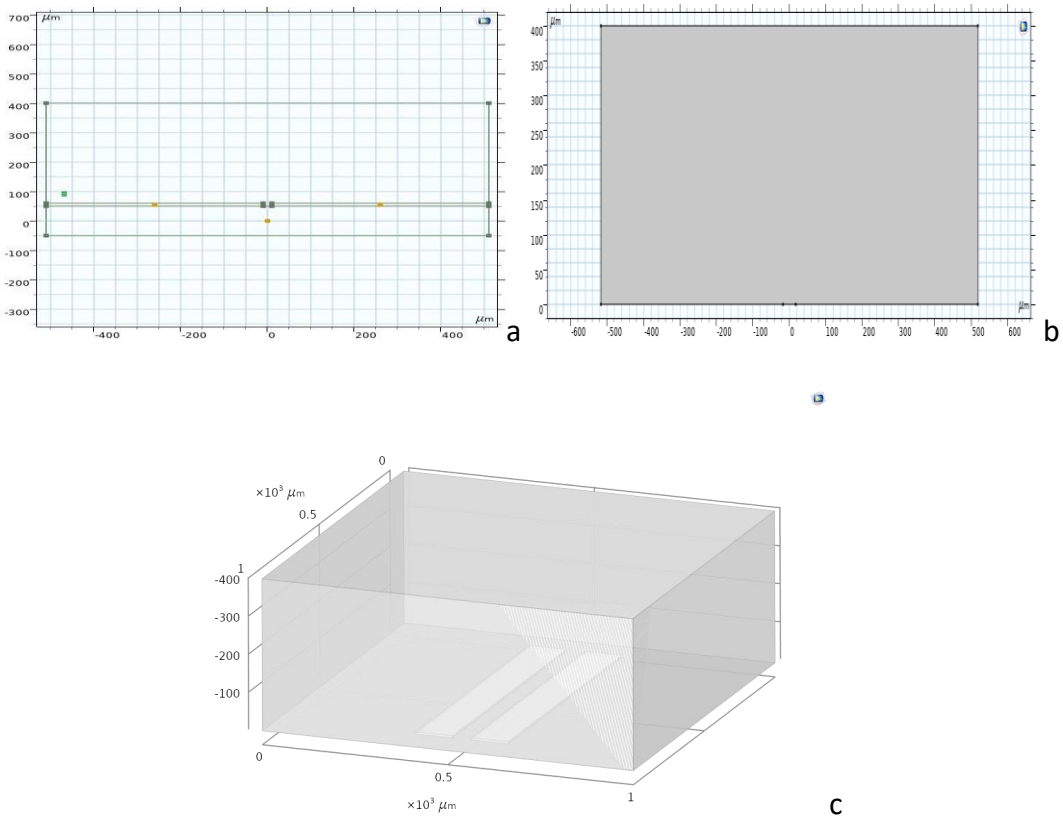

Figure 6.2: COMSOL 2D model (a) domain view, (b) transparent view, and (c) COMSOL 3D transparent view model of pair of coplanar $500\mu m$ wide and $1000\mu m$ long electrodes.

6.3.3 Material Settings

Gold is used as gold material deposited on a solid glass substrate. Glass is also used for chamber lid. Chamber is filled with water with desired conductance, which varies for different experiments, as shown in Tables 6.1 and 6.2. During all experiment density ($1\text{x}10^3\ kg/m^3$), dynamic viscosity ($1\text{x}10^{-3}\ Pa.s$), and relative permittivity (80.2) of the fluid remains constant, as shown in figure 6.3.

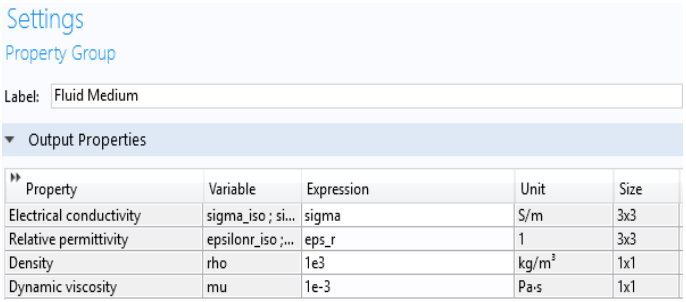

Figure 6.3: Physical settings for the fluid medium used for the properties of the fluid medium.

6.3.4 Boundary condition

Boundary conditions are the constraints necessary for a boundary value problem to ensure the solution's uniqueness [336]. Boundary conditions applied during fluid flow are discussed below:

6.3.4.1 Electrical Potential

The electrical potential (V) for the fluid flow is solved by the equation 6.1

$$\emptyset_{pot} = V_n + \sigma_q Z_{DL} \quad 6.1$$

Where σ_q is the fluid conductivity, and V_n is the potential applied to each electrode and is given by Equation 6.2

$$V_n = V_o e^{i\theta} \quad 6.2$$

Where V_0 is the applied potential, $i = \sqrt{-1}$ is an imaginary number, and θ is the phasor angle, and n is the number of the electrode at which potential is applied. For the current project, θ is always zero because there is no phase shifting in signals.

$$V_n = V_o \quad 6.3$$

Therefore, equation 6.1 becomes

$$\emptyset_{pot} = V_o + \sigma_q Z_{DL} \quad 6.4$$

Equation 6.4 is the potential applied as a boundary condition to the electrodes to solve for the EDL that forms the basis of the fluid flow. In Equation 6.1 and 6.4, Z_{DL} is the Debye's length impedance measured in Ωm^2 and is given by equation 6.5:

$$Z_{DL} = \frac{\lambda_D}{i\varepsilon\omega} \quad 6.5$$

Where ω is AC signal frequency given by the equation $2\pi f$ and λ_D is Debye's length given by equation 6.6:

$$\lambda_D = \frac{1}{\kappa^{-1}} \quad 6.6$$

Where κ^{-1} is the huckle's parameter, given by equation 6.7:

$$\kappa^{-1} = \sqrt{\frac{\varepsilon K_B T}{\sum_n Z_n^2 e^2 n_n^o}} \quad 6.7$$

Therefore, equation 6.6 becomes equation 6.8

$$\lambda_D = \sqrt{\frac{\sum_n Z_n^2 e^2 n_n^o}{\varepsilon K_B T}} \quad 6.8$$

Where Z is electron assumed Shell = 1, K_B is Boltzmann's constant= $1.38\text{x}10^{-23} m^2.kg.s^{-2}.K^{-1}$, T is Temperature= $293K$= $25^{\circ}C$, and ε is the absolute permittivity given by equation 6.9:

$$\varepsilon = \varepsilon_o.\varepsilon_r \quad 6.9$$

Where ε_o is vacuum permittivity = $8.85\text{x}10^{-12} F.m^{-1}$, and ε_r is the relative permittivity = 80.2, and n^o is the ionic concentration given by equation 6.10:

$$n^o = N_A \text{x} q \quad 6.10$$

Where N_A is Avagarod's Number = $6.022\text{x}10^{23} mol^{-1}$, and q is the electron charge = $1.6\text{x}10^{-19} C$.

Finally, the voltage drops across the double layer and is directly proportional to the zeta potential, $V_d\ (V)$ is given by equation 6.11:

$$V_d(x) = \frac{V_o}{2 + j\omega\pi x\lambda_D(\varepsilon/\sigma_q)} \quad 6.11$$

Where x is the centre of the interelectrode gap.

Equations 6.1 and 6.11 are applied to the electrodes to solve the fluid flow's electrical problem. An example is shown in figure 6.4.

6.3.4.2 Fluid Motion

Velocity for the fluid flow (v_{EOF}) is given by the equation 6.12:

$$v_{EOF} = \frac{1}{8\Lambda} \frac{\varepsilon V_o^2 \Omega^2}{\eta x (1+\Omega^2)^2} \quad 6.12$$

Where η is fluid's dynamic viscosity, Λ is the correction factor used to match the numerical and experimental results, v_{EOF} is maximum when $\Lambda = 1$. Λ is given by equation 6.13:

$$\Lambda = \frac{C_{DL}}{C_s + C_d} \quad 6.13$$

$C_{DL}$is Debye's length capacitance given by equation 6.14:

$$C_{DL} = \frac{\varepsilon}{\lambda_D} \quad 6.14$$

Where Ω is the dimensionless frequency given by equation 6.15:

$$\Omega = \omega x \frac{\varepsilon \pi \kappa}{\sigma_q 2} \quad 6.15$$

Equation 6.15 is applied to the electrodes to solve for the fluid flow. The condition is known as slip velocity. Figure 6.4 illustrates the boundary conditions of electrical (red) and ACEOF (black). As shown in figure 6.4, ACEOF inlet and outlet boundary conditions are set at 0 Pascals pressure conditions. Electrodes are set as slip velocity conditions (Equation 6.12), while all other boundaries are set as the no-slip condition. The electrical problem is solved by setting applied signals to the electrodes (Equation 6.11), while all other boundaries are set as electric insulation. Inlet and outlet are set as a periodic condition.

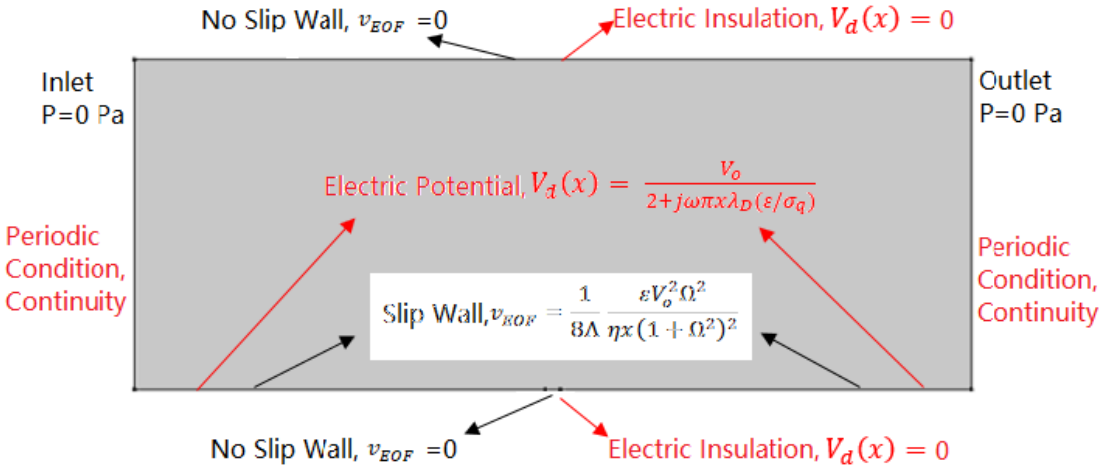

Figure 6.4: Boundary conditions for fluid flow settings representing slip and no-slip walls.

6.3.5 Parameters Setup

Parameters and setting variables are formulated based on the equations from 6.1 to 6.15. Correct SI units must be produced during this stage else the model does not follow the fluid flow.

6.3.6 Meshing

General meshing is applied to the electrodes and glass substrate, while; fluid dynamics meshing is applied to the fluid medium. Extra fine meshing is chosen to converge plots. Boundary elements and edges are further refined to free triangular sizing to avoid plotting artefacts in results.

6.3.7 Study and Simulations

The time-dependent study is chosen for ACEOF. Both studies were processed in parallel because creeping flow uses the electric currents module results. Therefore, processing the electric current module first and then solving for creeping flow is also possible. However, it slows the simulation speed while the outcome remains precisely the same.

6.4 Results and Discussion

6.4.1 Fluid velocity vs Frequency, fluid conductivity and Interelectrode gap

This section presents the influence of change in AC frequency, fluid conductivity, and interelectrode gap on v_{EOF} at $5V_{PP}$. AC frequency is investigated from $500Hz$ – $3kHz$, with a step-size of $500Hz$, while scales of fluid conductivity and interelectrode gaps correspond with the values mentioned in chapter 4. Chamber height for these experiments is set at $400\mu m$ because it is already established through experiments and is seen in the results later that chamber height does not influence the v_{EOF}. For all numerical simulations, $\Lambda = 1$ is used to achieve maximum velocity. Generally, trends in numerical results agree with experimental results, previous studies, and physical theory. However, the calculated numerical velocity is significantly higher than the experimental results in previous studies discussed in Chapter 3. It is due to 2D geometry and limitations already thoroughly discussed in chapter 3.

Results are plotted using MATLAB for fluid velocity as a function of frequency, for the fluid conductivity of $3mS/m$ (figure 6.5a), $7mS/m$ (figure 6.5b), $10mS/m$ (figure 6.5c), $14mS/m$ (figure 6.5d), and $20mS/m$ (figure 6.5e). Line plots in figure 6.5 (a-e) indicate the interelectrode gap.

6.4.1.1 Frequency Comparison

By comparing results in figure 6.5 (a-e) with the results in figure 4.19 (a-e), it is observed that velocity trends remain the same in numerical and experimental results with few exceptions. In both cases, optimised frequency remained $1kHz$ for most of the interelectrode gaps except for $20\mu m$ and $50\mu m$ interelectrode gaps where the optimised frequency is $800Hz$. Also, $75\mu m$ interelectrode gap moved to $1.5kHz$

from $1kHz$ at $3mS/m$ and $14mS/m$. On the other hand, the same conductivities, $100\mu m$ interelectrode gap shifted to $1kHz$ from $800Hz$ and $1.5kHz$ from $1kHz$. Finally, $150\mu m$ shows a frequency shift of $1.5kHz$ from $1kHz$, and $1kHz$ from $1.25kHz$ at fluid conductivity of $3mS/m$ and $10mS/m$, respectively.

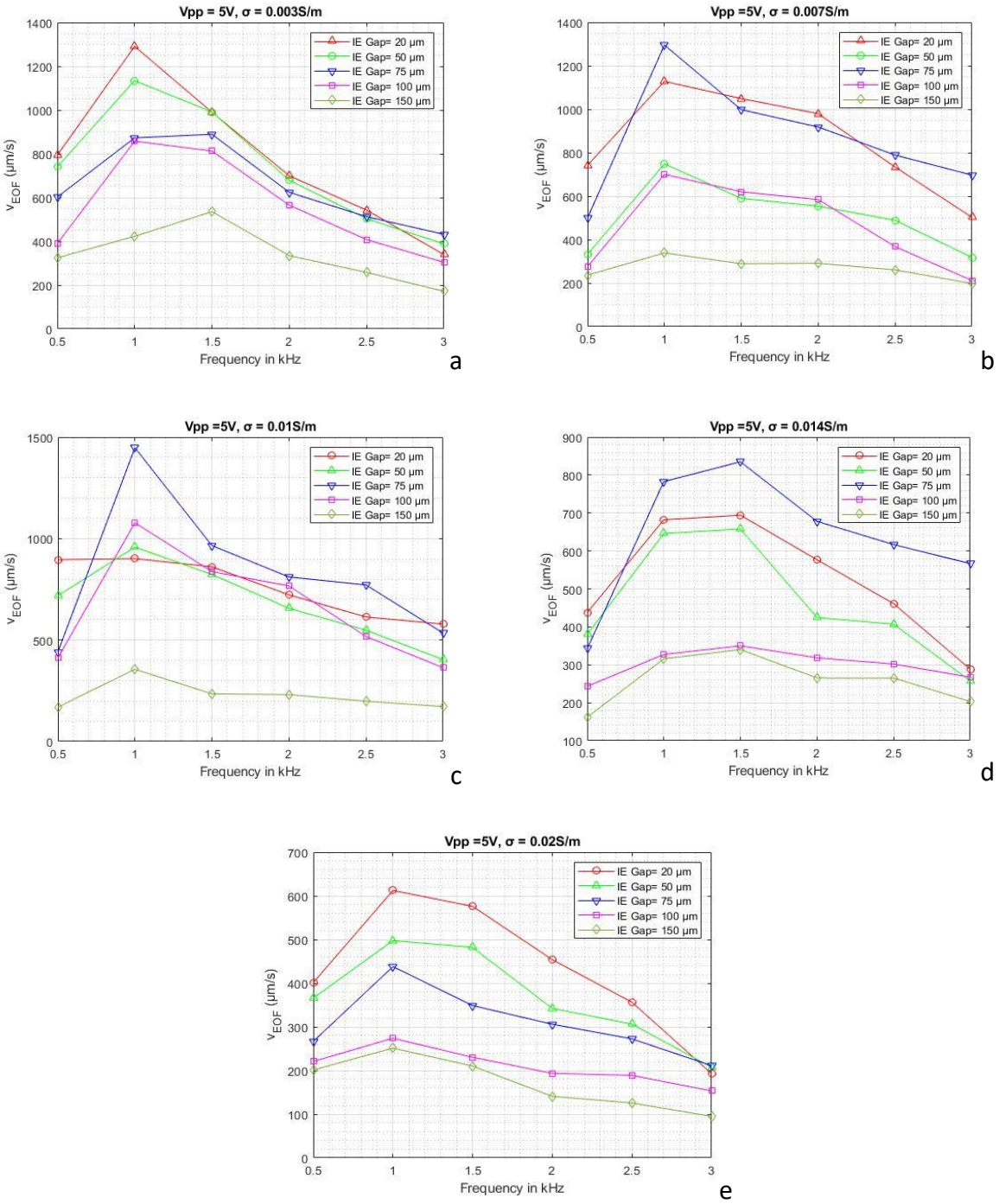

Figure 6.5: v_{EOF} measured for $20\mu m$ to $150\mu m$ interelectrode gap as a function of frequency, for the fluid conductivity of (a) $3mS/m$, (b) $7mS/m$, (c)$10mS/m$, (d)$14mS/m$ and (e) $20mS/m$.

6.4.1.2 Fluid Conductivity Comparison

Comparison of numerical and experimental velocity plots as a function of the interelectrode gap shows good agreement in terms of trends. However, there is an apparent mismatch between the velocity measurements. Furthermore, there are various anomalies. In Numerical results, maximum velocity occurs at 1.5kHz compared to 1kHz for 14mS/m, as shown in figure 6.6. All other velocities follow the same trend and optimum velocities matches except for $7mS/m$ where $50\mu m$ produces a stronger velocity response compared to $100\mu m$.

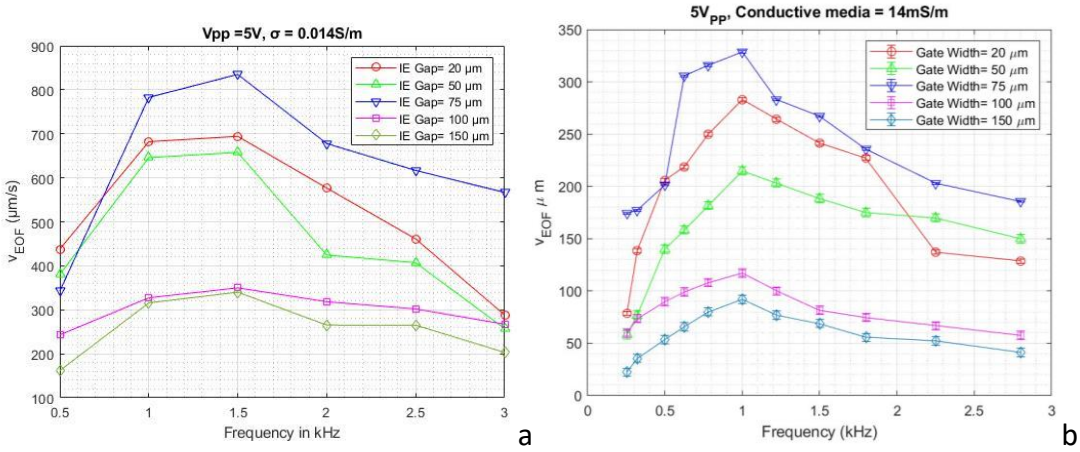

Figure 6.6: Velocity comparison (a) Numerical (b) Experimental results.

Furthermore, (figure 6.7) shows good agreement, with only one difference observed at $100\mu m$ interelectrode gap for fluid conductivity of $7mS/m$ where there is a dip observed in the velocity. Otherwise, velocity increases for the interelectrode gaps of $20\mu m$ to $100\mu m$ from $3mS/m$ to $10mS/m$ and decreases after this. Moreover, $150\mu m$ interelectrode gap velocity decreases from $3mS/m$ to $20mS/m$ with a slight fluctuation from $7mS/m$ to $10mS/m$.

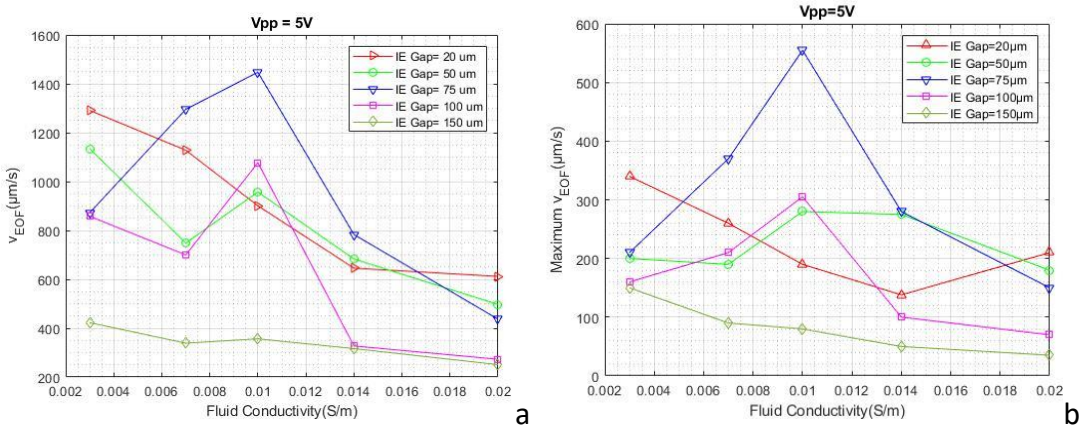

Figure 6.7: Maximum v_{EOF} measured for $20\mu m$ to $150\mu m$ interelectrode gap as a function of fluid conductivity (a) Numerical (b) Experimental.

6.4.1.3 Velocity Magnitude Comparisons

The highest velocity magnitude during both numerical and experimental investigation took place for $75\mu m$ interelectrode gap and $100\mu m$ for $10mS/m$ fluid conductivity. Working below $10mS/m$ is not acceptable because cell death during experiments releases salts in the fluid, increasing its conductivity percentage causing errors. However, at $5V_{PP}$ maximum experimental v_{EOF} is $555\mu m/s$ compared to numerical value $1450\mu m/s$. It shows that numerical fluid velocities have higher magnitudes than the experimental values. It is due to the limitations and assumptions discussed in chapters 2 and 3.

A comparison of maximum velocity occurring at different interelectrode gaps for the $10mS/m$ fluid conductivity is shown in figure 6.8. Velocity comparison is made at $10mS/m$ because it is optimised already during Chapter 4.

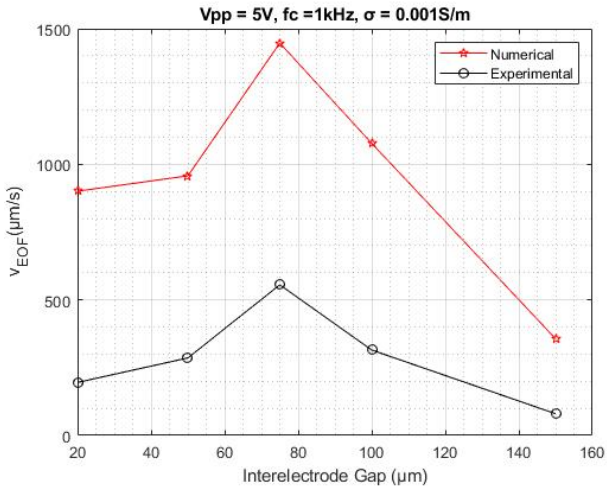

a

Figure 6.8: Numerical v_{EOF} (red plot line) vs experimental v_{EOF} (black plot line) at $75\mu m$ interelectrode gap and $10mS/m$ fluid conductivity.

Velocity is measured from the electrode edge in figure 6.7. Moreover, for numerical values $\Lambda = 1$. However, as suggested by the Green model, if Λ=0.25 correction factor to match results is used, results do not match, as shown in table 6.3.

Table 6.3: Correction factor Calculation between numerical and experimental results.

Interelectrode Gap (μm)	**Numerical v_{EOF} ($\mu m/s$)**	**Experimental v_{EOF} ($\mu m/s$)**	**Λ (2dp)**
20	900	195	0.22
50	957	285	0.30
75	1447	555	0.38
100	1077	315	0.30
150	356	80	0.22

Therefore, it is observed that the correction factor varies for different variables. It explains why studies using a Λ = 0.25 [197, 199, 201, 202, 203] as a correction factor cannot match results.

6.4.2 Velocity and particle displacement vs Chamber Height

It is established in chapter 4 that v_{EOF} is not influenced by chamber height. To confirm this, the fluid velocity is numerically studied as a chamber height function, calculated from $100\mu m$ – $1000\mu m$ at a step-size of $100\mu m$. Line plots from figure

6.8 show that changing chamber height from $100\mu m$ – $1000\mu m$ does not affect the fluid velocity; results are comparable to experimental work, as shown in figures 4.38 and 4.39. Moreover, particle displacement is directly proportional to the chamber height, as observed in figure 6.9 (a-f), while chamber height does not influence velocity.

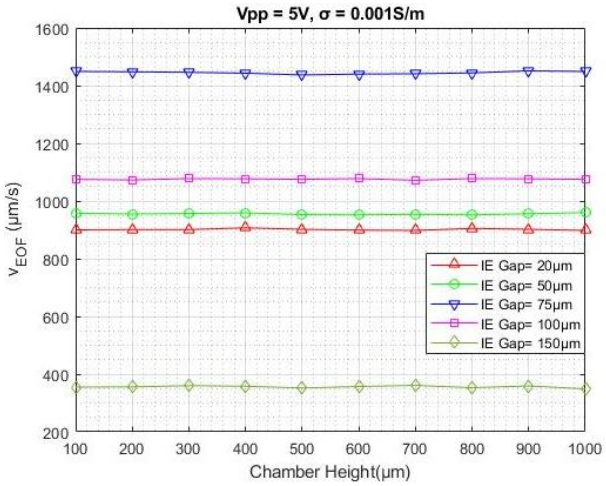

Figure 6.9: Maximum v_{EOF} measured for $20\mu m$ to $150\mu m$ interelectrode gap as a function of chamber height.

Figure 6.9 (a-f) depicts that for $20\mu m$ interelectrode gap, $10mS/m$ fluid conductivity, and $5V_{PP}$, $1kHz$ velocity remains constant as chamber height changes from $100\mu m$ to $600\mu m$. Results confirm experimental results that at $100\mu m$ chamber height, the particle displacement is diminished with the chamber height, and it increases as the chamber height increases. However, velocity in all cases remained the same $1200\mu m/s$.

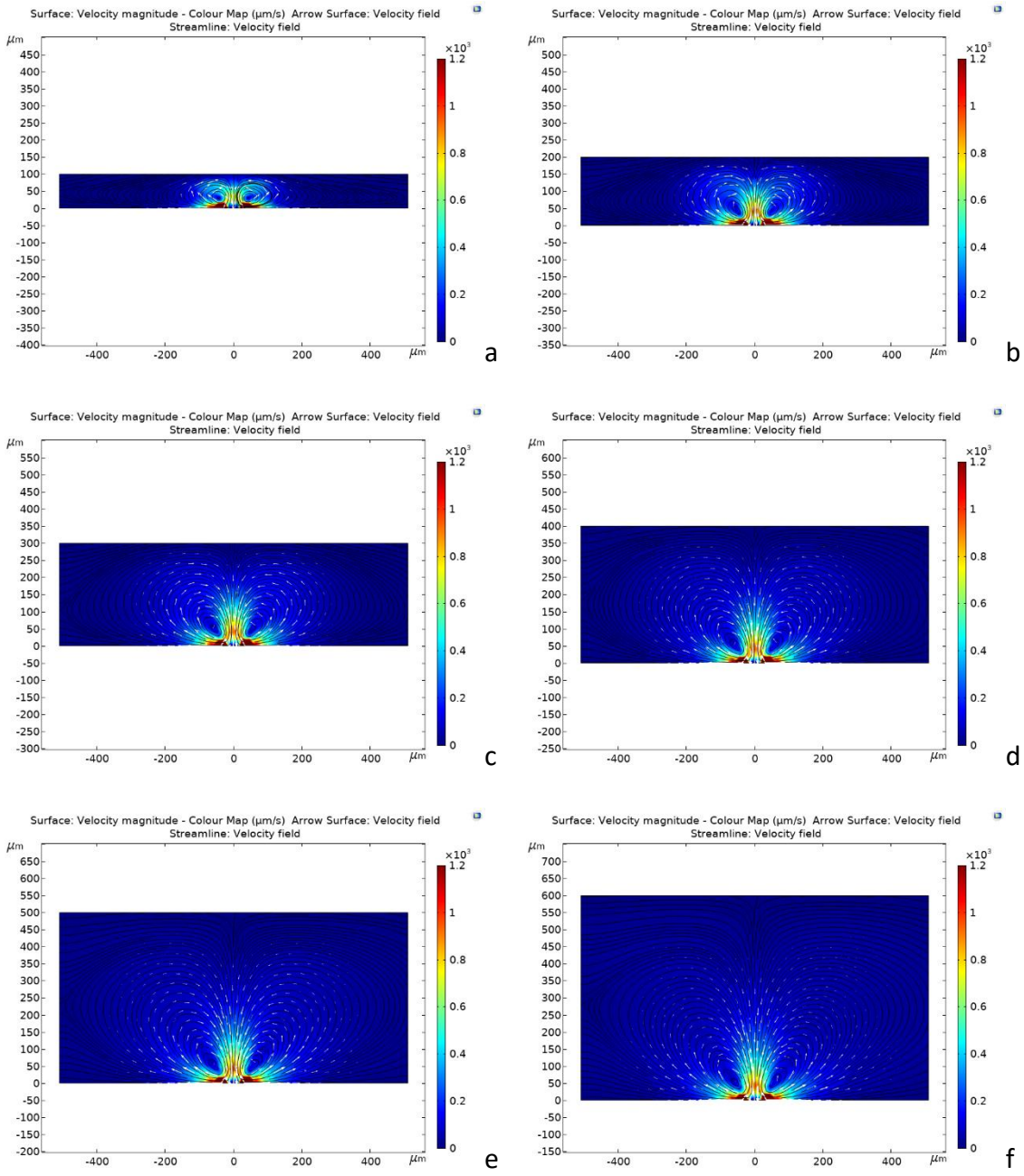

Figure 6.10: Vortex height for chamber height (a) $100\mu m$, (b) $200\mu m$, and (c) $300\mu m$, (d) $400\mu m$, (e) $500\mu m$, and (f) $600\mu m$.

These results are also an improvement on the work of Mohtar [278] on the chamber height effect on ACEOF velocity. In [278], despite streamlines being produced, there were artefacts present, creating a greater degree of mismatch between results. One improvement in this model is that the mathematical model contains modified mathematical equations, as discussed in chapter 3.

Measuring particle displacement from $2D$ plots is cumbersome. However, point in y-axis where v_{EOF} becomes minimum ($< 1\%$ of maximum velocity generated) is classified as maximum vortex height. This technique was adopted due to 2 reasons:

i. During experimental work, fluid velocity becomes negligible when maximum vortex height is achieved.

ii. In numerical simulations, no vortex is formed at the middle of the interelectrode gap, and velocity at that point reaches its minimum value, which is very close to $< 1\%$ of the maximum velocity.

To determine the effect of velocity on particle displacement, results are calculated at various interelectrode gaps. At $5V_{PP}, 1kHz, 10mS/m$. Chamber height is set at $1600\mu m$ to avoid diminishing the particle displacement due to the chamber lid.

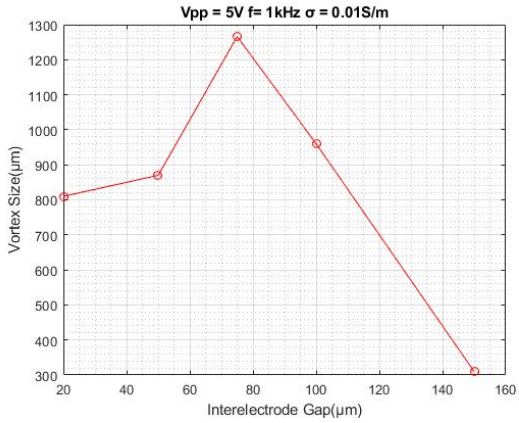

Figure 6.11: Particle displacement (μm) as a function of interelectrode gap at $5V_{PP}, 1kHz$ and fluid conductivity of $10mS/m$.

Results (figure 6.11) conclude that higher velocity produces the larger particle displacement and corresponds with the experimental result. The most significant particle displacement of $1356\mu m$ is produced numerically compared to the experimental value of $412\mu m$. Introducing a vortex correction factor (Λ_V) can make experimental and numerical vortex equal. Λ_V is the ratio between experimental results and numerical results. Table 6.4 lists down the vortex correction factor.

Table 6.4: Vortex Correction Factor.

Interelectrode Gap (μm)	Numerical Particle displacement (μm)	Experimental Particle displacement (μm)	Λ_V (2dp)
20	810	150	0.19
50	870	220	0.25
75	1356	412	0.30
100	980	280	0.28
150	330	70	0.21

6.4.3 Velocity vs AC signal

Applied AC signal significantly influences fluid velocity, as seen in figure 6.11. v_{EOF} is studied as a voltage function. Fluid velocity is studied at $5V_{PP}$, $7.5V_{PP}$, and $10V_{PP}$, $1kHz$ for all interelectrode gaps at for the fluid conductivity of $10mS/m$. Results show that the numerical analysis trend (figure 6.11) agrees with the experiment results. However, numerical and experimental magnitudes do not match. For example, with the voltage change from $5V_{PP}$ to $10V_{PP}$, a $\sim 45\%$ increase in voltage magnitude is observed in experimental results compared to a drastic 360% increase in numerical value. It is due to the assumptions discussed in chapters 2 and 3. Comparing the numerical value of $6660\mu m/s$ at $10V_{PP}, 1kHz$ for $75\mu m$ interelectrode gap, for $10mS/m$ conductance, to the experimental value of $800\mu m/s$ shows that the correction factor of $\Lambda = 0.12$ (2dp) is required to match results. Changing voltage from $5V_{PP}$ to $7.5V_{PP}$ increase fluid velocity by a maximum of 100.6%.

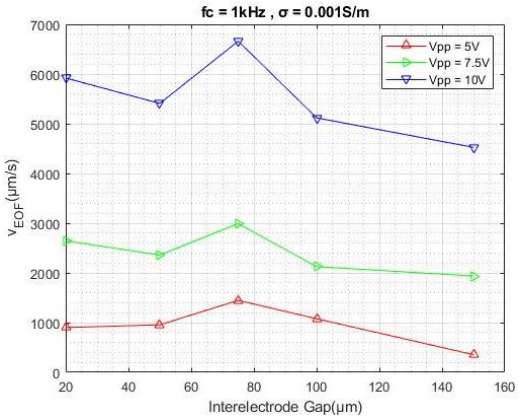

Figure 6.12: Maximum $v_{EOF}(\mu m/s)$ measured as a function of interelectrode gap, measured at $5V_{PP}$ (red plot line), $7.5V_{PP}$ (green plot line), and $10V_{PP}$ (blue plot line).

6.4.4 Fluid velocity as a function of distance from the electrode

Figure 6.13 illustrates the fluid velocity results as fluid moves away from the electrode. Results from figure 6.13a conclude a velocity drop of $72\%, 84\%, 86\%, 67\%,$ and 89% for the interelectrode gap of $20\mu m, 50\mu m, 75\mu m, 100\mu m,$ and $150\mu m$. Results are in good coherence with experimental results. However, a slightly higher percentage of velocity decrease was reported in the numerical study than experimental results. Furthermore, experimental velocity is approximately ten times less than numerical results, as seen in figure 6.13b.

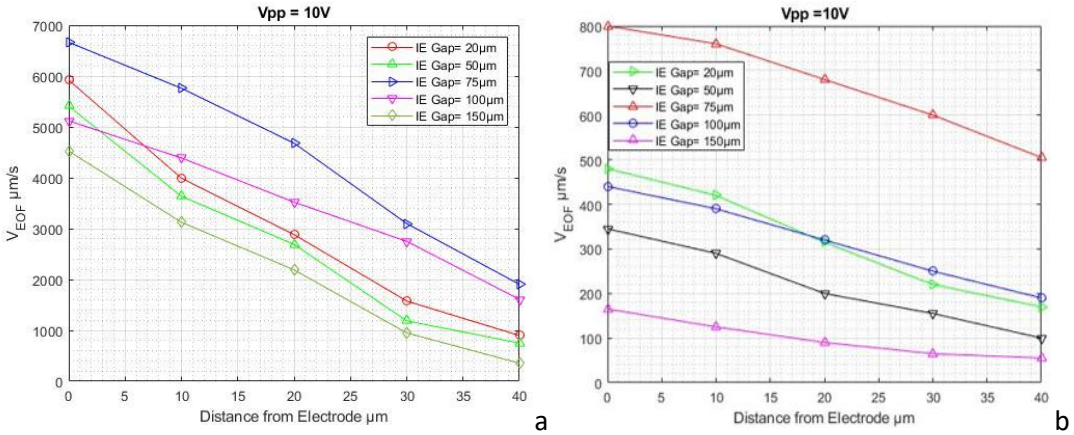

Figure 6.13: v_{EOF} $(\mu m/s)$ as measured from the distance from the electrode for the interelectrode gap of $20\mu m$ – $150\mu m$ (a) Numerical (b) Experimental

6.4.5 Velocity vs Electrode Width

In this section, velocity is measured as a function of electrode width for $75\mu m\ and\ 100\mu m$ interelectrode gap. Electrode width is a crucial factor in multielectrode geometry, as discussed in chapter 5, where it is explained that shorter electrode width is required to push cells over the electrode. If the electrode is wide enough, particles settle on top of the electrode, and therefore vortex does not push cells. Numerical analysis is performed for $1kHz$ at $10mS/m$ fluid conductivity for the electrode width from $50\mu m$ to $500\mu m$ with $50\mu m$ step-size. Results are concluded for $5V_{PP}$ (figure 6.13a) and $10V_{PP}$ (figure 6.13b).

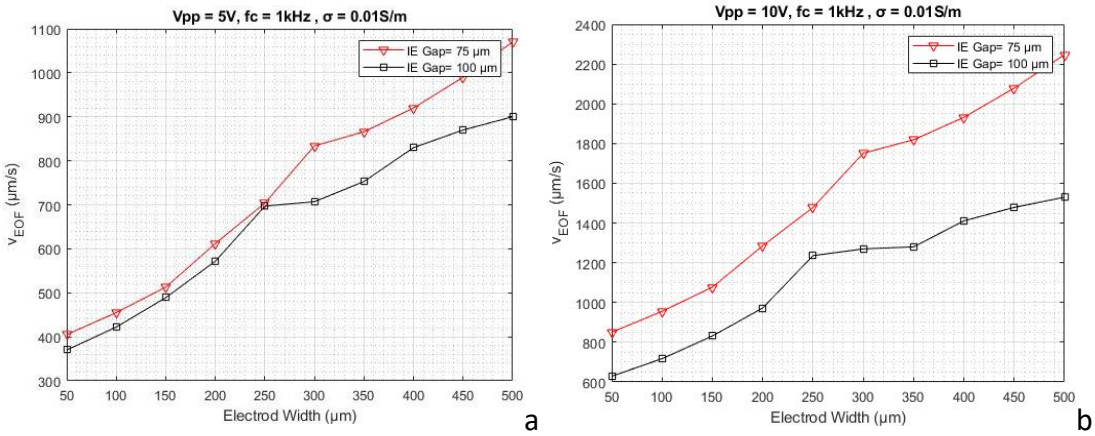

Figure 6.14: v_{EOF} $(\mu m/s)$ as a measure of electrode width at frequency 1kHz, fluid conductivity $10mS/m$, and interelectrode gap of $75\mu m$ (red plot line) and $100\mu m$ (black plot line) for V_{PP} (a) $5V$ and (b) $10V$.

Results show that $75\mu m$ interelectrode gap generates higher v_{EOF} compared to $100\mu m$ interelectrode gap for both $5V_{PP}$, and $10V_{PP}$. Moreover, velocity in $10V_{PP}$ is almost double than $5V_{PP}$ for all interelectrode gap. It is because the electric field generated by $10V_{PP}$ is double compared to the electric field generated by $5V_{PP}$.

In general, velocity for $75\mu m$ interelectrode gap is higher for both $5V_{PP}$ and $10V_{PP}$ and velocity increases as electrode width increases. It is because velocity depends on the electric field, which increases for higher AC signal, smaller interelectrode gap, and

wider electrodes. However, in $5V_{PP}$ velocities ranges are close to each other and almost match at $250\mu m$ electrode width, after which the gap between velocity range increases. On the other hand, for $10V_{PP}$ there is an evident gap that increases further after $250\mu m$ electrode width.

The highest velocity of $850\mu m/s$ and $620\mu m/s$ are recorded at $10V_{PP}$ for the interelectrode gap of $75\mu m$ and $100\mu m$, respectively. This velocity increases to $2240\mu m/s$ and $1370\mu m/s$ as electrode width reaches $500\mu m$ width. the fluid velocity is higher between $300\mu m$ up to $700\mu m$ electrode width where velocities match, after which v_{EOF} at $100\mu m$ interelectrode gap again starts to take over.

6.4.6 ACEOF Conclusion

1- Results from the numerical model correlate with the experimental results obtained in Chapter4 and 5. However, there is a slight difference in velocity magnitudes and particle displacement. It is due to the assumptions discussed in chapter 2 and the use of 2D geometry. Another possible reason is the presence of frictional forces between fluid and test particles during experiments, which is not the case in numerical analysis. Moreover, the maximum speed takes place in quite a thin layer of zeta potential, which is difficult to measure experimentally. However, in this chapter, results are matched by using the correction factor missing in the previous studies.

2- Moreover, in all previous studies, voltage analysis is not matched. For example, in the Green model, 2V is used in the experiment compared to 0.1V during numerical analysis. In contrast, numerical results are obtained at the same variables as the experimental work performed in this chapter.

3- Correspond with experimental results, maximum fluid velocity and particle displacement is achieved for the interelectrode gap of $75\mu m$ at $10V_{PP}, 1kHz$ while 100um interelectrode gap produces the next maximum fluid velocity and particle displacement. Moreover, a higher AC signal generates a larger velocity. Particle displacement is proportional to the chamber height.

4- Correction factor Λ and vortex correction factor Λ_V helps to match experimental and numerical results, and for each case, correction factors are different. Nevertheless, it stays very close to the 0.25 correction factor proposed by Green [197].

5- Higher frequency and conductivities correspond to the minimal to zero ACEOF response. Above and below optimised frequency velocity tends to zero.

6- $100\mu m$ interelectrode gap produces higher velocities at a smaller electrode width compared to $75\mu m$ interelectrode gap.

7- v_{EOF} is highest at the electrode edge and tends to zero as it is calculated away from the electrode edge.

8- An advantage of using the model discussed in this chapter is that it is performed for variables discussed in table 6.1, which is not found in previous studies. This model allowed EDL to form using the formula, whereas, in previous studies, EDL is always dealt with an assumed value between $(10nm - 100nm)$.

Based on the results summarised above, it is concluded that for ACEOF, $100\mu m$ interelectrode gap with $50\mu m$ width is used for the multielectrode geometry stage. AC signal of $10V_{PP}, 1kHz$ and $10mS/m$ fluid conductivity are the other parameters. These are the same parameters that are summarised in Chapter 4 for which optimum

particle displacement and v_{EOF} occurred. Using these parameters, a concentration factor of $100\ thousand$ is achieved during chapter 5.

6.5 Dielectrophoresis

6.5.1 Methodology

In this section, dielectrophoresis is studied as a function of the AC signal, frequency, and chamber height for a pair of electrodes. The experimental work and numerical study's critical difference is that yeast cells have no linear motion during experiments, and particles were already suspended in the chamber. However, particles move in the chamber with a translation motion in the numerical model. Numerical analysis is performed for the interelectrode gaps of $75\mu m$ and $100\mu m$ for the fluid conductivity of$10mS/m$. Apart from electric currents and creeping flow, particle tracking for fluid flow is also added to support the DEP system, as shown in figure 6.33. Particles' inlet speed is set during the creeping flow, while the particle tracing module supports particle physics. Inlet 2 is disabled during single-cell manipulation while it is enabled for cell separation.

Electric current, creeping flow, and particle tracing for fluid flow modules are used for the DEP physics model. The same mesh is used for the electroosmosis study. Finally, the stationary and frequency domain is used for study 1, while the time-dependent study is used for non-dielectrophoretic and dielectrophoretic studies. Material settings are set similar to the ACEOF model.

Electrodes are initialised with the AC signal during the electric currents module, while all other boundaries are set as insulators. Only inlet and outlet are set as boundary conditions during creeping flow, while all other boundaries are set as a wall. Apart from the outlet, all other boundaries are set as a wall condition during the particle

tracing fluid flow module. Drag force and dielectrophoresis force is applied to the fluid so that particle experience DEP when applied. Firstly particles were allowed to move through the chamber under no dielectrophoretic condition. Therefore, no particle was trapped. Instead, particles pass through the chamber without any deviation, as shown in figure 6.14. Hair-like projections are used in the plots to track the particle trajectory. The colour bar shows the particle velocity, which is measured in $\mu m/s$.

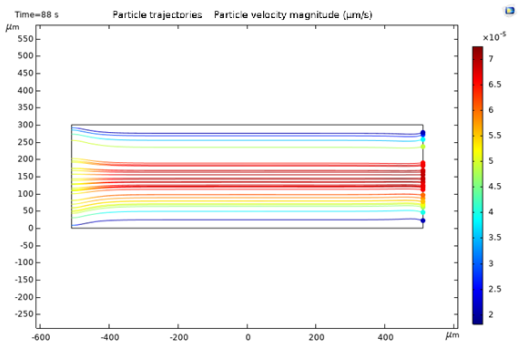

Figure 6.15: Simulation plot under no DEP condition.

The boundary condition for AC pDEP is given in figure 6.15.

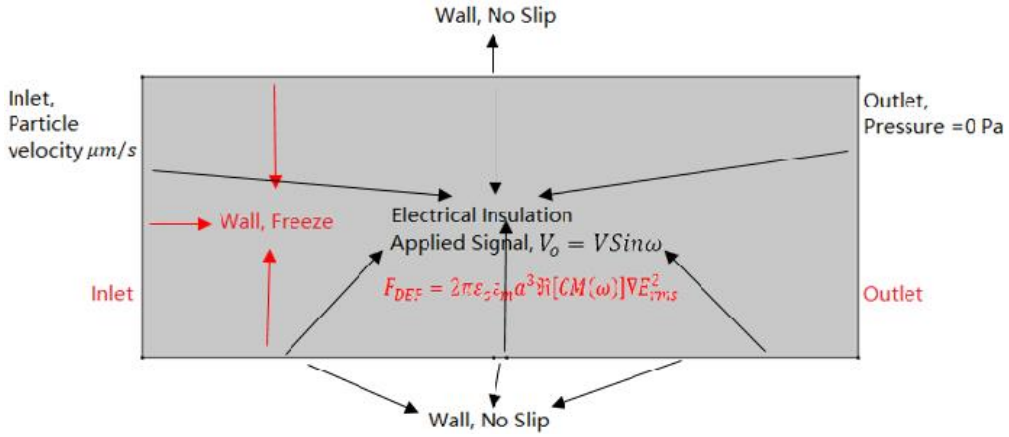

Figure 6.16:Dielectrophoretic boundary conditions.

However, as soon as the dielectrophoretic force is applied, particles get trapped on the electrode edge due to AC pDEP, as shown in figure 6.17a $(6.8s)$, 6.17b $(7s)$, and 6.17c $(8s)$.

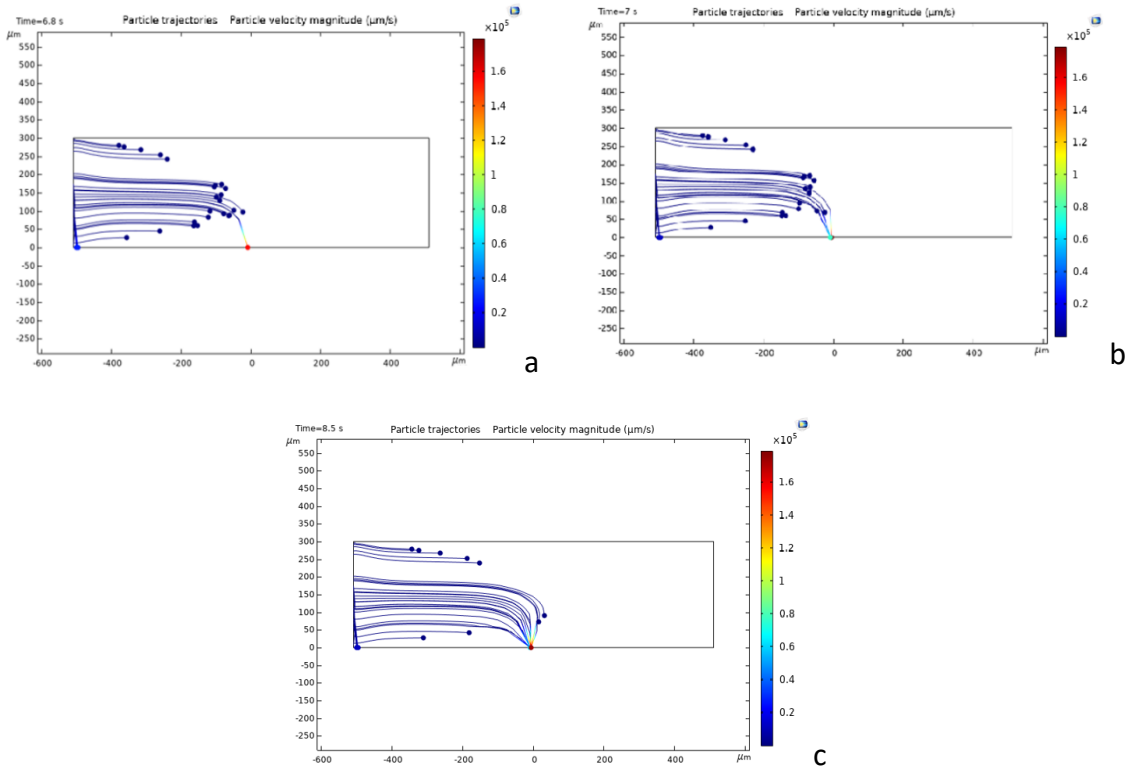

Figure 6.17: Simulation plot under DEP condition recorded at the time (a) 6.8s, (b) 7s, and (c) 8s.

As it can be seen that the first particle got trapped at $6.8s$ from the height of $200\mu m$ while particles above $250\mu m$ remained unaffected. It is because particles above $250\mu m$ are unaffected by the electric field as the electric field is weak at that point. Furthermore, particles have moved towards the electrode edge where a maximum electric field exists, causing the AC pDEP phenomenon.

6.5.2 v_{DEP} vs AC frequency, AC Signal, and Chamber Height

In this section, v_{DEP} is quantified as a function of the AC signal, AC frequency, and chamber height. v_{DEP} varies from the distance from the electrode, and it gets faster as it gets closer to the electrodes. Therefore, for this section, velocity is measured by the total distance moved from chamber height divided by the time it takes to get trapped at the electrode edge. AC signal is measured for $5V_{PP}, 10V_{PP}, 20V_{PP}$ for the AC signal frequency of $10kHz, 100kHz, 1MHz\ and\ 10MHz$. Performing AC

frequency analysis for more than $10MHz$ is irrelevant for this project as experiments are not performed after $10MHz$ either. On the other hand, chamber heights of $100\mu m, 200\mu m, and\ 300\mu m$ are performed. Due to COMSOL processing time constraints, analysis is limited to three-chamber heights only. For AC pDEP modelling $100\mu m$ interelectrode gap and 10mS/m fluid conductivity is chosen as the ACEOF process provides the optimum ACEOF velocity and vortex height at these parameters. During the analysis, all particles are entered into the chamber precisely at the specified chamber height of $100\mu m$, $200\mu m$, and $300\mu m$. Results are shown in figure 6.18 (a-c). In the plots, AC nDEP velocity is illustrated with a negative velocity, while AC pDEP velocity is shown with positive velocity.

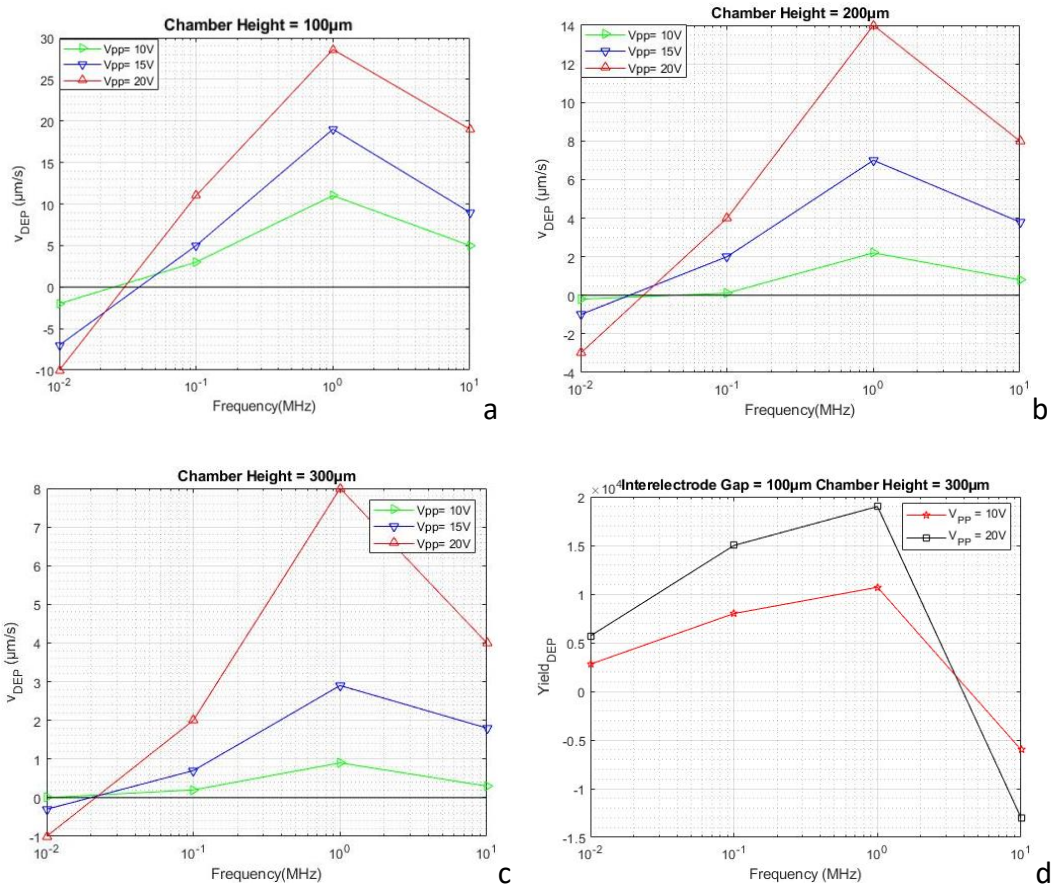

Figure 6.18: Numerical calculation of $v_{DEP}\ (\mu m/s)$ measured for $5V_{PP}$ (red plot line), $10V_{PP}$ (black plot line), and $20V_{PP}$ (blue plot line) for the chamber height of (a) $100\mu m$, (b) $200\mu m$, and (c) $300\mu m$. In the plots negative velocity shows nDEP and positive velocity shows AC pDEP (d) Experimental Results for comparison.

In general, it can be seen from the figure that the strongest AC pDEP occurs at $1MHz$. Moreover, at $10kHz$ nDEP (figure 6.18) took place, while at $100kHz$ and $10MHz$, AC pDEP occurs. It can be seen in figure 6.18 that during nDEP, particles have been pushed away from the electrodes towards the lowest field region.

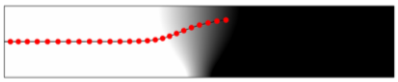

Figure 6.19:Simulation illustrating nDEP effect.

Results show that maximum v_{DEP} of $28.6\mu m/s$ is generated at $20V_{PP}$, $1MHz$, for the chamber height of $100\mu m$ which reduces to $14\mu m/s$ and $8\mu m/s$ for the chamber heights of $200\mu m$ and $300\mu m$ respectively. The results in figure 6.17 with the live yeast cell CM factor produced using MyDEP in figure 6.19 show that the numerical model follows the CM (Clausius Mossatti) factor.

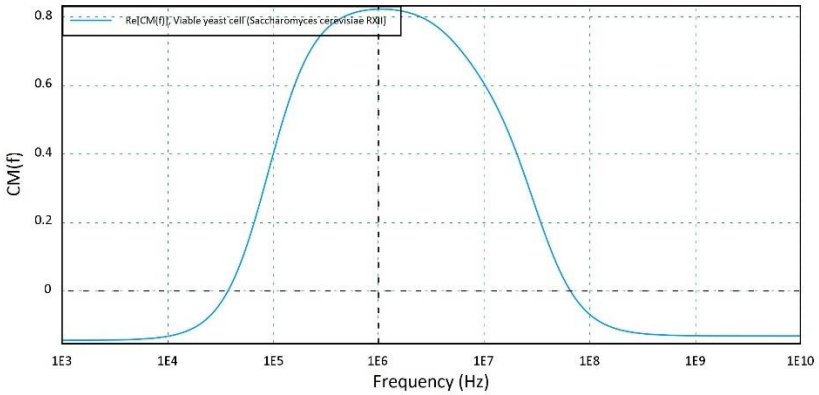

Figure 6.20: Clausius Mossatti factor for live yeast cells [108].

6.5.3 v_{DEP} vs Chamber Height

In this section, v_{DEP} is measured by the distance particle moved from the chamber height to the electrode divided by the time it travels. Comparing results for $20V_{PP}, 1MHz$ between $75\mu m$ and $100\mu m$ interelectrode gap as a function of chamber height depicts a minimal difference between velocities as shown in figure 6.21. Especially at $300\mu m$ chamber height, less than $1.5\mu m/s$ is recorded. Results

show excellent agreement with experimental work where v_{DEP} decreases with the chamber height.

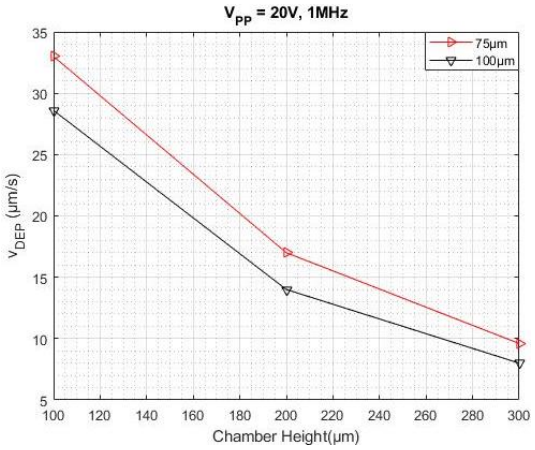

Figure 6.21: Numerical v_{DEP} $(\mu m/s)$ comparison for $75\mu m$ (red line) and $100\mu m$ (black line) interelectrode gaps as a function of chamber height (μm) at $20V_{PP}$, $1MHz$.

6.5.4 AC pDEP vs Time

Numerical analysis is performed for 80 seconds. AC pDEP response is measured as the particle collection percentage every 20 seconds. Results are shown in figure 6.45 for $10V_{PP}$, $1MHz$ and $20V_{PP}, 1MHz$. Particles are allowed to enter the chamber randomly, as shown in figures 6.22a and 6.22b and 6.22c, showing particle trapping using the highest electric field. Results show that $20V_{PP}$ yield a higher percentage than $10V_{PP}$ as shown in figure 6.23 for the chamber height of $300\mu m$. However, more particles were collected initially in experimental results, which plateaued as the experiment progressed. Numerical analysis shows results otherwise where more particles get trapped as time increases. In experimental work, all particles were suspended on top of electrodes, while numerical analysis starts with zero particles and increases over time.

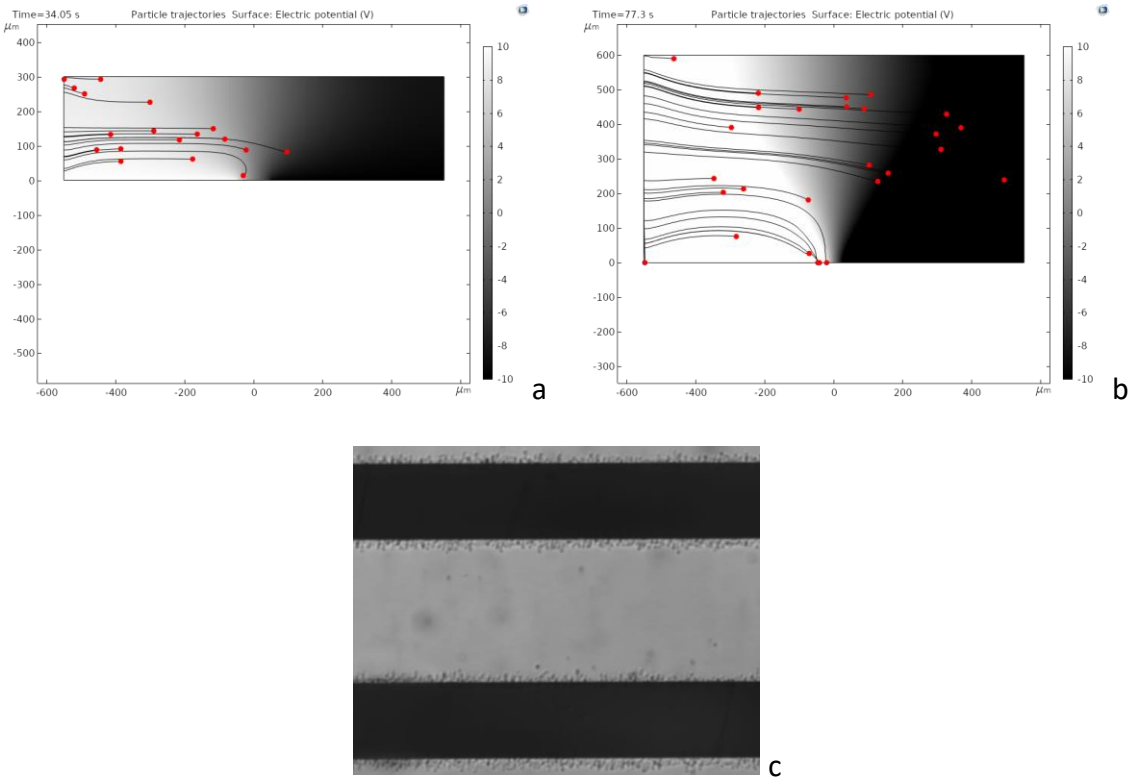

Figure 6.22: Particles entering the chamber at random heights for the chamber height of (a) $300\mu m$, (b) $600\mu m$ (c) cell capture at highest electric field region.

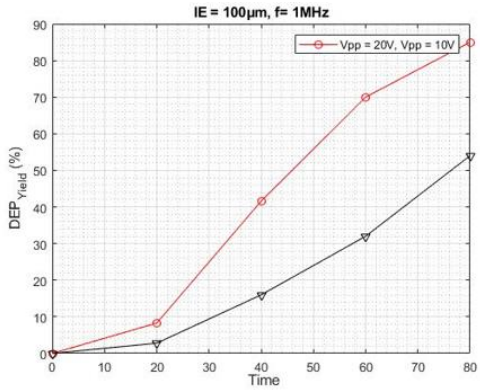

Figure 6.23 AC pDEP percentage yield at $10V_{PP}, 1MHz$ (black plot line) and $20V_{PP}, 1MHz$ (red plot line) for $100\mu m$ interelectrode gap entering at $300\mu m$ chamber height, as a subject of time (s).

6.5.5 AC pDEP v particle suspending point

Numerical analysis for v_{DEP} as a function of particle suspension point at $5\mu m, 25\mu m,$ and $50\mu m$ is shown in figure 6.24. This result is in coherence with experimental results as in both numerical analysis and experimental analysis, v_{DEP} near the electrode is higher than the point suspended further away. As the particle gets near the electrode edge, the electric field effect on the particles increases,

pulling the particle with greater force towards itself. However, the magnitude of numerical velocity is higher than the experimental velocity.

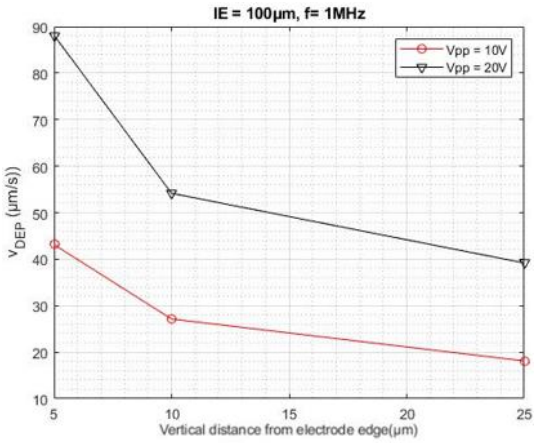

Figure 6.24: v_{DEP} measured at $10V_{PP}, 1MHz$ (black plot line) and $20V_{PP}, 1MHz$ (red plot line) as a function of particle's vertical distance (point of suspension) from the edge of the electrode.

6.5.6 Cell separation

Cell separation is not performed during experiments. However, it is demonstrated using numerical analysis to show the capacity of the designed device. Live and dead yeast cells are modelled, as discussed in chapter 2. The analysis is performed at $20V_{PP}, 1MHz$ for the fluid conductivity of $10mS/m$. Results confirm that at $1MHz$, live yeast cells (red) are separated from dead yeast cells (blue) and trapped at the electrode edge. On the other hand, dead yeast is removed from the chamber from the outlet. Figure 6.25a depicts that separation starts at 16.35s, and figure 6.25b shows that separation is completed at 19.75s.

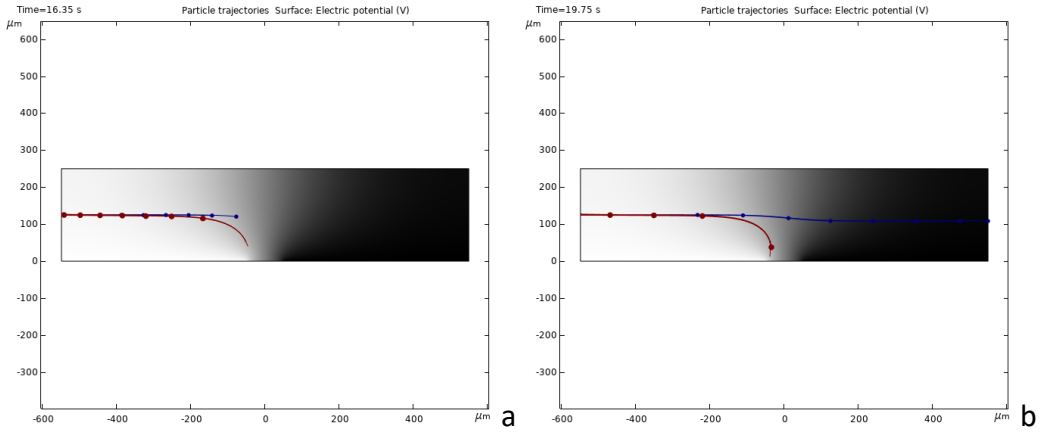

Figure 6.25: Dielectrophoretic based separation of live yeast cells from dead yeast cells (a) Separation begins at 16.35s (b) separation is completed at 19.75s.

This analysis provides designed device utilisation as a cell separator based on the cell's electrical properties.

6.5.7 DEP Conclusion

1- In both experimental and numerical results v_{DEP} increases with an increase in the AC signal, narrowing the interelectrode gap and decreasing chamber height. It is because higher AC signal, narrow interelectrode gap, and smaller chamber height apply higher electric field on the particles hence trapping particles faster. Moreover, in experimental and numerical results, $10kHz$ responds to nDEP while $100kHz, 1MHz$, and $10MHz$ produce AC pDEP. Moreover, in the numerical analysis, it is observed that as particles get closer to the electrode, then the particle v_{DEP} increases which are also observed during experimental results. Therefore, it is concluded that based on these results, numerical results are in excellent agreement with experimental results, where not only results in trends are matching, but also the magnitudes of velocity are identical.

2- $20V_{PP}, 1MHz$ provides with the highest v_{DEP} of $28.6\mu m/s$ at $100\mu m$ chamber height. Velocity decreases to $8\mu m/s$ at $300\mu m$ chamber height.

However, velocity increases as the particle come closer to the electrode. For instance, v_{DEP} of $90\mu m/s$ occurs when particles are at $5\mu m$ from the electrode edge. Moreover, $75\mu m$ and $100\mu m$ interelectrode gap produce almost the same v_{DEP} with only $1.5\mu m/s$ difference.

3- Higher AC pDEP trapping efficiency occurs as the processing time increases, which is another difference from the experimental results. It occurs because, during the experiments, particles were already present in the chamber and therefore got captured when electrodes are energised, which leaves fewer particles behind, and therefore DEP yield decreases with time. On the other hand, there is no particle present in the numerical analysis, and particles only get captured as particles move in the chamber; therefore, the yield is smaller in the beginning, but increases as more particles enter the chamber.

4- Numerical analysis confirms that live yeast cells separated from dead yeast cells based on their electrical properties at 1MHz.

5- The numerical analysis shows that particles suspended further away from the electrodes are not captured but are pulled down (figure 6.26) under the electric field's influence. For example, particles at $100\mu m$ height are moved down to $50\mu m$. It shows that using multielectrode can significantly improve DEP yield and processing time.

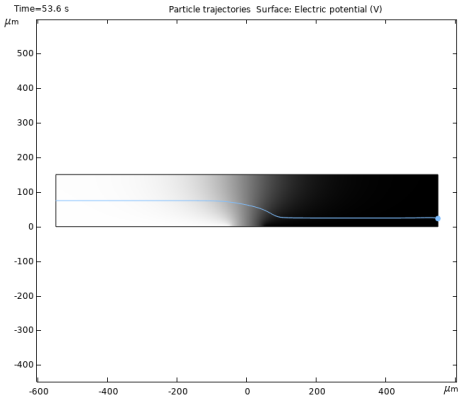

Figure 6.26: Particle pulled down under the influence of AC pDEP.

6.6 Multi-electrode Model

It is already established from sections 6.4 and 6.5 that using multielectrode instead of a pair of electrodes can offer an overall efficiency and faster processing time. Therefore, ten $100\mu m$ wide Au coplanar electrodes with $100\mu m$ interelectrode gap are designed on the glass substrate to investigate DEP and ACEOF response. $20V_{PP}, 1MHz$ AC signal is used for DEP analysis while $10V_{PP}, 1kHz$ is used to study ACEOF response. $10mS/m$ fluid conductivity and chamber height of $300\mu m$ is are used to study both responses. Electrodes Geometry is shown in figure 6.27, where E stands for electrodes.

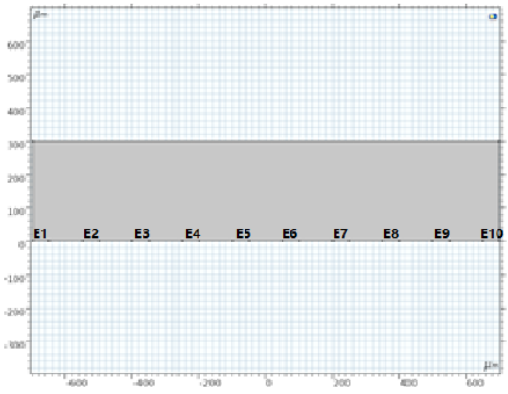

Figure 6.27: 2D model of Ten $50\mu m$ wide electrodes with $100\mu m$ interelectrode gap.

6.6.1 Multi-electrode Dielectrophoresis

In this section, AC pDEP response is analysed by calculating the percentage of cells captured as a function of the cell's linear speed. Initially, one cell is released per

second from the height of $300\mu m$, and analysis is conducted for $120 seconds$. $20V_{PP}, 1MHz$ is applied to the electrodes to generate the electric field (V/m). The electric field is shown in figure 6.28.

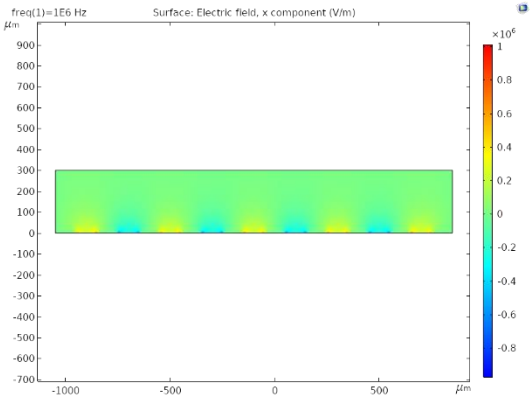

Figure 6.28: Electric field plot for ten electrodes geometry.

6.6.1.1 Linear speed vs the number of electrodes

6.6.1.1.1 *Fixed entry of cells*

This section analyses linear speed to estimate the rate at which cells are captured at the particular electrode. The analysis with 11 cells for the linear speed of $10\mu m/s$ – $40\mu m/s$ at the step size of $5\mu m/s$. All cells are released at the height of $300\mu m$.

Simulation results for the linear speeds of $10\mu m/s, 35\mu m/s$ and $40\mu m/s$ are shown in figures 6.29a, 6.29b, and 6.29c, respectively. It is observed from figure 6.29a that all the particles entering at $10\mu m/s$ are captured at the 1st electrode. In comparison, figure 6.29b shows that at $35\mu m/s$ all cells are captured at the 10th electrode. Furthermore, at $40\mu m/s$, cells are pulled down; however, they are not captured by the electrodes, as seen in figure 6.29c.

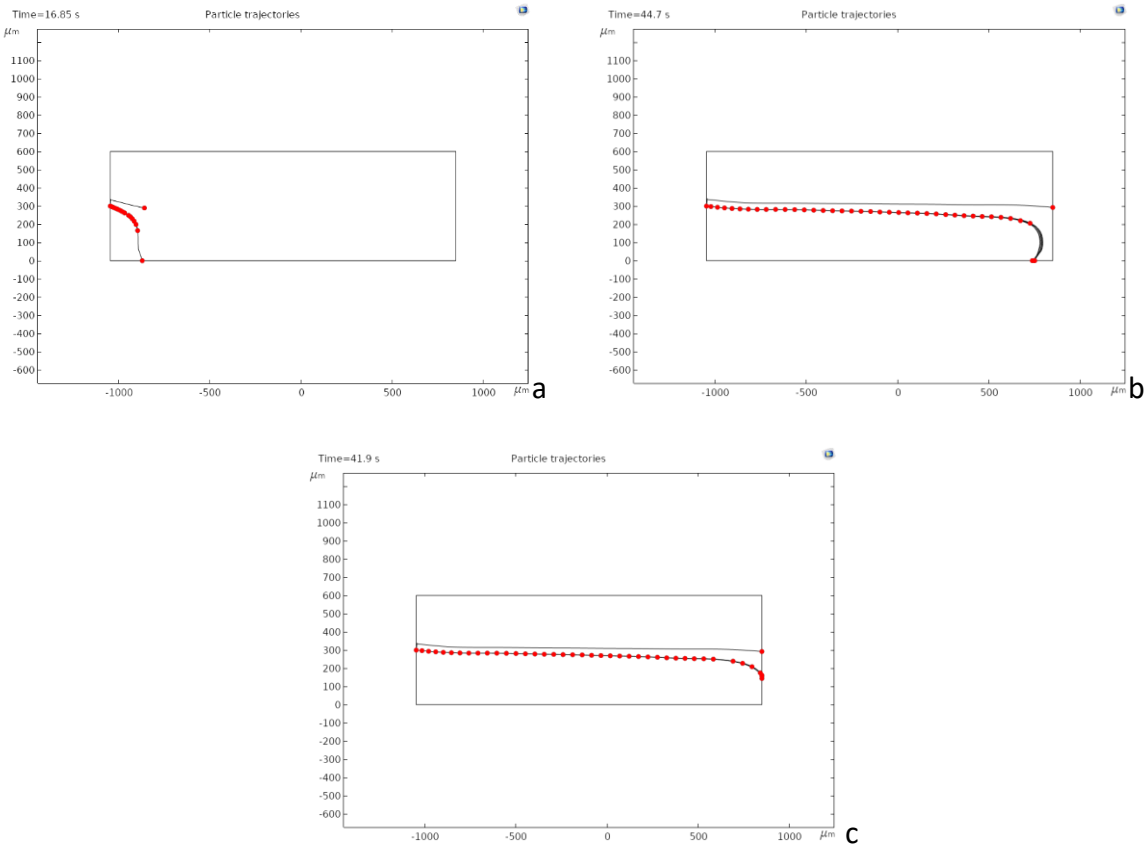

Figure 6.29: Numerical simulation of yeast cell trapping under the influence of $20V_{PP}$, $1MHz$ AC pDEP at linear speed (a) $10\mu m/s$, (b) $35\mu m/s$, and (c) $40\mu m/s$.

In general, lower linear speed provides higher cell yield on initial electrodes. For instance, at $10\mu m/s$ all 11 cells are captured at the first electrode edge, while at $35\mu m/s$ these cells are captured at the tenth electrode edge. Figure 6.30 illustrates the cell linear speed corresponding to the number of electrodes. It is evident from figure 6.29 that as cell linear speed increases, the electrode required to capture cells also increases. At $40\mu m/s$, cells are not trapped by any of the first ten electrodes. Therefore, based on the cell capturing trend discussed in figure 6.30, it is safe to argue that higher linear speed can be utilised using more than ten electrodes.

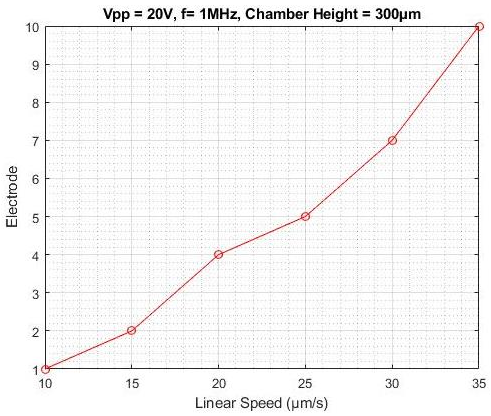

Figure 6.30: Particle trapping as a function of the given linear speed on the electrode number when all particles enter from the fixed height.

6.6.1.1.2 ***Random Entry of Cells***

In this section, the discussion is focused on the results of cell capture as a function of linear cell speed using AC pDEP when cells are allowed to enter the chamber from random heights. This analysis is essential because, in the experiments, cells move in the chamber at different heights. Eleven cells are used to observe cell tracking at the linear speed of $35\mu m/s, 39\mu m/s$, and $40\mu m/s$. 11 cells are used to observe the trend, and later simulations are repeated for 750 cells. Figure 6.31 shows no DEP condition when all particles are allowed to move freely in the chamber.

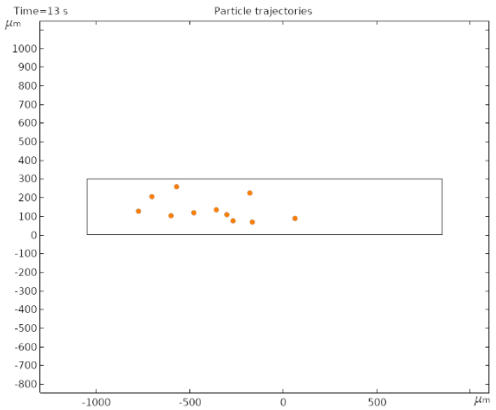

Figure 6.31: Numerical simulation of particles randomly passing through the chamber under no DEP condition.

It is observed that all 11 cells are captured at $35\mu m/s$ (Figure 6.32a) with the first nine electrodes, while at $40\mu m/s$ (Figure 6.32b), 10 out of 11 cells are trapped while the last cell is pulled down by $200\mu m$ but is not trapped. Therefore, it shows that

these cells can be trapped if more electrodes are used. However, as during experiments, only ten electrodes are used; therefore, the linear speed is decreased to $39\mu m/s$. The analysis is repeated for 11 cells at $39\mu m/s$ (Figure 6.32c). Results show that all 11 cells are captured on the electrode edge, with the 11^{th} cell getting captured at the 10^{th} electrode edge. It is also observed from the simulation that using $39\mu m/s$ linear speed also helps to capture cells $1.35seconds$ faster compared to $35\mu m/s$ linear speed.

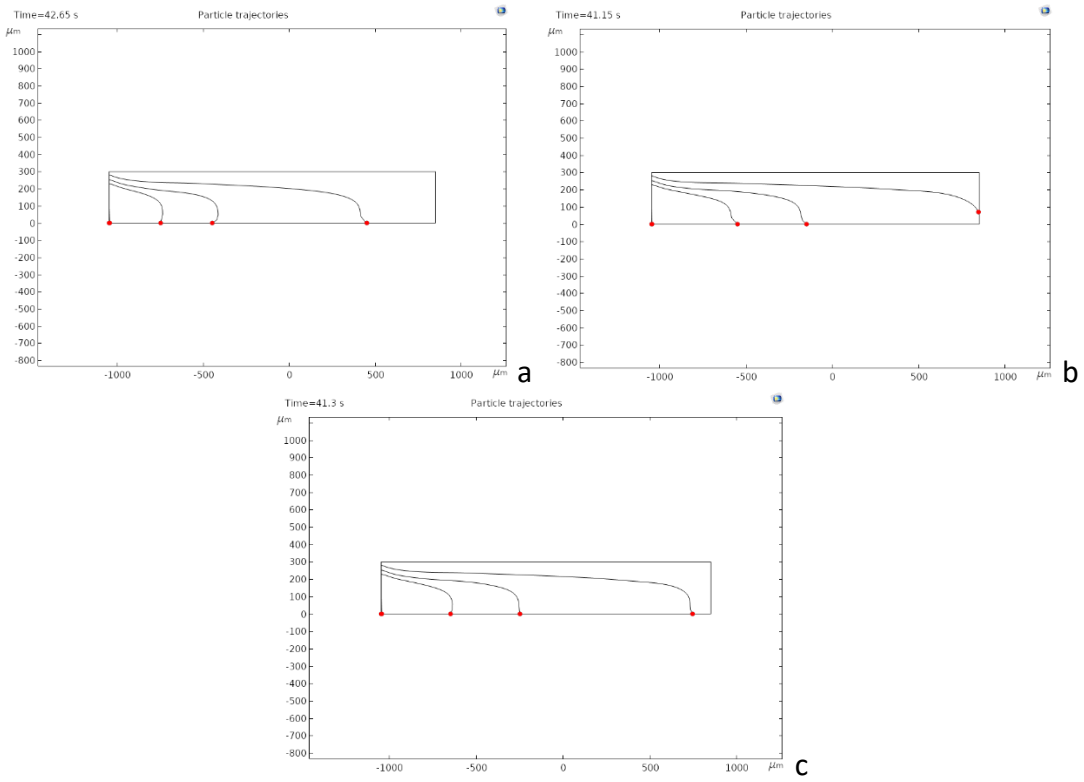

Figure 6.32: Particle trapping under AC pDEP influence at linear speed (a) $35\mu m/s$ (b) $40\mu m/s$, and (c) $39\mu m/s$.

Experiments are repeated with 750 cells at $39\mu m/s$ to observe cells captured by each electrode, as shown in figure 6.33. Results confirm that when cells are allowed to enter the chamber randomly, $\sim 70\%$ of cells are captured by the first five electrodes, and the last five electrodes capture the remaining cells. Moreover, only seven cells are captured by the last two electrodes. It is because cells near the

electrodes are captured while cells away from electrodes are pulled down as they move along the chamber by the electric field and eventually get trapped on the electrode edge. The overall loss of only six electrodes is observed out of 750, providing an AC pDEP efficiency of 99.2%. These results match with the cells per electrode analysis performed during chapter 5, where it is observed that the initial electrodes capture more cells compared to the later ones.

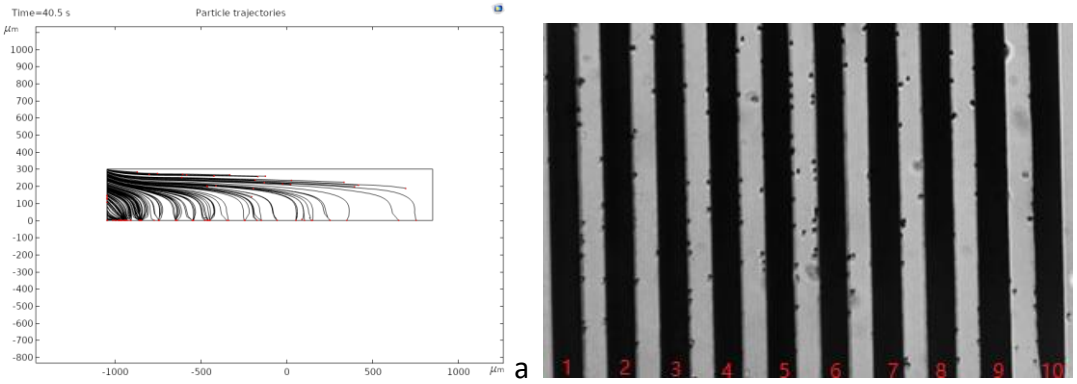

a b

Figure 6.33: Particle trapping on adjacent electrodes (a) Numerical (b) Experimental.

It is clear from the figure that most of the cells are captured by the first five electrodes, while very few cells are captured by the 9th and 10th electrodes. Figure 6.34 analyse total cells captured by each electrode at $30\mu m/s$, $35\mu m/s, 39\mu m/s$ and $40\mu m/s$.

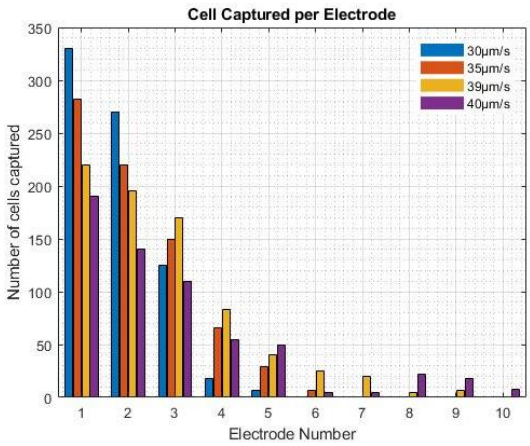

Figure 6.34: Number of cells captured as a function of the electrode number.

It can be observed from the bar graph that all cells are captured with the first five electrodes at $30\mu m/s$ and with the first six electrodes at $35\mu m/s$. However, the processing time is slow and takes more than an hour to complete. On the other hand, $39\mu m/s$ capture more cells than $40\mu m/s$. Cell count confirms only six cells lost by using $39\mu m/s$ compared to 74 cells lost by using $40\mu m/s$ cell linear speed. Moreover, most cells are captured by the first five electrodes compared to the last five in both cases. It is also observed from figure 6.33 that more cells are captured with the first five electrodes using $39\mu m/s$, and more cells are captured by $40\mu m/s$ with the last five electrodes. It is mainly because in $39\mu m/s$ out of 744 captured cells, 92% of cells are captured by the first five electrodes leaving only 59 cells for the last five electrodes to trap.

In contrast with $40\mu m/s$, 79% of cells are trapped out of the total captured cells of 676, which leaves 215 cells to pass from the last five electrodes, out of which 136 cells are trapped. Overall, more than 65% of trapped cells occurred during the first three electrodes in both cases. Matching these results obtained in chapter 5 shows similar trends, and hence it can be concluded that numerical results agree with the experimental analysis.

6.6.1.2 Multielectrode DEP Conclusion

This section results are performed using an electrode geometry of 10 individually addressable $50\mu m$ wide coplanar electrodes with an interelectrode gap of $100\mu m$ and chamber height of $300\mu m$. $300\mu m$ chamber height is used because it provides information about all cells in the range from 0um to $300\mu m$, including $100\mu m$ and $200\mu m$. Chamber is filled with $10mS/m$ conductive DIW, and electrodes are energised with $20V_{PP}, 1MHz$. In both experimental and numerical results, most of

the cells are trapped using the first few electrodes, after which cell capture decreases. Moreover, $39\mu m/s$ is the optimum velocity calculated using numerical analysis compared to $30\mu m/s$ using experimental results. Therefore, it can be concluded that experimental and numerical results match each other.

6.6.2 Multi-electrode ACEOF

Numerical analysis for ACEOF is performed for ten individually addressable electrodes, as shown in figure 6.26. It is because ten electrodes are used for AC pDEP, and cells are trapped on each electrode at $39\mu m/s$. However, the intensive literature review proves that the ACEOF model for more than three electrodes has never been produced. Moreover, for three electrodes model is presented for TWACEOF, ACEOF with phase-shifting signals. The model is expected to perform so that multielectrode produces a largely unified vortex.

A model with the geometry of $50\mu m$ wide Au electrodes with $100\mu m$ interelectrode gap is produced. Results are shown in figures 6.35a – 6.35i when fluid moves from the 1st electrode to the 10th electrode. Results show that the velocity has dropped to $400\mu m/s$ with ten electrodes. Although this fluid velocity does not match the experimentally observed fluid velocity, it still follows the trend as the experiments' velocity also decreased when switched to the ten electrodes. From figure 6.35a, it can be seen that one vortex is generated from electrode one. In contrast, the second vortex is produced from the 2nd electrode and expands almost to the 4th electrode. The vortex remains consistent throughout the figures from 6.35a to 6.35i. Results also show the drop-in velocity from $600\mu m/s\ to\ 400\mu m/s$ for $50\mu m$ wide electrodes and $100\mu m$ interelectrode gap.

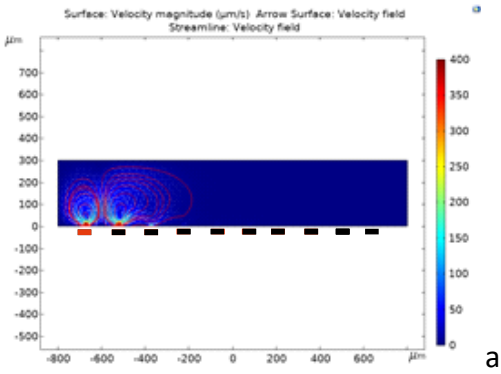

a

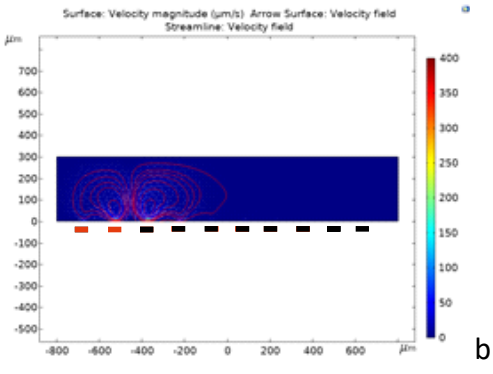

b

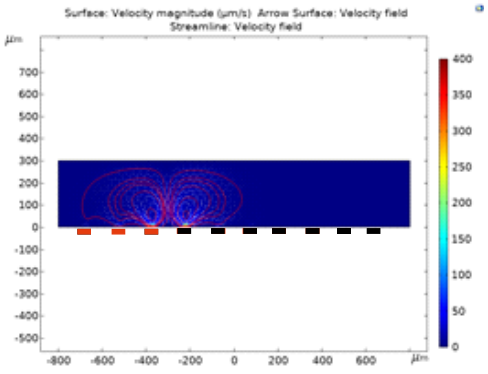

c

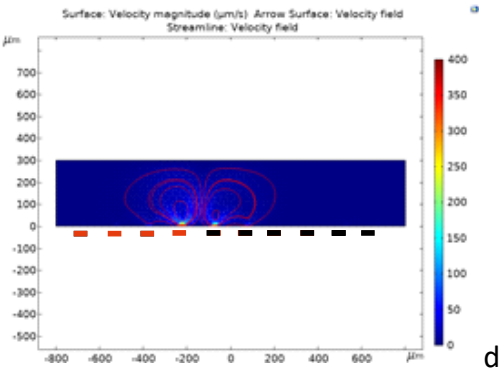

d

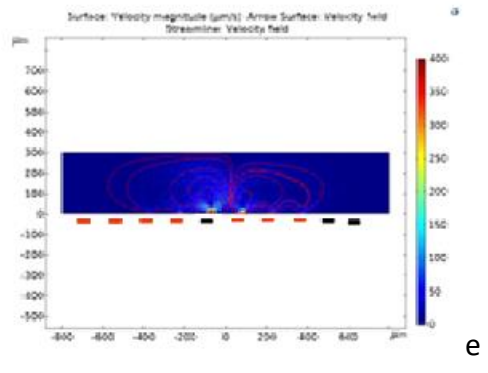

e

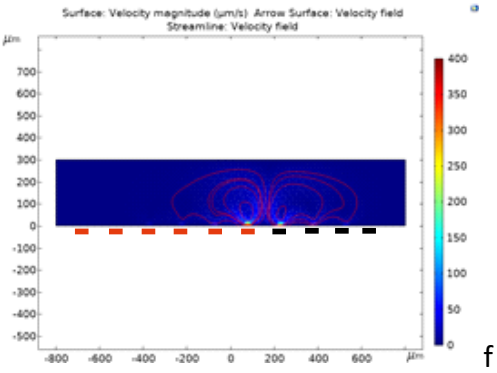

f

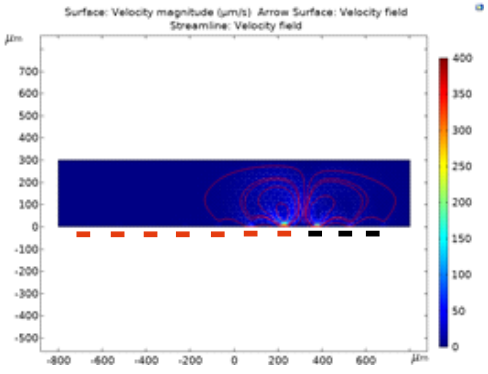

g

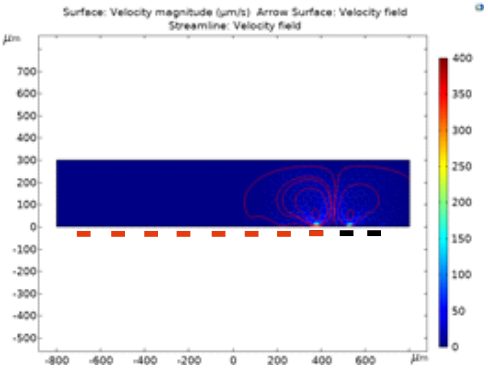

h

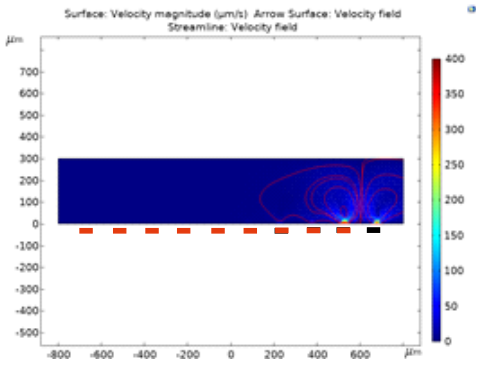

i

Figure 6.35: Numerical simulation of ACEOF with full switching pattern (a) first electrode (b) first two electrodes (c) first three electrodes (d) first four electrodes (e) first five electrodes (f) first six electrodes (g) first seven electrodes (h) first eight electrodes and (i) first nine electrodes.

Results confirm that all particles move towards the concentration area by switching electrodes properly. The electrode Pattern to generate fluid flow is given in table 6.5.

In table 6.5, 'E' stands for electrode, 'S' stands for signal, while 'G' stands for ground.

Table 6.5: Full Switching Pattern for MWACEOF.

Exp./Elec.	E1	E2	E3	E4	E5	E6	E7	E8	E9	E10	Observation	Figure
1	S	G	G	G	G	G	G	G	G	G	Forward Flow	6.34 a
2	S	S	G	G	G	G	G	G	G	G	Forward Flow	6.34 b
3	S	S	S	G	G	G	G	G	G	G	Forward Flow	6.34 c
4	S	S	S	S	G	G	G	G	G	G	Forward Flow	6.34 d
5	S	S	S	S	G	S	S	S	G	G	Forward Flow	6.34 e
6	S	S	S	S	S	S	G	G	G	G	Forward Flow	6.34 f
7	S	S	S	S	S	S	S	G	G	G	Forward Flow	6.34 g
8	S	S	S	S	S	S	S	S	G	G	Forward Flow	6.34 h
9	S	S	S	S	S	S	S	S	S	G	Forward Flow	6.34 i
10	S	S	S	S	S	G	G	G	G	G	Flow reversal	6.35

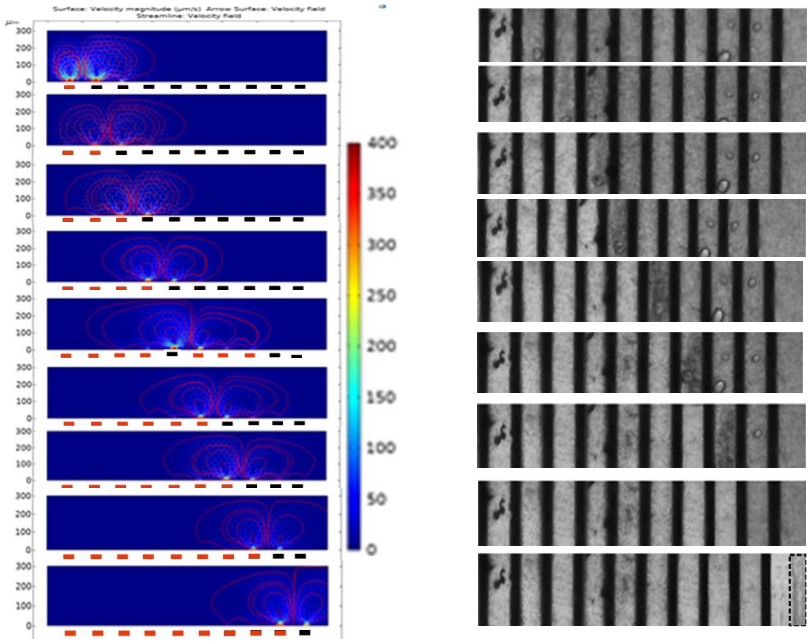

Figure 6.36: Numerical (right) and experimental (left) vortex comparison.

Figure 6.36 shows numerical and experimental results comparison. It can be seen from figure 6.36 that in both numerical and experimental results, vortices move diagonally from left to right as each electrode is initialised. Table 6.5 illustrates that for all experiments for forward fluid flow, a signal is applied to that particular electrode and all preceding electrodes. However, flow reversal took place for the 5th experiment (row 5) when the first five electrodes are switched on the signal, and the last five are connected to the ground. This anomalous flow is because EDL in the last five electrodes is formed faster in experiment 5 in the first five electrodes causing velocity to increase rapidly in the last five electrodes. It causes the second vortex to form more rapidly than the first one and become the dominant vortex, causing flow reversal. During flow reversal velocity of $9000\mu m/s$ is recorded compared to $400\mu m/s$ which is almost 22 times greater than normal v_{EOF}. The fluid flow moves backwards during the flow reversal, and the arrow surface is reversed, as shown in figure 6.37. The concept of surface arrow reversal at reverse electroosmosis flow is discussed in [335, 338]. This flow is called 'anomalous flow' in chapter 5. It is established in chapter 5 that despite the flow reversal taking place at a higher velocity

than normal fluid flow, this flow is not termed REOF because the flow reversal is originated from the perfect symmetry of the electrodes and has a velocity higher than REOF.

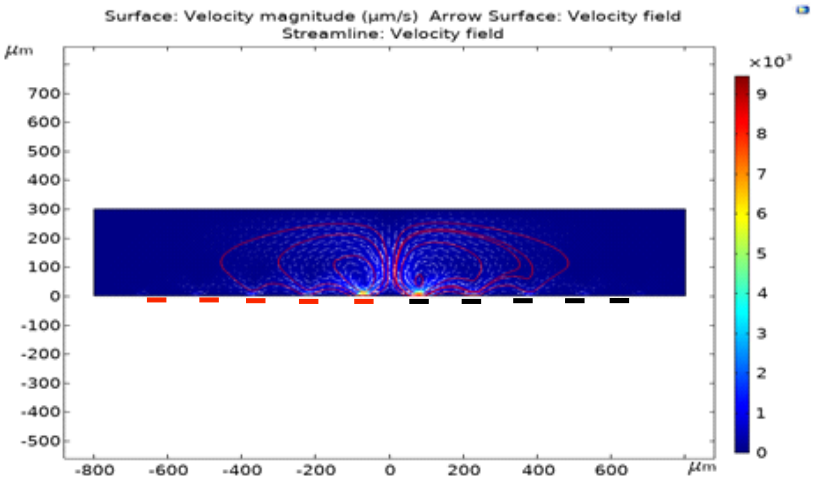

Figure 6.37: Numerical simulation of anomalous flow.

Various methods can be adapted to control flow reversal. One method is to decrease the AC signal magnitude applied to the last five electrodes compared to the first five electrodes. However, it is not appreciable since the project demands for symmetric AC signal. The second method is to increase chamber height, allowing the first vortex to form in time, avoiding the second vortex from becoming dominant, as shown in figure 6.38. It can be seen in figure 6.38 that flow again becomes normal as chamber height has increased to $1000\mu m$. Moreover, fluid flow direction follows the conventional ACEOF, and velocity has also dropped back to $400\mu m/s$ as well.

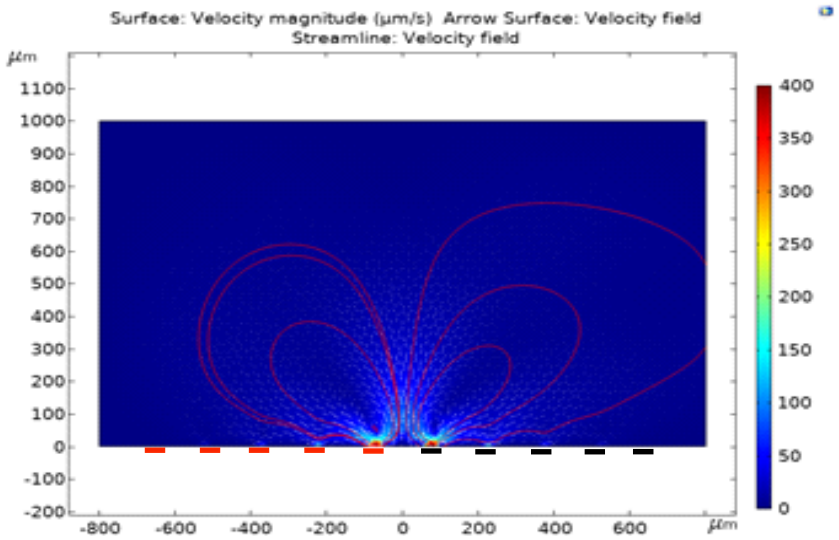

Figure 6.38: ACEOF produced with an increase in chamber height.

However, this method decreases the AC pDEP efficiency of the designed device, as not enough particles are trapped by AC pDEP at higher chamber heights. The third method is to switch electrodes so that the second vortex takes a longer time to form and does not get the chance to dominate the flow. The switching pattern in row 5 of Table 6.5 is found after using many different combinations, which generates the flow in the forward direction.

Finally, the last method to control flow reversal in symmetric geometry is to switch electrodes only when the particular electrode is required to produce ACEOF. It is termed as a 'partial switching pattern' in this project. Table 6.6 shows the electrode pattern used in the 'partial switching pattern'. In table 6.6, 'X' shows no connection condition. The results of the 'partial switching pattern' are shown in figures 6.38a – 6.38i. It is observed from the results that by using the partial switching combination, no flow reversal occurs. When the first five electrodes are switched to a signal, only the 6th electrode is connected to the ground causing typical vortices to form, and the second vortex does not dominate the flow. Therefore, causing fluid to move in the forward direction only. Figure 6.39a – 6.39i shows the results for the partial switching

pattern. Results also show a further decrease in fluid velocity from $400\mu m/s$ to $300\mu m/s$, which happened during the experimental results in chapter 5, where the partial switching pattern has a lower velocity than the full switching pattern.

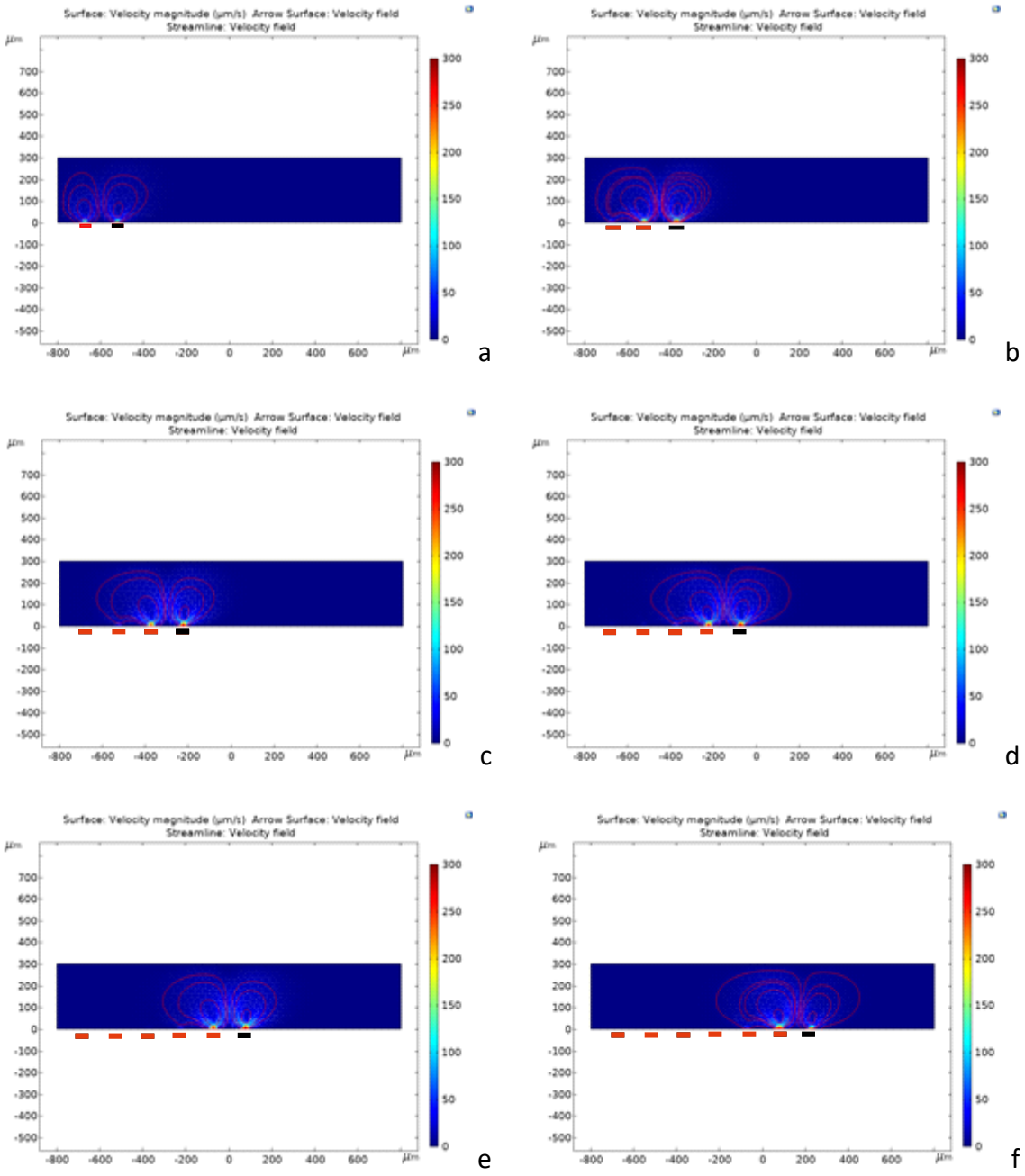

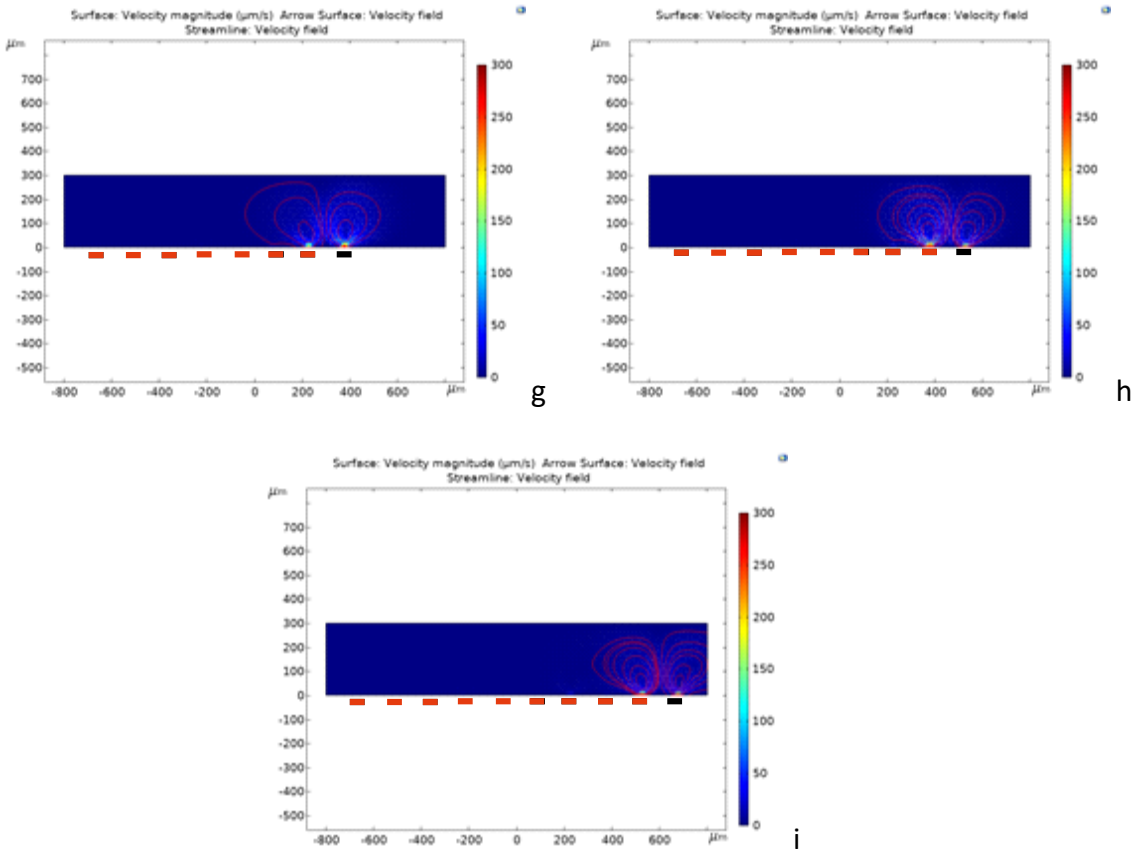

Figure 6.39: Numerical simulation of ACEOF with partial switching pattern (a) first electrode (b) first two electrodes (c) first three electrodes (d) first four electrodes (e) first five electrodes (f) first six electrodes (g) first seven electrodes (h) first eight electrodes and (i) first nine electrodes.

It is concluded both experimentally and numerically that ''partial switching pattern'' provides slower fluid flow speed at each electrode than 'full switching pattern'. Hence, while the 'partial switching pattern' guarantees no reversal flow, processing speed and efficiency are compromised. Efficiency is discussed for cell yield, which is discussed in chapter five. The velocity comparison is shown in figure 6.40.

Table 6.6: Partial Switching Pattern for MWACEOF.

Exp./Elec.	E1	E2	E3	E4	E5	E6	E7	E8	E9	E10	Observation	Figure
1	S	G	X	X	X	X	X	X	X	X	Forward Flow	6.39a
2	S	S	G	X	X	X	X	X	X	X	Forward Flow	6.39b
3	S	S	S	G	X	X	X	X	X	X	Forward Flow	6.39c
4	S	S	S	S	G	X	X	X	X	X	Forward Flow	6.39d
5	S	S	S	S	S	G	X	X	X	X	Forward Flow	6.39e
6	S	S	S	S	S	S	G	X	X	X	Forward Flow	6.39f
7	S	S	S	S	S	S	S	G	X	X	Forward Flow	6.39g
8	S	S	S	S	S	S	S	S	G	X	Forward Flow	6.39h
9	S	S	S	S	S	S	S	S	S	G	Forward Flow	6.39i

It is concluded both experimentally and numerically that ‘partial switching pattern’ provides slower fluid flow speed at each electrode than 'full switching pattern'. Therefore, while the ‘partial switching pattern’ assures no reversal flow, processing speed and efficiency get compromised. Efficiency is discussed for cell yield, which is discussed in chapter five. The velocity comparison is shown in figure 6.39. It is evident from the figure that for the 'full switching pattern', the velocity calculated is higher than the velocity calculated for the ''partial switching pattern’, which is similar to the results achieved in chapter 5. The reason for the lower velocity in the partial switching pattern is the weaker formation of EDL. Therefore provides a weaker processing speed.

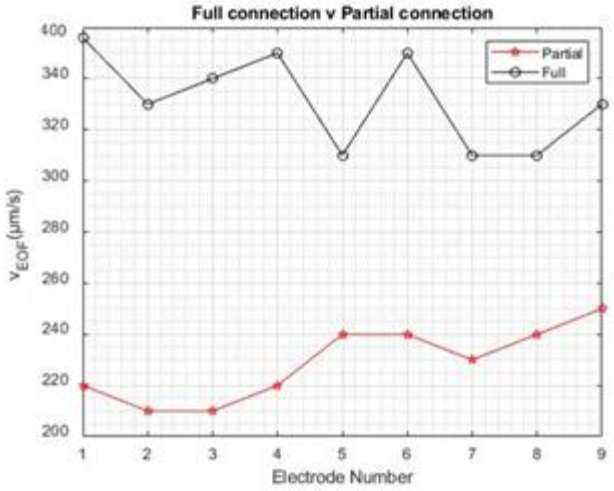

Figure 6.40: Numerical v_{EOF} $(\mu m/s)$ comparison between partial switching pattern (red plotline) and full switching pattern (black plotline) calculated at each electrode.

The numerical study is repeated with 12 electrodes to observe if fluid flow occurs at any combination using a "full connection pattern". However, no flow reversal is observed with any combination of electrodes (figure 6.41).

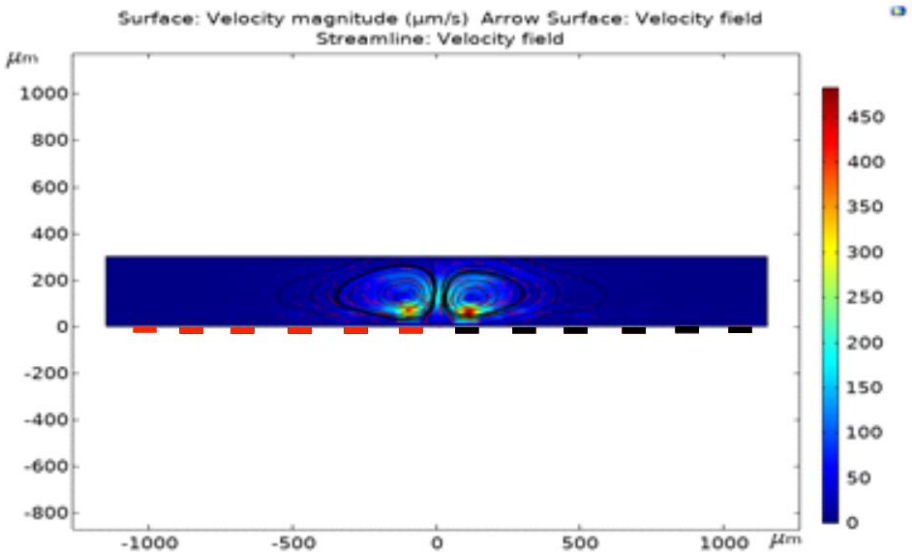

Figure 6.41: Forward flow observed at first six electrodes connected to signal and last six electrodes connected to ground; no flow reversal is observed for any electrode combination.

6.6.3 Multi-Vortex ACEOF Model

This study also purposes the model for multi-vortex ACEOF (MVACEOF), which means instead of having only two vortices, multi vortices takes place simultaneously. The motivation for this comes because it is observed in figures 6.34 (a-i) and 6.35 (a-i)

that the maximum vortex width reaches up to two electrodes. However, it starts to decay and become almost negligible after 3rd electrode is reached. It is illustrated again in figure 6.40a, where the first seven electrodes are on the signal, and the last three are ground. It can be seen from the figure that despite signal connection being connected to the first seven electrodes, still vortex width decays after the 3rd electrodes. It gives the total vortex width of $\sim 400 um$ because the analysis is performed on $50 \mu m$ wide electrodes with $100 \mu m$ the interelectrode gap. It leaves almost the first $\sim 600 \mu m$ width of the device unused while the cells are sitting there waiting for the next ACEOF pass to be pushed forward.

Moreover, in DEP analysis, more electrodes help capture more cells faster. However, ten individually addressable electrodes require ten individual connections in the experiments, as shown in chapter 5. It implies that for 'n' number of electrodes 'n' number of connections are required. Therefore, a numerical model is formed, which utilises multi-vortex ACEOF simultaneously. The model allows producing the device that is capable of:

i. Grouping the electrodes so that less than ten connections can control 'n' number of electrodes.
ii. Push maximum cells to the concentration area without using multiple ACEOF passes.

The last three electrodes are connected to the ground for all simulations during the investigation, as seen in figure 6.41. It can be observed that when the first electrode is connected to the ground, two additional vortices are formed. The figure also shows that there is still a gap between the 2nd and 3rd vortex despite two additional

vortices formed. When the first two electrodes are connected to the ground, along with the last three electrodes, it can be observed in figure 6.40c that the 2nd vortex width is stunted and limited to $\sim 250 \mu m$ while other vortices remain unaffected. Switching to the first three and last three electrodes to ground further limits the middle two vortices' width and limits each to $\sim 200 \mu m$ each, as shown in figure 6.42. Finally, switching to the first four electrodes to the ground, it can be seen that the 2nd vortex width is limited to $\sim 60 um$ while the 3rd vortex is limited to $\sim 200 \mu m$. Therefore, it can be concluded that each electrode can be connected with the fifth electrode. Therefore, it can be concluded from the simulation results that the 1st electrode can be connected with the 5th and 9th electrodes. In contrast, the 2nd electrode can be grouped with the 6th and 10th electrodes, and the pattern continues for the preceding electrodes. Therefore 'n' number of electrodes can be controlled with four connections only.

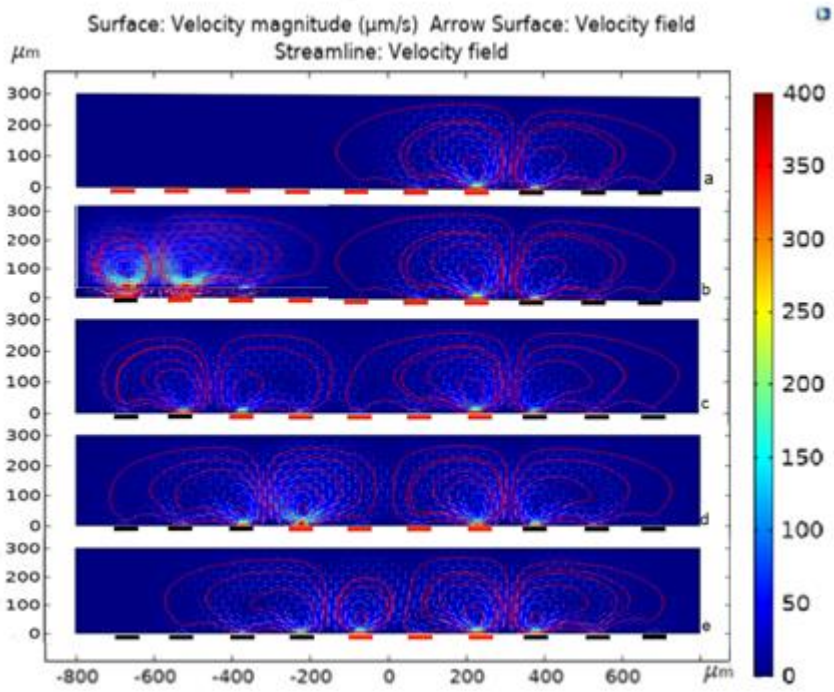

Figure 6.42: ACEOF vortex produced with last three electrodes grounded and (a) first electrode grounded (b) first two electrodes grounded (c) first three electrodes grounded (d) first four first electrodes grounded, and (e) first four electrodes

grounded. Red rectangles represent the signal, and black rectangles represent the ground.

6.6.3.1 Multielectrode ACEOF conclusion

1- Multielectrode numerical analysis shows excellent correlation with experimental results discussed in chapter 5. However, the difference between experimental and numerical velocity magnitudes exists. It is already thoroughly discussed that the difference occurred due to assumptions.

2- A multielectrode numerical model for ACEOF works for any pair of electrodes. Model is tested for asymmetric pair of electrodes (figure 6.43). Results show that the ACEOF model follows the pattern however v_{EOF} has decreased to $800\mu m/s$ compared to $900\mu m/s$ for the symmetric electrodes for $500\mu m$ wide electrodes.

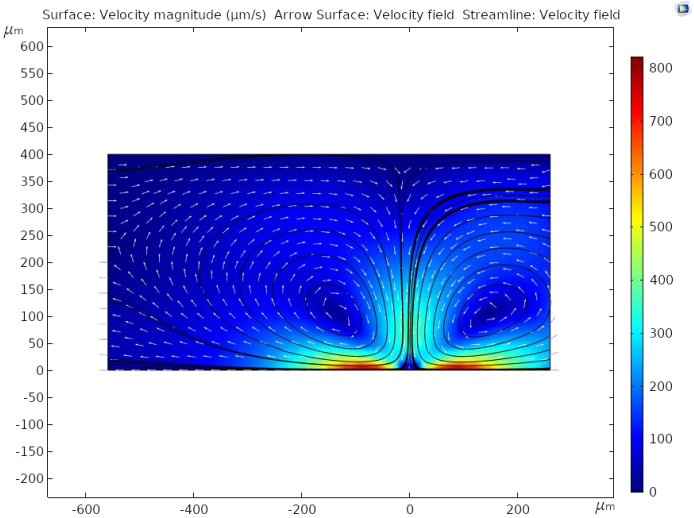

Figure 6.43: ACEOF simulation for asymmetric pair of electrodes.

3- 'Anomalous flow' produced during the numerical model agrees with the experimental study during which flow reversal occurred when the first five electrodes were switched to the signal. The magnitude of this reversal flow velocity is higher than the forward flow velocity. Moreover, no flow reversal

occurs during partial connection electrodes, which also follows the experimental results. Flow reversal vanished by increasing the chamber height.

4- The partial switching pattern provides system stability and guarantees no flow reversal. However, the processing speed is compromised.

5- The full switching pattern provides high processing speed and efficiency; however, it requires several attempts to get the correct electrode switching pattern that overcomes flow reversal.

6- Flow reversal was only observed in 10 electrodes geometry while using 2, 4, 6, 8, and even 12 electrodes; the flow reversal is not produced. Electrodes beyond 12 electrodes are not tested because experiments are performed on ten electrodes. However, there is a chance of producing flow reversal with higher pairs of electrodes.

7- A device with 'n' number of electrodes can be controlled by grouping each electrode with the 5th one.

6.7 Synopsis

This chapter presents with ACEOF and DEP model, which works very well for different geometries of electrodes. Moreover, both models perfectly fit with the experimental results discussed in chapters 4 and 5. Moreover, whilst the DEP model helped show cell separation, the ACEOF model predicted fluid behaviour with 12 electrodes and various geometries. The numerical study also confirms that ten $50\mu m$ wide electrodes with $100um$ interelectrode gap and $300\mu m$ chamber height provide maximum results in $10mS/m$ conductive DIW at $20V_{PP}, 1MHz$ for AC pDEP and $10V_{PP}, 1kHz$ for ACEOF. Finally, although a partial switching pattern gives the

insurance of no flow reversal, a full switching pattern provides better yield with faster processing speed. Therefore, a full switching pattern is used in the project.

7 Conclusion and Future Recommendations

7.1 Conclusion

The broad scope of this research work was to develop a hybrid microfluidic device that utilises AC Electrokinetic phenomena AC pDEP and ACEOF to produce a rapid and pure cell concentration factor of 100000 with an efficiency of $> 90\%$. Experimental results described in chapters 4 and 5 show that the specific research objectives outlined in chapter 1 have been successfully achieved. The novelty of the research is that the designed device described in chapter 5 can produce a concentration factor of > 400000 with an overall efficiency of $> 90\%$ by using a microfluidic device that contains ten individually addressable electrodes geometry. These numbers considerably improve the present-day cell concentration technologies mentioned in chapter 1. Moreover, the microfluidic device has utilised AC pDEP and ACEOF phenomena in such a way to improve previously cell concentration factors of mare 1200 using the AC pDEP and ACEOF phenomena described in chapter 3. Furthermore, both AC pDEP and ACEOF experimental results were validated using a COMSOL based numerical model in chapter 6. Chapter 6 added another novelty to the research by providing a numerical model for multi-vortex ACEOF and a model for anomalous flow discussed in chapter 5. Major conclusions are:

i. It was found in chapter 3 that using AC pDEP and ACEOF maximum concentration factor achieved is ~ 1200. It is because AC pDEP and ACEOF key parameters were not optimised thoroughly in those studies, which became the limiting factor for their research work. These parameters were found during chapter 2 and mainly included AC signal, AC frequency,

chamber height, interelectrode gap, and electrode width. Optimising these parameters were also critical because these provide information on maximum AC pDEP yield efficiency, ACEOF particle displacement, and velocity to achieve target cell concentration. By using a pair of coplanar electrodes, it was concluded that $75\mu m$ interelectrode gap, at the AC signal of $10V_{PP}$, $1kHz$ for $10mS/m$ fluid conductivity and chamber height of $500\mu m$ provides with maximum particle displacement and hence collects yeast cells at the distance of $430\mu m$ which is only $18\mu m$ higher particle displacement but almost 10 seconds faster collection than particle displacement achieved with $5V_{PP}$, $1kHz$ for $10mS/m$. However, less than 15% AC pDEP yield is achieved at chamber height of $500\mu m$ even with $20V_{PP}$, $1MHz$ voltage.

On the other hand, $100\mu m$ interelectrode gap produces a particle displacement of $290\mu m$ at $10V_{PP}$, $1kHz$ for $10mS/m$ with the chamber height of $300\mu m$. This chamber height corresponds to $\sim 49.3\%$ cell trapping at $20V_{PP}, 1MHz$. Using Chamber height less than $300\mu m$ provides higher AC pDEP but reduces ACEOF efficiency due to stunt particle displacement and possible flow reversal. Therefore, a compromise is made, and an AC signal of $20V_{PP}$, $1MHz$ for AC pDEP and $10V_{PP}$, $1kHz$ for ACEOF at fluid conductivity of $10mS/m$ is chosen along with $100\mu m$ interelectrode gap and $300\mu m$ chamber height.

ii. Results from chapter 4 were applied to ten individually addressable electrodes geometry. Parameters such as cell's linear velocity, the number of ACEOF passes and electrodes switching pattern were quantified to

achieve maximum AC pDEP yield efficiency, AC pDEP to ACEOF conversion efficiency, and cell concentration factor. Results concluded that a cell's linear speed of $30\mu m/s$ provides an AC pDEP yield of $> 95\%$. Furthermore, five and seven ACEOF waves provide a conversion efficiency of $> 90\%$ in both devices with $100\mu m \; and \; 50\mu m$. Finally, It is established that the concentration factor was also dependent on the total time AC pDEP was run. For 1000s, AC pDEP maximum concentration factor of 50000 is achieved, while in the 2000s, AC pDEP produced a concentration factor of 100000. The concentration factor increases to 430000 with 4000s AC pDEP. Therefore, the device offers an AC pDEP efficiency of $> 95\%, the$ conversion efficiency of $> 90\%$ and a concentration factor of > 48000 for 1000s AC pDEP, > 100000 for 2000s AC pDEP and > 430000 at 4000s AC pDEP. This concentration factor is more significant than the target concentration factor.

iii. The numerical model was built for AC pDEP and ACEOF to authorise experimental results described in chapters 4 and 5. Numerical analysis showed total coherent results for AC pDEP. However, ACEOF results showed a difference in results magnitude despite experiment and numerical trends being identical. Therefore, a correction factor was introduced to fix this difference whose value is in the range of $0.18 - 0.35$. In the end, a multi-vortex ACEOF numerical model was presented, which showed that if vortices were formed, each electrode could be grouped with each 5^{th} electrode. It allowed using $'n'$ of electrodes for cell trapping and concentration, controlled using only four

relay switches. Moreover, concave and convex geometries were also concluded that the device could purpose two cell concentration areas, increasing the cell concentration factor.

7.2 Future Work and Recommendations

At the end of the study, the following questions have arisen which requires future work and research:

a. How far could the concentration factor of the device be increased, and how?

A cell concentration factor of $> 400\ thousand$ is achieved using 4000s AC pDEP before applying MWACEOF. It is $300\ thousand$ greater than the target concentration factor set during chapter 1. However, the process takes almost $80min$ to complete, which is faster than the technologies listed in chapter 1 but still requires improvement. Decreasing AC pDEP time to 1000s improves the processing time by $50min$ but decreases the cell concentration factor to $50\ thousand$. Therefore, a system is required that can increase processing time without decreasing the cell concentration factor. One possible suggestion can be to use more electrodes, but as the number of electrodes increases, control switches also increase, making it cumbersome to control the device. Moreover, more electrodes mean more electrodes must be addressed using ACEOF, and the particles need to travel more distance to reach the concentration area. The multi-vortex ACEOF model addresses this issue, which shows that each electrode can be paired with the 5th electrode. This method will produce a 'n' number of electrodes geometry. $'n'$ is a number of electrodes as discussed in chapter 6. Because electrodes in MVACEOF are grouped and only controlled by four relay switches, any number of electrodes depending on

applications and device requirements can be built. However, will only four relay switches sufficient require experiments and further investigation? Hence, experiments should be performed with the 'n' number of electrodes using the multi-vortex numerical model to answer the improvement in the concentration factor and overall processing time.

b. How can the device's throughput be improved?

The device can process a 1.5mL solution at a flow rate of $45uL/min$ at the moment. This can be further increased by increasing the speed of the infusion pump. However, this will decrease overall DEP yield as the DEP trap will not get enough time to trap the cells. This problem is encountered by adding multiple electrode geometry, and the model is built for SWACEOF, which must be further explored.

c. How well the device responds to other types of cells and applications?

In this research, analysis is performed using only yeast cells as test particles. Therefore, the experimental analysis should be performed using different types of cells. The model for different cells is discussed in chapter 2 using MyDEP. Therefore, experiments should be performed using different cells to explore device performance.

The device's ability to handle different cells will help to investigate device capacity to function for different applications. For example, IVF procedure where motile sperm cells can be separated and enriched from the deformed sperm cells to improve the device's overall efficiency; or a liquid biopsy of CTCs to remove and enrich rare cancer cells for further studies and single-cell analysis. Furthermore, the device can be

implemented in air quality checks where allergens can be trapped and counted to investigate air quality.

d. How can the numerical model for ACEOF be improved?

The numerical model matches trends in the experimental process. However, the mismatch of velocity magnitude is due to the assumptions discussed in chapters 2, 3, and 6. Therefore, the model should be improved by using fewer assumptions. One possibility for this is to perform analysis using a 3D geometry model.

e. The anomalous flow observed during chapter 5 and chapter 6 requires further investigation to confirm if the flow is REOF or a new type of EHD flow?

In chapter 5, a flow reversal is observed and successfully overcome by deploying an intelligent switching technique. A similar flow reversal is also simulated in chapter 6, where an attempt is made to describe the reason for this flow reversal. This flow reversal has properties similar to REOF. However, the flow does not originate due to asymmetric electrode geometry or uneven AC signal, observed in all previous REOF studies discussed in chapter 3. Also, the flow is faster than conventional ACEOF and REOF; hence described as 'anomalous flow' in the study. This flow requires thorough investigation to describe if this anomalous fluid flow is flow reversal or a new type of EHD flow and the physics behind its originating. Studying how 'anomalous flow' could help to improve device applications in fluid mixing and fluid pumping.

f. Study analysis of Vortex structure?

Current studies focus on particle displacement that causes particles to concentrate in the cell concentration area. Therefore, ACEOF variables including AC signal, AC

frequency, fluid conductivity, and electrode geometry remained the attention. However, vortex structure and shape are not studied, which can add valuable information in cell collection, concentration, and isolation. In addition, vortex structure may also help to answer anomalous flow and flow reversal.

g. Analysing different electrode geometries?

Experiments and simulations are performed on parallel electrodes only. However, device ability must be checked with different electrodes' geometries, which can help open device applications in other fields.

h. Image Analysis and Machine Learning

Provided if I had more time, I would also like to do image analysis and machine learning. It can lead to the prediction of cell count in the long run. Also, image analysis can provide details of deformed and motile cells.

8 References

[1] P. T. Huong, S. Gurshaney, N. T. Binh, A. G. Pham, H. H. Nguyen, X. T. Nguyen, H. Pham-The, P. T. Tran, K. T. Vu, N. X. Duong, C. Pelucchi, C. La Vecchia, P. Boffetta, H. D. Nguyen, and H. N. Luu, "Emerging role of circulating tumor cells in gastric cancer," *Cancers,* vol. 12, no. 3, 2020.

[2] S. I. Hori, A. Herrera, J. J. Rossi, and J. Zhou, "Current advances in aptamers for cancer diagnosis and therapy," *Cancers,* vol. 10, no. 1, 2018.

[3] A. F. C. Rosli, S. R. A. Razak, and N. Zulkifle, "Bioinformatics analysis of differentially expressed genes in liver cancer for identification of key genes and pathways," *Malaysian Journal of Medicine and Health Sciences,* vol. 15, pp. 18-24, 2019.

[4] H. Mohammadi, S. F. Dehghan, M. B. Abdollahi, M. Kalantar, and M. Kaydany, "Effect of high light level on sperm parameters in mice," *Iran Occupational Health,* vol. 16, no. 4, pp. 13-21, 2019.

[5] J. O. Komolafe, A. M. Tijani, O. B. Komolafe, O. A. Oyedele, A. O. Fashanu, and A. S. Adeyemi, "Intrauterine in vivo fertilization: Low cost and low tech management of tubal factor infertility," *Clinical and Experimental Obstetrics and Gynecology,* vol. 45, no. 2, pp. 249-251, 2018.

[6] T. Takeda, M. Shirasaka, M. Sugiyama, R. Terashima, M. Kawaminami, and S. Kurusu, "In vivo evidence for possible up-regulating roles of lysophosphatidic acid around fertilization in rats," *Journal of Veterinary Medical Science,* vol. 80, no. 1, pp. 41-48, 2018.

[7] R. Azevedo, J. Soares, A. Peixoto, S. Cotton, L. Lima, L. L. Santos, and J. A. Ferreira, "Circulating tumor cells in bladder cancer: Emerging technologies

and clinical implications foreseeing precision oncology," *Urologic Oncology: Seminars and Original Investigations,* vol. 36, no. 5, pp. 221-236, 2018.

[8] D. Heymann, and M. Téllez-Gabriel, "Circulating tumor cells: The importance of single cell analysis," *Advances in Experimental Medicine and Biology*, Springer New York LLC, 2018, pp. 45-58.

[9] L. E. Lowes, and A. L. Allan, "Circulating Tumor Cells and Implications of the Epithelial-to-Mesenchymal Transition," *Advances in Clinical Chemistry*, Academic Press Inc., 2018, pp. 121-181.

[10] N. V. Nguyen, and C. P. Jen, "Impedance detection integrated with dielectrophoresis concentration platform for lung circulating tumor cells in a microfluidic channel," *Biosens Bioelectron,* vol. 121, pp. 10-18, Dec 15, 2018.

[11] H. Safarpour, S. Dehghani, R. Nosrati, N. Zebardast, M. Alibolandi, A. Mokhtarzadeh, and M. Ramezani, "Optical and electrochemical-based nano-aptasensing approaches for the detection of circulating tumor cells (CTCs)," *Biosensors and Bioelectronics,* vol. 148, 2020.

[12] A. Xiang, M. Xue, F. Ren, L. Wang, Z. Ye, D. Li, Q. Ji, G. Ji, and Z. Lu, "Highthroughput and continuous flow isolation of rare circulating tumor cells and clusters in gastric cancer from human whole blood samples using electromagnetic vibrationbased filtration," *Oncol Rep,* vol. 43, no. 6, pp. 1975-1985, Jun, 2020.

[13] C. Alix-Panabieres, and K. Pantel, "Liquid biopsy: from discovery to clinical implementation," *Mol Oncol,* vol. 15, no. 6, pp. 1617-1621, Jun, 2021.

[14] A. Baraniskin, and R. Schroers, "Liquid Biopsy and Other Non-Invasive Diagnostic Measures in PCNSL," *Cancers (Basel),* vol. 13, no. 11, May 28, 2021.

[15] C. Iglesias-López, A. Agustí, M. Obach, and A. Vallano, “Regulatory framework for advanced therapy medicinal products in Europe and United States,” *Frontiers in Pharmacology,* vol. 10, no. JULY, 2019.

[16] M. A. Hussain, M. Colicchia, J. Veerapen, D. Weeraman, M. N. Podaru, D. Jones, K. Suzuki, and A. Mathur, “Circulatory support and stem cell therapy in the management of advanced heart failure: A concise review of available evidence,” *Regenerative Medicine,* vol. 14, no. 6, pp. 585-593, 2019.

[17] S. Mohebbi, M. N. Nezhad, P. Zarrintaj, S. H. Jafari, S. S. Gholizadeh, M. R. Saeb, and M. Mozafari, “Chitosan in biomedical engineering: A critical review,” *Current Stem Cell Research and Therapy,* vol. 14, no. 2, pp. 93-116, 2019.

[18] P. Winograd, B. Di Pardo, C. M. Court, S. Sho, and J. S. Tomlinson, "Single-cell omics: Circulating tumor cells," *Single-Cell Omics: Volume 2: Application in Biomedicine and Agriculture*, pp. 37-54: Elsevier, 2019.

[19] M. Englhart, L. Soljic, and S. Sprunck, “Manual Isolation of Living Cells from the Arabidopsis thaliana Female Gametophyte by Micromanipulation,” *Methods Mol Biol,* vol. 1669, pp. 221-234, 2017.

[20] B. O. Bargmann, and K. D. Birnbaum, “Fluorescence activated cell sorting of plant protoplasts,” *J Vis Exp*, no. 36, Feb 18, 2010.

[21] M. van Seijen, A. L. Mooyaart, L. Mulder, M. Hoogstraat, C. A. Drukker, C. E. Loo, B. Pouw, G. S. Sonke, J. Wesseling, and E. H. Lips, “Concentration of high-grade tumors in breast cancer gene expression studies,” *Breast Cancer Research and Treatment,* vol. 168, no. 2, pp. 327-335, 2018.

[22] A. Ku, H. C. Lim, M. Evander, H. Lilja, T. Laurell, S. Scheding, and Y. Ceder, "Acoustic Concentration of Extracellular Vesicles from Biological Fluids," *Analytical Chemistry,* vol. 90, no. 13, pp. 8011-8019, 2018.

[23] C. Yamanaka, H. Wada, H. Eguchi, H. Hatano, K. Gotoh, T. Noda, D. Yamada, T. Asaoka, K. Kawamoto, H. Nagano, Y. Doki, and M. Mori, "Clinical significance of CD13 and epithelial mesenchymal transition (EMT) markers in hepatocellular carcinoma," *Japanese Journal of Clinical Oncology,* vol. 48, no. 1, pp. 52-60, 2018.

[24] V. Keyvani, M. Farshchian, S. A. Esmaeili, H. Yari, M. Moghbeli, S. R. K. Nezhad, and M. R. Abbaszadegan, "Ovarian cancer stem cells and targeted therapy," *Journal of Ovarian Research,* vol. 12, no. 1, 2019.

[25] M. Li, J. U. N. Ma, Y. Gao, and L. E. I. Yang, "Cell sheet technology: a promising strategy in regenerative medicine," *Cytotherapy,* vol. 21, no. 1, pp. 3-16, 2019.

[26] Z. Bai, Y. Deng, D. Kim, Z. Chen, Y. Xiao, and R. Fan, "An Integrated Dielectrophoresis-Trapping and Nanowell Transfer Approach to Enable Double-Sub-Poisson Single-Cell RNA Sequencing," *ACS Nano,* vol. 14, no. 6, pp. 7412-7424, Jun 23, 2020.

[27] R. Wang, Y. Xu, H. Liu, J. Peng, J. Irudayaraj, and F. Cui, "An integrated microsystem with dielectrophoresis concentration and impedance detection for detection of Escherichia coli," *Biomed Microdevices,* vol. 19, no. 2, pp. 34, Jun, 2017.

[28] P. Benhal, D. Quashie, Y. Kim, and J. Ali, "Insulator Based Dielectrophoresis: Micro, Nano, and Molecular Scale Biological Applications," *Sensors (Basel),* vol. 20, no. 18, Sep 7, 2020.

[29] E. Guzniczak, O. Otto, G. Whyte, T. Chandra, N. A. Robertson, N. Willoughby, M. Jimenez, and H. Bridle, “Purifying stem cell-derived red blood cells: a high-throughput label-free downstream processing strategy based on microfluidic spiral inertial separation and membrane filtration,” *Biotechnol Bioeng,* vol. 117, no. 7, pp. 2032-2045, Jul, 2020.

[30] R. Vaidyanathan, T. Yeo, and C. T. Lim, "Microfluidics for cell sorting and single cell analysis from whole blood," *Methods in Cell Biology*, M. Piel, D. Fletcher and J. Doh, eds., Academic Press Inc., 2018, pp. 151-173.

[31] W. Rust, "Regenerative medicine technologies applied to beta cell replacement: The industry perspective," *Transplantation, Bioengineering, and Regeneration of the Endocrine Pancreas: Volume 2*, pp. 519-526: Elsevier, 2019.

[32] X. An, and L. Chen, “Flow Cytometry (FCM) Analysis and Fluorescence-Activated Cell Sorting (FACS) of Erythroid Cells,” *Methods Mol Biol,* vol. 1698, pp. 153-174, 2018.

[33] J. C. Baret, O. J. Miller, V. Taly, M. Ryckelynck, A. El-Harrak, L. Frenz, C. Rick, M. L. Samuels, J. B. Hutchison, J. J. Agresti, D. R. Link, D. A. Weitz, and A. D. Griffiths, “Fluorescence-activated droplet sorting (FADS): efficient microfluidic cell sorting based on enzymatic activity,” *Lab Chip,* vol. 9, no. 13, pp. 1850-8, Jul 7, 2009.

[34] L. Yin, Z. Yang, Y. Wu, V. Denslin, C. C. Yu, C. A. Tee, C. T. Lim, J. Han, and E. H. Lee, “Label-free separation of mesenchymal stem cell subpopulations with distinct differentiation potencies and paracrine effects,” *Biomaterials,* vol. 240, pp. 119881, May, 2020.

[35] H. Zhuan, G. Zheng, and Y. Wang, “Advantages and application prospects of microfluidic chip technology in cell adhesion research,” *Chinese Journal of Tissue Engineering Research,* vol. 23, no. 22, pp. 3584-3590, 2019.

[36] J. Autebert, B. Coudert, F. C. Bidard, J. Y. Pierga, S. Descroix, L. Malaquin, and J. L. Viovy, “Microfluidic: An innovative tool for efficient cell sorting,” *Methods,* vol. 57, no. 3, pp. 297-307, 2012.

[37] V. Laxmi, S. Tripathi, S. S. Joshi, and A. Agrawal, “Microfluidic Techniques for Platelet Separation and Concentration,” *Journal of the Indian Institute of Science,* vol. 98, no. 2, pp. 185-200, 2018.

[38] Y. Cai, J. Wang, and K. Zou, “The Progresses of Spermatogonial Stem Cells Sorting Using Fluorescence-Activated Cell Sorting,” *Stem Cell Rev Rep,* vol. 16, no. 1, pp. 94-102, Feb, 2020.

[39] B. S. Broyles, S. C. Jacobson, and J. M. Ramsey, “Sample filtration, concentration, and separation integrated on microfluidic devices,” *Analytical Chemistry,* vol. 75, no. 11, pp. 2761-2767, 2003.

[40] B. Dutra, M. C. Mora, T. I. Gerhardson, B. Sporbert, A. Dufresne, K. R. Bittner, C. Lovewell, M. J. Rust, M. V. Tirabassi, L. Masi, B. Lipkens, and D. R. Kennedy, “A novel macroscale acoustic device for blood filtration,” *Journal of Medical Devices, Transactions of the ASME,* vol. 12, no. 1, 2018.

[41] M. Assenmacher, R. Manz, S. Miltenyi, A. Scheffold, and A. Radbruch, “Fluorescence-activated cytometry cell sorting based on immunological recognition,” *Clin Biochem,* vol. 28, no. 1, pp. 39-40, Feb, 1995.

[42] H. Feng, X. Wang, Z. Xu, X. Zhang, and Y. Gao, "Super-resolution fluorescence microscopy for single cell imaging," *Advances in Experimental Medicine and Biology*, Springer New York LLC, 2018, pp. 59-71.

[43] B. Zhu, and S. K. Murthy, “Stem Cell Separation Technologies,” *Curr Opin Chem Eng,* vol. 2, no. 1, pp. 3-7, Feb 1, 2013.

[44] D. M. Potashnikova, S. A. Golyshev, A. A. Penin, M. D. Logacheva, A. V. Klepikova, A. A. Zharikova, A. A. Mironov, E. V. Sheval, and I. A. Vorobjev, "FACS isolation of viable cells in different cell cycle stages from asynchronous culture for RNA sequencing," *Methods in Molecular Biology*, Humana Press Inc., 2018, pp. 315-335.

[45] B. A. Sutermaster, and E. M. Darling, “Considerations for high-yield, high-throughput cell concentration: fluorescence versus magnetic sorting. ,” *Sci Rep* vol. 9, pp. 125-8, 2019, 2019.

[46] Y. Sun, and P. Sethu, “Microfluidic Adaptation of Density-Gradient Centrifugation for Isolation of Particles and Cells,” *Bioengineering (Basel),* vol. 4, no. 3, Aug 2, 2017.

[47] M. Muratori, N. Tarozzi, F. Carpentiero, S. Danti, F. M. Perrone, M. Cambi, A. Casini, C. Azzari, L. Boni, M. Maggi, A. Borini, and E. Baldi, “Sperm selection with density gradient centrifugation and swim up: effect on DNA fragmentation in viable spermatozoa,” *Sci Rep,* vol. 9, no. 1, pp. 7492, May 16, 2019.

[48] D. Lee, and B. C. Jee, “Evaluation of normal morphology, DNA fragmentation, and hyaluronic acid binding ability of human spermatozoa after using four

different commercial media for density gradient centrifugation," *Clin Exp Reprod Med,* vol. 46, no. 1, pp. 8-13, Mar, 2019.

[49] Y. S. Tan, and Y. L. Lei, "Isolation of Tumor-Infiltrating Lymphocytes by Ficoll-Paque Density Gradient Centrifugation," *Methods Mol Biol,* vol. 1960, pp. 93-99, 2019.

[50] X. Hu, X. Dang, and M. Wu, "[Membrane separation technology in medical devices]," *Zhongguo Yi Liao Qi Xie Za Zhi,* vol. 38, no. 1, pp. 44-6, Jan, 2014.

[51] A. Gupta, S. Singh, B. Gonenc, M. Kobilarov, and I. Iordachita, "Toward Sclera-Force-Based Robotic Assistance for Safe Micromanipulation in Vitreoretinal Surgery," *Proc IEEE Sens,* vol. 2017, Oct-Nov, 2017.

[52] Z. Weize, A. Sobolevski, L. Bing, R. Yong, and L. Xinyu, "A force-controlled robotic micromanipulation system for mechanotransduction studies of Drosophila larvae," *Annu Int Conf IEEE Eng Med Biol Soc,* vol. 2014, pp. 6526-9, 2014.

[53] W. Kobayashi, A. Onishi, H. Y. Tu, Y. Takihara, M. Matsumura, K. Tsujimoto, M. Inatani, T. Nakazawa, and M. Takahashi, "Culture systems of dissociated mouse and human pluripotent stem cell–derived retinal ganglion cells purified by two-step immunopanning," *Investigative Ophthalmology and Visual Science,* vol. 59, no. 2, pp. 776-787, 2018.

[54] T. Weiss, S. Taschner-Mandl, P. F. Ambros, and I. M. Ambros, "Detailed protocols for the isolation, culture, concentration and immunostaining of primary human Schwann cells," *Methods in Molecular Biology*, Humana Press Inc., 2018, pp. 67-86.

[55] R. Gordon, “Biosensing with nanoaperture optical tweezers,” *Optics and Laser Technology,* vol. 109, pp. 328-335, 2019.

[56] J. S. Dam, P. J. Rodrigo, I. R. Perch-Nielsen, and J. Gluckstad, “Fully automated beam-alignment and single stroke guided manual alignment of counter-propagating multi-beam based optical micromanipulation systems,” *Opt Express,* vol. 15, no. 13, pp. 7968-73, Jun 25, 2007.

[57] L. Sun, Q. Chen, H. Lu, J. Wang, J. Zhao, and P. Li, “Electrodialysis with porous membrane for bioproduct separation: Technology, features, and progress,” *Food Res Int,* vol. 137, pp. 109343, Nov, 2020.

[58] S. Riethdorf, L. O'Flaherty, C. Hille, and K. Pantel, “Clinical applications of the CellSearch platform in cancer patients,” *Advanced Drug Delivery Reviews,* vol. 125, pp. 102-121, 2018.

[59] J. Zhang, S. Yan, D. Yuan, G. Alici, N. T. Nguyen, M. Ebrahimi Warkiani, and W. Li, “Fundamentals and applications of inertial microfluidics: a review,” *Lab Chip,* vol. 16, no. 1, pp. 10-34, Jan 7, 2016.

[60] P. Korkusuz, S. Köse, N. Yersal, and S. Önen, "Magnetic-based cell isolation technique for the selection of stem cells," *Methods in Molecular Biology*, Humana Press Inc., 2019, pp. 153-163.

[61] R. Lampignano, H. Schneck, M. Neumann, T. Fehm, and H. Neubauer, "Concentration, isolation and molecular characterization of EpCAM-negative circulating tumor cells," *Advances in Experimental Medicine and Biology*, Springer New York LLC, 2017, pp. 181-203.

[62] A. Mukherjee, and C. M. Schroeder, "Microfluidic methods in single cell biology," *Microfluidic Methods for Molecular Biology*, pp. 19-54: Springer International Publishing, 2016.

[63] J. F. Swennenhuis, and T. Leon, "Sample preparation methods following cellsearch approach compatible of single-cell whole-genome amplification: An overview," *Methods in Molecular Biology*, Humana Press Inc., 2015, pp. 57-67.

[64] M. A. Abdul Razak, K. F. Hoettges, H. O. Fatoyinbo, F. H. Labeed, and M. P. Hughes, "Efficient dielectrophoretic cell concentration using a dielectrophoresis-well based system," *Biomicrofluidics,* vol. 7, no. 6, pp. 64110, 2013.

[65] K. Yoon, H. W. Jung, and M. S. Chun, "Two-phase flow in microfluidic-chip design of hydrodynamic filtration for cell particle sorting," *Electrophoresis,* vol. 41, no. 10-11, pp. 1002-1010, Jun, 2020.

[66] J. Ducrée, P. Koltay, and R. Zengerle, "Microfluidics," *MEMS: A Practical Guide of Design, Analysis, and Applications*, pp. 667-727: Springer Berlin Heidelberg, 2006.

[67] Y. Bai, M. Gao, L. Wen, C. He, Y. Chen, C. Liu, X. Fu, and S. Huang, "Applications of Microfluidics in Quantitative Biology," *Biotechnol J,* vol. 13, no. 5, pp. e1700170, May, 2018.

[68] C. J. Ramirez-Murillo, J. M. de Los Santos-Ramirez, and V. H. Perez-Gonzalez, "Toward low-voltage dielectrophoresis-based microfluidic systems: A review," *Electrophoresis*, Nov 9, 2020.

[69] M. Turetta, F. Del Ben, G. Brisotto, E. Biscontin, M. Bulfoni, D. Cesselli, A. Colombatti, G. Scoles, G. Gigli, and L. L. Del Mercato, “Emerging technologies for cancer research: Towards personalized medicine with microfluidic platforms and 3D tumor models,” *Current Medicinal Chemistry,* vol. 25, no. 35, 2018.

[70] M. C. Kim, Z. Wang, R. H. W. Lam, and T. Thorsen, “Building a better cell trap: Applying Lagrangian modeling to the design of microfluidic devices for cell biology,” *Journal of Applied Physics,* vol. 103, no. 4, 2008.

[71] Y. Cheng, X. Ye, Z. Ma, S. Xie, and W. Wang, “High-throughput and clogging-free microfluidic filtration platform for on-chip cell separation from undiluted whole blood,” *Biomicrofluidics,* vol. 10, no. 1, pp. 014118, Jan, 2016.

[72] B. Sarno, D. Heineck, M. J. Heller, and S. Ibsen, “Dielectrophoresis: Developments and applications from 2010 to 2020,” *Electrophoresis*, Nov 16, 2020.

[73] K. F. Lei, "Electrokinetic manipulation of biomolecules," *Microfluidics: Control, Manipulation and Behavioral Applications*, pp. 167-184: Nova Science Publishers, Inc., 2013.

[74] Y. Zhao, C. Gao, and B. Van der Bruggen, “Technology-driven layer-by-layer assembly of a membrane for selective separation of monovalent anions and antifouling,” *Nanoscale,* vol. 11, no. 5, pp. 2264-2274, Jan 31, 2019.

[75] A. L. Nikolaev, B. I. Mitrin, E. V. Sadyrin, V. B. Zelentsov, A. R. Aguiar, and S. M. Aizikovich, "Mechanical properties of microposit S1813 thin layers," *Advanced Structured Materials*, Springer Science and Business Media Deutschland GmbH, 2020, pp. 137-146.

[76] Y. Qin, S. Puthiyakunnon, Y. Zhang, X. Wu, S. Boddu, B. Luo, and H. Fan, "Rapid and Specific Detection of Escherichia coli O157:H7 in Ground Beef Using Immunomagnetic Separation Combined with Loop-Mediated Isothermal Amplification," *Polish Journal of Food and Nutrition Sciences,* vol. 68, no. 2, pp. 115-123, 2018.

[77] X. Wang, L. Sun, H. Zhang, L. Wei, W. Qu, Z. Zeng, Y. Liu, and Z. Zhu, "Microfluidic chip combined with magnetic-activated cell sorting technology for tumor antigen-independent sorting of circulating hepatocellular carcinoma cells," *PeerJ,* vol. 2019, no. 4, 2019.

[78] "Erratum: An Optimized Procedure for Fluorescence-activated Cell Sorting (FACS) Isolation of Autonomic Neural Progenitors from Visceral Organs of Fetal Mice," *J Vis Exp*, no. 68, Oct 1, 2012.

[79] A. Dalili, E. Samiei, and M. Hoorfar, "A review of sorting, separation and isolation of cells and microbeads for biomedical applications: microfluidic approaches," *Analyst,* vol. 144, no. 1, pp. 87-113, 2019.

[80] Q. Luan, C. Macaraniag, J. Zhou, and I. Papautsky, "Microfluidic systems for hydrodynamic trapping of cells and clusters," *Biomicrofluidics,* vol. 14, no. 3, 2020.

[81] B. R. Ibarra-Ibarra, M. Franco, A. Paez, E. V. López, and F. Massó, "Improved efficiency of cardiomyocyte-like cell differentiation from rat adipose tissue-derived mesenchymal stem cells with a directed differentiation protocol," *Stem Cells International,* vol. 2019, 2019.

[82] G. Xin, W. Zhu, Y. Deng, J. Cheng, L. T. Zhang, A. J. Chung, S. De, and J. Lian, "Microfluidics-enabled orientation and microstructure control of

macroscopic graphene fibres," *Nat Nanotechnol,* vol. 14, no. 2, pp. 168-175, Feb, 2019.

[83] L. Wu, X. Qu, Y. Song, and C. Yang, "Biomimetic membrane enabled multivalent microfluidic chip for highly efficient concentration of circulating tumor cells." pp. 758-759.

[84] Z. Yu, and F. J. Richmond, "Regulatory considerations for genetically manipulated cell-based products," *Encyclopedia of Tissue Engineering and Regenerative Medicine*, pp. 295-302: Elsevier, 2019.

[85] W. E. Uspal, H. Burak Eral, and P. S. Doyle, "Engineering particle trajectories in microfluidic flows using particle shape," *Nature Communications,* vol. 4, 2013.

[86] Y. Ai, and S. Qian, "DC dielectrophoretic particle-particle interactions and their relative motions," *Journal of Colloid and Interface Science,* vol. 346, no. 2, pp. 448-454, 2010.

[87] J. G. Santiago, S. T. Wereley, C. D. Meinhart, D. J. Beebe, and R. J. Adrian, "A particle image velocimetry system for microfluidics," *Experiments in Fluids,* vol. 25, no. 4, pp. 316-319, 1998.

[88] A. P. Fields, and A. E. Cohen, "Anti-Brownian Traps for Studies on Single Molecules," *Methods in Enzymology*, Academic Press Inc., 2010, pp. 149-174.

[89] H. A. Stone, A. D. Stroock, and A. Ajdari, "Engineering flows in small devices: Microfluidics toward a lab-on-a-chip," *Annual Review of Fluid Mechanics*, Annual Reviews Inc., 2004, pp. 381-411.

[90] F. Ayela, O. Tillement, and J. Chevalier, "Rheology of nanofluids in microchannels." pp. 1013-1017.

[91] S. Savel'ev, F. Marchesoni, and F. Nori, "Stochastic transport of interacting particles in periodically driven ratchets," *Physical Review E - Statistical Physics, Plasmas, Fluids, and Related Interdisciplinary Topics,* vol. 70, no. 6, pp. 13, 2004.

[92] N. T. Nguyen, "Mixing in microscale," *Microfluidic Technologies for Miniaturized Analysis Systems*, pp. 117-155: Springer US, 2007.

[93] R. M. Erb, and B. B. Yellen, "Magnetic manipulation of colloidal particles," *Nanoscale Magnetic Materials and Applications*, pp. 563-590: Springer US, 2009.

[94] T. Kulrattanarak, R. G. M. van der Sman, C. G. P. H. Schroën, and R. M. Boom, "Classification and evaluation of microfluidic devices for continuous suspension fractionation," *Advances in Colloid and Interface Science,* vol. 142, no. 1-2, pp. 53-66, 2008.

[95] P. K. Wong, T. H. Wang, J. H. Deval, and C. M. Ho, "Electrokinetics in micro devices for biotechnology applications," *IEEE/ASME Transactions on Mechatronics,* vol. 9, no. 2, pp. 366-376, 2004.

[96] S. Panzarella, and W. Maroni, *Microfluidics: Control, manipulation and behavioral applications*: Nova Science Publishers, Inc., 2013.

[97] G. Gregolec, K. E. Roehl, and K. Czurda, "Chapter 8 Electrokinetic techniques," *Trace Metals and other Contaminants in the Environment*, Elsevier B.V., 2005, pp. 183-209.

[98] Á. V. Delgado, and F. González-Caballero, "Electrokinetic phenomena in suspensions," *Finely Dispersed Particles: Micro-, Nano-, and Atto-Engineering*, pp. 43-77: CRC Press, 2005.

[99] H. Morgan, N. G. Green, and T. Sun, "Electrokinetics Of Particles And Fluids," *Micro/Nano Technology Systems for Biomedical Applications: Microfluidics, Optics, and Surface Chemistry*: Oxford University Press, 2010.

[100] J. H. Masliyah, and S. Bhattacharjee, *Electrokinetic and Colloid Transport Phenomena*: John Wiley and Sons, 2005.

[101] H. A. Pohl, *Dielectrophoresis : the behavior of neutral matter in nonuniform electric fields*, Cambridge ; New York: Cambridge University Press, 1978.

[102] N. G. Green, "Dielectrophoresis and AC Electrokinetics," *CISM International Centre for Mechanical Sciences, Courses and Lectures*, Springer International Publishing, 2011, pp. 61-84.

[103] T. B. Jones, *Electromechanics of particles*, Digitally printed 1st pbk. ed., Cambridge ; New York: Cambridge University Press, 2005.

[104] T. Sun, and H. Morgan, "AC Electrokinetic Micro- and Nano-particle Manipulation and Characterization," *CISM International Centre for Mechanical Sciences, Courses and Lectures*, Springer International Publishing, 2011, pp. 1-28.

[105] Y. J. Lo, and U. Lei, “Measurement of the real part of the Clausius–Mossotti factor of dielectrophoresis for Brownian particles,” *Electrophoresis,* vol. 41, no. 1-2, pp. 137-147, 2020.

[106] Y. J. Lo, Y. Y. Lin, U. Lei, M. S. Wu, and P. C. Yang, “Measurement of the Clausius-Mossotti factor of generalized dielectrophoresis,” *Applied Physics Letters,* vol. 104, no. 8, 2014.

[107] Y. Y. Lin, Y. J. Lo, and U. Lei, "Measurement of the imaginary part of the clausius-mossotti factor of particle/cell via dual frequency electrorotation," *Micromachines,* vol. 11, no. 3, 2020.

[108] J. Cottet, O. Fabregue, C. Berger, F. Buret, P. Renaud, and M. Frénéa-Robin, "MyDEP: A New Computational Tool for Dielectric Modeling of Particles and Cells," *Biophysical Journal,* vol. 116, no. 1, pp. 12-18, 2019.

[109] A. Mortadi, A. El Melouky, E. G. Chahid, R. El Moznine, and O. Cherkaoui, "Studies of the clausius–Mossotti factor," *Journal of Physical Studies,* vol. 20, no. 4, pp. 4001-1-4001-4, 2016.

[110] G. H. Markx, Y. Huang, X. F. Zhou, and R. Pethig, "Dielectrophoretic characterization and separation of micro-organisms," *Microbiology,* vol. 140, no. 3, pp. 585-591, 1994.

[111] M. S. Talary, K. I. Mills, T. Hoy, A. K. Burnett, and R. Pethig, "Dielectrophoretic separation and concentration of CD34+ cell subpopulation from bone marrow and peripheral blood stem cells," *Med Biol Eng Comput,* vol. 33, no. 2, pp. 235-7, Mar, 1995.

[112] T. Z. Jubery, and P. Dutta, "A fast algorithm to predict cell trajectories in microdevices using dielectrophoresis," *Numerical Heat Transfer; Part A: Applications,* vol. 64, no. 2, pp. 107-131, 2013.

[113] M. P. Hughes, and K. F. Hoettges, *Microengineering in biotechnology*, New York: Humana, 2010.

[114] R. Martinez-Duarte, "Microfabrication technologies in dielectrophoresis applications-A review," *Electrophoresis,* vol. 33, no. 21, pp. 3110-3132, 2012.

[115] N. A. Rahman, F. Ibrahim, and B. Yafouz, “Dielectrophoresis for biomedical sciences applications: A review,” *Sensors (Switzerland),* vol. 17, no. 3, 2017.

[116] G. R. Pesch, and F. Du, “A review of dielectrophoretic separation and classification of non-biological particles,” *Electrophoresis*, 2020.

[117] R. C. Gallo-Villanueva, V. H. Perez-Gonzalez, B. Cardenas-Benitez, B. Jind, S. O. Martinez-Chapa, and B. H. Lapizco-Encinas, “Joule heating effects in optimized insulator-based dielectrophoretic devices: An interplay between post geometry and temperature rise,” *Electrophoresis,* vol. 40, no. 10, pp. 1408-1416, May, 2019.

[118] H. A. Pohl, and J. K. Pollock, "DIELECTROPHORETIC CELL-SORTING." p. 1016.

[119] E. Lee, "Electrophoresis of Porous Particles," *Interface Science and Technology*, Elsevier B.V., 2019, pp. 145-180.

[120] A. Ramos, H. Morgan, N. G. Green, and A. Castellanos, “Ac electrokinetics: A review of forces in microelectrode structures,” *Journal of Physics D: Applied Physics,* vol. 31, no. 18, pp. 2338-2353, 1998.

[121] M. Giesbers, J. M. Kleijn, and M. A. Cohen Stuart, “The electrical double layer on gold probed by electrokinetic and surface force measurements,” *Journal of Colloid and Interface Science,* vol. 248, no. 1, pp. 88-95, 2002.

[122] A. Ramos, H. Morgan, N. G. Green, and A. Castellanos, “AC electric-field-induced fluid flow in microelectrodes,” *Journal of Colloid and Interface Science,* vol. 217, no. 2, pp. 420-422, 1999.

[123] T. M. Squires, and S. R. Quake, “Microfluidics: Fluid physics at the nanoliter scale,” *Reviews of Modern Physics,* vol. 77, no. 3, pp. 977-1026, 2005.

[124] M. Z. Bazant, M. S. Kilic, B. D. Storey, and A. Ajdari, “Towards an understanding of induced-charge electrokinetics at large applied voltages in concentrated solutions,” *Advances in Colloid and Interface Science,* vol. 152, no. 1-2, pp. 48-88, 2009.

[125] C. Grosse, and A. V. Delgado, “Dielectric dispersion in aqueous colloidal systems,” *Current Opinion in Colloid and Interface Science,* vol. 15, no. 3, pp. 145-159, 2010.

[126] A. Ramos, P. García-Sánchez, and H. Morgan, “AC electrokinetics of conducting microparticles: A review,” *Current Opinion in Colloid and Interface Science,* vol. 24, pp. 79-90, 2016.

[127] D. Li, "Single-Phase Electrokinetic Flow in Microchannels," *Heat Transfer and Fluid Flow in Minichannels and Microchannels*, pp. 175-219: Elsevier Ltd., 2013.

[128] R. B. Schoch, J. Han, and P. Renaud, “Transport phenomena in nanofluidics,” *Reviews of Modern Physics,* vol. 80, no. 3, pp. 839-883, 2008.

[129] H. Matsumura, "Surface conductivity," *Electrical Phenomena at Interfaces: Fundamentals Measurements, and Applications, Second Edition, Revised and Expanded*, pp. 305-321: CRC Press, 2018.

[130] V. L. Shapovalov, and G. Brezesinski, “Breakdown of the Gouy - Chapman model for highly charged Langmuir monolayers: Counterion size effect,” *Journal of Physical Chemistry B,* vol. 110, no. 20, pp. 10032-10040, 2006.

[131] A. Martín-Molina, M. Quesada-Pérez, and R. Hidalgo-Álvarez, "Ionic structures in colloidal electric double layers: Ion size correlations," *Structure and Functional Properties of Colloidal Systems*, pp. 63-76: CRC Press, 2009.

[132] M. Quesada-Pérez, E. González-Tovar, A. Martín-Molina, M. Lozada-Cassou, and R. Hidalgo-Álvarez, "Overcharging in colloids: Beyond the Poisson-Boltzmann approach," *ChemPhysChem,* vol. 4, no. 3, pp. 234-248, 2003.

[133] R. Kant, and M. B. Singh, "Generalization of the Gouy-Chapman-Stern model of an electric double layer for a morphologically complex electrode: Deterministic and stochastic morphologies," *Physical Review E - Statistical, Nonlinear, and Soft Matter Physics,* vol. 88, no. 5, 2013.

[134] M. A. Brown, Z. Abbas, A. Kleibert, R. G. Green, A. Goel, S. May, and T. M. Squires, "Determination of surface potential and electrical double-layer structure at the aqueous electrolyte-nanoparticle interface," *Physical Review X,* vol. 6, no. 1, 2016.

[135] Y. Gu, and D. Li, "The ζ-potential of glass surface in contact with aqueous solutions," *Journal of Colloid and Interface Science,* vol. 226, no. 2, pp. 328-339, 2000.

[136] M. Z. Bazant, and T. M. Squires, "Induced-charge electrokinetic phenomena," *Current Opinion in Colloid and Interface Science,* vol. 15, no. 3, pp. 203-213, 2010.

[137] P. García-Sánchez, A. Ramos, and A. González, "Effects of Faradaic currents on AC electroosmotic flows with coplanar symmetric electrodes," *Colloids and Surfaces A: Physicochemical and Engineering Aspects,* vol. 376, no. 1-3, pp. 47-52, 2011.

[138] R. Baños, J. Arcos, O. Bautista, and F. Méndez, "Slippage effect on the oscillatory electroosmotic flow of power-law fluids in a microchannel," *Defect and Diffusion Forum,* vol. 399, pp. 92-101, 2020.

[139] V. Calero, P. Garcia-Sanchez, C. Honrado, A. Ramos, and H. Morgan, "AC electrokinetic biased deterministic lateral displacement for tunable particle separation," *Lab on a Chip,* vol. 19, no. 8, pp. 1386-1396, 2019.

[140] P. García-Sánchez, J. J. Arcenegui, H. Morgan, and A. Ramos, "Self-assembly of metal nanowires induced by alternating current electric fields," *Applied Physics Letters,* vol. 106, no. 2, 2015.

[141] N. G. Green, A. Ramos, A. González, H. Morgan, and A. Castellanos, "Fluid flow induced by nonuniform ac electric fields in electrolytes on microelectrodes. I. Experimental measurements," *Physical Review E - Statistical Physics, Plasmas, Fluids, and Related Interdisciplinary Topics,* vol. 61, no. 4, pp. 4011-4018, 2000.

[142] N. Islam, M. Lian, and J. Wu, "Enhancing microcantilever capability with integrated AC electroosmotic trapping," *Microfluidics and Nanofluidics,* vol. 3, no. 3, pp. 369-375, 2007.

[143] A. González, A. Ramos, N. G. Green, A. Castellanos, and H. Morgan, "Fluid flow induced by nonuniform ac electric fields in electrolytes on microelectrodes. II. A linear double-layer analysis," *Physical Review E - Statistical Physics, Plasmas, Fluids, and Related Interdisciplinary Topics,* vol. 61, no. 4, pp. 4019-4028, 2000.

[144] S. Talapatra, and S. Chakraborty, "Double layer overlap in ac electroosmosis," *European Journal of Mechanics, B/Fluids,* vol. 27, no. 3, pp. 297-308, 2008.

[145] J. J. Arcenegui, P. García-Sánchez, H. Morgan, and A. Ramos, "Electro-orientation and electrorotation of metal nanowires," *Physical Review E - Statistical, Nonlinear, and Soft Matter Physics,* vol. 88, no. 6, 2013.

[146] A. Ramos, A. González, A. Castellanos, N. G. Green, and H. Morgan, "Pumping of liquids with ac voltages applied to asymmetric pairs of microelectrodes," *Physical Review E - Statistical, Nonlinear, and Soft Matter Physics,* vol. 67, no. 5 2, pp. 056302/1-056302/11, 2003.

[147] M. R. Bown, and C. D. Meinhart, "AC electroosmotic flow in a DNA concentrator," *Microfluidics and Nanofluidics,* vol. 2, no. 6, pp. 513-523, 2006.

[148] E. M. Melvin, B. R. Moore, K. H. Gilchrist, S. Grego, and O. D. Velev, "On-chip collection of particles and cells by AC electroosmotic pumping and dielectrophoresis using asymmetric microelectrodes," *Biomicrofluidics,* vol. 5, no. 3, 2011.

[149] C. C. Huang, M. Z. Bazant, and T. Thorsen, "Ultrafast high-pressure AC electro-osmotic pumps for portable biomedical microfluidics," *Lab on a Chip,* vol. 10, no. 1, pp. 80-85, 2010.

[150] B. D. Storey, L. R. Edwards, M. S. Kilic, and M. Z. Bazant, "Steric effects on ac electro-osmosis in dilute electrolytes," *Physical Review E - Statistical, Nonlinear, and Soft Matter Physics,* vol. 77, no. 3, 2008.

[151] M. Z. Bazant, and T. M. Squires, "Induced-Charge Electrokinetic Phenomena: Theory and Microfluidic Applications," *Physical Review Letters,* vol. 92, no. 6, 2004.

[152] M. C. Calderer, D. Golovaty, O. Lavrentovich, and N. J. Walkington, "Modeling of nematic electrolytes and nonlinear electroosmosis," *SIAM Journal on Applied Mathematics,* vol. 76, no. 6, pp. 2260-2285, 2016.

[153] H. Feng, and T. N. Wong, "Induced-charge electro-osmosis in dielectric annuli," *Applied Mathematics and Computation,* vol. 333, pp. 133-144, 2018.

[154] Z. Ge, H. Yan, W. Liu, C. Song, R. Xue, and Y. Ren, “A numerical investigation of enhancing microfluidic heterogeneous immunoassay on bipolar electrodes driven by induced-charge electroosmosis in rotating electric fields,” *Micromachines,* vol. 11, no. 8, 2020.

[155] L. Højgaard Olesen, M. Z. Bazant, and H. Bruus, “Strongly nonlinear dynamics of electrolytes in large ac voltages,” *Physical Review E - Statistical, Nonlinear, and Soft Matter Physics,* vol. 82, no. 1, 2010.

[156] A. J. Moghadam, “Thermal transport characteristics of AC electrokinetic flow in a micro-annulus,” *Journal of Thermal Analysis and Calorimetry*, 2020.

[157] H. Sugioka, “Direct simulation of phase delay effects on induced-charge electro-osmosis under large ac electric fields,” *Physical Review E,* vol. 94, no. 2, 2016.

[158] C. Zhao, and C. Yang, “AC field induced-charge electroosmosis over leaky dielectric blocks embedded in a microchannel,” *Electrophoresis,* vol. 32, no. 5, pp. 629-637, 2011.

[159] N. Ellerington, T. Hubbard, and M. Kujath, “Electrokinetic movement of micro-objects in fluids using microelectromechanical system electrode arrays,” *Journal of Vacuum Science and Technology A: Vacuum, Surfaces and Films,* vol. 22, no. 3, pp. 831-836, 2004.

[160] P. García-Sánchez, A. Ramos, A. González, N. G. Green, and H. Morgan, “Flow reversal in traveling-wave electrokinetics: An analysis of forces due to ionic concentration gradients,” *Langmuir,* vol. 25, no. 9, pp. 4988-4997, 2009.

[161] P. Modarres, and M. Tabrizian, “Phase-controlled field-effect micromixing using AC electroosmosis,” *Microsystems and Nanoengineering,* vol. 6, no. 1, 2020.

[162] H. Sugioka, “Asymmetrical reverse vortex flow due to induced-charge electro-osmosis around carbon stacking structures,” *Physical Review E - Statistical, Nonlinear, and Soft Matter Physics,* vol. 83, no. 5, 2011.

[163] Z. Chen, and T. Hobo, “Chemically L-phenylalaninamide-modified monolithic silica column prepared by a Sol-Gel process for enantioseparation of dansyl amino acids by ligand exchange-capillary electrochromatography,” *Analytical Chemistry,* vol. 73, no. 14, pp. 3348-3357, 2001.

[164] S. H. Hyeung, K. Sangmo, and K. S. Yong, “An experimental study on the AC electroosmotic flow around a pair of electrodes in a microchannel,” *Journal of Mechanical Science and Technology,* vol. 21, no. 12, pp. 2237-2243, 2007.

[165] J. P. Urbanski, J. A. Levitan, D. N. Burch, T. Thorsen, and M. Z. Bazant, “The effect of step height on the performance of three-dimensional ac electro-osmotic microfluidic pumps,” *Journal of Colloid and Interface Science,* vol. 309, no. 2, pp. 332-341, 2007.

[166] M. Z. Bazant, M. S. Kilic, B. D. Storey, and A. Ajdari, “Nonlinear electrokinetics at large voltages,” *New Journal of Physics,* vol. 11, 2009.

[167] J. Cao, P. Cheng, and F. J. Hong, “Applications of electrohydrodynamics and Joule heating effects in microfluidic chips: A review,” *Science in China, Series E: Technological Sciences,* vol. 52, no. 12, pp. 3477-3490, 2009.

[168] P. Červenka, M. Přibyl, and D. Šnita, “Numerical study on AC electroosmosis in microfluidic channels,” *Microelectronic Engineering,* vol. 86, no. 4-6, pp. 1333-1336, 2009.

[169] W. Y. Ng, Y. C. Lam, and I. Rodríguez, "DC-biased AC-electrokinetic flow: A mechanistic investigation." pp. 64-66.

[170] P. Červenka, J. Hrdlička, M. Přibyl, and D. Šnita, “Toward high net velocities in AC electroosmotic micropumps based on asymmetric coplanar electrodes,” *IEEE Transactions on Industry Applications,* vol. 46, no. 5, pp. 1679-1691, 2010.

[171] B. G. Hawkins, and B. J. Kirby, “Electrothermal flow effects in insulating (electrodeless) dielectrophoresis systems,” *Electrophoresis,* vol. 31, no. 22, pp. 3622-3633, 2010.

[172] S. H. Huang, H. J. Hsueh, and K. Y. Hung, “Configurable AC electroosmotic generated in-plane microvortices and pumping flow in microchannels,” *Microfluidics and Nanofluidics,* vol. 8, no. 2, pp. 187-195, 2010.

[173] B. J. Kim, S. H. Lee, S. Rezazadeh, and H. J. Sung, “Simulation of an ac electro-osmotic pump with step microelectrodes,” *Physical Review E - Statistical, Nonlinear, and Soft Matter Physics,* vol. 83, no. 5, 2011.

[174] M. Motosuke, K. Yamasaki, A. Ishida, H. Toki, and S. Honami, “Improved particle concentration by cascade AC electroosmotic flow,” *Microfluidics and Nanofluidics,* vol. 14, no. 6, pp. 1021-1030, 2013.

[175] R. An, D. O. Wipf, and A. R. Minerick, “Spatially variant red blood cell crenation in alternating current non-uniform fields,” *Biomicrofluidics,* vol. 8, no. 2, 2014.

[176] Z. Yin, Y. J. Jian, L. Chang, R. Na, and Q. S. Liu, "Transient AC electro-osmotic flow of generalized Maxwell fluids through microchannels," Trans Tech Publications, 2014, pp. 216-223.

[177] A. Salari, M. Navi, and C. Dalton, “A novel alternating current multiple array electrothermal micropump for lab-on-a-chip applications,” *Biomicrofluidics,* vol. 9, no. 1, 2015.

[178] A. Boymelgreen, G. Yossifon, and T. Miloh, “Propulsion of Active Colloids by Self-Induced Field Gradients,” *Langmuir,* vol. 32, no. 37, pp. 9540-9547, 2016.

[179] X. Wu, P. Ramiah Rajasekaran, and C. R. Martin, “An Alternating Current Electroosmotic Pump Based on Conical Nanopore Membranes,” *ACS Nano,* vol. 10, no. 4, pp. 4637-4643, 2016.

[180] M. Ghandchi, and R. H. Vafaie, “AC electrothermal actuation mechanism for on-chip mixing of high ionic strength fluids,” *Microsystem Technologies,* vol. 23, no. 5, pp. 1495-1507, 2017.

[181] K. Yoshida, T. Sato, S. I. Eom, J. W. Kim, and S. Yokota, “A study on an AC electroosmotic micropump using a square pole – Slit electrode array,” *Sensors and Actuators, A: Physical,* vol. 265, pp. 152-160, 2017.

[182] W. Zhao, X. Liu, F. Yang, K. Wang, J. Bai, R. Qiao, and G. Wang, “Study of Oscillating Electroosmotic Flows with High Temporal and Spatial Resolution,” *Analytical Chemistry,* vol. 90, no. 3, pp. 1652-1659, 2018.

[183] M. Vázquez-Piñón, H. Hwang, M. J. Madou, L. Kulinsky, and S. O. Martínez-Chapa, “Comparison of two-dimensional and three-dimensional carbon electrode geometries affecting bidirectional electroosmotic pumping,” *Journal of Micro and Nano-Manufacturing,* vol. 7, no. 2, 2019.

[184] M. Vazquez-Pinon, B. Pramanick, F. G. Ortega-Gama, V. H. Perez-Gonzalez, L. Kulinsky, M. J. Madou, H. Hwang, and S. O. Martinez-Chapa, “Hydrodynamic channeling as a controlled flow reversal mechanism for bidirectional AC electroosmotic pumping using glassy carbon microelectrode arrays,” *Journal of Micromechanics and Microengineering,* vol. 29, no. 7, 2019.

[185] T. Miloh, and J. Nagler, “Electrorotation of leaky-dielectric and conducting microspheres in asymmetric electrolytes and angular velocity reversal,” *Electrophoresis,* vol. 41, no. 15, pp. 1296-1307, 2020.

[186] H. Y. Hafeez, and C. E. Ndikilar, "Boundary layer equations in fluid dynamics," *Applications of Heat, Mass and Fluid Boundary Layers*, pp. 67-94: Elsevier, 2020.

[187] O. C. Okoye, and B. O. Bolaji, "Physics of fluid motion," *Applications of Heat, Mass and Fluid Boundary Layers*, pp. 1-22: Elsevier, 2020.

[188] M. M. Gregersen, L. H. Olesen, A. Brask, M. F. Hansen, and H. Bruus, “Flow reversal at low voltage and low frequency in a microfabricated ac electrokinetic pump,” *Physical Review E - Statistical, Nonlinear, and Soft Matter Physics,* vol. 76, no. 5, 2007.

[189] E. M. Wasson, T. A. Douglas, and R. V. Davalos, "Mechanical and electrical principles for separation of rare cells," *Microfluidic Methods for Molecular Biology*, pp. 253-294: Springer International Publishing, 2016.

[190] F. Bai, X. He, X. Yang, R. Zhou, and C. Wang, “Three dimensional phase-field investigation of droplet formation in microfluidic flow focusing devices with experimental validation,” *International Journal of Multiphase Flow,* vol. 93, pp. 130-141, 2017.

[191] M. Wörner, “Numerical modeling of multiphase flows in microfluidics and micro process engineering: A review of methods and applications,” *Microfluidics and Nanofluidics,* vol. 12, no. 6, pp. 841-886, 2012.

[192] J. Oh, R. Hart, J. Capurro, and H. Noh, “Comprehensive analysis of particle motion under non-uniform AC electric fields in a microchannel,” *Lab on a Chip,* vol. 9, no. 1, pp. 62-78, 2009.

[193] Z. R. Tang, M. R. Malik, T. L. Shi, J. Gong, L. Nie, and G. L. Liao, "Modelling and fabrication of 3-D Carbon-MEMS for dielectrophoretic manipulation of micro/nanoparticles in fluids," Trans Tech Publications Ltd, 2009, pp. 435-440.

[194] L. Yonghong, Z. Zhan, X. Jing, P. Cheng, F. Zhen, and D. Lidong, "Studies on dielectrophoretic separation using biochips with different electrode shapes."

[195] A. Ramos, H. Morgan, N. G. Green, and A. Castellanos, “AC Electric-Field-Induced Fluid Flow in Microelectrodes,” *J Colloid Interface Sci,* vol. 217, no. 2, pp. 420-422, Sep 15, 1999.

[196] A. Ajdari, “Pumping liquids using asymmetric electrode arrays,” *Physical Review E - Statistical Physics, Plasmas, Fluids, and Related Interdisciplinary Topics,* vol. 61, no. 1, pp. R45-R48, 2000.

[197] N. G. Green, A. Ramos, A. González, H. Morgan, and A. Castellanos, “Fluid flow induced by nonuniform ac electric fields in electrolytes on microelectrodes. III. Observation of streamlines and numerical simulation,” *Physical Review E - Statistical Physics, Plasmas, Fluids, and Related Interdisciplinary Topics,* vol. 66, no. 2, 2002.

[198] S. Wall, “The history of electrokinetic phenomena,” *Current Opinion in Colloid and Interface Science,* vol. 15, no. 3, pp. 119-124, 2010.

[199] F. Björk, B. Sederholm, J. Trägårdh, and B. Olofsson, "Electroosmosis - A method applied for handling of moisture in foundations."

[200] H. A. Pohl, and I. Hawk, “Separation of living and dead cells by dielectrophoresis,” *Science,* vol. 152, no. 3722, pp. 647-649, 1966.

[201] J. P. Schwar, “Particle Separations by Nonuniform Electric Fields in Liquid Dielectrics, Batch Methods,” *Journal of the Electrochemical Society,* vol. 107, no. 5, pp. 383-385, 1960.

[202] H. A. Pohl, and J. S. Crane, “Dielectrophoresis of Cells,” *Biophysical Journal,* vol. 11, no. 9, pp. 711-727, 1971.

[203] Y. Huang, and R. Pethig, “Electrode design for negative dielectrophoresis,” *Measurement Science and Technology,* vol. 2, no. 12, pp. 1142-1146, 1991.

[204] R. Pethig, and G. H. Markx, “Applications of dielectrophoresis in biotechnology,” *Trends in Biotechnology,* vol. 15, no. 10, pp. 426-432, 1997.

[205] Y. Huang, X. B. Wang, F. F. Becker, and P. R. C. Gascoyne, “Introducing dielectrophoresis as a new force field for field-flow fractionation,” *Biophysical Journal,* vol. 73, no. 2, pp. 1118-1129, 1997.

[206] N. G. Green, and H. Morgan, “Separation of submicrometre particles using a combination of dielectrophoretic and electrohydrodynamic forces,” *Journal of Physics D: Applied Physics,* vol. 31, no. 7, pp. L25-L30, 1998.

[207] N. G. Green, H. Morgan, and J. J. Milner, “Manipulation and trapping of sub-micron bioparticles using dielectrophoresis,” *Journal of Biochemical and Biophysical Methods,* vol. 35, no. 2, pp. 89-102, 1997.

[208] M. P. Hughes, H. Morgan, F. J. Rixon, J. P. H. Burt, and R. Pethig, "Manipulation of herpes simplex virus type 1 by dielectrophoresis," *Biochimica et Biophysica Acta - General Subjects,* vol. 1425, no. 1, pp. 119-126, 1998.

[209] A. P. Brown, K. R. Milner, D. W. E. Allsopp, and W. B. Betts, "Characteristic dielectrophoretic collection of 20nm latex beads measured by an impedance technique," *Electronics Letters,* vol. 34, no. 20, pp. 1934-1936, 1998.

[210] T. Schnelle, T. Müller, G. Gradl, S. G. Shirley, and G. Fuhr, "Dielectrophoretic manipulation of suspended submicron particles," *Electrophoresis,* vol. 21, no. 1, pp. 66-73, 2000.

[211] F. Arai, M. Ogawa, and T. Fukuda, "Bilateral control system for laser micromanipulation by force feedback," *Advanced Robotics,* vol. 14, no. 5, pp. 381-383, 2000.

[212] S. Ogata, T. Yasukawa, and T. Matsue, "Dielectrophoretic manipulation of a single chlorella cell with dual-microdisk electrode," *Bioelectrochemistry,* vol. 54, no. 1, pp. 33-37, 2001.

[213] J. Voldman, R. A. Braff, M. Toner, M. L. Gray, and M. A. Schmidt, "Holding forces of single-particle dielectrophoretic traps," *Biophysical Journal,* vol. 80, no. 1, pp. 531-542, 2001.

[214] M. P. Hughes, "Strategies for dielectrophoretic separation in laboratory-on-a-chip systems," *Electrophoresis,* vol. 23, no. 16, pp. 2569-2582, 2002.

[215] M. P. Hughes, "Dielectrophoretic behavior of latex nanospheres: Low-frequency dispersion," *Journal of Colloid and Interface Science,* vol. 250, no. 2, pp. 291-294, 2002.

[216] P. R. C. Gascoyne, and J. Vykoukal, “Particle separation by dielectrophoresis,” *Electrophoresis,* vol. 23, no. 13, pp. 1973-1983, 2002.

[217] H. Zhou, L. R. White, and R. D. Tilton, “Lateral separation of colloids or cells by dielectrophoresis augmented by AC electroosmosis,” *Journal of Colloid and Interface Science,* vol. 285, no. 1, pp. 179-191, 2005.

[218] M. Borgatti, L. Altomare, M. Baruffa, E. Fabbri, G. Breveglieri, G. Feriotto, N. Manaresi, G. Medoro, A. Romani, M. Tartagni, R. Gambari, and R. Guerrieri, “Separation of white blood cells from erythrocytes on a dielectrophoresis (DEP) based 'Lab-on-a-chip' device,” *International journal of molecular medicine,* vol. 15, no. 6, pp. 913-920, 2005.

[219] M. Wiklund, C. Günther, R. Lemor, M. Jäger, G. Fuhr, and H. M. Hertz, “Ultrasonic standing wave manipulation technology integrated into a dielectrophoretic chip,” *Lab on a Chip,* vol. 6, no. 12, pp. 1537-1544, 2006.

[220] D. Yan, C. Yang, N. T. Nguyen, and X. Huang, "Measurement of transient electrokinetic flow in microchannels using micro-piv technique." pp. 223-232.

[221] C. H. Tai, S. K. Hsiung, C. Y. Chen, M. L. Tsai, and G. B. Lee, “Automatic microfluidic platform for cell separation and nucleus collection,” *Biomedical Microdevices,* vol. 9, no. 4, pp. 533-543, 2007.

[222] Q. Yuan, N. Islam, and J. Wu, “AC electrokinetics based capture of yeast cells from ultra-fast through-flow for sensitive detection,” *Micro and Nano Letters,* vol. 12, no. 11, pp. 901-906, 2017.

[223] S. D. E. Kushigbor, Z. Tang, and L. Yobas, "Railing Nanoparticles Along Activated Tracks Towards Continuous-Flow Electrokinetic Concentration from Blood Plasma." pp. 2249-2252.

[224] C. H. Han, S. Y. Woo, A. Sharma, and J. Jang, "Rapid and selective electrokinetic concentration of bacteria using AC signal superposition on two coplanar electrodes." pp. 1315-1317.

[225] V. Bacheva, F. Paratore, S. Rubin, G. V. Kaigala, and M. Bercovici, “Tunable Bidirectional Electroosmotic Flow for Diffusion-Based Separations,” *Angewandte Chemie - International Edition,* vol. 59, no. 31, pp. 12894-12899, 2020.

[226] G. H. Markx, J. Rousselet, and R. Pethig, “DEP-FFF Field-flow fractionation using non-uniform electric fields,” *Journal of Liquid Chromatography and Related Technologies,* vol. 20, no. 16-17, pp. 2857-2872, 1997.

[227] M. Scott, R. Paul, and K. V. I. S. Kaler, “Theory of frequency-dependent polarization of general planar electrodes with zeta potentials of arbitrary magnitude in ionic media: 1. Theoretical foundations and general results,” *Journal of Colloid and Interface Science,* vol. 230, no. 2, pp. 377-387, 2000.

[228] M. Scott, K. V. I. S. Kaler, and R. Paul, “Theoretical model of electrode polarization and AC electroosmotic fluid flow in planar electrode arrays,” *Journal of Colloid and Interface Science,* vol. 238, no. 2, pp. 449-451, 2001.

[229] A. Ramos, A. González, N. G. Green, H. Morgan, and A. Castellanos, “Comment on "theoretical model of electrode polarization and AC electroosmotic fluid flow in planar electrode arrays",” *Journal of Colloid and Interface Science,* vol. 243, no. 1, pp. 265-266, 2001.

[230] H. Jiang, B. Yan, H. Yang, and R. Antonio, “Driving mechanism of AC EO and calculation of velocity,” *Zhongguo Jixie Gongcheng/China Mechanical Engineering,* vol. 18, no. 14, pp. 1672-1675, 2007.

[231] A. B. D. Brown, C. G. Smith, and A. R. Rennie, “Pumping of water with ac electric fields applied to asymmetric pairs of microelectrodes,” *Physical Review E - Statistical Physics, Plasmas, Fluids, and Related Interdisciplinary Topics,* vol. 63, no. 1, 2001.

[232] N. Loucaides, A. Ramos, and G. E. Georghiou, “Novel systems for configurable AC electroosmotic pumping,” *Microfluidics and Nanofluidics,* vol. 3, no. 6, pp. 709-714, 2007.

[233] N. G. Loucaides, G. E. Georghiou, and C. D. Charalambous, “Numerical simulation of the dielectrophoretic concentration of DNA particles and the effect of AC electroosmosis,” *Journal of Physics: Conference Series,* vol. 61, no. 1, pp. 718-723, 2007.

[234] B. P. Cahill, L. J. Heyderman, J. Gobrecht, and A. Stemmer, “Electro-osmotic pumping on application of phase-shifted signals to interdigitated electrodes,” *Sensors and Actuators, B: Chemical,* vol. 110, no. 1, pp. 157-163, 2005.

[235] P. K. Wong, C. Y. Chen, T. H. Wang, and C. M. Ho, "An AC electroosmotic processor for biomolecules." pp. 20-23.

[236] N. G. Green, "Particle movement in microelectrode structures in AC electric fields, under the influence of dielectrophoresis and electrohydrodynamics." pp. 63-66.

[237] L. Tanguy, and L. Nicu, “Controlled localization and enhanced gathering of particles on microfabricated concentrators assisted by ac-electro-osmosis,” *Journal of Applied Physics,* vol. 105, no. 10, 2009.

[238] E. B. Cummings, and A. K. Singh, “Dielectrophoresis in microchips containing arrays of insulating posts: Theoretical and experimental results,” *Analytical Chemistry,* vol. 75, no. 18, pp. 4724-4731, 2003.

[239] Y. Zhang, T. N. Wong, C. Yang, and K. T. Ooi, “Electroosmotic flow in irregular shape microchannels,” *International Journal of Engineering Science,* vol. 43, no. 19-20, pp. 1450-1463, 2005.

[240] K. Adamiak, "AC electroosmotic flow in electrolytes generated toy two coplanar microelectrodes." pp. 574-577.

[241] P. Pham, I. Texier, A. S. Larrea, R. Blanc, F. Revol-Cavalier, H. Grateau, and F. Perraut, “Numerical design of a 3-D microsystem for bioparticle dielectrophoresis: The Pyramidal Microdevice,” *Journal of Electrostatics,* vol. 65, no. 8, pp. 511-520, 2007.

[242] H. K. Yang, H. R. Ao, Y. Wang, and H. Y. Jiang, “Velocity calculation of the electro-osmotic flow on the surface of microelectrode caused by AC electric field,” *Harbin Gongye Daxue Xuebao/Journal of Harbin Institute of Technology,* vol. 40, no. 11, pp. 1732-1735, 2008.

[243] A. J. Moghadam, “Exact solution of AC electro-osmotic flow in a microannulus,” *Journal of Fluids Engineering, Transactions of the ASME,* vol. 135, no. 9, 2013.

[244] A. J. Moghadam, “Effect of periodic excitation on alternating current electroosmotic flow in a microannular channel,” *European Journal of Mechanics, B/Fluids,* vol. 48, pp. 1-12, 2014.

[245] M. Mpholo, C. G. Smith, and A. B. D. Brown, “Low voltage plug flow pumping using anisotropic electrode arrays,” *Sensors and Actuators, B: Chemical,* vol. 92, no. 3, pp. 262-268, 2003.

[246] D. S. Liao, J. Raveendran, S. Golchi, and A. Docoslis, “Fast and sensitive detection of bacteria from a water droplet by means of electric field effects and micro-Raman spectroscopy,” *Sensing and Bio-Sensing Research,* vol. 6, pp. 59-66, 2015.

[247] K. F. Hoettges, M. P. Hughes, A. Cotton, N. A. E. Hopkins, and M. B. McDonnell, “Optimizing Particle Collection for Enhanced Surface-Based Biosensors,” *IEEE Engineering in Medicine and Biology Magazine,* vol. 22, no. 6, pp. 68-74, 2003.

[248] S. Debesset, C. J. Hayden, C. Dalton, J. C. T. Eijkel, and A. Manz, “An AC electroosmotic micropump for circular chromatographic applications,” *Lab on a Chip,* vol. 4, no. 4, pp. 396-400, 2004.

[249] Marcos, C. Yang, K. T. Ooi, T. N. Wong, and J. H. Masliyah, “Frequency-dependent laminar electroosmotic flow in a closed-end rectangular microchannel,” *Journal of Colloid and Interface Science,* vol. 275, no. 2, pp. 679-698, 2004.

[250] Marcos, Y. J. Kang, K. T. Ooi, C. Yang, and T. N. Wong, “Frequency-dependent velocity and vorticity fields of electro-osmotic flow in a closed-end cylindrical microchannel,” *Journal of Micromechanics and Microengineering,* vol. 15, no. 2, pp. 301-312, 2005.

[251] J. Wu, Y. Ben, D. Battigelli, and H. C. Chang, “Long-range AC electroosmotic trapping and detection of bioparticles,” *Industrial and Engineering Chemistry Research,* vol. 44, no. 8, pp. 2815-2822, 2005.

[252] J. Wu, Y. Ben, and H. C. Chang, “Particle detection by electrical impedance spectroscopy with asymmetric-polarization AC electroosmotic trapping,” *Microfluidics and Nanofluidics,* vol. 1, no. 2, pp. 161-167, 2005.

[253] P. K. Wong, C. Y. Chen, T. H. Wang, and C. M. Ho, “Electrokinetic bioprocessor for concentrating cells and molecules,” *Analytical Chemistry,* vol. 76, no. 23, pp. 6908-6914, 2005.

[254] Z. Gagnon, and H. C. Chang, “Aligning fast alternating current electroosmotic flow fields and characteristic frequencies with dielectrophoretic traps to achieve rapid bacteria detection,” *Electrophoresis,* vol. 26, no. 19, pp. 3725-3737, 2005.

[255] P. García-Sánchez, A. Ramos, N. G. Green, and H. Morgan, “Experiments on AC electrokinetic pumping of liquids using arrays of microelectrodes,” *IEEE Transactions on Dielectrics and Electrical Insulation,* vol. 13, no. 3, pp. 670-677, 2006.

[256] S. H. Huang, S. K. Wang, H. S. Khoo, and F. G. Tseng, "AC electroosmotic generated in-plane microvortices for stationary or continuous fluid mixing." pp. 1349-1352.

[257] J. Wu, and N. Islam, “A simple method to integrate in situ nano-particle focusing with cantilever detection,” *IEEE Sensors Journal,* vol. 7, no. 6, pp. 957-958, 2007.

[258] C. Wei, C. W. Hsu, and C. C. Wang, "The role of electro-osmosis and dielectrophoresis in collection of micro/nano size particles in low frequency AC electric field."

[259] N. G. Loucaides, A. Ramos, and G. E. Georghiou, "Trapping and manipulation of nanoparticles by using jointly dielectrophoresis and AC electroosmosis."

[260] S. Park, and A. Beskok, “Alternating current electrokinetic motion of colloidal particles on interdigitated microelectrodes,” *Analytical Chemistry,* vol. 80, no. 8, pp. 2832-2841, 2008.

[261] S. Loire, and I. Mezic, "Joint use of traveling wave dielectrophoresis and AC-electroosmosis for particle manipulation." pp. 643-648.

[262] P. Tathireddy, Y. H. Choi, and M. Skliar, “Particle AC electrokinetics in planar interdigitated microelectrode geometry,” *Journal of Electrostatics,* vol. 66, no. 11-12, pp. 609-619, 2008.

[263] H. Yang, H. Jiang, H. Ao, A. R. Reyes, and P. Garcia-Sanchez, "A symmetry electrode array for AC and traveling wave electroosmosis pumping."

[264] V. Studer, A. Pépin, Y. Chen, and A. Ajdari, “An integrated AC electrokinetic pump in a microfluidic loop for fast and tunable flow control,” *Analyst,* vol. 129, no. 10, pp. 944-949, 2004.

[265] Y. Wang, Y. K. Suh, and S. Kang, “A study on the slip velocity on a pair of asymmetric electrodes for AC-electroosmosis in a microchannel,” *Journal of Mechanical Science and Technology,* vol. 23, no. 3, pp. 874-884, 2009.

[266] J. J. Capurro, and H. Noh, "Characterization of AC electrokinetic forces using pressure-driven flow in a microchannel." pp. 1061-1069.

[267] R. Yokokawa, Y. Manta, M. Namura, Y. Takizawa, N. C. H. Le, and S. Sugiyama, “Individual evaluation of DEP, EP and AC-EOF effects on λDNA molecules in a DNA concentrator,” *Sensors and Actuators, B: Chemical,* vol. 143, no. 2, pp. 769-775, 2010.

[268] J. Wang, and H. D. Ou-Yang, "Optical tweezers as a force sensor for separating dielectrophoresis and AC electroosmosis forces."

[269] W. H. Yeo, F. L. Chou, G. Fotouhi, K. Oh, B. T. Stevens, H. Y. Tseng, D. Gao, A. Q. Shen, J. H. Chung, and K. H. Lee, “Size-selective immunofluorescence of Mycobacterium tuberculosis cells by capillary- and viscous forces,” *Lab on a Chip,* vol. 10, no. 22, pp. 3178-3181, 2010.

[270] Y. M. Senousy, and C. K. Harnett, “Fast three dimensional ac electro-osmotic pumps with nonphotolithographic electrode patterning,” *Biomicrofluidics,* vol. 4, no. 3, 2010.

[271] S. Valagerahally Puttaswamy, S. Sivashankar, C. H. Yeh, R. J. Chen, and C. H. Liu, “Electrodynamically actuated on-chip flow cytometry with low shear stress for electro-osmosis based sorting using low conductive medium,” *Microelectronic Engineering,* vol. 87, no. 12, pp. 2582-2591, 2010.

[272] Z. Liu, M. F. M. Speetjens, A. J. H. Frijns, and A. A. Van Steenhoven, "Continuous particle separation with ac electro-osmosis and dielectrophoresis in a microchannel." pp. 177-182.

[273] N. Islam, and J. Reyna, “Bi-directional flow induced by an AC electroosmotic micropump with DC voltage bias,” *Electrophoresis,* vol. 33, no. 7, pp. 1191-1197, 2012.

[274] N. G. Loucaides, A. Ramos, and G. E. Georghiou, “Dielectrophoretic and AC electroosmotic trapping of DNA: Numerical simulation incorporating fluid dynamics and steric particle effects,” *Journal of Electrostatics,* vol. 69, no. 2, pp. 111-118, 2011.

[275] A. Ishida, H. Toki, M. Motosuke, and S. Honami, “Particle accumulation by AC electroosmosis in microfluidic device with co-planar electrodes,” *Journal of Thermal Science and Technology,* vol. 7, no. 3, pp. 475-486, 2012.

[276] M. N. Mohtar, K. F. Hoettges, and M. P. Hughes, “Factors affecting particle collection by electro-osmosis in microfluidic systems,” *Electrophoresis,* vol. 35, no. 2-3, pp. 345-351, 2014.

[277] M. N. Mohtar, M. U. Ziaudin Ahamed, N. F. Ismail, N. A. Yunus, and S. Shafie, “Effect of interelectrode gap to the manipulations of particle using AC electroosmosis,” *International Journal of Control Theory and Applications,* vol. 9, no. 31, pp. 31-36, 2016.

[278] K. F. Hoettges, M. B. McDonnell, and M. P. Hughes, “Continuous flow nanoparticle concentration using alternating current-electroosmotic flow,” *Electrophoresis,* vol. 35, no. 4, pp. 467-473, 2014.

[279] C. Wei, and L. C. Wu, "The effect of frequency on the flow and particle collection patterns under electroosmosis," Trans Tech Publications Ltd, 2014, pp. 59-62.

[280] D. Das, Z. Yan, N. V. Menon, Y. Kang, V. Chan, and C. Yang, “Continuous detection of trace level concentration of oil droplets in water using microfluidic AC electroosmosis (ACEO),” *RSC Advances,* vol. 5, no. 86, pp. 70197-70203, 2015.

[281] J. H. Chen, Y. C. Lee, and W. H. Hsieh, “AC electroosmotic microconcentrator using a face-to-face, asymmetric electrode pair with expanded sections in the bottom electrode,” *Microfluidics and Nanofluidics,* vol. 20, no. 5, 2016.

[282] M. L. Y. Sin, V. Gau, J. C. Liao, D. A. Haake, and P. K. Wong, “Active manipulation of quantum dots using ac electrokinetics,” *Journal of Physical Chemistry C,* vol. 113, no. 16, pp. 6561-6565, 2009.

[283] M. Costella, M. Frénéa-Robin, J. Marchalot, J. Moreau, O. Andreiev, M. Canva, and P. Charette, "Surface plasmon resonance imaging enhanced by dielectrophoresis and AC-electroosmosis."

[284] E. Du, and S. P. Manoochehri, "Numerical simulation of AC electrothermal microfluidic pumping." pp. 487-493.

[285] H. Mirzajani, C. Cheng, J. Wu, C. S. Ivanoff, E. Najafi Aghdam, and H. Badri Ghavifekr, “Design and characterization of a passive, disposable wireless AC-electroosmotic lab-on-a-film for particle and fluid manipulation,” *Sensors and Actuators, B: Chemical,* vol. 235, pp. 330-342, 2016.

[286] Q. Yuan, J. Wu, E. Greenbaum, and B. R. Evans, “A resettable in-line particle concentrator using AC electrokinetics for distributed monitoring of microalgae in source waters,” *Sensors and Actuators, B: Chemical,* vol. 244, pp. 265-274, 2017.

[287] C. Zhao, Z. Ge, Y. Song, and C. Yang, “Electrokinetically driven continuous-flow concentration of colloidal particles by Joule heating induced temperature gradient focusing in a convergent-divergent microfluidic structure,” *Scientific Reports,* vol. 7, no. 1, 2017.

[288] Z. Zheng, B. Jing, M. Sorci, G. Belfort, and Y. Zhu, “Accelerated insulin aggregation under alternating current electric fields: Relevance to amyloid kinetics,” *Biomicrofluidics,* vol. 9, no. 4, 2015.

[289] Y. Chiang, C. Tsou, B. C. Chen, and R. H. Chou, “Glass-based microchip with finger electrodes for the formation, collection, and biointeractions of liposomes,” *Journal of Micro/ Nanolithography, MEMS, and MOEMS,* vol. 17, no. 2, 2018.

[290] Y. Song, P. Chen, M. T. Chung, R. Nidetz, Y. Park, Z. Liu, W. McHugh, T. T. Cornell, J. Fu, and K. Kurabayashi, “AC Electroosmosis-Enhanced Nanoplasmofluidic Detection of Ultralow-Concentration Cytokine,” *Nano Letters,* vol. 17, no. 4, pp. 2374-2380, 2017.

[291] M. S. Parvez, M. F. Rubby, S. Iqbal, and N. Islam, "DC-biased AC electrokinetics effect on V-shaped electrode patterns for microfluidics applications."

[292] S. Hu, J. T. Lyu, and G. Y. Si, “Analysis and Modeling of Electro-osmosis Based on the Modified Poisson-Boltzmann Equation,” *Dongbei Daxue Xuebao/Journal of Northeastern University,* vol. 40, no. 3, pp. 447-451, 2019.

[293] T. Zhou, J. Chen, E. Kropp, and L. Kulinsky, “Guided Electrokinetic Assembly of Polystyrene Microbeads onto Photopatterned Carbon Electrode Arrays,” *ACS Applied Materials and Interfaces,* vol. 12, no. 31, pp. 35647-35656, 2020.

[294] M. Selmi, and H. Belmabrouk, “AC electroosmosis effect on microfluidic heterogeneous immunoassay efficiency,” *Micromachines,* vol. 11, no. 4, 2020.

[295] M. Nagai, K. Kato, S. Soga, T. S. Santra, and T. Shibata, “Scalable parallel manipulation of single cells using micronozzle array integrated with bidirectional electrokinetic pumps,” *Micromachines,* vol. 11, no. 4, 2020.

[296] X. Chen, and Z. Wu, “Design and numerical simulation of a novel microfluidic electroosmotic micromixer with three electrode pairs,” *Journal of Chemical Technology and Biotechnology,* vol. 94, no. 6, pp. 1991-1997, 2019.

[297] J. Wang, M. T. Wei, J. A. Cohen, and H. D. Ou-Yang, “Mapping alternating current electroosmotic flow at the dielectrophoresis crossover frequency of a colloidal probe,” *Electrophoresis,* vol. 34, no. 13, pp. 1915-1921, 2013.

[298] X. Wang, X. B. Wang, and P. R. C. Gascoyne, “General expressions for dielectrophoretic force and electrorotational torque derived using the Maxwell stress tensor method,” *Journal of Electrostatics,* vol. 39, no. 4, pp. 277-295, 1997.

[299] F. L'Hostis, N. G. Green, H. Morgan, and M. Alkaisi, "Solid state AC electroosmosis micro pump on a Chip." pp. 282-285.

[300] B. J. Kim, S. Y. Yoon, H. J. Sung, and C. G. Smith, “Simultaneous mixing and pumping using asymmetric microelectrodes,” *Journal of Applied Physics,* vol. 102, no. 7, 2007.

[301] T. A. Moore, and Y. Lai, "AC electroosmotic micropumping with a square spiral microelectrode array." pp. 157-160.

[302] F. O. Morin, F. Gillot, and H. Fujita, “Modeling the mechanisms driving ac electro-osmotic flow on planar microelectrodes,” *Applied Physics Letters,* vol. 91, no. 6, 2007.

[303] M. Stubbe, M. Holtappels, and J. Gimsa, “A new working principle for ac electro-hydrodynamic on-chip micro-pumps,” *Journal of Physics D: Applied Physics,* vol. 40, no. 21, pp. 6850-6856, 2007.

[304] J. Hrdlička, P. Cervenka, M. Přibyl, and D. Snita, “Zig-zag arrangement of four electrodes for ac electro-osmotic micropumps,” *Physical Review E - Statistical, Nonlinear, and Soft Matter Physics,* vol. 84, no. 1, 2011.

[305] N. A. Mishchuk, T. Heldal, T. Volden, J. Auerswald, and H. Knapp, “Micropump based on electroosmosis of the second kind,” *Electrophoresis,* vol. 30, no. 20, pp. 3499-3506, 2009.

[306] J. C. Lei, C. C. Chang, and C. Y. Wang, “Electro-osmotic pumping through a bumpy microtube: Boundary perturbation and detection of roughness,” *Physics of Fluids,* vol. 31, no. 1, 2019.

[307] W. Liu, Y. Ren, Y. Tao, Y. Li, and Q. Wu, “On traveling-wave field-effect flow control for simultaneous induced-charge electroosmotic pumping and mixing in microfluidics: Physical perspectives and theoretical analysis,” *Journal of Micromechanics and Microengineering,* vol. 28, no. 5, 2018.

[308] X. Gao, and Y. Li, “Simultaneous microfluidic pumping and mixing using an array of asymmetric 3D ring electrode pairs in a cylindrical microchannel by the AC electroosmosis effect,” *European Journal of Mechanics, B/Fluids,* vol. 75, pp. 361-371, 2019.

[309] N. Sasaki, T. Kitamori, and H. B. Kim, “Experimental and theoretical characterization of an AC electroosmotic micromixer,” *Analytical Sciences,* vol. 26, no. 7, pp. 815-819, 2010.

[310] A. Usefian, and M. Bayareh, “Numerical and experimental study on mixing performance of a novel electro-osmotic micro-mixer,” *Meccanica,* vol. 54, no. 8, pp. 1149-1162, 2019.

[311] N. Sasaki, T. Kitamori, and H. B. Kim, “AC electroosmotic micromixer for chemical processing in a microchannel,” *Lab on a Chip,* vol. 6, no. 4, pp. 550-554, 2006.

[312] S. J. Kim, and B. J. Yoon, “Analytical study of AC electroosmotic mixing in 2-dimensional microchannel with time periodic surface potential,” *Biomicrofluidics,* vol. 13, no. 2, 2019.

[313] N. G. Green, "Electrode polarisation, dielectrophoresis and electrorotation." pp. 193-198.

[314] N. G. Green, H. Morgan, and A. Ramos, "AC electric field microfluidic control in microsystems." pp. 425-432.

[315] A. Ramos, A. González, A. Castellanos, N. G. Green, and H. Morgan, "Pumping of electrolytes using arrays of asymmetric pairs of microelectrodes subjected to ac voltages." pp. 187-192.

[316] P. García-Sánchez, A. Ramos, N. G. Green, and H. Morgan, “Traveling-wave electrokinetic micropumps: Velocity, electrical current, and impedance measurements,” *Langmuir,* vol. 24, no. 17, pp. 9361-9369, 2008.

[317] M. Vázquez Piñón, B. Cárdenas Benítez, B. Pramanick, V. H. Perez-Gonzalez, M. J. Madou, S. O. Martinez-Chapa, and H. Hwang, “Direct current-induced breakdown to enhance reproducibility and performance of carbon-based interdigitated electrode arrays for AC electroosmotic micropumps,” *Sensors and Actuators, A: Physical,* vol. 262, pp. 10-17, 2017.

[318] G. A. Lyngdoh, R. Kumar, N. M. A. Krishnan, and S. Das, “Dynamics of confined water and its interplay with alkali cations in sodium aluminosilicate hydrate gel: Insights from reactive force field molecular dynamics,” *Physical Chemistry Chemical Physics,* vol. 22, no. 41, pp. 23707-23724, 2020.

[319] H. A. Rouabah, B. Y. Park, R. B. Zaouk, M. J. Madou, H. Morgan, and N. G. Green, "Increasing the fluid flow velocity in a microchannel using 3D non-metallic electrodes." pp. 1784-1785.

[320] N. A. M. Yunus, M. N. Mohtar, K. M. Almadhagi, and I. A. Halin, "Dielectrophoresis and AC electroosmosis force on fluid motion in microfluidic using latex particles," *Pertanika Journal of Science and Technology,* vol. 25, no. S, pp. 333-342, 2017.

[321] X. Guo, K. Xie, R. J. Campbell, and Y. Lai, "3D stepped electrodes on a flexible substrate with permanently bonded poly(dimethylsiloxane) channels for moving microfluid," *Journal of Vacuum Science and Technology B:Nanotechnology and Microelectronics,* vol. 31, no. 2, 2013.

[322] S. N. Ibrahim, L. Murray, J. J. Evans, and M. M. Alkaisi, "Trapping single cells: Comparison between sandwiched insulation with back contact (SIBC) and planar biochip," Trans Tech Publications Ltd, 2012, pp. 188-194.

[323] B. Sercu, J. Peixoto, K. Demeestere, T. Van Elst, and H. Van Langenhove, "Odors treatment: Biological technologies," *Odors in the Food Industry*, pp. 125-158: Springer US, 2006.

[324] B. K. Cho, "Ultrasonic technology," *Nondestructive Evaluation of Food Quality: Theory and Practice*, pp. 213-234: Springer Berlin Heidelberg, 2010.

[325] R. J. Martín-Palma, and A. Lakhtakia, "Vapor-Deposition Techniques," *Engineered Biomimicry*, pp. 383-398: Elsevier Inc., 2013.

[326] W. W. Leung, "Simulation of centrifugal recovery of protein in biopharmaceutical production using atspin simulator." p. 2261.

[327] V. O. Bereka, I. V. Bozhko, V. A. Brzhezitsky, Y. Haran, and Y. A. Trotzenko, “Simulation of the electric field in the electrode system to create of a pulsed barrier discharge in atmospheric air in the presence of water in a droplet-film state,” *Technical Electrodynamics,* vol. 2020, no. 2, pp. 17-22, 2020.

[328] S. Wang, X. Sun, G. Li, C. Jia, G. Li, and W. Zhang, “Study on the multi-level resistance-switching memory and memory-state-dependent photovoltage in pt/Nd:SrTiO3 junctions,” *Nanoscale Research Letters,* vol. 13, no. 1, 2018.

[329] G. Yıldırım, M. H. Sarwary, A. Al-Dahawi, O. Öztürk, Ö. Anıl, and M. Şahmaran, “Piezoresistive behavior of CF- and CNT-based reinforced concrete beams subjected to static flexural loading: Shear failure investigation,” *Construction and Building Materials,* vol. 168, pp. 266-279, 2018.

[330] R. Luttge, *Nano- and Microfabrication for Industrial and Biomedical Applications: Second Edition*: Elsevier Inc., 2016.

[331] S. Franssila, and S. Tuomikoski, "MEMS Lithography," *Handbook of Silicon Based MEMS Materials and Technologies: Second Edition*, pp. 427-443: Elsevier Inc., 2015.

[332] Y. Krivoshapkina, M. Kaestner, and I. W. Rangelow, "Tip-based nanolithography methods and materials," *Frontiers of Nanoscience*, Elsevier Ltd, 2016, pp. 497-542.

[333] H. Zhang, N. Zhang, M. Gilchrist, and F. Fang, “Advances in precision micro/nano-electroforming: A state-of-the-art review,” *Journal of Micromechanics and Microengineering,* vol. 30, no. 10, 2020.

[334] M. M. Gregersen, L. H. Olesen, A. Brask, M. F. Hansen, and H. Bruus, "Characterization of flow reversal in anodically bonded glass-based ac electrokinetic micropumps." pp. 35-37.

[335] N. Laohakunakorn, V. V. Thacker, M. Muthukumar, and U. F. Keyser, “Electroosmotic flow reversal outside glass nanopores,” *Nano Letters,* vol. 15, no. 1, pp. 695-702, 2015.

[336] A. Bahmanyaran, and K. Jafari, "Electrostatic MEMS switch with vertical beams and body biasing," *Lecture Notes in Electrical Engineering*, Springer Verlag, 2019, pp. 1017-1022.

[337] P. Kielanowski, A. Odzijewicz, and E. Previato, "Modeling the dynamics of a charged drop of a viscous liquid," *Trends in Mathematics*, Springer, 2019, pp. 188-194.

[338] J. Mc Hugh, K. Andresen, and U. F. Keyser, “Cation dependent electroosmotic flow in glass nanopores,” *Applied Physics Letters,* vol. 115, no. 11, 2019.

9 Appendix

9.1 Chapter 5 Additional Data

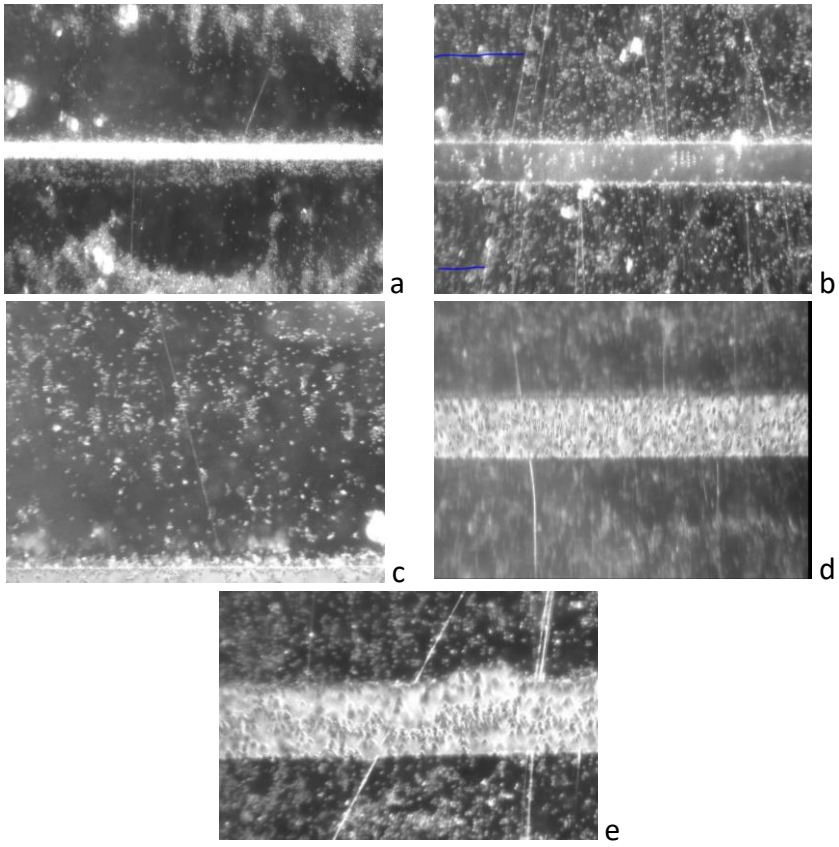

Figure 9.1:Interlectrode Gaps for two electrode Geometry (a) $20\mu m$ (b) $50\mu m$ (c) $75\mu m$ (d) $100\mu m$, and (e) $150\mu m$.

9.2 Chapter 5 Additional Data

9.2.1 Syringe Pump

A translational motion with a chosen length and speed is necessary for the syringe pump to function. Therefore, a stepper motor (NEMA 17 42HS4013A4 SUMTOR, $1.8°$ Step angle) is used to build the syringe pump, driven by DRV8825. These components are connected to an Arduino UNO R3 microcontroller. The DRV8825 circuit diagram is shown in figure 8.2. Arduino board is energized by a 5V supply.

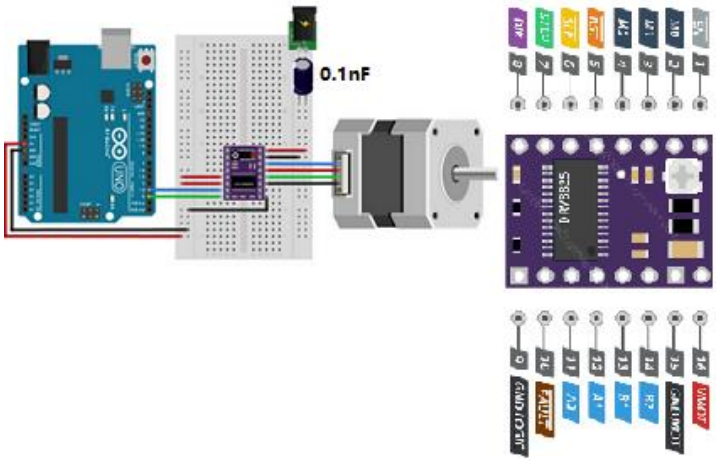

Figure 9.2: The schematic diagram of the motor driver circuit.

The syringe support is designed with a 3D printer. The motor rotational movement is converted into a syringe translational movement through a system of worm gear. The syringe plunger is fixed on the blue support. The rest of the syringe is immobilized with other 3D printed pieces fixed on a rail with screws and nuts. The designed syringe pump is shown in figure 8.3.

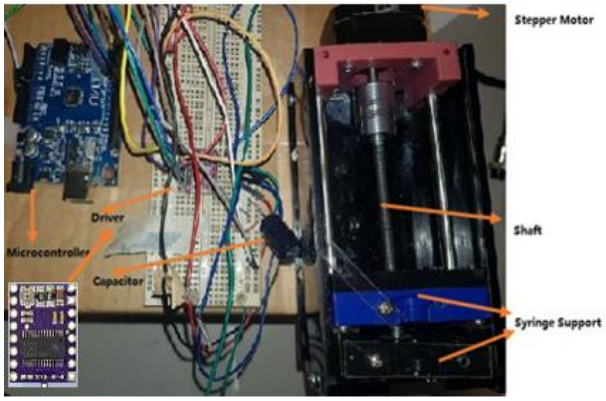

Figure 9.3: The syringe pump designed and programmed to dispense sample on the device.

$1.8°$ step angle NEMA stepper motor provides $200\ steps/turn$. The driver is used at the micro-stepping of $1/32$ logic to provide smooth movement at low speeds. For this purpose, M0, M1, and M2 pins of driver are set at high. The shaft has a leadscrew pitch of $1mm$, and $2mm$ pitch, therefore, it runs at $6400steps/mm$. It is achieved

when DRV8825 generates 2.1A current. For 12V supply, 2.1A current is generated at $V_{REF} = 1.75V$. A $0.1nF$ capacitor is used to maintain this reference voltage.

9.3 Chapter 6 Additional Data

9.3.1 Interelectrode Gap = $20\mu m$

9.3.1.1 Fluid Conductivity = $3mS/m$

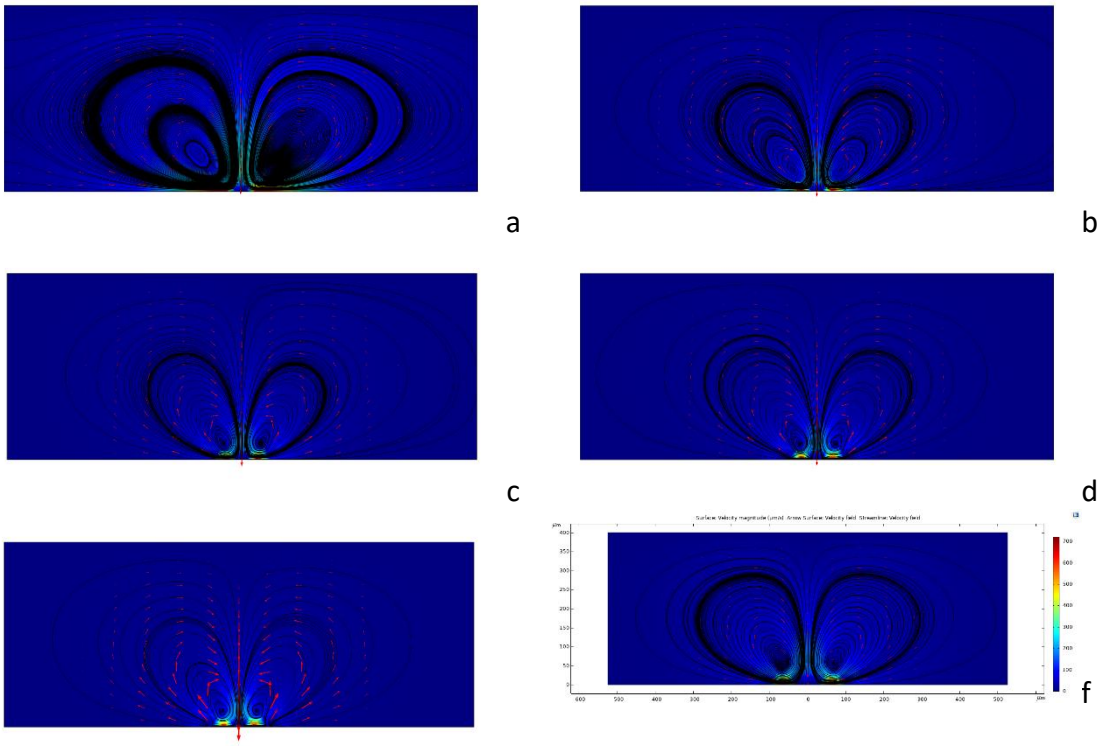

a b c d e f

Figure 9.4: Simulations for $20\mu m$ interelectrode gap, $3mS/m$ at $5V_{PP}$ (a) $500Hz$ (b) $1kHz$ (c) $1.5kHz$ (d) $2kHz$ (e) $2.5kHz$ (f) $3kHz$

9.3.1.2 Fluid Conductivity = $7mS/m$

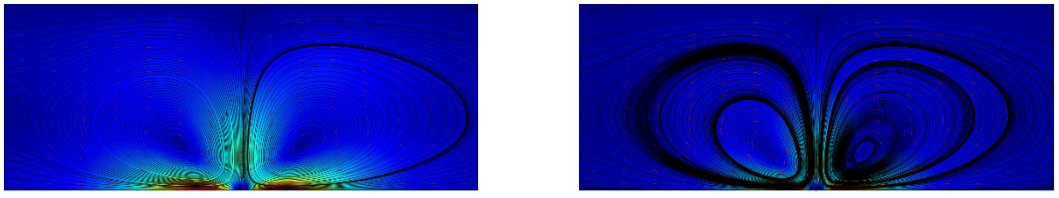

a b

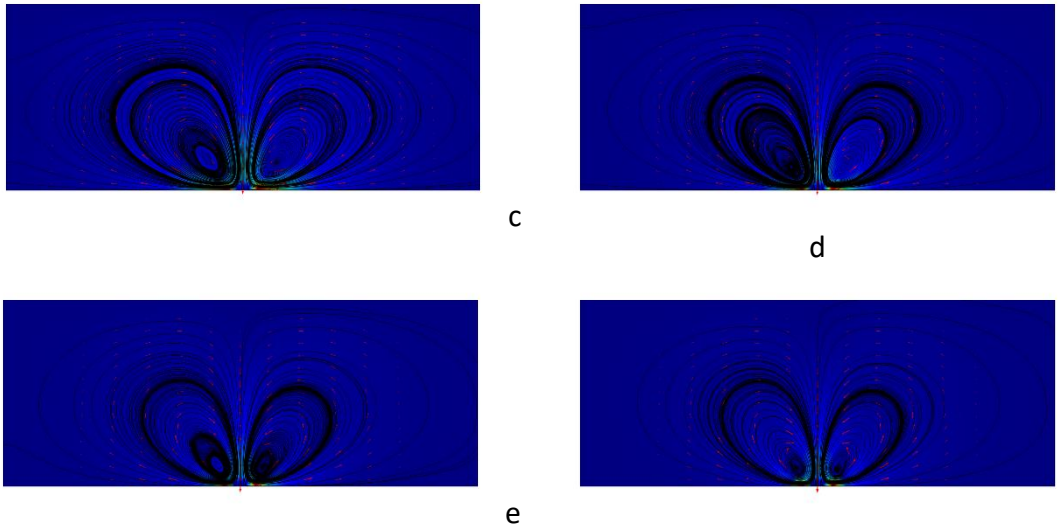

Figure 9.5: Simulations for $20\mu m$ interelectrode gap, $7mS/m$ at $5V_{PP}$ (a) $500Hz$ (b) $1kHz$ (c) $1.5kHz$ (d) $2kHz$ (e) $2.5kHz$ (f) $3kHz$

9.3.1.3 Fluid Conductivity = $10mS/m$

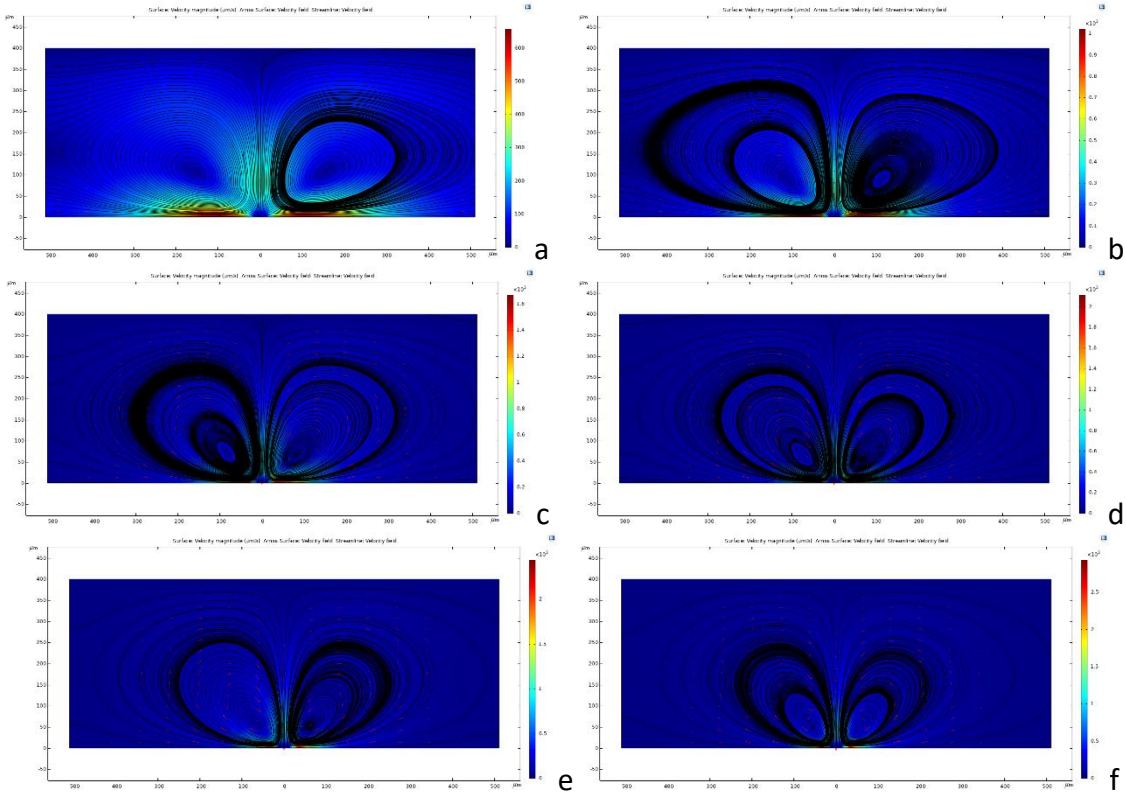

Figure 9.6: Simulations for $20\mu m$ interelectrode gap, $10mS/m$ at $5V_{PP}$ (a) $500Hz$ (b) $1kHz$ (c) $1.5kHz$ (d) $2kHz$ (e) $2.5kHz$ (f) $3kHz$

9.3.1.4 Fluid Conductivity = $14mS/m$

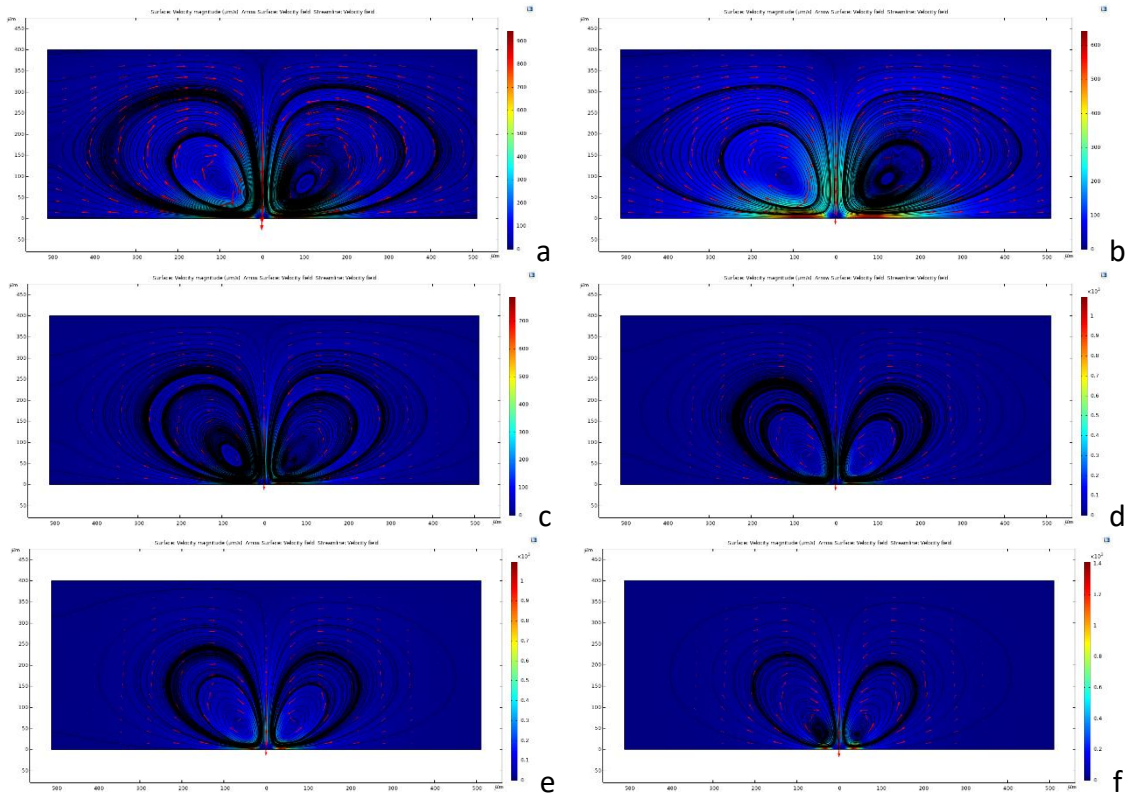

Figure 9.7: Simulations for $20\mu m$ interelectrode gap, $14mS/m$ at $5V_{PP}$ (a) $500Hz$ (b) $1kHz$ (c) $1.5kHz$ (d) $2kHz$ (e) $2.5kHz$ (f) $3kHz$

9.3.1.5 Fluid Conductivity = $20mS/m$

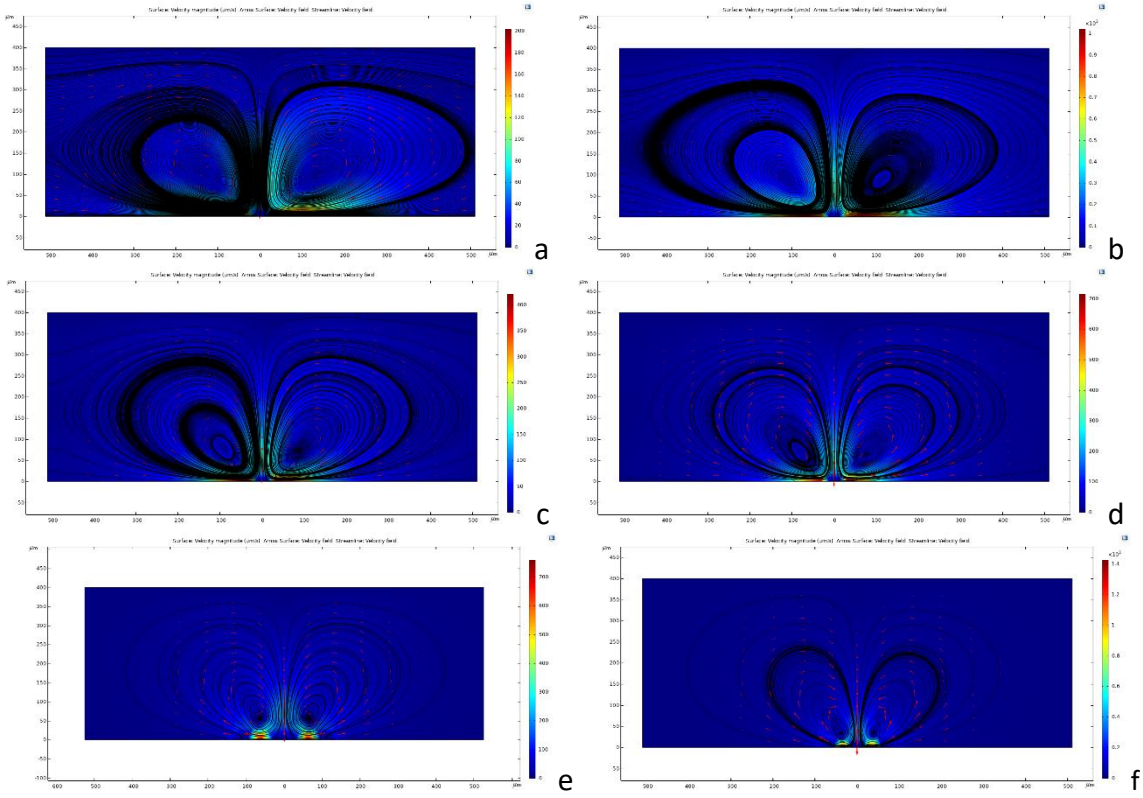

Figure 9.8: Simulations for $20\mu m$ interelectrode gap, $20mS/m$ at $5V_{PP}$ (a) $500Hz$ (b) $1kHz$ (c) $1.5kHz$ (d) $2kHz$ (e) $2.5kHz$ (f) $3kHz$

9.3.2 Interelectrode Gap = $50\mu m$

9.3.2.1 Fluid Conductivity = $3mS/m$

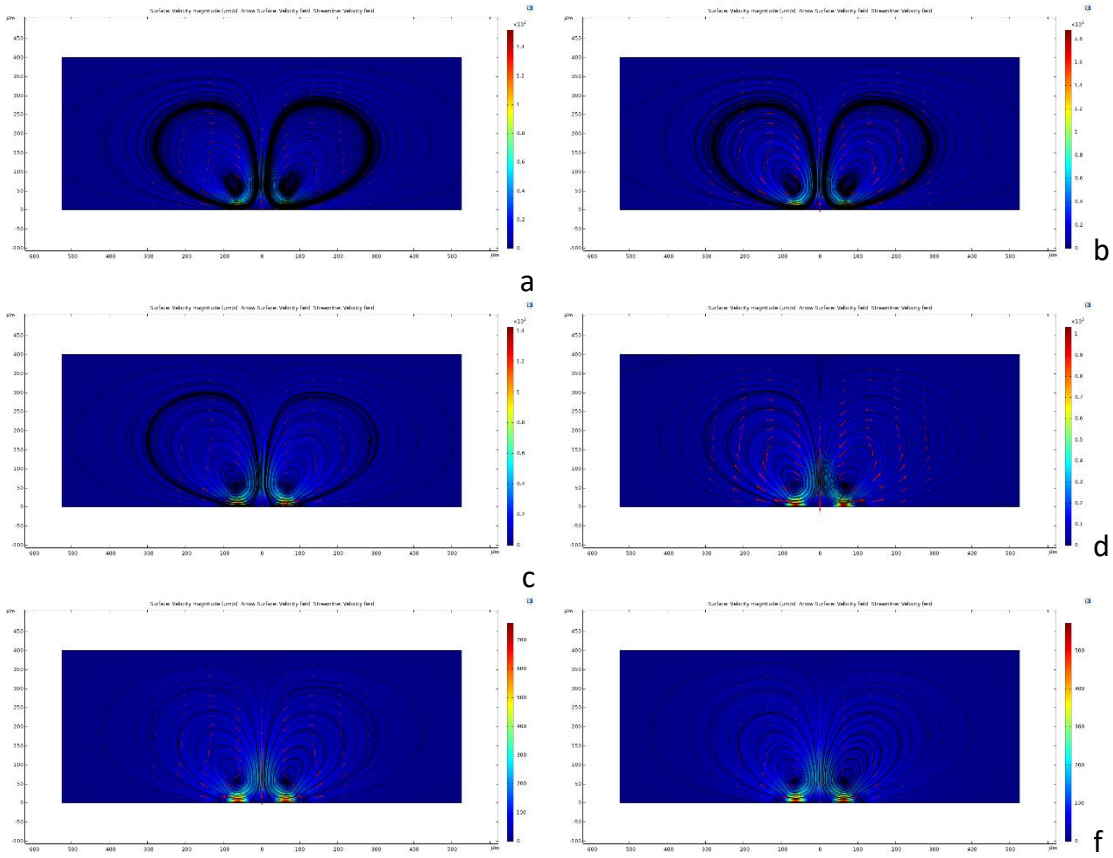

Figure 9.9: Simulations for $50\mu m$ interelectrode gap, $3mS/m$ at $5V_{PP}$ (a) $500Hz$ (b) $1kHz$ (c) $1.5kHz$ (d) $2kHz$ (e) $2.5kHz$ (f) $3kHz$

9.3.2.2 Fluid Conductivity = $7mS/m$

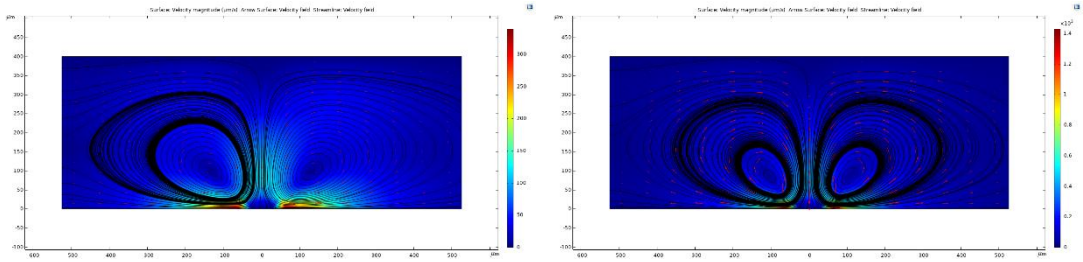

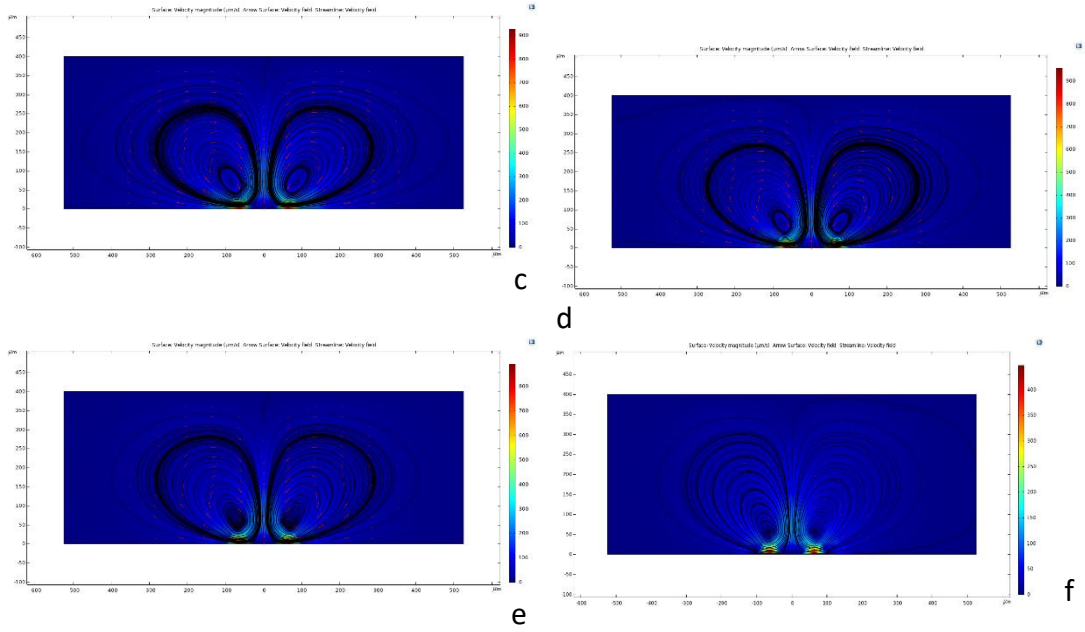

Figure 9.10: Simulations for $50\mu m$ interelectrode gap, $7mS/m$ at $5V_{PP}$ (a) $500Hz$ (b) $1kHz$ (c) $1.5kHz$ (d) $2kHz$ (e) $2.5kHz$ (f) $3kHz$

9.3.2.3 Fluid Conductivity = $10mS/m$

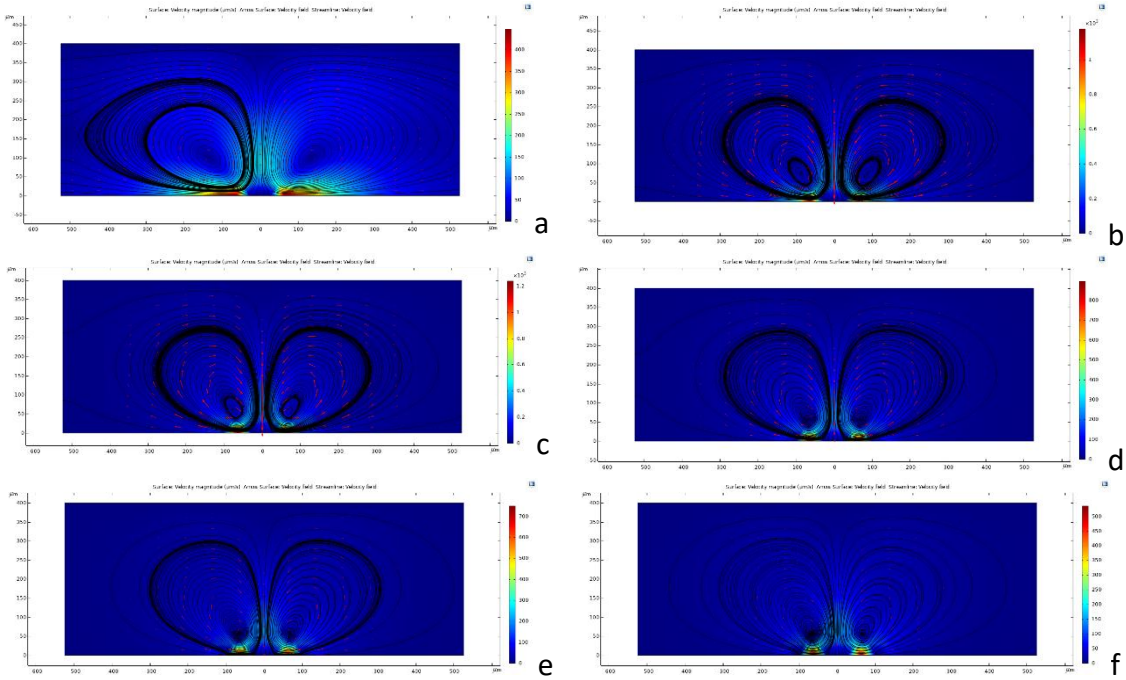

Figure 9.11: Simulations for $50\mu m$ interelectrode gap, $10mS/m$ at $5V_{PP}$ (a) $500Hz$ (b) $1kHz$ (c) $1.5kHz$ (d) $2kHz$ (e) $2.5kHz$ (f) $3kHz$

9.3.2.4 Fluid Conductivity = $14mS/m$

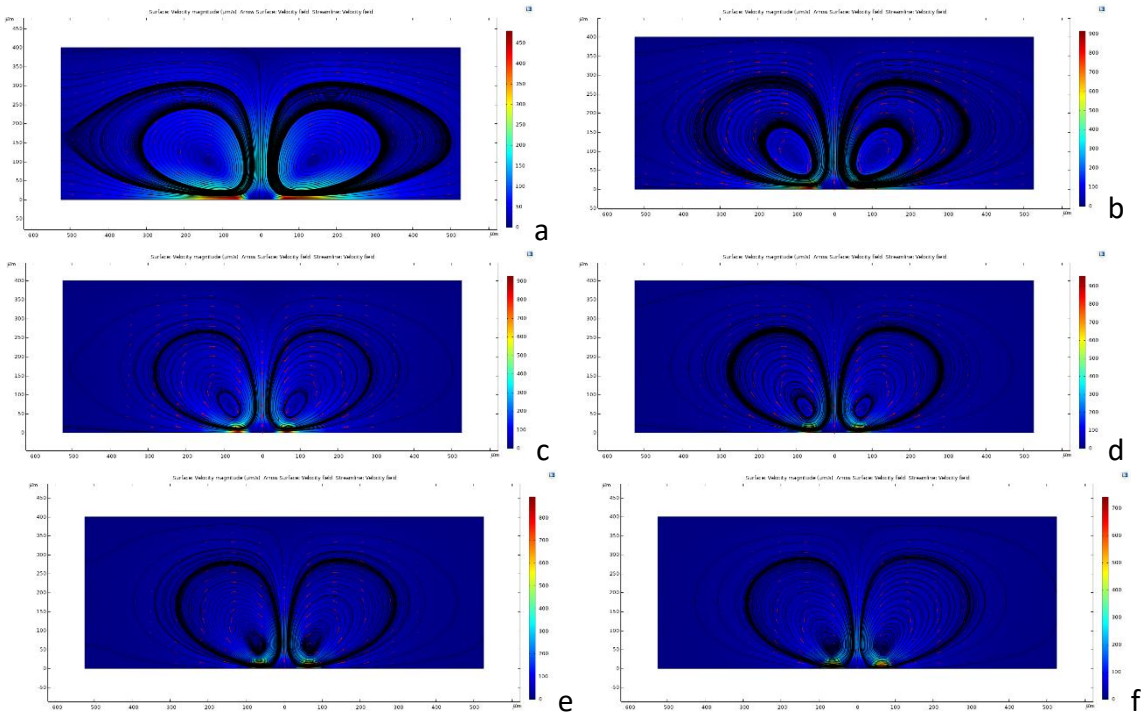

Figure 9.12: Simulations for $50\mu m$ interelectrode gap, $14mS/m$ at $5V_{PP}$ (a) $500Hz$ (b) $1kHz$ (c) $1.5kHz$ (d) $2kHz$ (e) $2.5kHz$ (f) $3kHz$

9.3.2.5 Fluid Conductivity = $20mS/m$

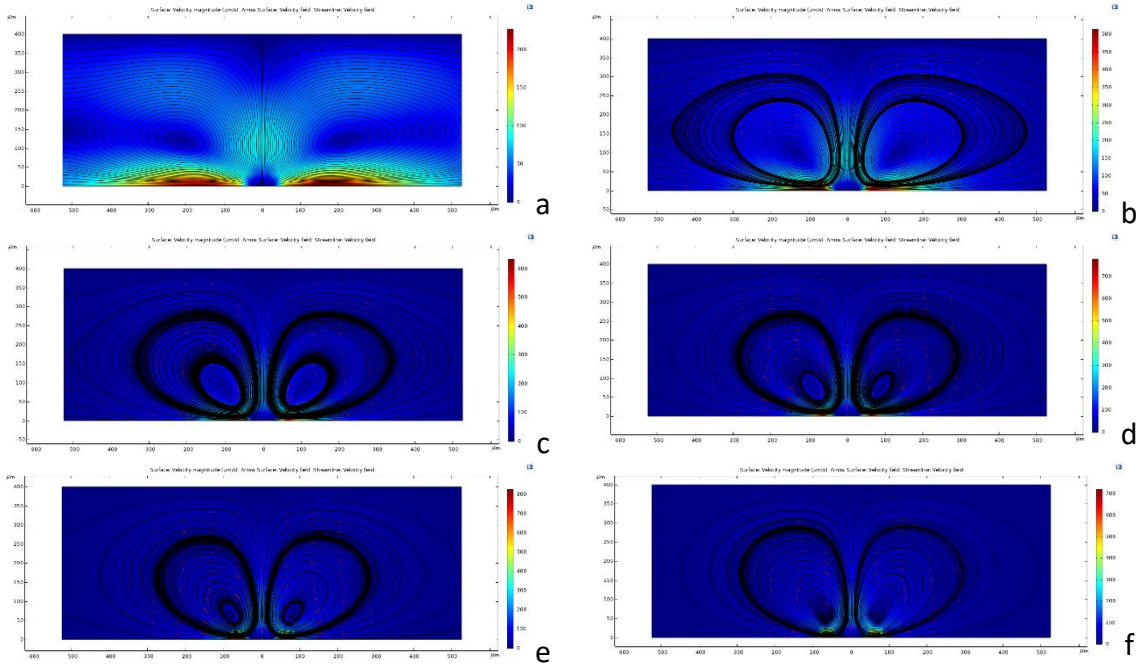

Figure 9.13: Simulations for $50\mu m$ interelectrode gap, $20mS/m$ at $5V_{PP}$ (a) $500Hz$ (b) $1kHz$ (c) $1.5kHz$ (d) $2kHz$ (e) $2.5kHz$ (f) $3kHz$

9.3.3 Interelectrode Gap = $75\mu m$

9.3.3.1 Fluid Conductivity = $3mS/m$

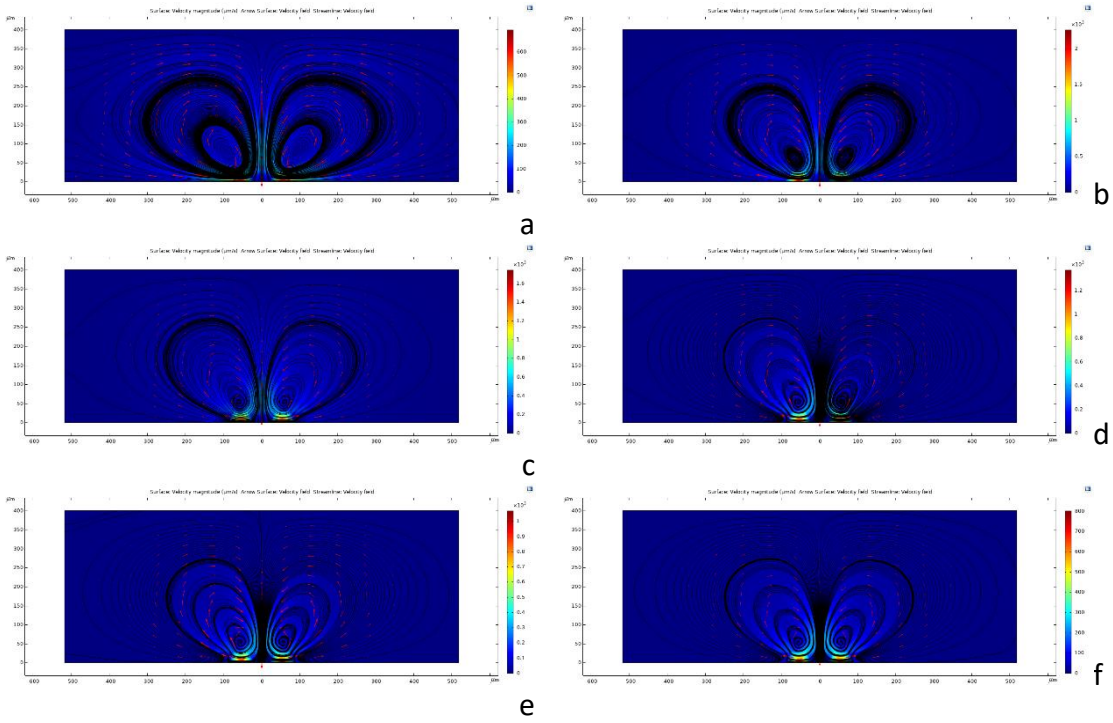

Figure 9.14: Simulations for 75 interelectrode gap, $3mS/m$ at $5V_{PP}$ (a) $500Hz$ (b) $1kHz$ (c) $1.5kHz$ (d) $2kHz$ (e) $2.5kHz$ (f) $3kHz$

9.3.3.2 Fluid Conductivity = $7mS/m$

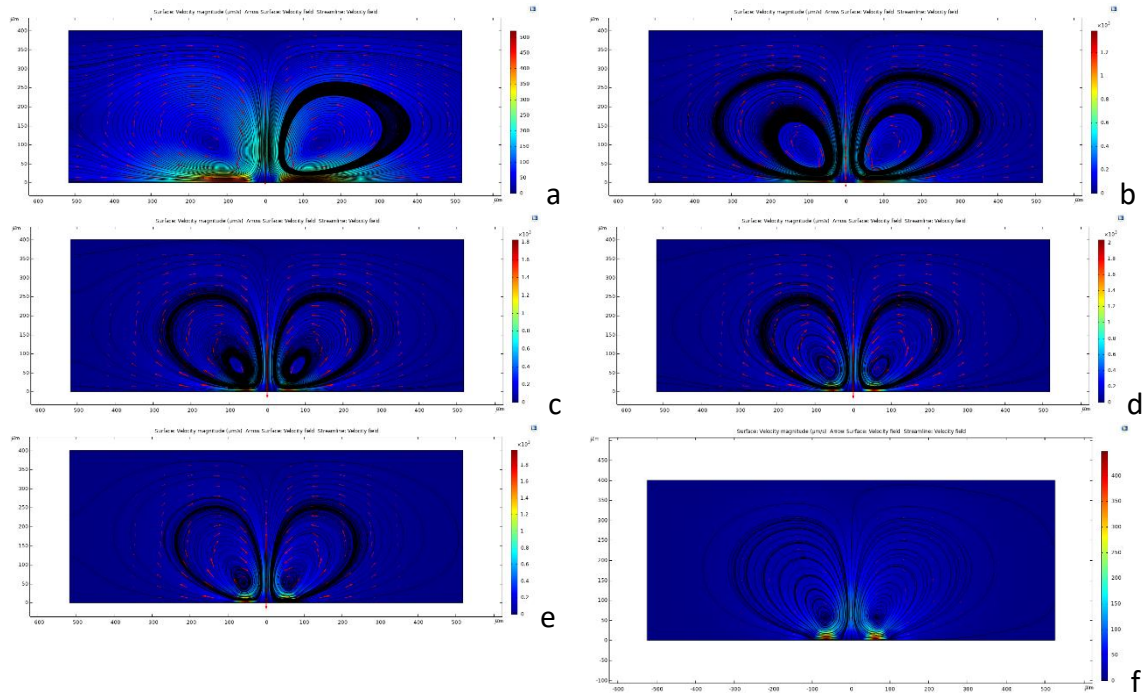

Figure 9.15: Simulations for $75\mu m$ interelectrode gap, $7mS/m$ at $5V_{PP}$ (a) $500Hz$ (b) $1kHz$ (c) $1.5kHz$ (d) $2kHz$ (e) $2.5kHz$ (f) $3kHz$

9.3.3.3 Fluid Conductivity = $10mS/m$

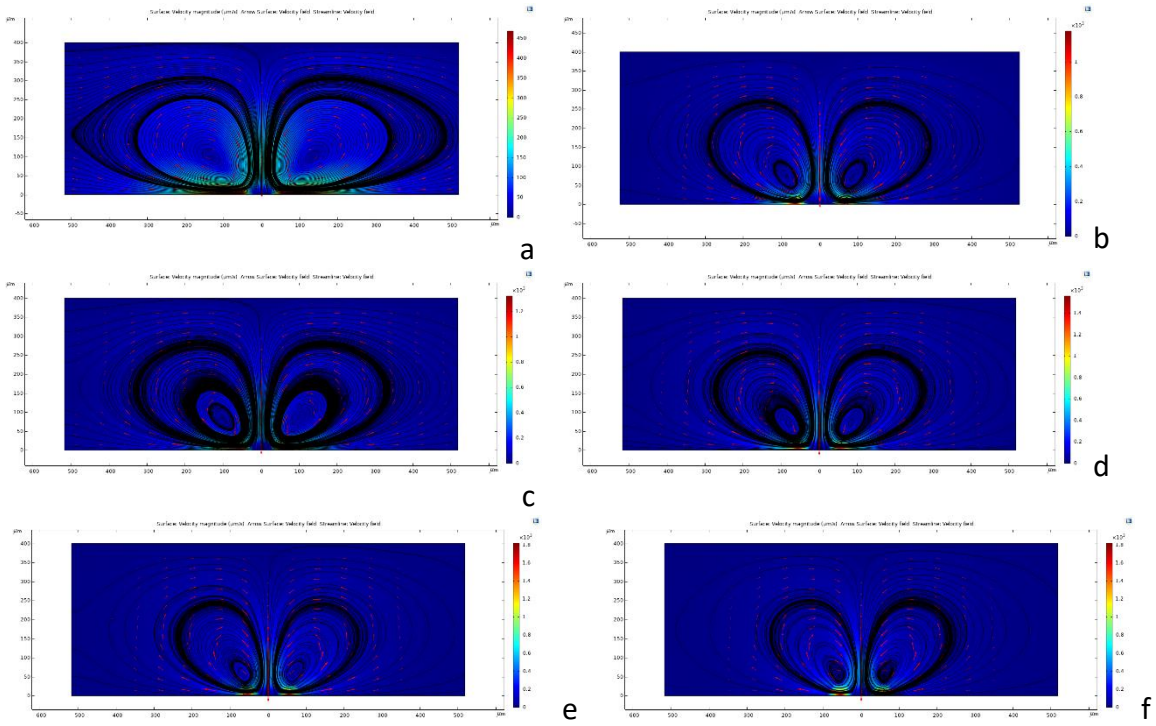

Figure 9.16: Simulations for $75\mu m$ interelectrode gap, $10mS/m$ at $5V_{PP}$ (a) $500Hz$ (b) $1kHz$ (c) $1.5kHz$ (d) $2kHz$ (e) $2.5kHz$ (f) $3kHz$

9.3.3.4 Fluid Conductivity = $14mS/m$

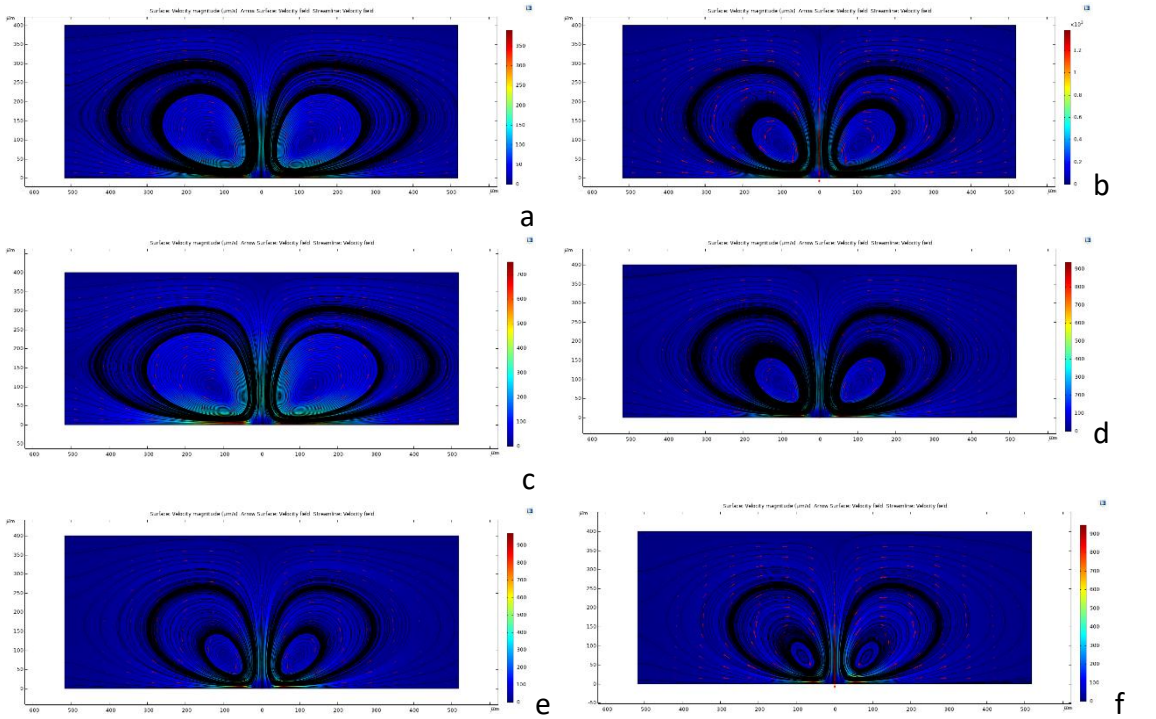

Figure 9.17: Simulations for $75\mu m$ interelectrode gap, $14mS/m$ at $5V_{PP}$ (a) $500Hz$ (b) $1kHz$ (c) $1.5kHz$ (d) $2kHz$ (e) $2.5kHz$ (f) $3kHz$

9.3.3.5 Fluid Conductivity = $20mS/m$

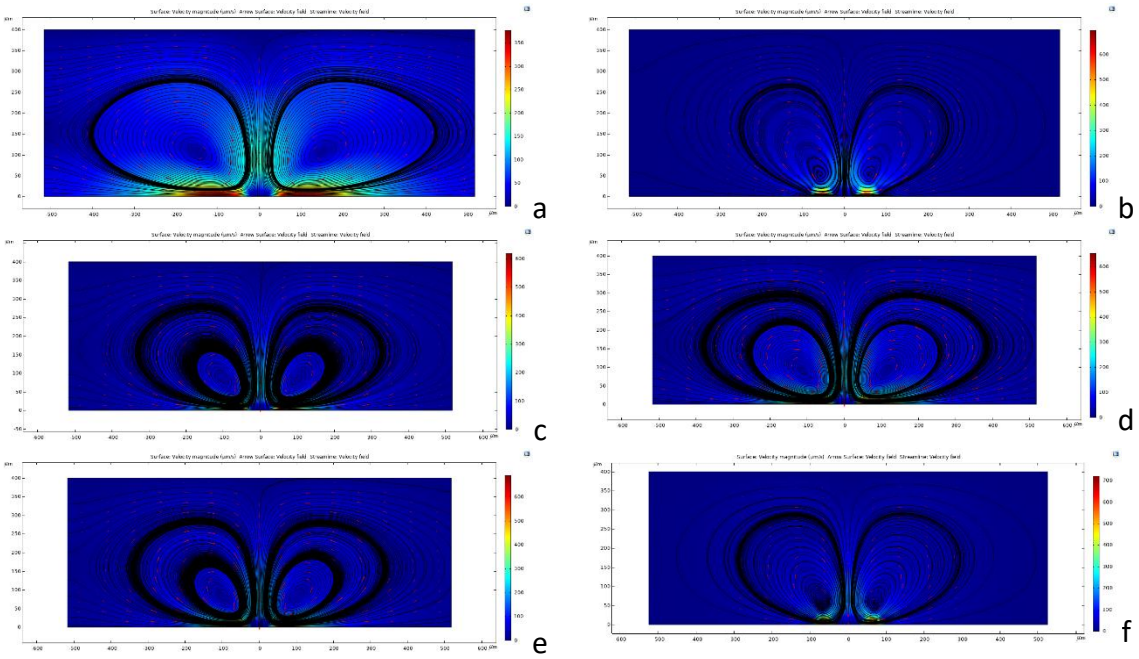

Figure 9.18: Simulations for $75\mu m$ interelectrode gap, $20mS/m$ at $5V_{PP}$ (a) $500Hz$ (b) $1kHz$ (c) $1.5kHz$ (d) $2kHz$ (e) $2.5kHz$ (f) $3kHz$

9.3.4 Interelectrode Gap = $100\mu m$

9.3.4.1 Fluid Conductivity = $3mS/m$

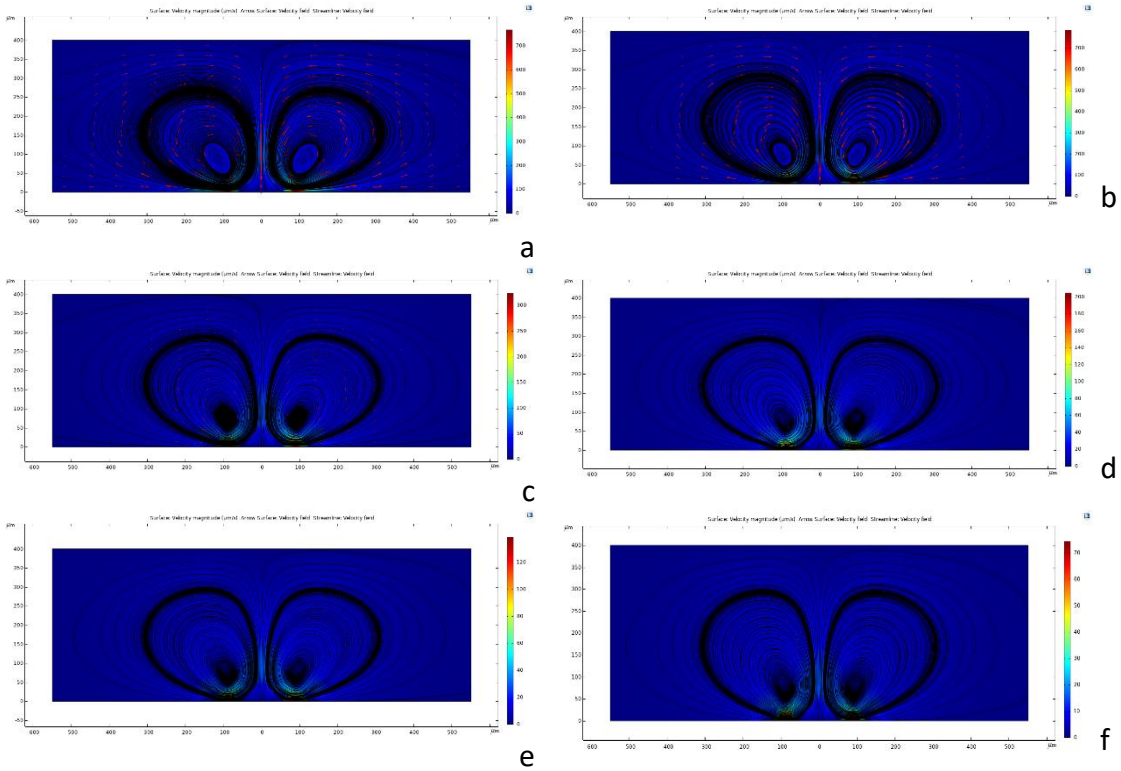

Figure 9.19: Simulations for $100\mu m$ interelectrode gap, $3mS/m$ at $5V_{PP}$ (a) $500Hz$ (b) $1kHz$ (c) $1.5kHz$ (d) $2kHz$ (e) $2.5kHz$ (f) $3kHz$

9.3.4.2 Fluid Conductivity = $7mS/m$

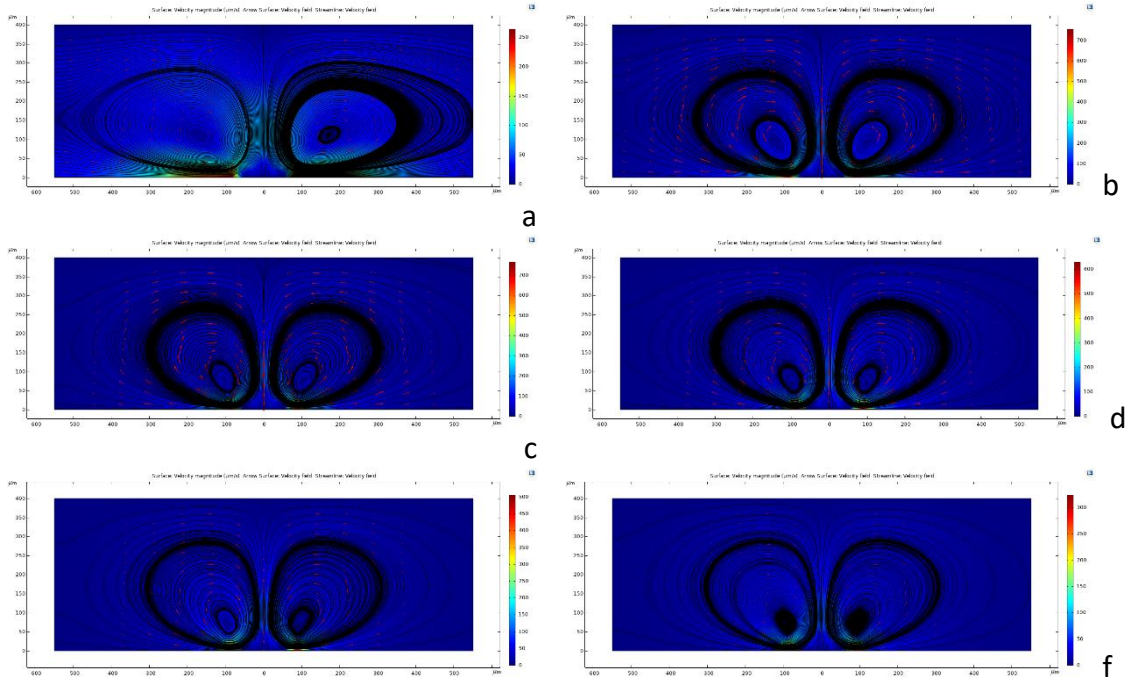

Figure 9.20: Simulations for $100\mu m$ interelectrode gap, $7mS/m$ at $5V_{PP}$ (a) $500Hz$ (b) $1kHz$ (c) $1.5kHz$ (d) $2kHz$ (e) $2.5kHz$ (f) $3kHz$

9.3.4.3 Fluid Conductivity = $10mS/m$

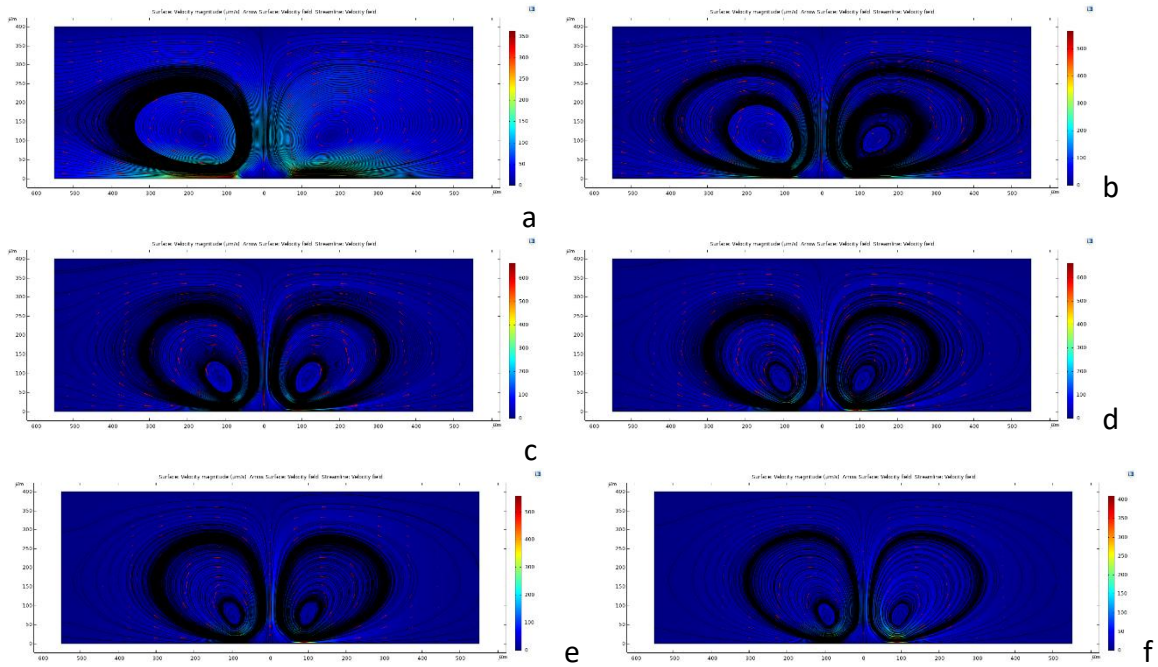

Figure 9.21: Simulations for$100\mu m$ interelectrode gap, $10mS/m$ at $5V_{PP}$ (a) $500Hz$ (b) $1kHz$ (c) $1.5kHz$ (d) $2kHz$ (e) $2.5kHz$ (f) $3kHz$

9.3.4.4 Fluid Conductivity = $14mS/m$

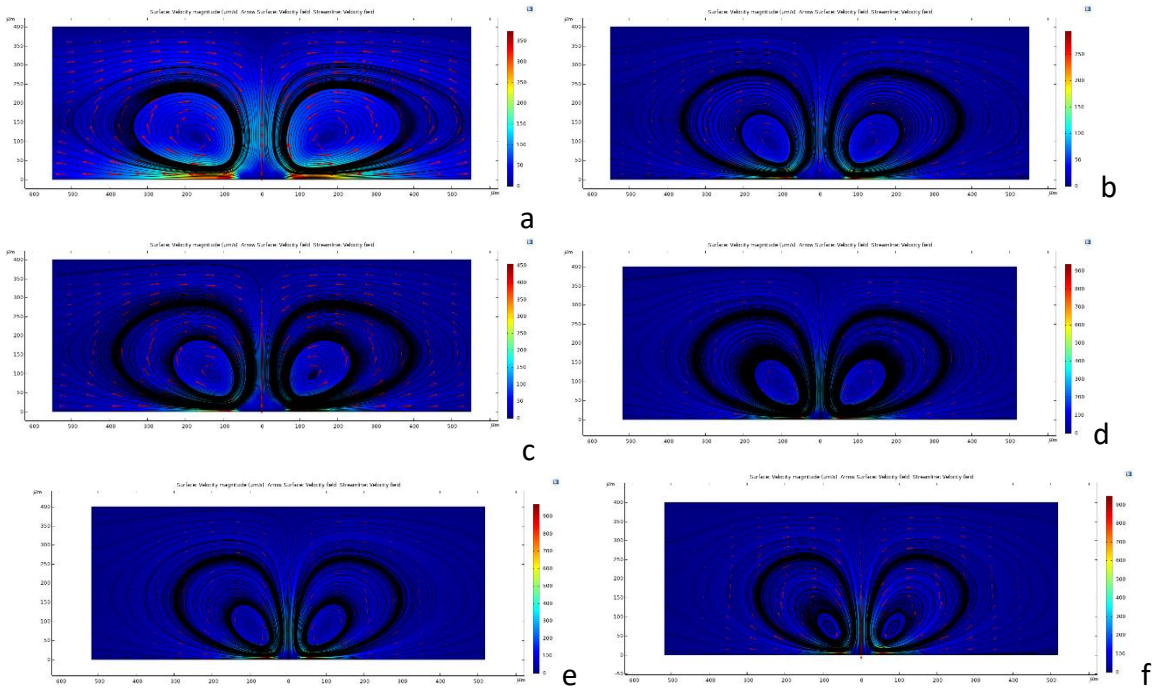

Figure 9.22: Simulations for $100\mu m$ interelectrode gap, $14mS/m$ at $5V_{PP}$ (a) $500Hz$ (b) $1kHz$ (c) $1.5kHz$ (d) $2kHz$ (e) $2.5kHz$ (f) $3kHz$

9.3.4.5 Fluid Conductivity = $20mS/m$

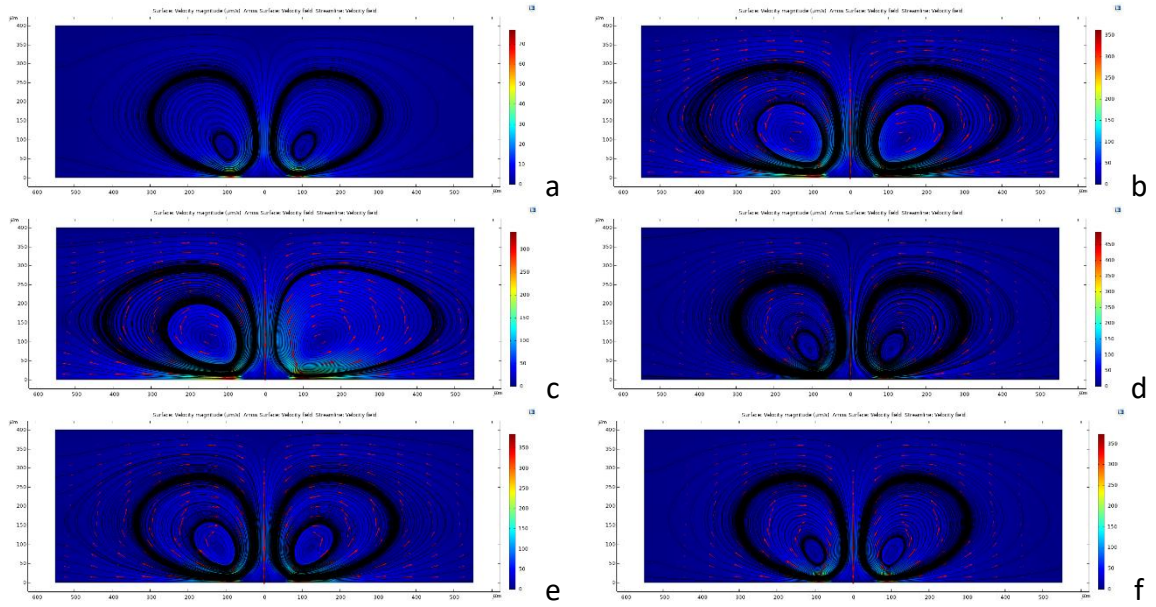

Figure 9.23: Simulations for $100\mu m$ interelectrode gap, $20mS/m$ at $5V_{PP}$ (a) $500Hz$ (b) $1kHz$ (c) $1.5kHz$ (d) $2kHz$ (e) $2.5kHz$ (f) $3kHz$

9.3.5 Interelectrode Gap = $150\mu m$

9.3.5.1 Fluid Conductivity = $3mS/m$

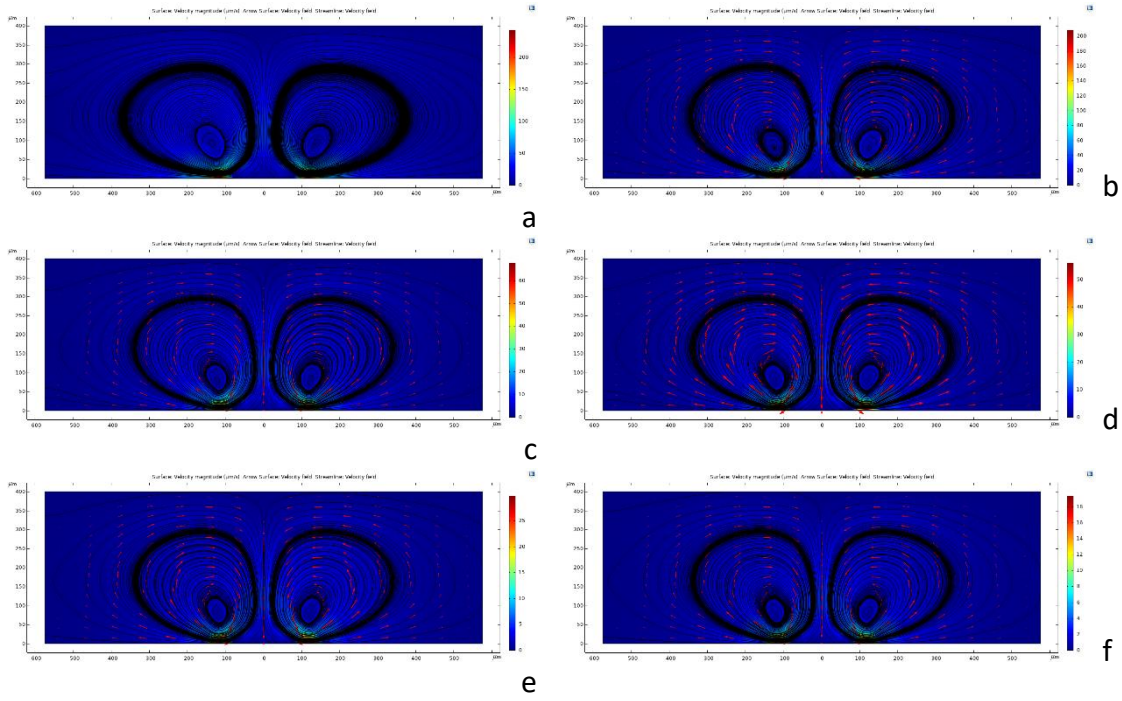

Figure 9.24: Simulations for $150\mu m$ interelectrode gap, $3mS/m$ at $5V_{PP}$ (a) $500Hz$ (b) $1kHz$ (c) $1.5kHz$ (d) $2kHz$ (e) $2.5kHz$ (f) $3kHz$

9.3.5.2 Fluid Conductivity = $7mS/m$

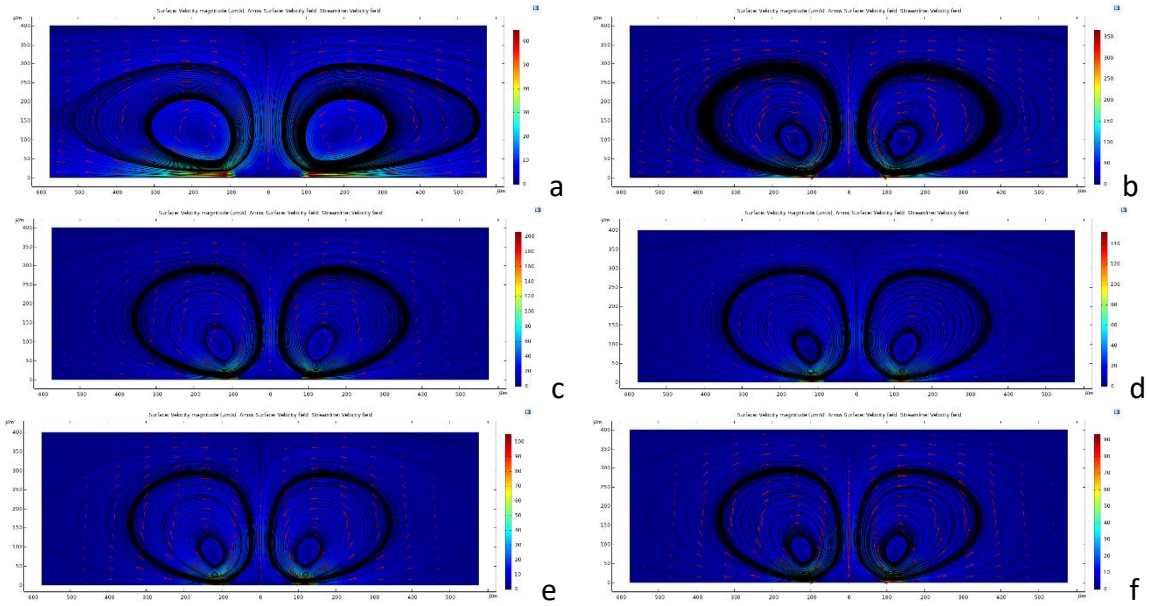

Figure 9.25: Simulations for $150\mu m$ interelectrode gap, $7mS/m$ at $5V_{PP}$ (a) $500Hz$ (b) $1kHz$ (c) $1.5kHz$ (d) $2kHz$ (e) $2.5kHz$ (f) $3kHz$

9.3.5.3 Fluid Conductivity = 10mS/m

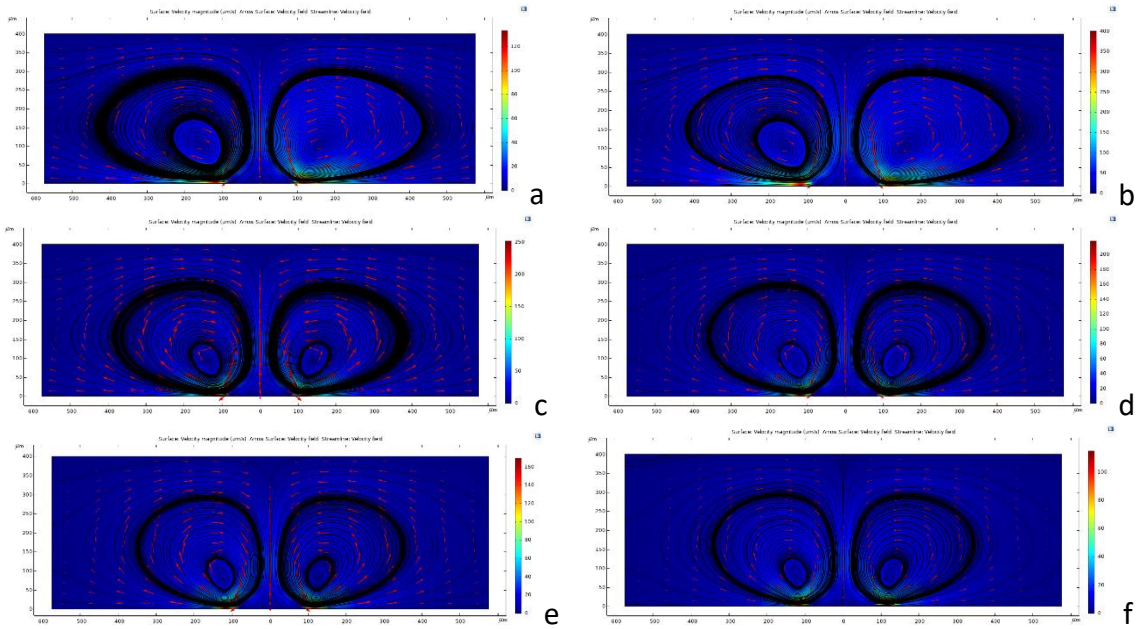

Figure 9.26: Simulations for150μm interelectrode gap, $10mS/m$ at $5V_{PP}$ (a) $500Hz$ (b) $1kHz$ (c) $1.5kHz$ (d) $2kHz$ (e) $2.5kHz$ (f) $3kHz$

9.3.5.4 Fluid Conductivity = 14mS/m

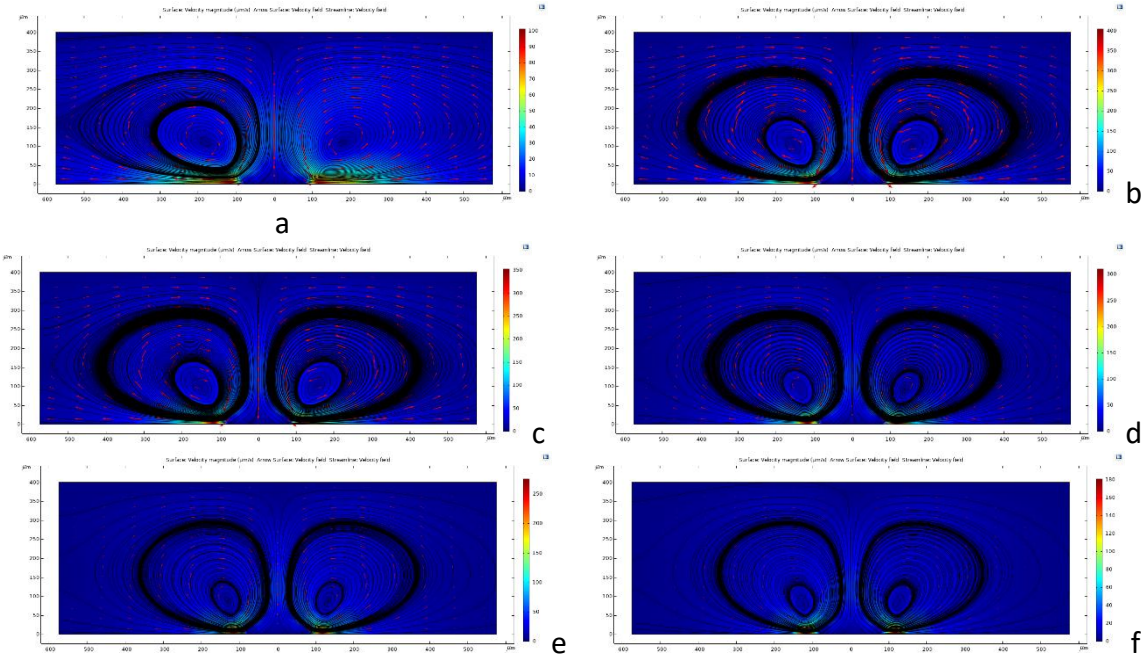

Figure 9.27: Simulations for $150\mu m$ interelectrode gap, $14mS/m$ at $5V_{PP}$ (a) $500Hz$ (b) $1kHz$ (c) $1.5kHz$ (d) $2kHz$ (e) $2.5kHz$ (f) $3kHz$

9.3.5.5 Fluid Conductivity = 20mS/m

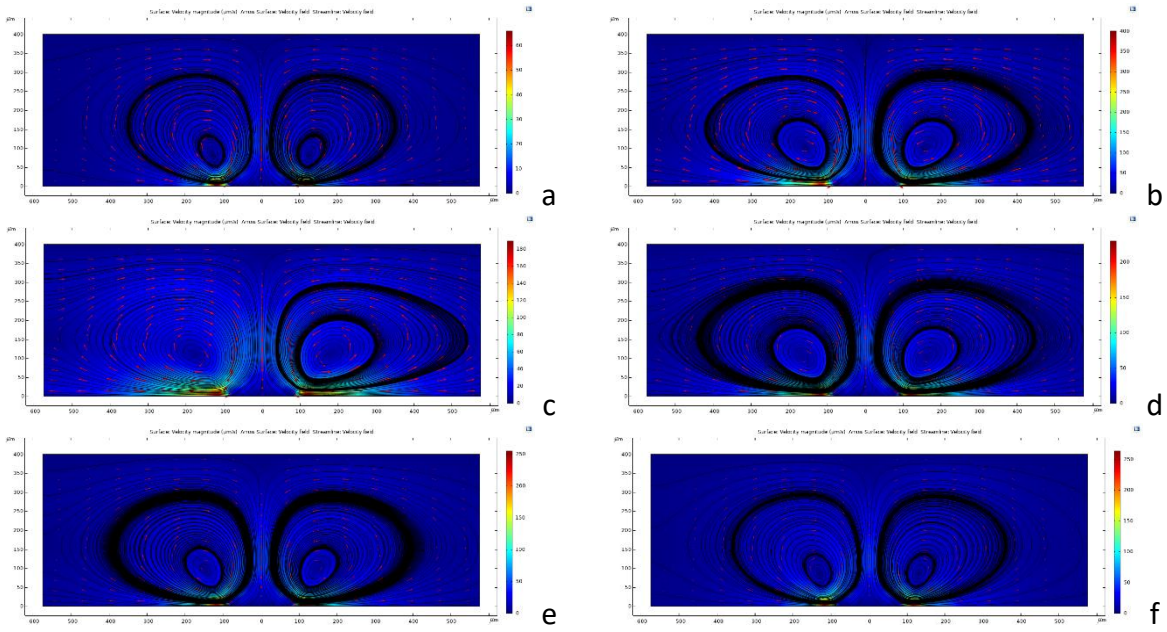

Figure 9.28: Simulations for $150\mu m$ interelectrode gap, $20mS/m$ at $5V_{PP}$ (a) $500Hz$ (b) $1kHz$ (c) $1.5kHz$ (d) $2kHz$ (e) $2.5kHz$ (f) $3kHz$.

9.3.6 Useful Numerical Values

No of electrodes 2 (electrodes $500\mu m$ wide)

1 – (x =0, y = 0) – expecting $0\mu m$ /s velocity this is in the middle of the electrodes where fluid velocity should become 0, it is confirmed for all.

2 – Results were obtained on the x – axis at 3 different points to obtain the results (-70, 0), (-150,0), (-80,0) and average was obtained)

3 – Velocities were also obtained between the centre of the rolls as well.

4 – On y axis velocity was also obtained at different points on the y axis and was realised that as move away velocity start to decrease.

5 – Particle displacement on x axis and y – axis was also obtained as follow:
i. On x axis where velocity start to roll back .

ii. Height of vortex on y axis where it rolls back.

V = 5V

Inter electrode Gap = 20 μm

Fluid Conductivity = 3mS/m

	f(kHz)	v (μm/s) (-100,0)	v (μm/s) (75,0)	v (μm/s) (100, 0)	v (μm/s) (250, 0)	v (μm/s) (500, 0)	v (μm/s) (75,50)	v (μm/s) (75,100)	v (μm/s) (75,15 0)	v (μm/s) (75,20 0)	Vortex X axis (μm/s)	Vortex Y – axis (μm/s)
1	0.5	760.23	1093.2 1	784.12	94.12	12.67	181.23	153.12	183.41	148.31	477.12	391.32
2	1	594.32	872.67	472.33	44.89	5.11	296.26	128.92	115.42	85.725	345.19 (9.85)	392.75 (6.5)
3	1.5	293.45	390.12	295.05	18.59	2.23	278.90	115.32	10.5.29	80.32	312.01	344.12
4	2	243.60	129.27	245.81	12.23	1.21	280.42	104.23	93.12	72.67	274.12	283.12
5	2.5	191.28	42.56	181.29	7.32	0.78	201.12	99.12	91.45	61.19	209.12	187.19
6	3	139.10	39.19	159.12	3.19	0.32	174.78	74.33	71.11	46.89	178.19	158.91

Fluid Conductivity = 7mS/m

	f(kHz)	v (μm/s) (-100,0)	v (μm/s) (75,0)	v (μm/s) (100, 0)	v (μm/s) (250, 0)	v (μm/s) (500, 0)	v (μm/s) (75,50)	v (μm/s) (75,100)	v (μm/s) (75,15 0)	v (μm/s) (75,20 0)	Vortex X axis (μm/s)	Vortex Y – axis (μm/s)
1	0.5	682.19	741.90	665.19	181.28	9.01	198.91	176.47	184.12	144.78	343.75	301.10
2	1	882.85	1158.3 9	894.21	282.54	27.30	211.05	178.56	187.67	155.82	476.68	388.90
3	1.5	729.03	1048.9 1	703.10	157.37	12.018	146.24	126.21	173.45	137.98	383.24	333.68
4	2	546.64	979.55	592.16	106.40	6.70	181.89	119.30	151.30	139.80	340.28	310.22
5	2.5	438.41	734.12	412.95	35.13	4.30	291.34	124.12	116.71	115.44	290.18	281.90
6	3	366.19	502.30	362.10	25.17	2.71	322.19	116.71	105.03	98.09	273.19	278.09

Fluid Conductivity = 10mS/m

	f(kHz)	v (μm/s) (-100,0)	v (μm/s) (75,0)	v (μm/s) (100, 0)	v (μm/s) (250, 0)	v (μm/s) (500, 0)	v (μm/s) (75,50)	v (μm/s) (75,100)	v (μm/s) (75,15 0)	v (μm/s) (75,20 0)	Vortex X axis (μm/s)	Vortex Y – axis (μm/s)
1	0.5	467.45	896.12	437.20	324.98	76.91	193.15 1	171.53	163.03	129.54	409.12	280.44
2	1	871.19	1009.9 7	861.98	408.12	49.79	206.98	206.87	198.98	162.19	484.29	375.17
3	1.5	772.20	961.10	773.10	241.31	24.91	198.01	179.41	144.21	127.28	410.81	336.19
4	2	775.87	922.60	757.87	96.94	13.21	204.51	163.12	172.41	138.60	340.28	281.32
5	2.5	663.90	713.49	663.32	126.66	8.91	182.17	169.64	131.45	101.09	331.29	306.48
6	3	450.89	678.10	407.89	91.78	6.17	178.19	154.17	123.91	89.10	307.49	274.10

Fluid Conductivity = 14mS/m

	f(kHz)	v (μm/s) (-100,0)	v (μm/s) (75,0)	v (μm/s)	v (μm/s)	v (μm/s)	v (μm/s)	v (μm/s)	v (μm/s)	v (μm/s)	Vortex X axis (μm/s)	Vortex Y – axis (μm/s)

				(100, 0)	(250, 0)	(500, 0)	(75,50)	(75,100)	(75,150)	(75,200)		
1	0.5	259.20	380.41	268.10	21.11	3.08	189.50	92.67	39.833	23.47	253.16	287.13
2	1	508.55	645.87	498.68	91.71	14.02	203.32	79.74	57.19	33.54	378.11	335.53
3	1.5	394.19	607.76	402.26	51.14	6.74	178.23	88.55	49.68	38.77	319.95	312.13
4	2	220.49	424.53	222.42	21.48	2.67	85.04	46.198	30.41	26.81	272.31	288.90
5	2.5	210.40	407.00	217.49	19.77	2.71	83.11	41.96	32.81	25.91	266.39	256.96
6	3	147.61	257.30	141.61	9.89	1.29	78.10	37.89	27.98	17.10	208.10	227.90

Fluid Conductivity = 20mS/m

	f(kHz)	v ($\mu m/s$) (-100,0)	v ($\mu m/s$) (75,0)	v ($\mu m/s$) (100, 0)	v ($\mu m/s$) (250, 0)	v ($\mu m/s$) (500, 0)	v ($\mu m/s$) (75,50)	v ($\mu m/s$) (75,100)	v ($\mu m/s$) (75,150)	v ($\mu m/s$) (75,200)	Vortex X axis ($\mu m/s$)	Vortex Y – axis ($\mu m/s$)
1	0.5	187.92	201.20	189.33	63.63	12.76	68.20	28.90	20.10	19.90	289.30	290.10
2	1	577.89	612.29	583.19	162.33	29.70	191.11	158.90	89.10	77.19	409.19	412.11
3	1.5	440.18	576.01	442.70	62.89	10.12	151.21	98.21	75.96	51.06	373.90	337.92
4	2	312.47	453.85	326.18	36.04	5.20	104.41	46.00	35.82	36.37	340.28	322.43
5	2.5	257.32	456.45	258.46	24.74	3.43	65.537	39.26	28.07	28.99	273.19	296.29
6	3	139.20	192.862	140.660	5.52	0.52	60.42	30.884	21.673	23.19	209.10	254.33

Inter electrode Gap = 50 μm

Fluid Conductivity = 3mS/m

	f(kHz)	v ($\mu m/s$) (-100,0)	v ($\mu m/s$) (75,0)	v ($\mu m/s$) (100, 0)	v ($\mu m/s$) (250, 0)	v ($\mu m/s$) (500, 0)	v ($\mu m/s$) (75,50)	v ($\mu m/s$) (75,100)	v ($\mu m/s$) (75,150)	v ($\mu m/s$) (75,200)	Vortex X axis ($\mu m/s$)	Vortex Y – axis ($\mu m/s$)
1	0.5	183.19	1039.67	329.55	28.22	6.89	145.58	85.17	60.06	58.30		
2	1	223.90	1234.50	243.32	39.88	4.54	153.14	71.75	47.89	49.66		
3	1.5	252.36	991.10	264.41	20.129	2.17	117.90	70.90	48.08	42.26		
4	2	164.30	669.33	164.53	11.52	1.22	94.31	44.11	35.05	30.00		
5	2.5	63.45	503.11	82.30	6.81	0.08	67.11	36.56	28.05	25.03		
6	3	51.78	388.17	44.03	3.91	0.05	52.35	30.36	21.70	19.60		

Fluid Conductivity = 7mS/m

	f(kHz)	v ($\mu m/s$) (-100,0)	v ($\mu m/s$) (75,0)	v ($\mu m/s$) (100, 0)	v ($\mu m/s$) (250, 0)	v ($\mu m/s$) (500, 0)	v ($\mu m/s$) (75,50)	v ($\mu m/s$) (75,100)	v ($\mu m/s$) (75,150)	v ($\mu m/s$) (75,200)	Vortex X axis ($\mu m/s$)	Vortex Y – axis ($\mu m/s$)
1	0.5	266.73	332.19	273.73	82.10	16.01	70.91	39.61	27.31	32.626		
2	1	501.29	748.49	575.91	110.79	16.78	160.91	83.28	59.73	48.91		
3	1.5	271.15	590.12	287.81	41.46	5.41	81.77	49.96	33.57	32.39		
4	2	183.98	553.47	164.81	28.61	3.44	74.11	41.24	30.02	28.16		
5	2.5	133.23	489.19	131.74	17.07	1.9	66.76	30.12	23.67	21.85		
6	3	37.89	317.99	40.11	6.34	0.62	28.20	15.21	12.27	10.80		

Fluid Conductivity = 10mS/m

	f(kHz)	v ($\mu m/s$) (-100,0)	v ($\mu m/s$) (75,0)	v ($\mu m/s$) (100, 0)	v ($\mu m/s$) (250, 0)	v ($\mu m/s$) (500, 0)	v ($\mu m/s$) (75,50)	v ($\mu m/s$) (75,100)	v ($\mu m/s$) (75,150)	v ($\mu m/s$) (75,200)	Vortex X axis ($\mu m/s$)	Vortex Y – axis ($\mu m/s$)
1	0.5	334.10	718.19	363.34	122.24	23.78	89.01	57.32	49.34	31.57		
2	1	462.22	917.80	391.44	61.01	8.75	100.41	66.10	54.28	44.374		
3	1.5	221.89	823.22	229.48	29.03	4.88	88.09	46.44	34.57	33.88		
4	2	124.90	656.21	131.21	13.59	1.96	48.98	29.17	21.78	20.39		
5	2.5	88.67	548.26	81.52	10.19	1.34	40.19	20.54	16.09	14.54		
6	3	42.99	303.05	43.76	6.67	0.73	41.54	27.09	19.62	16.54		

Fluid Conductivity = 14mS/m

	f(kHz)	v ($\mu m/s$) (-100,0)	v ($\mu m/s$) (75,0)	v ($\mu m/s$) (100, 0)	v ($\mu m/s$) (250, 0)	v ($\mu m/s$) (500, 0)	v ($\mu m/s$) (75,50)	v ($\mu m/s$) (75,100)	v ($\mu m/s$) (75,150)	v ($\mu m/s$) (75,200)	Vortex X axis ($\mu m/s$)	Vortex Y – axis ($\mu m/s$)
1	0.5	367.18	437.89	383.17	125.76	30.89	71.44	33.47	22.39	21.887		
2	1	479.19	682.11	501.19	97.89	16.78	107.54	50.30	38.98	21.19		
3	1.5	256.19	644.21	246.10	40.99	5.98	89.56	46.08	34.09	31.19		
4	2	161.23	576.74	158.90	23.278	4.30	83.64	52.69	41.21	32.61		
5	2.5	74.212	461.11	81.27	18.00	2.19	71.98	34.81	23.45	22.20		
6	3	39.10	288.19	36.17	12.67	1.39	50.34	22.09	17.41	16.17		

Fluid Conductivity = 20mS/m

	f(kHz)	v ($\mu m/s$) (-100,0)	v ($\mu m/s$) (75,0)	v ($\mu m/s$) (100, 0)	v ($\mu m/s$) (250, 0)	v ($\mu m/s$) (500, 0)	v ($\mu m/s$) (75,50)	v ($\mu m/s$) (75,100)	v ($\mu m/s$) (75,150)	v ($\mu m/s$) (75,200)	Vortex X axis ($\mu m/s$)	Vortex Y – axis ($\mu m/s$)
1	0.5	181.34	165.72	178.11	182.91	69.03	87.19	39.71	22.19	29.79		
2	1	397.88	497.43	411.67	136.77	27.65	110.13	51.62	42.89	48.29		
3	1.5	324.19	461.91	327.10	65.72	10.15	80.37	43.72	32.91	34.11		
4	2	265.30	462.18	264.40	39.39	5.9	76.91	41.02	28.77	28.66		
5	2.5	178.76	446.29	182.40	25.98	3.86	60.23	34.95	27.61	27.85		
6	3	63.59	407.36	56.19	12.91	1.55	43.01	24.34	18.18	15.98		

Inter electrode Gap = 75 μm

Fluid Conductivity = 3mS/m

	f(kHz)	v ($\mu m/s$) (-100,0)	v ($\mu m/s$) (75,0)	v ($\mu m/s$) (100, 0)	v ($\mu m/s$) (250, 0)	v ($\mu m/s$) (500, 0)	v ($\mu m/s$) (75,50)	v ($\mu m/s$) (75,100)	v ($\mu m/s$) (75,150)	v ($\mu m/s$) (75,200)	Vortex X axis ($\mu m/s$)	Vortex Y – axis ($\mu m/s$)
1	0.5	327.89	502.19	319.89	50.89	8.56	78.42	43.11	27.66	31.09	327.89	
2	1	288.90	1491.20	287.67	39.53	5.66	198.19	119.34	83.53	66.84	288.90	
3	1.5	44.28	1019.10	49.01	16.91	2.19	126.34	68.57	45.82	40.34	44.28	
4	2	33.98	923.92	34.92	8.56	1.18	147.02	53.21	39.19	28.22	33.98	
5	2.5	42.11	812.39	52.30	6.00	0.72	76.11	42.18	27.76	24.07	42.11	
6	3	50.19	732.19	51.19	5.87	0.66	66,17	33.16	19.78	21.19	50.19	

Fluid Conductivity = 7mS/m

	f(kHz)	v ($\mu m/s$) (-100,0)	v ($\mu m/s$) (75,0)	v ($\mu m/s$) (100, 0)	v ($\mu m/s$) (250, 0)	v ($\mu m/s$) (500, 0)	v ($\mu m/s$) (75,50)	v ($\mu m/s$) (75,100)	v ($\mu m/s$) (75,150)	v ($\mu m/s$) (75,200)	Vortex X axis ($\mu m/s$)	Vortex Y – axis ($\mu m/s$)
1	0.5	482.07	499.12	465.13	191.22	50.07	172.06	42.98	24.67	38.87		
2	1	813.21	1395.67	811.18	153.67	27.04	185.98	87.54	65.00	68.49		
3	1.5	570.71	997.89	593.19	75.66	13.95	181.69	105.28	78.00	77.01		
4	2	375.57	918.19	375.24	47.03	6.48	182.62	116.30	76.29	74.49		
5	2.5	170.52	789.12	177.88	24.03	3.91	176.99	85.95	61.89	57.74		
6	3	47.33	696.78	44.19	18.05	2.03	109.31	59.67	40.59	38.86		

Fluid Conductivity = 10mS/m

	f(kHz)	v ($\mu m/s$) (-100,0)	v ($\mu m/s$) (75,0)	v ($\mu m/s$) (100, 0)	v ($\mu m/s$) (250, 0)	v ($\mu m/s$) (500, 0)	v ($\mu m/s$) (75,50)	v ($\mu m/s$) (75,100)	v ($\mu m/s$) (75,150)	v ($\mu m/s$) (75,200)	Vortex X axis ($\mu m/s$)	Vortex Y – axis ($\mu m/s$)
1	0.5	399.10	440.87	401.56	146.02	28.24	61.96	36.86	19.81	29.48		
2	1	670.20	1247.89	690.22	91.11	12.004	231.50	116.15	85.67	80.07		
3	1.5	737.78	965.36	740.55	139.02	22.34	163.71	87.32	58.09	61.10		
4	2	566.78	910.81	572.34	79.62	11.49	177.69	92.62	61.35	61.77		
5	2.5	350.41	871.11	349.84	45.96	6.22	206.07	98.87	66.92	63.29		
6	3	207.33	834.32	209.87	35.05	4.56	147.52	81.53	58.19	53.88		

Fluid Conductivity = 14mS/m

	f(kHz)	v ($\mu m/s$) (-100,0)	v ($\mu m/s$) (75,0)	v ($\mu m/s$) (100, 0)	v ($\mu m/s$) (250, 0)	v ($\mu m/s$) (500, 0)	v ($\mu m/s$) (75,50)	v ($\mu m/s$) (75,100)	v ($\mu m/s$) (75,150)	v ($\mu m/s$) (75,200)	Vortex X axis ($\mu m/s$)	Vortex Y – axis ($\mu m/s$)
1	0.5	288.89	342.76	298.69	73.567	12.98	55.39	25.57	16.16	19.15		
2	1	731.47	1082.75	774.03	162.01	30.31	152.31	89.19	63.22	62.19		
3	1.5	627.77	735.01	631.17	180.85	38.05	107.36	48.06	26.12	32.89		
4	2	518.91	677.89	524.09	87.99	15.26	112.30	48.51	37.30	37.21		
5	2.5	422.67	616.78	429.87	69.19	9.56	115.93	62.77	42.34	38.78		
6	3	331.31	566.66	335.02	48.11	6.52	91.12	51.74	35.98	35.09		

Fluid Conductivity = 20mS/m

	f(kHz)	v ($\mu m/s$) (-100,0)	v ($\mu m/s$) (75,0)	v ($\mu m/s$) (100, 0)	v ($\mu m/s$) (250, 0)	v ($\mu m/s$) (500, 0)	v ($\mu m/s$) (75,50)	v ($\mu m/s$) (75,100)	v ($\mu m/s$) (75,150)	v ($\mu m/s$) (75,200)	Vortex X axis ($\mu m/s$)	Vortex Y – axis ($\mu m/s$)

1	0.5	350.20	366.70	349.89	154.78	36.92	108.27	37.87	24.55	32.45		
2	1	676.20	737.89	680.19	276.77	46.96	152.78	48.69	14.38	35.18		
3	1.5	406.50	548.73	404.19	71.38	11.62	94.73	42.88	32.87	32.65		
4	2	453.61	506.02	461.12	105.66	18.14	66.28	33.47	26.67	29.20		
5	2.5	406.74	502.40	412.77	77.89	12.85	71.36	35.60	28.90	29.19		
6	3	378.27	481.08	371.11	82.49	12.75	70.59	37.01	27.34	28.03		

Inter electrode Gap = 100 μm

Fluid Conductivity = 3mS/m

	f(kHz)	v (μm/s) (-100,0)	v (μm/s) (75,0)	v (μm/s) (100, 0)	v (μm/s) (250, 0)	v (μm/s) (500, 0)	v (μm/s) (75,50)	v (μm/s) (75,100)	v (μm/s) (75,150)	v (μm/s) (75,200)	Vortex X axis (μm/s)	Vortex Y – axis (μm/s)
1	0.5	357.18	489.19	326.89	47.32	6.38	57.86	28.71	22.21	23.67		
2	1	434.56	657.81	466.81	32.81	4.21	58.44	36.41	26.26	21.18		
3	1.5	228.31	312.65	232.04	10.19	1.21	22.29	14.01	10.48	9.34		
4	2	139.62	165.19	137.22	5.77	0.72	13.87	7.45	6.31	6.06		
5	2.5	88.92	107.61	82.24	3.68	0.47	9.25	5.28	4.32	3.96		
6	3	44.19	54.19	44.02	1.92	0.20	6.35	3.24	2.23	1.98		

Fluid Conductivity = 7mS/m

	f(kHz)	v (μm/s) (-100,0)	v (μm/s) (75,0)	v (μm/s) (100, 0)	v (μm/s) (250, 0)	v (μm/s) (500, 0)	v (μm/s) (75,50)	v (μm/s) (75,100)	v (μm/s) (75,150)	v (μm/s) (75,200)	Vortex X axis (μm/s)	Vortex Y – axis (μm/s)
1	0.5	235.61	175.37	241.89	128.42	27.88	54.67	18.89	10.11	17.58		
2	1	600.89	700.01	601.11	91.19	15.61	84.71	43.46	33.06	28.55		
3	1.5	510.14	620.22	512.25	54.37	7.07	60.77	40.69	29.93	29.23		
4	2	434.58	584.07	433.42	29.19	3.18	47.12	28.31	22.01	20.61		
5	2.5	245.93	367.96	351.18	19.69	2.51	43.65	22.33	16.96	16.27		
6	3	200.81	211.49	201.11	10.31	1.84	23.14	14.97	10.33	9.89		

Fluid Conductivity = 10mS/m

	f(kHz)	v (μm/s) (-100,0)	v (μm/s) (75,0)	v (μm/s) (100, 0)	v (μm/s) (250, 0)	v (μm/s) (500, 0)	v (μm/s) (75,50)	v (μm/s) (75,100)	v (μm/s) (75,150)	v (μm/s) (75,200)	Vortex X axis (μm/s)	Vortex Y – axis (μm/s)
1	0.5	124.19	111.38	147.89	133.10	46.78	47.89	18.19	7.92	20.54		
2	1	469.19	577.80	488.94	139.10	26.67	70.67	34.19	26.03	24.70		
3	1.5	494.29	537.32	489.10	66.79	8.91	71.66	40.48	27.22	27.61		
4	2	494.79	566.45	484.38	47.63	5.41	55.41	34.53	26.31	25.84		
5	2.5	397.19	517.28	389.52	27.90	3.14	41.19	24.43	17.89	16.26		

6	3	268.19	363.36	273.10	15.87	1.91	30.14	17.65	12.41	12.09		

Fluid Conductivity = 14mS/m

	f(kHz)	v (μm/s) (-100,0)	v (μm/s) (75,0)	v (μm/s) (100, 0)	v (μm/s) (250, 0)	v (μm/s) (500, 0)	v (μm/s) (75,50)	v (μm/s) (75,100)	v (μm/s) (75,150)	v (μm/s) (75,200)	Vortex X axis (μm/s)	Vortex Y – axis (μm/s)
1	0.5	74.76	45.41	74.59	101.59	58.86	34.19	27.19	19.18	21.99		
2	1	256.66	341.40	234.48	180.88	47.56	90.95	40.47	27.98	33.89		
3	1.5	384.50	414.30	378.61	96.74	18.71	54.66	25.88	20.11	12.89		
4	2	374.44	404.09	374.17	53.71	8.99	74.20	31.63	21.44	21.28		
5	2.5	370.52	466.78	350.82	36.76	5.53	60.26	28.87	20.66	19.20		
6	3	309.78	404.69	294.12	21.19	2.82	36.22	27.59	20.35	19.89		

Fluid Conductivity = 20mS/m

	f(kHz)	v (μm/s) (-100,0)	v (μm/s) (75,0)	v (μm/s) (100, 0)	v (μm/s) (250, 0)	v (μm/s) (500, 0)	v (μm/s) (75,50)	v (μm/s) (75,100)	v (μm/s) (75,150)	v (μm/s) (75,200)	Vortex X axis (μm/s)	Vortex Y – axis (μm/s)
1	0.5	62.00	33.08	60.56	105.67	89.19	53.19	25.66	7.35	26.35		
2	1	313.42	337.23	313.96	81.316	18.48	61.78	24.87	15.61	16.74		
3	1.5	290.80	249.90	290.18	145.52	16.76	52.55	19.89	12.89	13.65		
4	2	252.54	218.39	263.47	70.41	12.89	41.78	18.37	12.74	13.94		
5	2.5	316.20	301.98	308.89	49.97	7.98	55.86	25.67	16.54	15.98		
6	3	251.54	267.19	253.19	18.54	2.21	34.14	18.87	13.86	12.34		

Inter electrode Gap = 150 μm

Fluid Conductivity = 3mS/m

	f(kHz)	v (μm/s) (-100,0)	v (μm/s) (75,0)	v (μm/s) (100, 0)	v (μm/s) (250, 0)	v (μm/s) (500, 0)	v (μm/s) (75,50)	v (μm/s) (75,100)	v (μm/s) (75,150)	v (μm/s) (75,200)	Vortex X axis (μm/s)	Vortex Y – axis (μm/s)
1	0.5	158.93	7.53	44.72	29.88	4.04	22.87	11.28	9.64	8.57		
2	1	128.04	34.54	122.78	16.27	1.58	10.94	5.48	4.20	2.22		
3	1.5	39.19	2.18	35.60	4.02	0.42	6.31	3.09	2.5	2.41		
4	2	35.89	2.08	34.48	3.34	0.33	4.34	2.59	2.08	1.91		
5	2.5	16.81	0.56	17.89	1.98	0.18	2.54	1.48	1.09	0.98		
6	3	11.78	0.22	11.67	1.34	0.12	1.5	0.94	0.73	0.64		

Fluid Conductivity = 7mS/m

	f(kHz)	v (μm/s) (-100,0)	v (μm/s) (75,0)	v (μm/s) (100, 0)	v (μm/s) (250, 0)	v (μm/s) (500, 0)	v (μm/s) (75,50)	v (μm/s) (75,100)	v (μm/s) (75,150)	v (μm/s) (75,200)	Vortex X axis (μm/s)	Vortex Y – axis (μm/s)
1	0.5	38.34	5.61	36.22	27.71	5.86	12.87	4.11	1.72	2.81		
2	1	136.71	14.41	138.81	26.88	6.89	32.14	15.12	7.81	11.22		
3	1.5	116.72	8.09	109.21	29.01	3.34	24.41	14.13	11.06	10.89		
4	2	92.81	4.59	91.11	11.74	1.26	14.58	7.53	5.41	4.91		

5	2.5	64.44	2.87	60.54	7.37	0.73	8.34	5.21	4.05	3.65		
6	3	55.68	5.86	58.15	5.49	0.61	7.31	4.49	3.48	3.21		

Fluid Conductivity = 10mS/m

	f(kHz)	v (μm/s) (-100,0)	v (μm/s) (75,0)	v (μm/s) (100, 0)	v (μm/s) (250, 0)	v (μm/s) (500, 0)	v (μm/s) (75,50)	v (μm/s) (75,100)	v (μm/s) (75,150)	v (μm/s) (75,200)	Vortex X axis (μm/s)	Vortex Y – axis (μm/s)
1	0.5	70.49	6.88	69.18	83.19	26.71	26.10	10.64	7.88	14.87		
2	1	245.12	43.93	255.69	107.23	19.64	56.44	22.09	17.28	18.04		
3	1.5	139.51	7.85	134.55	27.81	4.18	24.35	12.67	8.64	9.32		
4	2	130.59	40.11	130.72	22.232	2.86	20.341	9.81	7.48	4.12		
5	2.5	105.12	19.17	98.14	13.75	1.57	16.47	9.02	6.48	6.22		
6	3	73.42	6.98	71.89	8.34	0.81	10.62	5.43	4.31	4.02		

Fluid Conductivity = 14mS/m

	f(kHz)	v (μm/s) (-100,0)	v (μm/s) (75,0)	v (μm/s) (100, 0)	v (μm/s) (250, 0)	v (μm/s) (500, 0)	v (μm/s) (75,50)	v (μm/s) (75,100)	v (μm/s) (75,150)	v (μm/s) (75,200)	Vortex X axis (μm/s)	Vortex Y – axis (μm/s)
1	0.5	62.19	2.65	61.91	45.01	8.77	22.64	8.94	2.91	4.23		
2	1	226.89	4.67	245.77	102.30	14.15	49.67	19.87	15.11	16.64		
3	1.5	203.33	30.68	200.01	82.01	11.13	43.07	19.46	14.32	16.17		
4	2	177.81	12.34	165.18	44.36	5.45	39.78	15.47	11.45	10.899		
5	2.5	163.23	2.75	165.03	29.74	3.13	30.15	15.56	10.83	9.55		
6	3	101.89	6.25	103.13	13.89	1.45	20.04	9.63	6.91	6.82		

Fluid Conductivity = 20mS/m

	f(kHz)	v (μm/s) (-100,0)	v (μm/s) (75,0)	v (μm/s) (100, 0)	v (μm/s) (250, 0)	v (μm/s) (500, 0)	v (μm/s) (75,50)	v (μm/s) (75,100)	v (μm/s) (75,150)	v (μm/s) (75,200)	Vortex X axis (μm/s)	Vortex Y – axis (μm/s)
1	0.5	42.13	1.89	41.19	5.74	0.66	7.12	3.54	2.46	2.52		
2	1	214.77	3.66	221.17	96.78	16.87	53.74	23.78	18.01	19.20		
3	1.5	155.78	3.89	150.17	68.91	7.28	17.78	14.22	9.66	8.21		
4	2	133.52	3.71	130.65	58.01	11.35	35.86	12.89	8.91	9.56		
5	2.5	127.89	3.63	125.70	44.47	6.21	28.09	11.85	9.46	9.67		
6	3	97.11	3.63	94.91	28.11	3.15	27.78	13.76	10.02	9.87		

Chamber Height

Electrode 75μm 1kHz at 10ms/m

	Chamber Height(μm)	Velocity (at 50 μm,0)
1	100	1212.4
2	200	1224.5
3	300	1216.2
4	400	1243.0
5	500	1211.2
6	600	1220.2

7	700	1217.5
8	800	1222.4
9	900	1211.7
10	1000	1226.2

	Chamber Height(μm)	20 μm	50 μm	75 μm	100 μm	150 μm
1	100	100	100	100	100	100
2	200	200	200	200	200	200
3	300	300	300	300	300	
4	400	400	400	400	400	
5	500	483	486	480		
6	600	485	487	485		
7	700	485	490	485		

Electrode Length

This decides what should be our electrode geometry that is electrode gap and width

Electrode 75 μm 1kHz at 10ms/m

	Electrode Length(μm)	Velocity (at 47.5,0) 5V	Velocity (at 47.5,0) 10V
1	100	505	2450
2	200	513	2570
3	300	812	4000
4	400	1034	5100
5	500	1444	6660
6	600	966	4800
7	700	924	4350
8	800	883	3900
9	900	765	3670
10	1000	650	3200
11	1100	678	3300

Electrode 100μm 1kHz at 10ms/m

	Electrode Length(μm)	Velocity (60,0) 5V	Velocity (at 60,0) 10V
1	100	642	3000
2	200	652	3200
3	300	712	3700
4	400	887	4200
5	500	1077	5200
6	600	893	4150
7	700	918	4300

8	800	928	4400
9	900	989	4500
10	1000	1009	5000
11	1100	899	4100

Velocity vs AC Signal

Conductivity 10mS/cm and 1kHz AT 500 μm WIDE ELECTRODE

Calculated from the right middle of the electrode and edges.

	Interelectrode Gap (um)	v(um/s) @5V	v(um/s) @7.5V	v(um/s) @10V
1	20	1009.97	2645.32	5920.79
2	50	917.80	2360.18	5408.65
3	75	1247.89	2991.70	6662.40
4	100	557.80	2125.98	5118.30
5	150	341.65	1937.88	4525.50

P – DEP on cells capture

Speed 10 μm /s = Total cells 20. At 1MHz

	Chamber Height (μm)	2V	5V	10V	15V	20V
1	250	2um pull	10um pull	25um pull	Full in (45.34s)	Full pull in 36.37s
2	200	4um	17	50um pull	Full Pull in 38.80s	Full pull in 32.71s
3	150	12um	30um	Full pull in 37.90s	Full Pull 34.19	Full Pull 29.80

Speed 20 μm /s = Total cells 20.

	Chamber Height (μm)	2V	5V	10V	15V	20V
1	250	no	No	8um pull	Pulled by 25um	Some cells captured at 33.7s some still moved on but were

						pulled down by 200um.
2	200	no	6um	28um	105um (however at 2MHz captured)	Full pull in 19.8sec
3	150	2um	14um pull	45um pull	Full Pull 19.6s	Full Pull 18.7s

Speed 30 μm /s = Total cells 20.

	Chamber Height (μm)	2V	5V	10V	15V	20V
1	250	0	0	2um	Pulled by 18um	Pulled by 40um
2	200	0	0	21um	Pulled by 85um	Captured at 14.45s
3	150	no	8um	Pull down by 25um	Pulled at 17.2s	Full pull 14.1s

Speed at 40 μm /s

	Chamber Height (μm)	2V	5V	10V	15V	20V
1	250	no	No	No	2um	Pulled by 25um
2	200	no	no	8um	75um	Full pull in 12.8sec
3	150	no	6um pull	15um pull	Pulled to 125um	Full Pull 10.50s

<u>Cell separation using p – DEP via comsol.</u>

Multi - electrode AC pDEP.

Chamber Height (μm)	10Vpp	15Vpp	20Vpp
250	8^{th} Electrode at 91.6sec	5^{th} Elect. in 44.30sec	2electrode Edge in 19sec
300	None	On top of 6^{th} at 15Vpp. In 65.20sec.	3 and 4^{th} Elec 33.40sec.

400	None	7th and 8th elec 20Vpp 93.1s	7th and 8th elec 20Vpp 67.5s

At 10Vpp nothing happened.

20Vpp final now checking maximum speed we can deal with to make process fast. Keeping Height 300um height.

Speed μm /s	Capture Electrode	Time (sec)
10	1st	73.30
20	1st	62.35
30	2nd	57.40
40	3rd	33.40
50	5th	36.30
60	6th	36.30
70	6th	35.10
80	7th	34.90
90	8th	35.75
100	8th	35.50
110	9th	35.10
120	10th	34.25